

SANDIA REPORT

SAND2004-3226

Unlimited Release

Printed August 2004

THE SANDIA GEOMODEL Theory and User's Guide

A.F. Fossum, and R.M. Brannon

Prepared by
Sandia National Laboratories
Albuquerque, New Mexico 87185 and Livermore, California 94550

Sandia is a multiprogram laboratory operated by Sandia Corporation,
a Lockheed Martin Company, for the United States Department of Energy's
National Nuclear Security Administration under Contract DE-AC04-94AL85000.

Approved for public release; further dissemination unlimited.



Sandia National Laboratories

Issued by Sandia National Laboratories, operated for the United States Department of Energy by Sandia Corporation.

NOTICE: This report was prepared as an account of work sponsored by an agency of the United States Government. Neither the United States Government, nor any agency thereof, nor any of their employees, nor any of their contractors, subcontractors, or their employees, make any warranty, express or implied, or assume any legal liability or responsibility for the accuracy, completeness, or usefulness of any information, apparatus, product, or process disclosed, or represent that its use would not infringe privately owned rights. Reference herein to any specific commercial product, process, or service by trade name, trademark, manufacturer, or otherwise, does not necessarily constitute or imply its endorsement, recommendation, or favoring by the United States Government, any agency thereof, or any of their contractors or subcontractors. The views and opinions expressed herein do not necessarily state or reflect those of the United States Government, any agency thereof, or any of their contractors.

Printed in the United States of America. This report has been reproduced directly from the best available copy.

Available to DOE and DOE contractors from
U.S. Department of Energy
Office of Scientific and Technical Information
P.O. Box 62
Oak Ridge, TN 37831

Telephone: (865)576-8401
Facsimile: (865)576-5728
E-Mail: reports@adonis.osti.gov
Online ordering: <http://www.osti.gov/bridge>

Available to the public from
U.S. Department of Commerce
National Technical Information Service
5285 Port Royal Rd
Springfield, VA 22161

Telephone: (800)553-6847
Facsimile: (703)605-6900
E-Mail: orders@ntis.fedworld.gov
Online order: <http://www.ntis.gov/help/ordermethods.asp?loc=7-4-0#online>



SAND2004-3226
Unlimited Release
Printed August 2004

THE SANDIA GEOMODEL

Theory and User's Guide

Arlo F. Fossum and Rebecca M. Brannon
Geomechanics, Dept. 6117
Sandia National Laboratories
PO BOX 5800
Albuquerque, NM 87185

Abstract

The mathematical and physical foundations and domain of applicability of Sandia's GeoModel are presented along with descriptions of the source code and user instructions. The model is designed to be used in conventional finite element architectures, and (to date) it has been installed in five host codes without requiring customizing the model subroutines for any of these different installations. Although developed for application to geological materials, the GeoModel actually applies to a much broader class of materials, including rock-like engineered materials (such as concretes and ceramics) and even to metals when simplified parameters are used. Nonlinear elasticity is supported through an empirically fitted function that has been found to be well-suited to a wide variety of materials. Fundamentally, the GeoModel is a generalized plasticity model. As such, it includes a yield surface, but the term "yield" is generalized to include *any* form of inelastic material response including microcrack growth and pore collapse. The geomodel supports deformation-induced anisotropy in a limited capacity through kinematic hardening (in which the initially isotropic yield surface is permitted to translate in deviatoric stress space to model Bauschinger effects). Aside from kinematic hardening, however, the governing equations are otherwise isotropic. The GeoModel is a genuine unification and generalization of simpler models. The GeoModel can employ up to 40 material input and control parameters in the rare case when all features are used. Simpler idealizations (such as linear elasticity, or Von Mises yield, or Mohr-Coulomb failure) can be replicated by simply using fewer parameters. For high-strain-rate applications, the GeoModel supports rate dependence through an overstress model.

Intentionally Left Blank

Acknowledgements

The authors are grateful for the support received over the years from a number of Sandia project managers and colleagues who have provided financial support and encouraged the development and enhancement of this general geomaterial model for use in Sandia computer codes. The initial development of the model was begun under a project led by Mike Stone under the U.S. Department of Energy (DOE) Advanced Computational Technology Initiative (ACTI) program. Additional development was made under an Engineering Sciences Research Foundation (ESRF) project led by Hal Morgan; a Defense Programs (DP) Penetration project led first by Jim Hickerson and later by Danny Frew; several DOE Accelerated Strategic Computing Initiative (ASCI) Design and Qualification (DQ) Materials & Physics Models (M&PM) projects led by Mike McGlaun and Justine Johannes, a Hard and Deeply Buried Target (HDBT) project led by Paul Yarrington and Shawn Burns; a Model Accreditation Via Experimental Sciences For Nuclear Weapons (MAVEN) laboratory testing project led by Moo Lee, two LDRD projects, one led by Larry Costin and the other by Rich Regueiro; and an Army Research Laboratory (ARL) project led by Bill Bruchey.

The authors acknowledge individual contributions of Steve Akers, Lupe Arguello, Paul Booker, Kevin Brown, Ted Carney, Mike Chiesa, Jim Cox, Kent Danielson, Mike Forrestal, Craig Foster, Joanne Fredrich, Lew Glenn, Ed Hoffman, Dave Holcomb, John Holland, Joe Jung, Daniel Kletzli, Colby Lavin, Estaban Marin, Yvonne Murray, Bill Oberkampf, Bill Olsson, John Pott, Tom Pucik, Jonathan Rath, Sal Rodriguez, Bill Scherzinger, Paul Senseny, Allen Shirley, Len Schwer, Steve Sobolik, Bob Swift, Tom Voth, Tom Warren, Joel Wirth, and Mike Wong, who have provided code support, user feedback, bug fixes, theoretical discussions, and constructive criticism.

The first author, AFF, would like to express his sincere appreciation to Rebecca Brannon for painstakingly going through each line of coding in the material model subroutine checking theoretical soundness, debugging, documenting, and suggesting improvements. The quality of the model has vastly improved as a result. The second author, RMB, appreciates the numerous program managers and other supporters who have given Arlo Fossum sufficient time and resources to assemble a relatively comprehensive set of components that *ideally* should be discussed in any material model resource document (theory, code, verification, validation, calibration instructions, and datasets for various materials). RMB admires Arlo Fossum for his mentoring, enthusiasm, unflinching sense of humor, and his remarkable ability to discern the salient physics evident in disparate geomechanical data. Our compatible skills and temperaments have established the foundation for an effective and enduring materials modeling team. Finally, both authors are grateful to our family members for their patience and support during the many late-night hours required to reach this year's model development and dissemination goals.

Arlo Fossum
affossu@sandia.gov

Rebecca Brannon
rbrann@sandia.gov

Sandia National Laboratories
August 30, 2004.

Contents

Acknowledgements	v
Introduction	1
GeoModel overview	2
<i>Features of the GeoModel</i>	2
<i>Limitations of the GeoModel</i>	3
Notation	7
Typesetting conventions	7
Vector and Tensor notation	7
The Stress Tensor	9
Stress invariants	11
Derivatives of the stress invariants	12
Special stress states	13
<i>HYDROSTATIC (HYD)</i>	13
<i>TRIAXIAL (TXC and TXE)</i> :	14
<i>SIMPLE/PURE SHEAR and PRESSURE-SHEAR LOADING (SHR)</i>	18
Spatial and Reference stress (frame indifference)	19
Lode coordinates	20
<i>Octahedral yield profile visualization</i>	22
<i>Meridional yield profile visualization</i>	23
<i>Closed-form solution for ordered eigenvalues</i>	24
GeoModel theory	25
Elasticity	26
<i>Nonlinear elasticity</i>	27
<i>Assigning values to the elastic constants</i>	27
The elastic limit (yield surface)	28
<i>The cap function, f_c</i>	36
<i>Elastic-plastic coupling</i>	37
<i>Meridional shear limiter function, F_f</i>	38
<i>The complete GeoModel yield function</i>	42
<i>The “J3TYPE” Lode-angle function, Γ</i>	43
Advancing the solution (groundwork discussion)	47
Evolution equations	50
<i>Evolution equation for the porosity-related internal state variable, κ</i>	50
<i>Evolution equation for the kinematic hardening backstress tensor</i>	58
Advancing the solution (final step, consistency parameter)	60
<i>Formal equivalence with oblique return algorithms</i>	60
<i>Quasistatic inelastic tangent stiffness tensor</i>	61
<i>Stability issues</i>	61
Rate Dependence	63
Viscoplasticity model overview	63
Viscoplasticity model derivation	66
<i>Limiting case</i>	68
Assigning a value to the characteristic material time	70
Thermodynamics considerations	71
GeoModel Numerical Solution scheme	72
Role of the GeoModel within a finite-element program	72
Spatial stability (mesh dependence/loss of strong ellipticity)	74
GeoModel files, subroutines, memory requirements, and model installation requirements.	75

Arguments passed to and from the GeoModel driver routine.....	76
PLOTTABLE OUTPUT	77
GeoModel algorithm	78
<i>Rate independent (inviscid) part of the viscoplasticity equations</i>	78
<i>Viscous part of the viscoplasticity equations</i>	78
Software “confidence building” activities	79
<i>Preliminary convergence testing</i>	86
Verification: single-element problems (regression suite)	87
<i>Other single-element tests</i>	92
Verification: Hendren & Ayier pressurized cylinder	93
Elastic free-field wave form (finite-element verification)	95
Parameterization (calibration)	96
Nonlinear elasticity	97
Elastic-plastic coupling	98
Triaxial Compression	99
Parameterization: Rate dependence	102
Building confidence in the physical theory	104
Post-calibration Triaxial loading.....	105
Field-scale penetration	106
Free field wave form for spherical shock loading.....	107
Closing Remarks	108
APPENDIX A: Parameterizing the GeoModel	A-1
APPENDIX B: Nomenclature and Data Sets	B-1
Model Parameters	
(User Input)	B-2
Internal State Variables	
(Plotable Output)	B-8
Dataset for Salem Limestone	B-14
Dataset for Sidewinder Tuff.....	B-15
Dataset for lab scale intact Climax Granite	B-16
Dataset for field scale jointed Climax Granite.....	B-17
Dataset for 23MPa Concrete	B-18
Dataset for Conventional Strength Portland Concrete.....	B-19
Datasets for mimicking classical (simplified) models	B-20
<i>Von-Mises material</i>	B-21
<i>Maximum Principal Stress failure</i>	B-21
<i>Tresca</i>	B-22
<i>Mohr-Coulomb</i>	B-22
<i>Sub-input set for linear elasticity</i>	B-26
<i>Sub-input set for “turning off” all rate dependence</i>	B-26
<i>Sub-input set for disabling kinematic hardening</i>	B-26
<i>Sub-input set for associativity</i>	B-26
<i>Sub-input set for disabling cap and crush curve</i>	B-26
<i>Sub-input set for disabling tensile cut-off limits</i>	B-26

REFERENCES

Figures

Figure 1.0.	GeoModel continuous yield surface.	1
Figure 1.1.	Distinction between a yield surface and the limit surface.	5
Figure 3.1.	Typical hydrostatic (pressure vs. volumetric strain) compression data.	13
Figure 3.2.	Triaxial compression (TXC) and triaxial extension (TXE).....	15
Figure 3.3.	Triaxial and CSD load paths.....	16
Figure 3.4.	An octahedral yield profile.....	22
Figure 3.5.	Distortion of the meridional profile when using non-isomorphic stress measures. 23	
Figure 4.1.	Backstress and shifted stress.	31
Figure 4.2.	Qualitatively meridional profile shapes resulting from (a) porosity alone, (b) microcracks alone, and (c) porosity and microcracks in combination.	33
Figure 4.3.	Distinction between two-surface upper-bound models and the GeoModel.	33
Figure 4.4.	Basic shapes of the three key functions that characterize the composite shape of the yield surface.....	35
Figure 4.5.	GeoModel cap function	36
Figure 4.6.	Kinematic hardening.	40
Figure 4.7.	Yield surface evolution with both microcracking and porosity.	40
Figure 4.8.	Shear limiter function (unshifted and shifted).....	41
Figure 4.9.	Octahedral yield profiles, plotted at allowable values of the strength ratio.	45
Figure 4.10.	Lode angle function (for various ψ strength ratios) plotted vs. the Lode angle varying from -30 degrees (TXE) to $+30$ degrees (TXC).	46
Figure 4.11.	Hardening mechanisms.	50
Figure 4.12.	A conventional porosity crush curve (dashed) and state path (solid).....	52
Figure 4.13.	The Gurson theory for porous yield surfaces compared with the GeoModel cap function at various values of the internal state variable κ . Qualitatively, the theories are similar.	53
Figure 4.14.	Relationship between (a) hydrostatic pressure vs. volumetric strain data, (b) the GeoModel X-function, and (c) a traditional porosity vs. pressure crush curve.	54
Figure 4.15.	Continuously differentiable GeoModel yield function and some characteristic dimensions.	56
Figure 4.16.	Meridional plane in which the magnitude of the stress deviator “r” is plotted against (which is proportional to the pressure “p”)	58
Figure 4.17.	The effect of kinematic hardening on the meridional plane that contains the backstress.....	59
Figure 5.1.	Rate dependence.....	64
Figure 5.2.	High-rate weighting factor at various initial states.....	68
Figure 5.3.	Rate dependence in uniaxial strain loading of a nonhardening pressure-insensitive material.	69
Figure 6.1.	Meaning of the “SHEAR” output variable.....	77
Figure 7.1.	Screen shot of the MS Excel interface for the GeoModel material-model driver (MMD).	83
Figure 7.2.	Subcycling test for hydrostatic loading.	86
Figure 7.3.	Rate of convergence.	86
Figure 7.4.	Unconfined compression.	88
Figure 7.5.	20 MPa triaxial compression.....	89
Figure 7.6.	Reduced triaxial extension.	90
Figure 7.7.	Plane Strain.....	91

Figure 7.8a.	Crush curve and hydrostatic loading verification.....	92
Figure 7.8b.	Rate dependence TXE/TXC ratio verification for triaxial load/unload.	92
Figure 7.9.	Hendron & Ayier verification problem.....	94
Figure 7.10.	Spherical cavity geometry.....	95
Figure 7.11.	Finite-element vs. analytical/numerical elastic wave velocity at 470 meters from a velocity spherical cavity source at 204 meters.....	95
Figure 8.1.	Meridional limit curves for some materials already parameterized to the GeoModel.....	96
Figure 8.2.	Nonlinear elasticity in shear.....	97
Figure 8.3.	Nonlinear elasticity in hydrostatic loading.....	97
Figure 8.4.	Elastic-plastic coupling: deformation-induced changes in elastic moduli (Salem Limestone).....	98
Figure 8.5.	Shear failure limit curve compared with concrete data.....	99
Figure 8.6.	Progression of the hardening yield surface (family of blue lines) under a triaxial compression test (red path), illustrated with correspondence of the meridional plane to the stress-strain diagram.....	100
Figure 8.7.	Shear-enhanced dilatation under compression.....	101
Figure 8.8.	Kolsky (split Hopkinson) bar apparatus used to obtain data in Fig. 8.9.....	102
Figure 8.9.	Suitability of the GeoModel overstress rate-dependence model to match observed data.....	103
Figure 9.1.	(a) GeoModel prediction of uniaxial strain loading. (b) GeoModel predictions of triaxial stress-strain response at various confining pressures.....	105
Figure 9.2.	After the GeoModel was fitted to laboratory-scale material property tests, it was used to predict projectile penetration depth using spherical cavity expansion analysis.....	106
Figure 9.3.	Spherical cavity geometry.....	107
Figure 9.4.	GeoModel + JAS3D finite-element prediction (blue) vs. measured (red) velocity and displacement at 470 m. from a spherical cavity velocity source at 204 meters.	107
Figure A.1.	Ideal hydrostatic parameterization data.....	A-2
Figure A.2.	Less-preferable hydrostatic parameterization data.....	A-2
Figure A.3.	Data representative of a triaxial compression parameterization test.....	A-3
Figure A.4.	A family of TXC tests conducted to failure.....	A-5
Figure A.5.	TXC stress-strain plots and extraction of their peak values to construct the meridional limit curve (data are for porcelanite).....	A-6
Figure A.6.	The Lode function information originally shown in Fig. 4.10 of the main report, now displayed with a transformed ordinate.....	A-10
Figure A.7.	A sketch of how data might be distributed at non-triaxial states.....	A-10
Figure B.1.	Other yield surface shapes supported by the GeoModel.....	B-20
Figure B.2.	Classical simplified yield surfaces in the octahedral plane.....	B-20
Figure B.3.	A stress at the limit state under Mohr-Coulomb theory.....	B-22

Intentionally Left Blank

THE SANDIA GEOMODEL

Theory and User's Guide

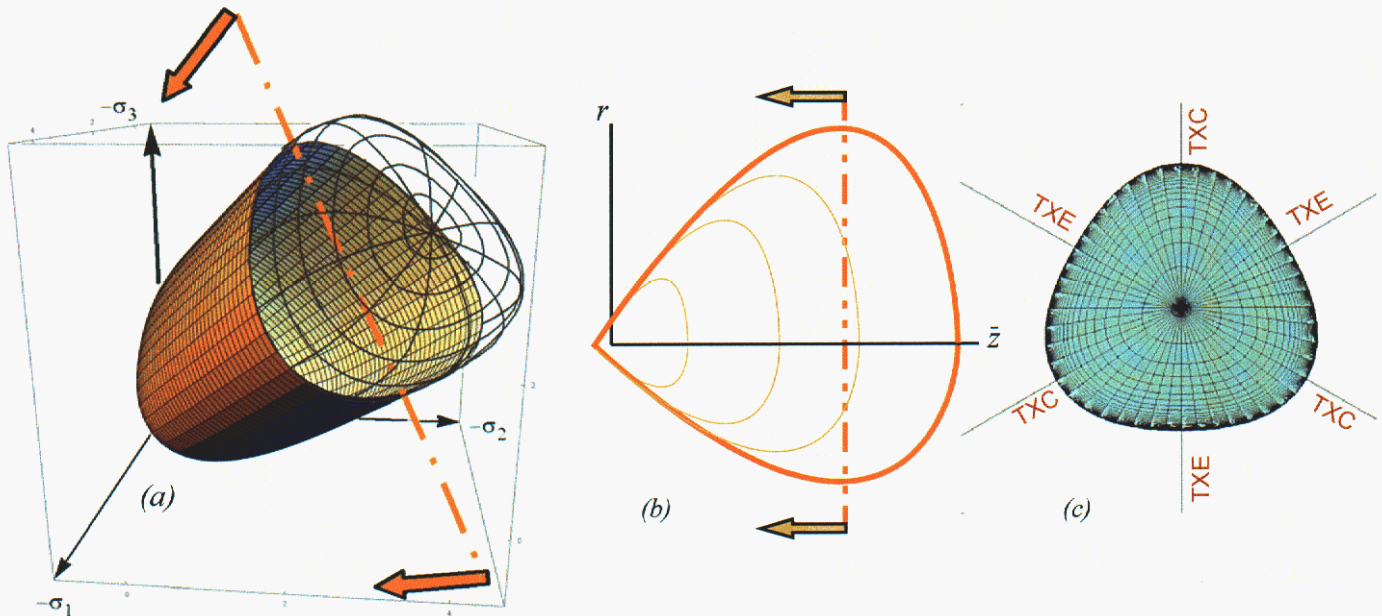


Figure 1.0. *GeoModel continuous yield surface.* (a) **three-dimensional view** in principal stress space with the high pressure “cap” shown as a wire frame, (b) **the meridional “side” view** (thick line) with the cap shown on the more compressive right-hand side of the plot using cylindrical coordinates in which z points along the compressive [111] direction, and (c) **the octahedral view**, which corresponds to looking down the hydrostat (onto planes perpendicular to the [111] direction).

1. Introduction

Simulating deformation and failure of natural geological materials (such as limestone, granite, and frozen soil) as well as rock-like engineered materials (such as concrete [46] and ceramics [2]) is at the core of a broad range of applications, including exploration and production activities for the petroleum industry, structural integrity assessment for civil engineering problems, and penetration resistance and debris field predictions for the defense community. For these materials, the common feature is the presence of microscale flaws such as porosity (which permits inelasticity even in purely hydrostatic loading) and networks of microcracks (leading to low strength in the absence of confining pressure, non-negligible nonlinear elasticity, rate-sensitivity, and differences in material behavior under triaxial extension compared to triaxial compression).

For computational tractability, and to allow relatively straightforward model parameterization using standard laboratory tests, the Sandia GeoModel [15] strikes a balance between first-principals micromechanics and phenomenological, homogenized, and semi-empirical modeling strategies. The over-arching goal is to provide a unified general-purpose constitutive model that can be used for any geological or rock-like material, that is predictive over a wide range of porosities and strain rates. Being a unified theory, the Geo-

Model can simultaneously model *multiple* failure mechanisms, or (by using only a small subset of the available parameters) it can duplicate simpler idealized yield models such as classic Von Mises plasticity and Mohr-Coulomb failure. Thus, exercising this model can require as many as 40 parameters for extremely complicated materials to only 2 or 3 parameters for idealized simplistic materials. The model parameters are defined in the nomenclature table (Appendix B). Appendix A gives step-by-step instructions for using experimental data to assign values to the GeoModel parameters.

GeoModel overview

The GeoModel shares some features with earlier work by Schwer and Murry [42] in that a Pelessone function [34] permits dilatation and compaction strains to occur simultaneously. For stress paths that result in brittle deformation, failure is associated ultimately with the attainment of a peak stress and work-softening deformation. Tensile or extensile microcrack growth dominates the micromechanical processes that result in macroscopically dilatant (volume increasing) strains even when all principal stresses are compressive. At low pressure, porous brittle materials can fail by shear localization and exhibit strain-softening behavior. At higher pressures, they can undergo strain-hardening deformation associated with macroscopically compactive volumetric strain (i.e. void collapse). Features and limitations of the GeoModel are summarized below.

Features of the GeoModel

Depending on how the model parameters are set, the GeoModel is capable of any of the following model features

- Linear and nonlinear, associative or non-associative Drucker-Prager plasticity.
- Linear and nonlinear, associative or non-associative Mohr-Coulomb plasticity.
- Linear or nonlinear, associative or non-associative Willam-Warnke plasticity.
- Von Mises perfect plasticity.
- Tresca perfect plasticity.
- Sandler-Rubin two-surface cap plasticity (approximated).
- Three-invariant, mixed hardening, continuous surface cap plasticity.
- Linear or nonlinear shear failure with or without kinematic hardening.
- Nonlinear compaction function (pressure-volume) with isotropic hardening.
- Three Lode-Angle functions (i.e., non-circular or circular octahedral yield profile).
- Linear or non-linear elasticity.
- Rate-independent or strain-rate-sensitive yield surface.
- Flexibility that permits reducing the model (and the number of required parameters). to other more classical failure models.
- Pressure and shear dependent compaction (similar to p - α models *hydrostatic* loading, but generalized to include shear effects in general loading).
- Ubiquitous jointing (i.e., support for a network of many randomly oriented faults).

Limitations of the GeoModel.

- The GeoModel version that is described in this report treats the material as initially isotropic. Kinematic hardening is the only mechanism for deformation-induced anisotropy. Enhanced versions of the GeoModel that support arbitrary anisotropic jointing are available but not documented here.
- The elasticity model is hypoelastic rather than hyperelastic.
- While the hydrostatic crush curve is quite general, only an elliptic cap function is available for modeling shear effects on pore collapse and other mechanisms of plastic volume reduction. Alternative cap models (such as the Gurson function) can be incorporated in future revisions if needed.
- The host code is responsible for satisfying frame indifference (by calling the GeoModel using conjugate *reference* stress and strain rate measures).
- The GeoModel describes material response up to the *onset* of softening. The host code is responsible for handling material post-peak softening and the accompanying change in type of the governing equations to ensure mesh-size independence.
- The GeoModel is not extensively parameterized (or even tested) for tensile loading, though it is thoroughly validated in compression.
- Compared with simple idealized models (which are well known to give unsatisfactory results in non-trivial structural applications), the GeoModel is computationally intensive, though less so than many other models of comparable complexity.
- The GeoModel is limited to relatively small distortional (shape changing) strains, though large volume changes are permitted. Arbitrarily large rotations are permitted if the host code manages the reference stress and strain measures properly (see page 76).
- The triaxial extension/compression strength ratio is presumed constant. It does not vary with pressure, nor does it evolve in time.

The GeoModel predicts observed material response, without explicitly addressing *how* the material behaves as it does. The GeoModel reflects subscale inelastic phenomena *en ensemble* by phenomenologically matching observed data to interpolation functions. Considerations guiding the structure of the GeoModel’s material response functions are (1) consistency with microscale theory, (2) computational tractability, (3) suitability to capture trends in characterization data, and (4) physics-based judgements about how a material should behave in application domains where controlled experimental data cannot be obtained.

Fundamentally, the GeoModel is a *generalized* and *unified* plasticity model. Here, the term “plasticity” is defined very broadly to include any mechanism of inelastic deformation. Primarily, the source of inelastic deformation in geological materials (or in rock-like materials such as concrete and ceramics) is growth and coalescence of microcracks and pores. Under massive confining pressures, inelasticity could include plasticity in its traditional dislocation sense or, more generally, might result from other microphysical mechanisms (internal locking, phase transformation, twinning, etc.).

The GeoModel is phenomenological and semi-empirical because the physical *mechanisms* of inelastic material behavior are handled in an *ensemble* manner, without explicitly partitioning and modeling each possible contributor to the inelasticity. The GeoModel makes no *explicit* reference to microscale properties such as porosity, grain size, or crack density. Instead, the overall combined effects of the microstructure are modeled by casting the macroscale theory in terms of macroscale variables that are realistic to measure in the laboratory. For example, inelastic compaction followed by shear-enhanced dilatation has long been attributed to an initial phase of void collapse followed later by microcracks opening in shear. The GeoModel is exceptionally capable of matching this type of observed compaction/dilatation data, but it does so without demanding that the user supply information about essentially unknowable porosity or microcrack distributions within the material.

Being a generalized plasticity model, the GeoModel presumes that there exists a convex contiguous “**elastic domain**” of stress states for which the material response can be construed to be elastic. The boundary of the elastic domain is called the **yield surface**. When loading is severe enough that continuing to apply elasticity theory would produce a stress state lying outside the yield surface, the material response will instead be inelastic and a different set of equations must then be solved. Aside from supporting kinematic hardening, the GeoModel is isotropic, which means that the criterion for the onset of plasticity depends only on the three principal values of the stress tensor, $(\sigma_1, \sigma_2, \sigma_3)$, but not on the principal directions. Consequently, as illustrated in Fig. 1.0 (page 1), the yield surface may be visualized as a 2D surface embedded in a 3D space where the axes are the principal stresses. The elastic domain is the interior of this surface. The **hydrostat** is the [111] direction, along which all three principal stresses are equal. Any plane that contains the hydrostat is called a **meridional plane**. Any “side view” cross-section of the yield surface on a meridional plane is called a **meridional profile**. Any plane perpendicular to the hydrostat is called an **octahedral plane**, and any cross-section of the yield surface on an octahedral plane is called an **octahedral profile**.

Mathematically, the yield surface may be expressed in terms of a **yield function** $f(\sigma_1, \sigma_2, \sigma_3)$. When hardening is permitted, the yield function additionally depends on **internal state variables** that quantify the underlying microstructure (e.g. porosity). Points on the yield surface satisfy $f = 0$ and therefore, because the equation $f(\sigma_1, \sigma_2, \sigma_3) = 0$ is phrased in terms of three independent variables, the yield surface may be visualized in the 3D Cartesian space, called **stress space***. When the yield function additionally depends on internal state variables, different values for the internal state variables result in different yield surfaces in stress space. Points within the elastic domain satisfy $f < 0$. Brittle materials are very weak in tension, but they can deform elastically under a much broader range of stress states in compression. Consequently, the elastic domain (and therefore its boundary, the yield surface) resides primarily in the compressive

* Some people prefer that this be called Haigh-Westergaard space [31] so that the phrase “stress-space” may be reserved for the higher-dimensional space defined by the set of all tensors that commute with the stress tensor.

part of stress space where all three principal stresses are negative. Thus, the typical rock yield surface shown in Fig. 1.0(a) is actually being viewed from the *compressive* [111] direction. The “cap” part of that yield surface (shown as a wire frame in Fig. 1.0) reflects the fact that, unlike solid metals, inelasticity can occur in rocks even under purely hydrostatic compression as a consequence of void collapse.

A **yield surface** is the boundary of *elastically* obtainable stress states, whereas a **limit surface** is the boundary of stresses that are quasi-statically obtainable *by any quasi-static means*, elastic or plastic. Points *outside* the limit surface can be reached only transiently in dynamic loading via viscoplastic rate dependence. Points outside a yield surface might be attainable through a hardening process, but points outside the limit surface are not attainable via *any* quasistatic process. Points on the limit surface define the onset of material softening. Consequently, a state on the limit surface is attainable at least once, but might not be attainable thereafter. The GeoModel simulates material response only up to the limit state. The GeoModel does not simulate subsequent softening, if any, because softening usually induces a change in type of the partial differential equations for momentum balance, which therefore requires a response from the host code to alter its solution algorithm (perhaps by inserting void or by activating special elements that accommodate displacement discontinuities).

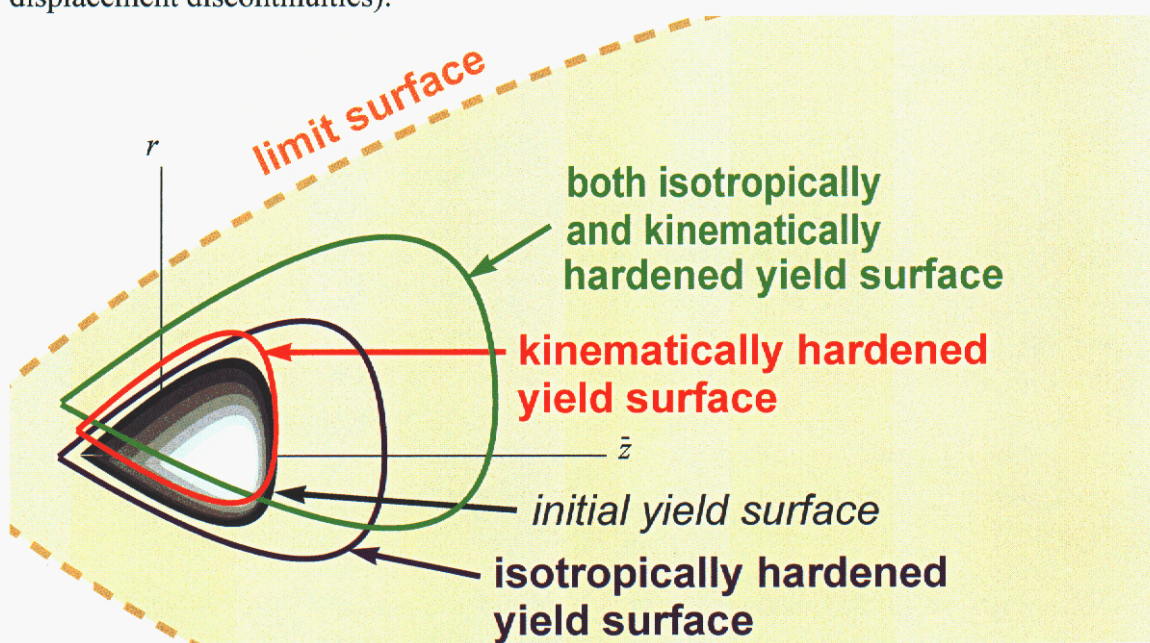


Figure 1.1. Distinction between a yield surface and the limit surface. This sketch shows meridional profiles of an initial yield surface along with hardened yield surfaces that might evolve from the initial surface. All achievable stress states (and therefore all possible yield surfaces) are contained within the limit surface. Fig. 1.0(b), for example, depicts a family of yield surfaces, all bounded by the limit surface.

Since the GeoModel does not include post-softening stress response, the limit surface may be regarded as fixed — it does not evolve (i.e., move around in stress space) as a yield surface can. Since the limit surface contains all attainable stress states, it follows that the set of all possible yield surfaces is contained within the limit surface (see Fig. 1.1). Plasticity induces microstructural changes that permit the yield surface to evolve through

time, effectively changing the initial material into a mechanically *different* material. A material can have an infinite number of yield surfaces generated via various path-dependent hardening processes, but it can have only one limit surface. Limit surface characterization is accomplished by performing numerous experiments all the way to the point of material rupture (catastrophic failure). Each such experiment can have only one peak stress state. Post-peak softening in a material might lead to a stress at rupture that is smaller than at the peak, but it is the collection of *peak* — not rupture — stress states that defines the limit surface. Of course, mapping out the limit surface for a given material requires using a *new sample* for every experiment, which itself introduces uncertainty regarding variability in material composition and microstructure. Presently, the GeoModel treats the limit surface (and each yield surface) as a sharp threshold boundary. Work is underway to allow these boundaries in stress space to be “fuzzy” to better account for natural material variability.

The set of all possible *yield* surfaces is contained within the limit surface. Porous materials are capable of inelastic deformation even under purely hydrostatic loading. Consequently, porous materials tend to have *closed* convex yield surfaces. Once all pores are crushed out, however, a material can withstand an unlimited amount of pressure. Thus, as indicated in Fig. 1.1, the *limit* surface for any material will always be an *open* convex set.

Despite being developed primarily for geological applications, the GeoModel is truly a unification of many classical plasticity models. For example, by using only a small subset of available parameters, the GeoModel can be instructed to behave precisely like a classical hardening or non-hardening Von Mises model, in which case the yield surface becomes a cylinder centered about the [111] direction. Other classical models such as Drucker-Prager plasticity, Tresca theory, maximum principal stress theory, and Mohr-Coulomb theory are also supported in the GeoModel by using the simplified input sets summarized in Appendix B. Replicating analytical results from simplified theories is an important aspect of verification of the GeoModel. However, full use of nearly all GeoModel features is often required to adequately *validate* the model for realistic rock-like materials.

To describe in greater detail how the GeoModel supports its broad range of micro-mechanisms of failure in a mathematical and computational framework, Chapters 2 and 3 first summarize our notation and outline some important concepts and conventions about the nature of stress. Chapter 4 describes the GeoModel theory (elasticity, yield surface definition and evolution, etc.). The computational algorithm, subroutines, and plotable output will be discussed in Chapter 6, followed by software quality assurance in Chapter 7. Chapters 8 and 9 summarize verification and validation tests that have been completed to date for a variety of materials. Model parameters (as well as descriptions of internal state variables and other symbols used in this report) are defined in Appendix B, along with sample input sets for realistic and idealized materials. Instructions for determining appropriate model parameters from laboratory data are provided in Appendix A.

2. Notation

Typesetting conventions

Throughout this report, **blue variables** are user input parameters and **green variables** are internal state variables available for plotting in the numerical implementation. At the discretion of the host code in which the GeoModel is run, several other field variables (e.g., stress) may be additionally available for plotting.

Vector and tensor equations will be presented using indicial Cartesian notation in which repeated indices within a term are understood to be summed from 1 to 3 while non-repeated indices are free and take values 1 through 3. Upon occasion, vectors and tensors will be written in symbolic or “direct” notation in which the number of “tildes” beneath a symbol equals the tensorial order of that variable. For example, s , \underline{v} , and $\underline{\underline{T}}$ would denote a scalar, a vector, and a tensor, respectively.

Vector and Tensor notation

For this report, the following standard operations and definitions from vector and tensor analysis will be employed:

$$\text{Dot product between two vectors: } \underline{u} \bullet \underline{v} = u_1 v_1 + u_2 v_2 + u_3 v_3 = u_k v_k. \quad (2.1)$$

$$\text{Dot product between a tensor and a vector: } \underline{y} = \underline{\underline{A}} \bullet \underline{x} \text{ means } y_i = A_{ik} x_k. \quad (2.2)$$

$$\text{Dot product between a tensor and a tensor: } \underline{\underline{C}} = \underline{\underline{A}} \bullet \underline{\underline{B}} \text{ means } C_{ij} = A_{ik} B_{kj}. \quad (2.3)$$

$$\text{Kronecker delta: } \delta_{ij} = \begin{cases} 1 & \text{if } i=j \\ 0 & \text{if } i \neq j \end{cases}. \quad (2.4)$$

$$\text{Identity tensor: } \underline{\underline{I}} \text{ is the tensor whose } ij \text{ components are } \delta_{ij} \text{ and whose component matrix is therefore the } 3 \times 3 \text{ identity matrix.} \quad (2.5)$$

$$\text{Inner product between two tensors: } \underline{\underline{A}} : \underline{\underline{B}} = A_{ij} B_{ij}. \quad (2.6)$$

$$\text{Magnitude of a vector: } \|\underline{v}\| = \sqrt{v_k v_k} = \sqrt{\sum_{k=1}^3 v_k^2}. \quad (2.7)$$

$$\text{Magnitude of a tensor: } \|\underline{\underline{A}}\| = \sqrt{A_{ij} A_{ij}} = \sqrt{\sum_{i=1}^3 \sum_{j=1}^3 A_{ij}^2}. \quad (2.8)$$

$$\text{Trace of a tensor } \underline{\underline{A}}: \quad \text{tr} \underline{\underline{A}} = A_{11} + A_{22} + A_{33} = A_{kk}. \quad (2.9)$$

$$\text{Deviatoric part of a tensor: } \underline{\underline{A}}^{\text{dev}} = \underline{\underline{A}} - \frac{1}{3}(\text{tr} \underline{\underline{A}}) \underline{\underline{I}}, \text{ or } A_{ij}^{\text{dev}} = A_{ij} - \frac{1}{3}A_{kk} \delta_{ij}. \quad (2.10)$$

$$\text{First invariant (trace) of a tensor } \underline{\underline{A}}: \quad I_1^A = \text{tr} \underline{\underline{A}} = A_{kk}. \quad (2.11)$$

$$\text{Second invariant of a tensor } \underline{\underline{A}}: \quad J_2^A = \frac{1}{2} \text{tr}[(\underline{\underline{A}}^{\text{dev}})^2]. \quad (2.12)$$

$$\text{Third invariant of a tensor } \underline{\underline{A}}: \quad J_3^A = \frac{1}{3} \text{tr}[(\underline{\underline{A}}^{\text{dev}})^3]. \quad (2.13)$$

Throughout this report, invariants of the stress tensor $\underline{\underline{\sigma}}$ will be written without the superscript identifier. For example, J_2 means the same thing as J_2^σ . The GeoModel supports kinematic hardening in which the **shifted stress tensor** $\underline{\underline{\xi}}$ is defined $\underline{\underline{\xi}} = \underline{\underline{\sigma}} - \underline{\underline{\alpha}}$, where $\underline{\underline{\alpha}}$ is the backstress tensor (defined later). The invariants I_1, J_2, J_3 in the non-hardening theory will become $I_1^\xi, J_2^\xi, J_3^\xi$ when kinematic hardening is used.

In materials modeling, tensors are often regarded as higher-dimensional vectors. The inner product between two tensors, $\underline{\underline{A}}$ and $\underline{\underline{B}}$, is isomorphic to (i.e., geometrically analogous to) the dot product between two vectors. This permits the “magnitude” of a tensor, the “direction” of a tensor, and the “angle” between two tensors to be defined in manners analogous to ordinary vector definitions. The direction of a tensor plays a role in the GeoModel by defining the outward normal to the yield surface (which is actually a hyper-surface in higher-dimensional tensor space). Likewise, the angle between two tensors is used to quantify the concept of non-normality, discussed later.

The derivatives of a scalar-valued function f that depends on a second-order tensor $\underline{\underline{\sigma}}$ as well as depending on a scalar κ are given by

$$\frac{\partial f}{\partial \underline{\underline{\sigma}}} \text{ is a second-order tensor with } ij \text{ components } \frac{\partial f}{\partial \sigma_{ij}}. \quad (2.14)$$

$$\frac{\partial f}{\partial \kappa} \text{ is a scalar.} \quad (2.15)$$

Other derivatives are defined similarly. For example, the derivative of a second-order tensor $\underline{\underline{A}}$ with respect to a another second-order tensor $\underline{\underline{B}}$ is a fourth-order tensor with $ijkl$ components $\partial A_{ij} / \partial B_{kl}$. Fourth-order tensors do not play a significant role in the GeoModel theory. The only truly important fourth-order tensor is the plastic tangent stiffness tensor, formally equal to the derivative of the stress rate with respect to the strain rate.

3. The Stress Tensor

This section defines the stress tensor, its principal values, its invariants, and its sign convention. This chapter describes four canonical stress paths used to parameterize the GeoModel: hydrostatic (HYD), triaxial compression (TXC), triaxial extension (TXE), and shear (SHR). For transient dynamics, the GeoModel additionally requires Hugoniot and/or Kolsky (split Hopkinson) bar data to parameterize the viscoplasticity*. This chapter defines the distinction between the spatial Cauchy stress and the unrotated “reference” stress. In preparation for a detailed discussion of the GeoModel theory, this chapter closes with a detailed description of “stress space” and Lode coordinates.

The **stress tensor** $\underline{\underline{\sigma}}$, is defined such that the **traction** vector \underline{t} (i.e., force per unit area), acting on any given plane with unit normal \underline{n} , is given by

$$\underline{t} = \underline{\underline{\sigma}} \bullet \underline{n}. \quad (3.1)$$

Of course, the traction and normal vectors may be described in terms of their Cartesian components, $\{t_1, t_2, t_3\}$ and $\{n_1, n_2, n_3\}$ with respect to an orthonormal basis. The stress tensor has a 3×3 Cartesian component matrix such that the above equation may be written in matrix form as

$$\begin{bmatrix} t_1 \\ t_2 \\ t_3 \end{bmatrix} = \begin{bmatrix} \sigma_{11} & \sigma_{12} & \sigma_{13} \\ \sigma_{21} & \sigma_{22} & \sigma_{23} \\ \sigma_{31} & \sigma_{32} & \sigma_{33} \end{bmatrix} \begin{bmatrix} n_1 \\ n_2 \\ n_3 \end{bmatrix}, \quad (3.2)$$

or in indicial form as

$$t_i = \sigma_{ij} n_j, \quad (3.3)$$

where (recalling the implied summation convention) the repeated index “ j ” is understood to be summed from 1 to 3 and the non-repeated “free” index “ i ” appearing in each term takes values from 1 to 3 so that the above equation is actually a compact representation of three separate equations (one for each value of the free index).

The stress is symmetric, which means that $\sigma_{ij} = \sigma_{ji}$. In continuum mechanics, and in this report, stress is taken *positive* in tension. This sign convention can be the source of considerable confusion, especially when discussing stress invariants. For example, the trace of the stress, I_1 , is positive in tension. However, brittle materials have very low strength in tension. Consequently, most of the functions defined in this report are nontrivial over only a small range of the tensile states where I_1 is positive. On the other hand,

* Until rate dependence is discussed separately in Chapter 5, all incremental or rate equations in this report are understood to apply only under quasistatic loading and may therefore be regarded as “inviscid” equations. Incorporating viscoplastic rate dependence requires, as a pre-requisite, solution of these quasistatic inviscid equations.

most of the GeoModel functions are non-trivial over a relatively large range of compressive states where I_1 is negative. To help manage the sign convention problem, we will introduce a new notation that an over-bar on a variable denotes the *negative*. Specifically, for any variable x ,

$$\bar{x} \equiv -x \quad \text{DEFINITION OF THE "OVER-BAR."} \quad (3.4)$$

In our plots of any variable that varies as a function of I_1 , we will usually employ an abscissa of \bar{I}_1 , which (being the negative of I_1) is positive in compression. Any variable typeset with an overbar will be positive more often than negative in most applications.

The **principal stresses** are the eigenvalues ($\sigma_1, \sigma_2, \sigma_3$) of the stress matrix, positive in tension. Their negatives ($\bar{\sigma}_1, \bar{\sigma}_2, \bar{\sigma}_3$) are positive in compression.* When cast in terms of the principal basis (i.e., the orthonormal eigenvectors of the stress matrix), the diagonal components of the stress matrix will equal the principal stresses, and the off-diagonals will be zero.

The **stress deviator** $\underline{\underline{S}}$ is the deviatoric part of the stress (see Eq. 2.10):

$$\underline{\underline{S}} = \underline{\underline{\sigma}} - \frac{1}{3}(\text{tr}\underline{\underline{\sigma}})\underline{\underline{I}}. \quad (3.5)$$

Loosely speaking, the stress deviator is a *tensor* measure of shear stress. An overall scalar measure of shear will be defined later. The quantity $\frac{1}{3}(\text{tr}\underline{\underline{\sigma}})$ is called the **mean stress**, and we will denote it by p . The negative of the mean stress, $\bar{p} = -p$, is called the **pressure**, and is positive in compression. Noting that the mean stress (or pressure) is simply a multiple of I_1 , its value is an invariant, meaning that the sum of diagonal stress components will have the same value regardless of the orthonormal coordinate system used to describe the stress components. The principal directions of the stress deviator are the same as those for the stress itself, and the principal values for the stress deviator are related to the principal stresses by

$$s_1 = \sigma_1 - \frac{1}{3}(\sigma_1 + \sigma_2 + \sigma_3) \quad (3.6)$$

$$s_2 = \sigma_2 - \frac{1}{3}(\sigma_1 + \sigma_2 + \sigma_3) \quad (3.7)$$

$$s_3 = \sigma_3 - \frac{1}{3}(\sigma_1 + \sigma_2 + \sigma_3). \quad (3.8)$$

The trace of $\underline{\underline{S}}$ is zero, which implies that the numerically largest principal value of any nonzero stress *deviator* will always be positive and the smallest will always be negative. In model parameterization tests, a sufficiently high confining pressure \bar{p} is typically superimposed on the stress deviator to make all principal *stress* components compressive even though the principal deviatoric stresses always have mixed signs.

* Of course, if principal stresses are ordered such that $\sigma_1 \leq \sigma_2 \leq \sigma_3$, then the barred principal stresses will be ordered $\bar{\sigma}_1 \geq \bar{\sigma}_2 \geq \bar{\sigma}_3$.

Stress invariants

The trace operator is an invariant, which means its value will be the same regardless of which orthonormal basis is used for the stress components. Being symmetric, the stress tensor has a total of *three* independent invariants:

$$I_1 = \text{tr} \underline{\underline{\sigma}} = \sigma_1 + \sigma_2 + \sigma_3 \quad (3.9)$$

$$J_2 = \frac{1}{2} \text{tr} \underline{\underline{\mathcal{S}}}^2 = \frac{1}{2} (s_1^2 + s_2^2 + s_3^2) \quad (3.10)$$

$$J_3 = \frac{1}{3} \text{tr} \underline{\underline{\mathcal{S}}}^3 = \frac{1}{3} (s_1^3 + s_2^3 + s_3^3). \quad (3.11)$$

The fact that these invariants are computed from the *stress* tensor $\underline{\underline{\sigma}}$ is sometimes emphasized by typesetting them as I_1^σ , J_2^σ , and J_3^σ . Similarly defined invariants for some *other* tensor $\underline{\underline{\xi}}$ would be typeset as $\{I_1^\xi, J_2^\xi, J_3^\xi\}$. Invariants for a tensor $\underline{\underline{\alpha}}$ would be written $\{I_1^\alpha, J_2^\alpha, J_3^\alpha\}$, and so forth. Any invariant written without a clarifying superscript should be understood to be a *stress* invariant.

The mean stress p is defined to be the average of the principal stresses, whereas pressure \bar{p} is just the negative of mean stress:

$$\text{mean stress: } p = \frac{I_1}{3} \quad \text{pressure: } \bar{p} = \frac{\bar{I}_1}{3}, \text{ where } \bar{I}_1 \equiv -I_1. \quad (3.12)$$

Superimposing an extra pressure \bar{P} on *any* stress state causes the pressure to increase from \bar{p} to $\bar{p} + \bar{P}$, while having no effect on the stress deviator and therefore no effect on the second and third invariants. Because the stress *deviator* $\underline{\underline{\mathcal{S}}}$ has a zero trace, it can be shown that J_3 also equals the determinant of the stress deviator so that $J_3 = s_1 s_2 s_3$, and the second invariant can be written alternatively as $J_2 = -(s_1 s_2 + s_2 s_3 + s_3 s_1)$.

Equation (3.10) shows that the invariant J_2 is never negative, which permits us to define a supplemental stress invariant, the **signed equivalent shear stress** τ as

$$\tau = \text{sign}[\sqrt{J_2}, J_3]. \quad (3.13)$$

The “transfer of sign” operator* is defined

$$\text{sign}[x, y] = \begin{cases} |x| & \text{if } y \geq 0 \\ -|x| & \text{if } y < 0 \end{cases}. \quad (3.14)$$

As defined, the equivalent shear stress will have a numerical sign that is positive in triaxial extension states (defined below), negative in triaxial compression, and it will be identically equal to the applied shear stress if the stress tensor happens to be in a state of pure shear (also defined below).

* which is an intrinsic function in most computing languages

For clarity, the values of the invariants have been shown here in terms of the principal values of the stress and its deviator. However, because the trace operation gives the same result regardless of which basis is used, the invariants are computed in practice directly from fully-populated 3×3 component matrices, thereby avoiding the need for an expensive eigenvalue analysis.

Derivatives of the stress invariants

For *isotropic* material modeling, each scalar-value function of stress, $\phi(\underline{\underline{\sigma}})$, is presumed to depend only on the principal stress values, not on the principal stress directions. Equivalently, the function $\phi(\underline{\underline{\sigma}})$ is isotropic if and only if it may be expressed alternatively as a function of the three stress invariants I_1, J_2, J_3 . In situations where the derivative of ϕ with respect to stress is required, the chain rule can be applied as follows:

$$\frac{\partial \phi}{\partial \sigma_{ij}} = \frac{\partial \phi}{\partial I_1} \frac{\partial I_1}{\partial \sigma_{ij}} + \frac{\partial \phi}{\partial J_2} \frac{\partial J_2}{\partial \sigma_{ij}} + \frac{\partial \phi}{\partial J_3} \frac{\partial J_3}{\partial \sigma_{ij}}. \quad (3.15)$$

In symbolic tensor notation, this expansion is written as

$$\frac{\partial \phi}{\partial \underline{\underline{\sigma}}} = \frac{\partial \phi}{\partial I_1} \frac{dI_1}{d\underline{\underline{\sigma}}} + \frac{\partial \phi}{\partial J_2} \frac{dJ_2}{d\underline{\underline{\sigma}}} + \frac{\partial \phi}{\partial J_3} \frac{dJ_3}{d\underline{\underline{\sigma}}}. \quad (3.16)$$

Because the three invariants are each proper functions of the stress tensor, their derivatives may be computed in advance:

$$\frac{dI_1}{d\underline{\underline{\sigma}}} = \underline{\underline{I}} \quad = \text{the identity tensor} \quad (3.17)$$

$$\frac{dJ_2}{d\underline{\underline{\sigma}}} = \underline{\underline{S}} \quad = \text{dev}(\underline{\underline{\sigma}}) \quad = \text{the stress deviator} \quad (3.18)$$

$$\frac{dJ_3}{d\underline{\underline{\sigma}}} = \underline{\underline{T}} \quad = \text{dev}(\underline{\underline{S}}^2) \quad = \text{the "Hill" tensor} \quad (3.19)$$

Thus, Eq. (3.16) may be written

$$\frac{\partial \phi}{\partial \underline{\underline{\sigma}}} = \left(\frac{\partial \phi}{\partial I_1} \right) \underline{\underline{I}} + \left(\frac{\partial \phi}{\partial J_2} \right) \underline{\underline{S}} + \left(\frac{\partial \phi}{\partial J_3} \right) \underline{\underline{T}}. \quad (3.20)$$

Of particular interest is the trace of the above expression, $\text{tr}(\partial \phi / \partial \underline{\underline{\sigma}})$. Since both $\underline{\underline{S}}$ and $\underline{\underline{T}}$ are deviatoric, the result is

$$\text{tr} \left(\frac{\partial \phi}{\partial \underline{\underline{\sigma}}} \right) = 3 \left(\frac{\partial \phi}{\partial I_1} \right). \quad (3.21)$$

The factor of 3 appears simply because $\text{tr} \underline{\underline{I}} = 3$. This, by the way, is a good example of the fallibility of indicial notation. Specifically,

$$\text{tr} \left(\frac{\partial \phi}{\partial \underline{\underline{\sigma}}} \right) = \sum_{k=1}^3 \frac{\partial \phi}{\partial \sigma_{kk}} \neq \frac{\partial \phi}{\partial \sum_{k=1}^3 \sigma_{kk}}. \quad (3.22)$$

Special stress states

This section defines the four main stress states that are used to parameterize the GeoModel. These are hydrostatic loading (HYD), triaxial compression (TXC), triaxial extension (TXE), and shear (SHR). The purpose of the GeoModel is to interpolate realistically between known material response at these canonical states to describe material behavior under *general* stress states.

HYDROSTATIC (HYD). Loading is “**hydrostatic**” when components of the stress tensor are of the form

$$[\underline{\underline{\sigma}}] = \begin{bmatrix} -\bar{p} & 0 & 0 \\ 0 & -\bar{p} & 0 \\ 0 & 0 & -\bar{p} \end{bmatrix} \quad \text{for hydrostatic stress states.} \quad (3.23)$$

In practice, the pressure \bar{p} is usually compressive (and therefore positive). Hydrostatic testing is very important to parameterization of the GeoModel because it indirectly characterizes the influence of material porosity. When hydrostatically loaded to a high pressure and then unloaded, a *non-porous* material will trace through the same stress states on both the loading and unloading curves. A *porous* material, on the other hand, will unload along a *different* path. If possible, hydrostatic testing for the GeoModel should be conducted to sufficiently high pressures to compress out all pores, as indicated in Fig. 3.1.*

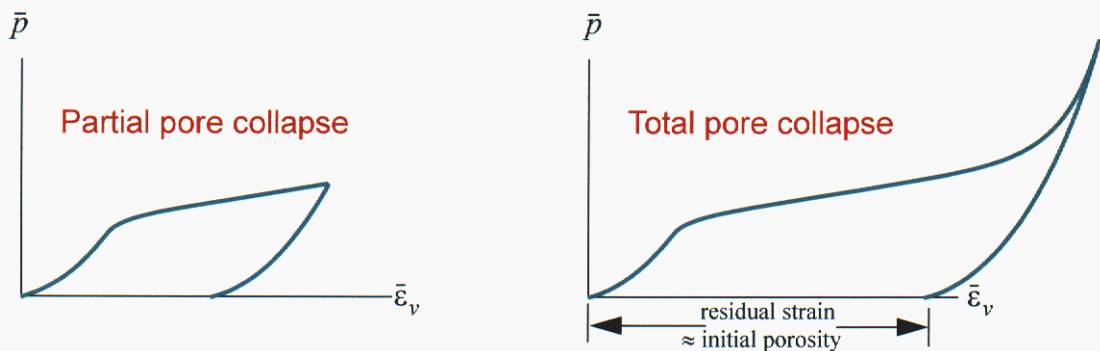


Figure 3.1. Typical hydrostatic (pressure vs. volumetric strain) compression data. Total pore collapse is achieved when the unloading curve (here shown as nonlinearly elastic) is tangent to the loading curve. In this case, the residual volumetric strain approximately equals the initial porosity.

* Assuming that the matrix material is plastically incompressible, the porosity is $1 - e^{\bar{\epsilon}_v^{\text{residual}}}$, where $\bar{\epsilon}_v^{\text{residual}}$ is the *logarithmic* (Hencky) residual strain after full void collapse. If the residual strain is small, a Taylor series expansion of this formula gives porosity $\approx \bar{\epsilon}_v^{\text{residual}}$.

When a material is loaded under hydrostatic *tension* instead of compression, inelastic response is again possible, but the mechanism of failure is catastrophic growth and coalescence of microcracks, resulting in material softening and, ultimately, complete loss of load carrying ability.

TRIAXIAL (TXC and TXE): Loading is “**triaxial**” whenever two principal stresses (denoted σ_L and called the “lateral” stresses) are equal to each other, but distinct from the third “axial” principal stress (denoted σ_A). Thus, with respect to the principal basis,

$$[\underline{\sigma}] = \begin{bmatrix} \sigma_A & 0 & 0 \\ 0 & \sigma_L & 0 \\ 0 & 0 & \sigma_L \end{bmatrix} \quad \text{for triaxial stress states,} \quad (3.24)$$

and

$$[\underline{s}] = \frac{\sigma_A - \sigma_L}{3} \begin{bmatrix} 2 & 0 & 0 \\ 0 & -1 & 0 \\ 0 & 0 & -1 \end{bmatrix} \quad \text{for triaxial stress states.} \quad (3.25)$$

Also,

$$I_1 = \sigma_A + 2\sigma_L \quad \text{for triaxial stress states} \quad (3.26a)$$

$$J_2 = \frac{1}{3}(\sigma_A - \sigma_L)^2 \quad \text{for triaxial stress states} \quad (3.26b)$$

$$J_3 = \frac{2}{27}(\sigma_A - \sigma_L)^3 \quad \text{for triaxial stress states.} \quad (3.26c)$$

The *signed* equivalent shear stress for triaxial loading is

$$\tau = \frac{\sigma_A - \sigma_L}{\sqrt{3}} \quad (3.27)$$

The invariants defined here may be written alternatively in terms of *compressive* stress measures as

$\bar{I}_1 = \sqrt{3}\bar{\tau} + 3\bar{\sigma}_L$	$J_2 = \bar{\tau}^2$	$\bar{J}_3 = \frac{2\sqrt{3}}{9}\bar{\tau}^3$
--	----------------------	---

(3.28)

where

$$\bar{\tau} = \frac{\bar{\sigma}_A - \bar{\sigma}_L}{\sqrt{3}}. \quad (3.29)$$

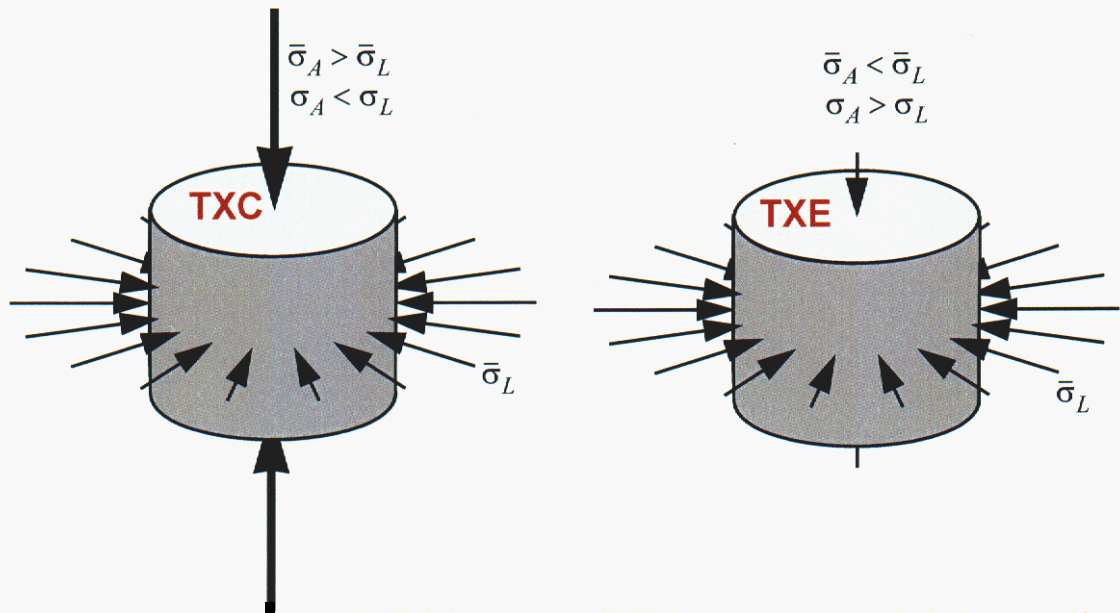


Figure 3.2. *Triaxial compression (TXC) and triaxial extension (TXE)* Two principal stresses (the lateral stress) are equal. For TXC, the axial stress is more compressive than the lateral stress. For TXE, the axial stress is less compressive than the lateral stress. In the labels, $\bar{\sigma} = -\sigma$; stress σ is positive in tension while stress $\bar{\sigma}$ is positive in compression.

The term “triaxial” is a bit of a misnomer because there are not really three independent loads applied — the lateral stresses are equal. These experiments are normally performed on cylindrical test specimens with the lateral load supplied by a pressure bath. For **triaxial compression (TXC)** the axial stress is more compressive than the lateral stress. For **triaxial extension (TXE)** the axial stress is not necessarily *tensile* — it is merely *less compressive* than the lateral stress. For TXC, the specimen changes shape such that its length-to-diameter ratio decreases. For TXE, the length-to-diameter ratio *increases* even though the length and diameter might *individually* both decrease. Uniaxial stress *compression* (also called **unconfined compression**) is a special form of TXC in which the axial stress is compressive and *the lateral stress is zero*. Uniaxial stress *extension* is a special form of TXE in which the axial stress is tensile and the lateral stress is zero. **Uniaxial strain compression**, which is typical in flyer-plate impact experiments is a special case of TXC in which the axial stress is compressive, while the lateral *strain* is zero (making the lateral stress also compressive, but less compressive than the axial stress). **Biaxial tension** is a special case of TXC in which the lateral stress is tensile and the *axial* stress is zero. **Biaxial compression** is a special case of TXE in which the lateral stress is com-

pressive and the axial stress is zero. According to Eq. (3.27), the signed shear stress satisfies $\bar{\tau} > 0$ for TXC, whereas $\bar{\tau} < 0$ for TXE. Consequently, Eq. (3.28) shows that $\bar{J}_3 > 0$ (and hence $J_3 < 0$) for TXC, while $\bar{J}_3 < 0$ (and hence $J_3 > 0$) for TXE. Of course, $J_2 > 0$ for *both* TXC and TXE because it is the *square* of $\bar{\tau}$.

In typical triaxial experiments, the lateral stress is held fixed (via a pressure bath) while only the axial stress is varied. In this case, Eq. (3.28) implies that

$$\frac{d\bar{\tau}}{d\bar{I}_1} = \frac{1}{\sqrt{3}} \text{ for triaxial stress loading with fixed lateral stress.} \quad (3.30)$$

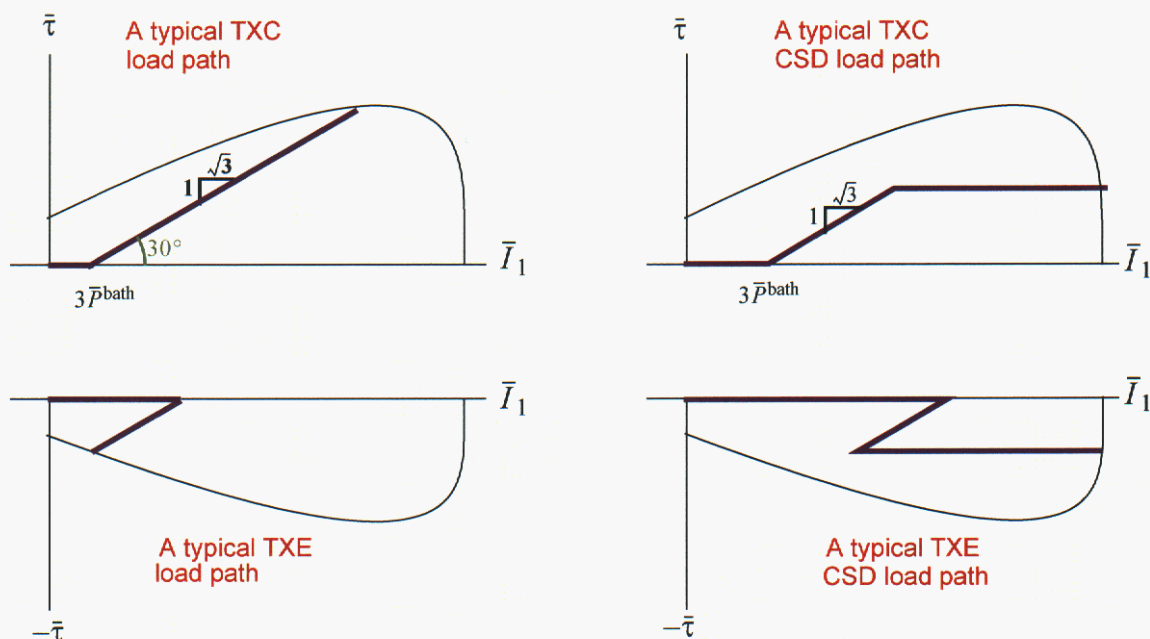


Figure 3.3. *Triaxial and CSD load paths.* The material is first compressed hydrostatically to a pre-selected bath pressure \bar{P}^{bath} ; at this point, the value of the first stress invariant is $I_1 = -3\bar{P}^{\text{bath}}$ and therefore $\bar{I}_1 = 3\bar{P}^{\text{bath}}$. When the triaxial leg begins, the lateral stress is held constant ($\bar{\sigma}_L = \bar{P}^{\text{bath}}$) while the axial stress is varied. This causes both the first and second invariants to change such that the path in this stress plot is a straight line with slope $1/\sqrt{3}$. For simple triaxial loading, the stress difference is increased until material failure occurs. For CSD loading, the stress difference is increased to a pre-selected value, and then held fixed while all stress components are thereafter varied equally until failure occurs.

Being easily achieved in the laboratory, TXC and TXE data are essential to parameterize the GeoModel. In a typical triaxial test, the material is first loaded hydrostatically in a pressure bath until all three principal stresses reach a compressive pressure \bar{P}^{bath} . Thereafter, the lateral stresses are held fixed at this value ($\bar{\sigma}_L = \bar{P}^{\text{bath}}$) while the axial stress is then increased beyond \bar{P}^{bath} . For some experiments, the axial stress might be increased only until the stress difference reaches a given value, after which all stresses are again increased by equal amounts. These are called **constant stress difference (CSD)**

experiments. Typically, these experiments are run to the point of material failure. Periodic partial unloading during a test reveals yielding if the unloading stress-strain curve has a noticeably different slope than the loading curve (without unloading, it would be impossible to definitively distinguish plasticity from non-linear elasticity).

As illustrated in Fig. 3.3, a series of TXC experiments at various bath pressures and/or stress differences results in a family of $(\bar{I}_1, \bar{\tau})$ stress-at-*yield* points that map out the TXC meridional profile of the GeoModel yield surface. Similar experiments under TXE map out the TXE meridional profile. Usually, the TXE failure envelope will be shaped similarly to the TXC envelope, but lower in magnitude because, at a given value of I_1 , the value of $\sqrt{J_2}$ at failure is generally lower for TXE than for TXC. A plot of the failure envelope in $\bar{\tau}$ vs. I_1 space is essentially equivalent to the meridional “side” view of the yield surface (Fig. 1.0b), except with the axes scaled differently. The TXE experiments are mapping out the cross-section of the yield surface along which pressure varies while staying on the “base” of the triangular octahedral profile in Fig. 1.0c (page 1), whereas TXC experiments reveal how the apex of the triangle varies with pressure. For metals, there is little difference between the stress intensity required to initiate failure in TXC compared to TXE. However, for brittle materials, the difference is quite noticeable and (according to idealized microphysical theories) can be attributed to internal frictional resistance to shear crack growth. Because friction increases with pressure, the material strengths in TXC and TXE tend to increase with pressure but in approximately the same proportions so that the ratio of TXC strength to TXE strength is approximately pressure independent. Consequently, the TXE profiles shown in Fig. 3.3 are shaped identically to the TXC profiles except smaller in magnitude.

Another form of triaxial loading, commonly used for dynamic material testing, is **uniaxial strain**, in which the lateral *strain* ε_L is held constant. If the lateral strain ε_L is held constant while continuing to compress axially, the lateral compressive *stress* $\bar{\sigma}_L$ will increase to prevent lateral motion. For uniaxial strain, $\dot{\varepsilon}_L = 0$, and therefore Hooke’s law* in rate form reduces to

$$\text{Uniaxial strain: } \dot{\bar{\sigma}}_A = \left(K + \frac{4}{3}G\right)\dot{\varepsilon}_A \quad \text{and} \quad \dot{\bar{\sigma}}_L = \frac{\nu}{1-\nu}\dot{\bar{\sigma}}_A = \left(K - \frac{2G}{3}\right)\dot{\varepsilon}_A, \quad (3.31)$$

where K and G are, respectively, the tangent elastic bulk and shear moduli.

For uniaxial strain, the rate of the signed equivalent shear stress and the rate of the first stress invariant are

$$\text{Uniaxial strain: } \dot{\bar{\tau}} = \frac{2G\dot{\varepsilon}_A}{\sqrt{3}} \quad \text{and} \quad \dot{\bar{I}}_1 = 3K\dot{\varepsilon}_A, \quad (3.32)$$

and therefore the path through stress space is a straight line with slope

* The general form of Hooke’s law, applicable to any form of triaxial loading, is given in Eq. (4.11). Eq. (3.31) is a special case of Eq. (4.11) in which $\dot{\varepsilon}_L = 0$, with Eq. (4.13) used to express Young’s modulus E and Poisson’s ratio ν in terms of K and G .

$$\frac{d\bar{\tau}}{d\bar{I}_1} = \frac{1}{\sqrt{3}} \frac{2G}{3K} = \frac{1}{\sqrt{3}} \left(\frac{1-2\nu}{1+\nu} \right) \text{ for triaxial stress with fixed lateral strain, (3.33)}$$

where ν is Poisson’s ratio. Since Poisson’s ratio typically varies between 0 and $1/2$,* this result shows that the trajectory in the meridional profile will generally have a shallower slope under uniaxial strain loading than under uniaxial stress loading. This result should make some intuitive sense. Uniaxial strain experiments are conducted by applying increasing levels of compression in the axial direction while holding the lateral strain fixed. As the axial strain is compressed, the material “wants” to expand laterally, but is not permitted to — a lateral compressive force prevents this outward motion. This constraining lateral compression makes \bar{I}_1 larger than it would be when lateral expansion is unconstrained. The larger \bar{I}_1 results in a shallower slope in the stress trajectory.

SIMPLE/PURE SHEAR and PRESSURE-SHEAR LOADING (SHR).

A material is in a state of **simple shear** with respect to a given coordinate system if the stress matrix in that system is of the form

$$[\underline{\sigma}] = [\underline{S}] = \begin{bmatrix} 0 & s & 0 \\ s & 0 & 0 \\ 0 & 0 & 0 \end{bmatrix} \text{ for simple shear, (3.34)}$$

where s is the shear stress. The eigenvalues of this matrix are $\{s, -s, 0\}$. In general, any stress state that is deviatoric with one eigenvalue being zero is said to be a **pure shear** [27, p. 16]. (Thus, simple shear is a special type of pure shear). For an isotropic material model like the GeoModel, yield depends only on the principal stresses, so there is no practical difference between simple and pure shear (except when the model is anisotropic because of kinematic hardening).

For conducting material characterization experiments, **pure shear** of the form

$$[\underline{\sigma}] = [\underline{S}] = \begin{bmatrix} s & 0 & 0 \\ 0 & -s & 0 \\ 0 & 0 & 0 \end{bmatrix} \text{ for pure shear (3.35)}$$

is most convenient. For brittle materials, pure shear is difficult to attain because one of the eigenvalues is always tensile. Frequently, pure shear is superimposed with enough confining hydrostatic pressure to make all principal stresses negative (compressive). Specifically, superimposing the hydrostatic loading of Eq.(3.23) onto the shear stress of Eq. (3.35), gives a state of **combined pressure-shear (SHR)** loading:

* Strictly speaking, positive definiteness of the elastic stiffness tensor merely requires $-1 < \nu < 1/2$. Whereas negative Poisson’s ratio has been observed in man-made materials with re-entrant microstructures, it has not (to our knowledge) been reported for naturally occurring materials. Performance of the GeoModel has not been verified for materials with negative Poisson’s ratio.

$$[\underline{\sigma}] = \begin{bmatrix} s - \bar{p} & 0 & 0 \\ 0 & -s - \bar{p} & 0 \\ 0 & 0 & -\bar{p} \end{bmatrix} \quad \text{for combined pressure-shear loading.} \quad (3.36)$$

The invariants for combined pressure-shear loading are

$$I_1 = -3\bar{p} \quad \text{for combined pressure-shear loading} \quad (3.37a)$$

$$J_2 = \tau^2 \quad \text{for combined pressure-shear loading} \quad (3.37b)$$

$$J_3 = 0 \quad \text{for combined pressure-shear loading} \quad (3.37c)$$

$$\tau = |s|. \quad (3.38)$$

Spatial and Reference stress (frame indifference)

The spatial Cauchy stress tensor defined in Eq. (3.1) is the “familiar” stress tensor used in everyday engineering applications. Let us now denote that stress by $\underline{\sigma}^{\text{spatial}}$. The elasticity component of solids models requires knowledge of both the *initial* and *current* configurations. Moreover, the principle of material frame indifference demands that if a *second* problem were considered that had the same initial configuration, but a current configuration that is identical to the current configuration of the first problem, except also rigidly rotated, then the predicted spatial stresses for the second problem should be identical to those of the first problem, except rigidly rotated by the same amount. This concept is quite different from a mere basis change because the *initial configuration* is identical for both problems.

Satisfying material frame indifference in a *spatial* context can be computationally expensive and error-prone because anisotropic internal state variables (such as directions of material fibers or orientation of the backstress) must be rotated *into* the spatial frame, and special “objective” rates must be integrated in constitutive models. A mathematically equivalent (and numerically more accurate and efficient) strategy instead applies the constitutive model within an *unrotated* reference configuration. With this approach, rotation of internal variables is not required, and all rates that appear in the constitutive model are more easily integrated *true* rates instead of co-rotational rates.

If $\underline{\mathbf{R}}$ is the proper orthogonal tensor (found from a polar decomposition of the deformation) that characterizes the material rotation, then the unrotated stress is simply

$$\underline{\sigma}^{\text{unrotated}} = \underline{\mathbf{R}}^T \bullet \underline{\sigma}^{\text{spatial}} \bullet \underline{\mathbf{R}} \quad (3.39)$$

By working in the unrotated reference configuration, the GeoModel predicts the stresses for the non-rotating problem. Upon receiving the GeoModel’s update of the unrotated stress, the host code then rotates the predicted stress back into the spatial frame. Roughly speaking, this approach will give results identical to a spatial constitutive model that is cast in terms of polar objective rates.

For problems involving massive material rotation (e.g., turbine blades, vortices, tumbling rock fragments, etc.), the “unrotation” strategy can give considerably more accurate answers because the host code may, optionally, use the rotation tensor \mathbf{R}^n at the beginning of the time step when computing the starting value of $\underline{\underline{\sigma}}^{\text{unrotated}}$, but then the host code may use \mathbf{R}^{n+1} at the *end* of the step when recasting the updated value of $\underline{\underline{\sigma}}^{\text{unrotated}}$ (output of the GeoModel) to the spatial frame. Hence, this approach supports so-called “strong objectivity” [38] in a very natural way.

Throughout the remainder of this report, the “stress” $\underline{\underline{\sigma}}$ must be understood to be the *unrotated* stress $\underline{\underline{\sigma}}^{\text{unrotated}}$. Likewise all other vector or tensor variables (such as the strain rate) mentioned in this report are understood to be cast in the unrotated configuration (material frame). Any host code that uses the GeoModel must (1) perform these unrotation operations, (2) call the GeoModel, and then (3) re-rotate the result back to the spatial frame upon return. For more information, see page 76.

Lode coordinates

Any isotropic yield function may be expressed in terms of the principal stresses $(\sigma_1, \sigma_2, \sigma_3)$. Therefore, the yield surface may be visualized in a 3D space for which the Cartesian coordinates are these principal stresses. The value of the yield function $f(\sigma_1, \sigma_2, \sigma_3)$ must be independent of the ordering of the eigenvalues. Therefore, as seen in Fig. 1.0 (page 1), the yield surface must have 120° rotational symmetry about the [111] (hydrostat) direction and reflective symmetry about the TXE and TXC axes in the octahedral plane (i.e., the view looking down the [111] axis).

The **principal Cartesian coordinates** $(\sigma_1, \sigma_2, \sigma_3)$ comprise an adequate choice for characterizing stress space, but the yield function is often cast in terms of different independent variables to exploit the yield surface’s natural symmetries optimally. The natural symmetries suggest instead using cylindrical $(r, \bar{\theta}, z)$ coordinates — called **Lode cylindrical coordinates** — for which the z -axis is parallel with the [111] symmetry axis. We have placed a bar on the symbol $\bar{\theta}$ for the angular coordinate because we intend to define it so that it will be positive in TXC and negative in TXE. A constant $\bar{\theta}$ plane is a **meridional plane**, and a plot of r vs. z . at a given value of $\bar{\theta}$ is called a **meridional profile**. Because most of the yield surface resides in the compressive domain where $z < 0$, we will usually display meridional profiles as r vs. \bar{z} (where $\bar{z} = -z$). Any constant- z plane is an **octahedral plane**, and any cross-section looking down the [111] axis (i.e., on a plane of constant z) is in an **octahedral profile**. Meridional and octahedral profiles are illustrated in Fig. 1.0 (page 1).

In this report, the Lode angle $\bar{\theta}$ is defined so that it equals zero in SHR. It varies from -30° in TXE to $+30^\circ$ in TXC. Superimposing pressure on a stress state changes only the axial z -coordinate, leaving the octahedral $(r, \bar{\theta})$ coordinates unchanged, which makes Lode coordinates a natural choice when decomposing tensors in to their isotropic and deviatoric parts. The radial r coordinate equals the magnitude of the stress deviator. The z coordinate is proportional to the mean stress. The angular coordinate is a measure of the

relative proportions of the principal values of the stress deviator. Thus, as the Lode angle varies from -30° to $+30^\circ$, the stress transitions through TXE, SHR, and TXC states. Cylindrical Lode coordinates are especially useful because they may be expressed in terms of stress invariants, thereby eliminating the need for an eigenvalue decomposition.

The axial z -coordinate is positive on the tensile part of the hydrostat, so \bar{z} is positive on the compressive hydrostat. We define the Lode angle $\bar{\theta}$ to be positive in TXC and negative in TXE. The change in variables from principal coordinates to Lode coordinates permits the yield function $f(\sigma_1, \sigma_2, \sigma_3)$ to be alternatively expressed in the form $f(r, \bar{\theta}, \bar{z})$. When phrased in terms of Lode coordinates, the yield function needs to be defined only over a 60° sextant on any octahedral plane. The symmetry properties of the yield surface may be used to reconstruct the octahedral profile over the full range from 0° to 360° .

Performing these necessary but tedious coordinate transformations from principal stresses to cylindrical Lode coordinates, it can be shown [31] that the cylindrical Lode coordinates may be determined directly from the I_1 , J_2 , and J_3 scalar stress invariants, eliminating the need for an eigenvalue analysis. Specifically,

$$r = \sqrt{2J_2} \quad (3.40a)$$

$$\sin 3\bar{\theta} = -\frac{J_3}{2} \left(\frac{3}{J_2}\right)^{3/2} \quad (3.40b)$$

$$\bar{z} = \frac{\bar{I}_1}{\sqrt{3}} \quad (3.40c)$$

The square root coefficients are merely by-products of the coordinate transformations. For example, since the z -coordinate is the projection of the stress onto the $[111]$ axis, the $\sqrt{3}$ appears because the magnitude of the $[111]$ vector is $\sqrt{3}$. The Lode radius r is zero if $J_2=0$. Also, the Lode angle $\bar{\theta}$ is undefined when $J_2=0$, which should not be too disturbing since the angular coordinate for any cylindrical system is undefined when the point in question lies on the symmetry axis (which, in this case, is the $[111]$ hydrostat).

Later, when we give the mathematical formulation for the GeoModel yield function, it will be phrased as $f(r, \bar{\theta}, \bar{z})$. Using the above formulas, the yield function is ultimately implemented in the form $f(I_1, J_2, J_3)$. The invariant J_3 influences only the Lode angle. When simpler yield models (Drucker-Prager) are independent of the third stress invariant, they are therefore independent of the Lode angle, which makes their octahedral yield profile a circle. The GeoModel must include a *non-circular* yield profile to reproduce TXE/TXC strength differences clearly evident in the data for geological materials. Thus, the GeoModel must necessarily use all three Lode coordinates (equivalently, all three stress invariants).

Octahedral yield profile visualization. Given a yield function $f(r, \bar{\theta}, \bar{z})$, yield profiles may be generated by solving $f = 0$ to obtain r expressed as a function of $(\bar{\theta}, \bar{z})$. A meridional profile is generated by plotting r vs. \bar{z} at a fixed value of $\bar{\theta}$. An octahedral profile, which corresponds to a yield surface cross-section at a given value of \bar{z} , describes how the Lode radius at yield varies with the Lode angle. Rather than plotting r vs. $\bar{\theta}$, octahedral profiles are obtained by parametrically plotting Cartesian coordinates

$$x_1 = r \cos \bar{\Theta} \text{ and } x_2 = r \sin \bar{\Theta} \tag{3.41}$$

Here, $\bar{\Theta}$ is an angle that varies over the full range from 0 to 360°. The Lode angle $\bar{\theta}$, which is permitted to vary only over the range from -30° to 30°, is generated from the full-range angle $\bar{\Theta}$ by the sawtooth function

$$\bar{\theta} = \frac{1}{3} \text{ArcSin}[\sin(3\bar{\Theta})] \tag{3.42}$$

With $\bar{\theta}$ known, the value of corresponding Lode radius r can be found from the yield condition, and finally, the family of (x_1, x_2) points on the octahedral yield profile may be generated parametrically as $\bar{\Theta}$ varies from 0 to 360°, as illustrated in Fig. 3.4.

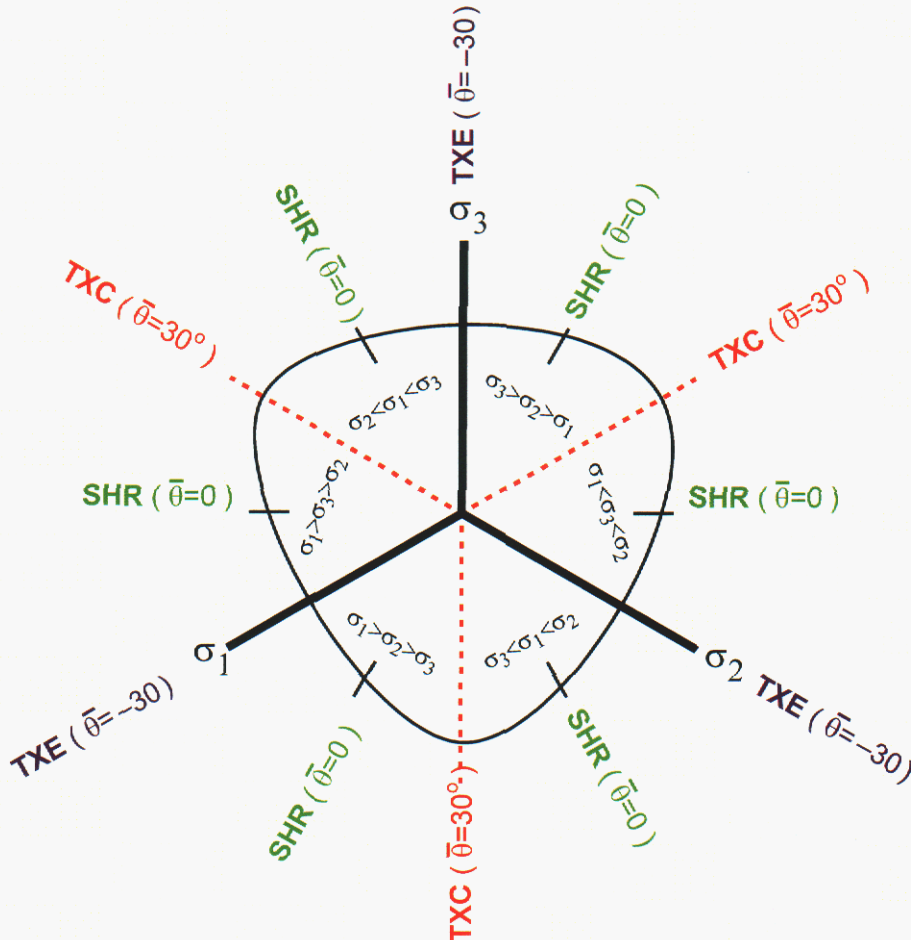


Figure 3.4. An octahedral yield profile. Geometrical materials tend to be stronger in TXC than in TXE, which is why the TXC axes are always on an apex of the rounded triangle (i.e., farther from the origin, corresponding to higher strength). The Lode angle $\bar{\theta}$ alternates cyclically from -30° in TXE to 30° in TXC because the yield threshold must be independent of the eigenvalue ordering.

Meridional yield profile visualization. To draw a *geometrically accurate* meridional cross-section of the yield surface, the profile should be plotted as r vs. \bar{z} for a given value of $\bar{\theta}$. Typically, we will plot the TXC ($\bar{\theta} = 30^\circ$) profile. Using the r and \bar{z} Lode coordinates as the axes in a meridional plot ensures that lengths and angles in the meridional profile will equal corresponding lengths and angles in stress space. Many times, however, we will depict a geometrically *distorted* view of the meridional profile by instead plotting $\bar{\tau}$ vs. \bar{I}_1 , where the signed equivalent shear stress $\bar{\tau}$ equals $\pm\sqrt{J_2}$, depending on whether the loading is closer to TXE or TXC. Recalling from Eqs. (3.40a) and (3.40c) that $\sqrt{J_2} = r/\sqrt{2}$ and $\bar{I}_1 = \sqrt{3}\bar{z}$, a plot of $\bar{\tau}$ vs. \bar{I}_1 is equivalent to changing the aspect ratio of an r vs. \bar{z} plot by a factor of $\sqrt{6} = 2.45$, as illustrated in Fig. 3.5. Thus, whenever we plot the meridional profile as $\bar{\tau}$ vs. \bar{I}_1 , keep in mind that the actual meridional cross-section in stress space is smaller in width by a factor of 2.45. Meridional profile distortion is an issue only when ascertaining the direction of the yield surface normal. Figure 3.5 shows that the normal to the yield profile in a distorted plot does *not* correspond to the normal in stress space.

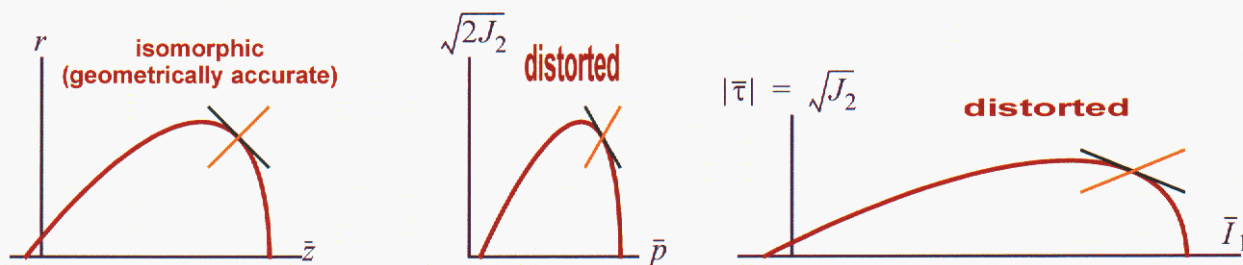


Figure 3.5. Distortion of the meridional profile when using non-isomorphic stress measures. Only a plot of r vs. z will result in a geometrically accurate depiction of a meridional cross-section of stress space for which angles and lengths are preserved. The middle plot shows the magnitude of the stress deviator plotted against the pressure, resulting in a plot eccentricity of $1/\sqrt{3} = 0.577$. The last plot shows the equivalent shear stress plotted against the first stress invariant, for a plot eccentricity of $\sqrt{6} = 2.45$.

Closed-form solution for ordered eigenvalues. Recalling that Lode cylindrical coordinates merely represent a coordinate change from the principal coordinates $(\sigma_1, \sigma_2, \sigma_3)$ to a new set of coordinates $(r, \bar{\theta}, z)$, it follows that inverse transformation formulas should exist for obtaining the principal stresses from Lode coordinates. Each distinct sextant in Fig. 3.4 merely corresponds to a different eigenvalue ordering. Regardless of the sextant in which the stress resides, $\bar{\theta} = 30^\circ$ falls on the pi-plane axis corresponding to the smallest eigenvalue, whereas $\bar{\theta} = -30^\circ$ falls on the axis of the largest eigenvalue. Therefore, transformation formulas that convert cylindrical coordinates back to Cartesian coordinates only need to be defined over the range from -30° through $+30^\circ$ to determine the *ordered* eigenvalues.

Letting the compressive eigenvalues be ordered $\bar{\sigma}_3 \leq \bar{\sigma}_2 \leq \bar{\sigma}_1$, the *tensile* eigenvalues must be ordered $\sigma_3 \geq \sigma_2 \geq \sigma_1$, and the inverse transformation formulas are

$$\text{low:} \quad \sigma_1 = \frac{z}{\sqrt{3}} - \frac{r}{\sqrt{2}} \left[\cos \bar{\theta} + \frac{\sin \bar{\theta}}{\sqrt{3}} \right] = \frac{I_1}{3} - \sqrt{J_2} \left[\cos \bar{\theta} + \frac{\sin \bar{\theta}}{\sqrt{3}} \right] \quad (3.43a)$$

$$\text{middle:} \quad \sigma_2 = \frac{z}{\sqrt{3}} + \frac{\sqrt{2}}{\sqrt{3}} r \sin \bar{\theta} = \frac{I_1}{3} + \frac{2}{\sqrt{3}} \sqrt{J_2} \sin \bar{\theta} \quad (3.43b)$$

$$\text{high:} \quad \sigma_3 = \frac{z}{\sqrt{3}} + \frac{r}{\sqrt{2}} \left[\cos \bar{\theta} - \frac{\sin \bar{\theta}}{\sqrt{3}} \right] = \frac{I_1}{3} + \sqrt{J_2} \left[\cos \bar{\theta} - \frac{\sin \bar{\theta}}{\sqrt{3}} \right] \quad (3.43c)$$

These formulas constitute a closed-form solution for the ordered eigenvalues of *any* real symmetric 3×3 matrix, not just a stress.* Using these formulas, any yield function that is stated in terms of principal stresses, $f(\sigma_1, \sigma_2, \sigma_3)$, can be immediately re-cast into a form expressed in terms of stress invariants, $f(I_1, J_2, J_3)$, which is more convenient for plasticity modeling because it can be differentiated without an eigenvector analysis (see Eq. 3.16). For example, any material model that seeks to initiate failure when the largest tensile principal stress σ_3 reaches a critical value, σ_3^{crit} , can do so by simply substituting Eq. (3.43c) into the failure criterion, $\sigma_3 = \sigma_3^{\text{crit}}$. The above closed-form solution for ordered eigenvalues is applied in Appendix B (page B-22) to convert the Mohr-Coulomb theory of failure into a formulation expressed in terms of stress invariants, as required in the GeoModel.

* The solution quoted here is equivalent to the closed form solution derived by Malvern [32] via a trigonometric substitution. Malvern's angle α is a Lode angle, but defined to be zero in TXE and 60° in TXC.

4. GeoModel theory

Being a generalized plasticity theory, the GeoModel is founded upon an additive decomposition of the strain rate $\dot{\underline{\underline{\varepsilon}}}$ into separate contributors: $\dot{\underline{\underline{\varepsilon}}}^e$ from elastic straining and $\dot{\underline{\underline{\varepsilon}}}^p$ from inelastic straining:

$$\dot{\underline{\underline{\varepsilon}}} = \dot{\underline{\underline{\varepsilon}}}^e + \dot{\underline{\underline{\varepsilon}}}^p. \quad (4.1)$$

The GeoModel permits the host code to employ any definition of the strain so long as its rate is conjugate to the stress $\underline{\underline{\sigma}}$ in the sense that the work rate per unit volume is given by

$$\underline{\underline{\sigma}} : \dot{\underline{\underline{\varepsilon}}}. \quad (4.2)$$

To satisfy the principle of material frame indifference, the host code must cast the stresses and strain rates in an unrotated configuration. At present, all implementations of the GeoModel have approximated the strain rate by the unrotated symmetric part of the velocity gradient:

$$\dot{\varepsilon}_{ij} \approx \frac{1}{2} \left(\frac{\partial v_m}{\partial x_n} + \frac{\partial v_n}{\partial x_m} \right) R_{mi} R_{nj}, \quad (4.3)$$

where \mathbf{v} is the velocity vector, \mathbf{x} is the current spatial position vector, and the tensor $\underline{\underline{R}}$ is the rotation from the polar decomposition of the deformation gradient. The conjugate stress is the unrotated Cauchy stress defined in Eq. 3.39. Henceforth, all references to the stress σ_{ij} and the strain rate $\dot{\varepsilon}_{ij}$ must be understood to be the *unrotated* stress and strain rate.

All GeoModel material parameterizations to date have been based on the above approximation for the strain rate. Using a different choice for the conjugate stress and strain rate measures would, of course, entail adjusting material parameters appropriately. The strain rate in Eq. (4.3) is an approximation because, for general deformations, it is not precisely equal to the rate of any proper function of the deformation*. The approximate strain rate in Eq. (4.3) exactly equals the unrotated logarithmic (Hencky) strain rate for any deformation having stationary principal stretch directions. It is an excellent approximation to the Hencky strain rate even when principal stretch directions change orientation as long as the shear strains remain small (volumetric strains may be arbitrarily large). For geological applications, material rupture generally occurs well before shear strains become large, so Eq. (4.3) is a prudent choice for the strain rate measure. If, however, the model is to be subjected to significant cyclical loading (e.g. fatigue), then a proper strain rate should be used instead of Eq. (4.3) even if the distortional strains are always small.

* Paths can be devised for which the starting and ending configurations are identical, but the time integral of $\dot{\varepsilon}_{ij}$ does not evaluate to zero [11].

Elasticity

The GeoModel supports both linear and nonlinear hypoelasticity*. The GeoModel presumes the material is elastically isotropic and that the elastic stiffness tensor C_{ijkl} is itself isotropic (i.e., deformation-induced elastic anisotropy is not included). Consequently, the stress is governed by a rate form of Hooke's law:

$$\dot{\sigma}_{ij} = C_{ijkl} \dot{\varepsilon}_{kl}^e. \quad (4.4)$$

Because the elastic tangent stiffness tensor, C_{ijkl} , is presumed to be isotropic, Eq. (4.4) can be written as two separate and much simpler equations, one for the volumetric response and the other for the deviatoric response:

$$\dot{\bar{p}} = K \dot{\bar{\varepsilon}}_v^e \quad (4.5)$$

and

$$\dot{S}_{ij} = 2G \dot{\gamma}_{ij}^e. \quad (4.6)$$

Here, G and K are the *tangent* shear and bulk elastic moduli; \bar{p} is the pressure (negative of the mean stress); $\dot{\bar{\varepsilon}}_v^e$ is the volumetric elastic strain rate computed by the trace operation,

$$\dot{\bar{\varepsilon}}_v^e = \dot{\bar{\varepsilon}}_{kk}^e, \quad (4.7)$$

S_{ij} is the stress deviator; and $\dot{\gamma}_{ij}^e$ is the deviatoric part of the elastic strain rate, defined

$$\dot{\gamma}_{ij}^e \equiv \dot{\varepsilon}_{ij}^e - \frac{1}{3} \dot{\bar{\varepsilon}}_v^e \delta_{ij}. \quad (4.8)$$

We have used the overbar (which, recall, simply denotes the negative of a variable) in our equation for the pressure-volume response because the mean stress is typically compressive (negative) in most applications of the GeoModel and therefore \bar{p} and $\bar{\varepsilon}_v^e$ are typically positive. Of course, Eq. (4.5) remains valid for volumetric expansion ($\bar{\varepsilon}_v^e < 0$) and tensile mean stresses ($\bar{p} < 0$) as well. No overbar is used in Eq. (4.8) because deviatoric tensors always have eigenvalues of mixed signs.

For *linear* elasticity, the user merely specifies constant values for the bulk modulus K and the shear modulus G . For nonlinear elasticity, the moduli are stress-dependent *tangent* moduli (i.e., slopes of the tangents to the stress-strain curves). Three parameters are available for fitting the nonlinear tangent bulk modulus K to laboratory data obtained from unloading curves in hydrostatic compression. Similarly, three parameters are available for fitting the nonlinear tangent shear modulus G indirectly from triaxial test data. Additional elastic parameters are available for materials whose elastic properties are affected by inelastic deformation (see Eqs. 4.33 and 4.34). Step-by-step instructions for determining elastic properties from measured data are provided in Appendix A.

* "Hypoelastic" means the stress can be written as a function of the strain, but is *not* derivable from an energy potential. When a potential exists, then the formulation is "hyperelastic."

Nonlinear elasticity. At the user's option, the GeoModel supports nonlinear elasticity by permitting the elastic tangent moduli to vary with the stress according to

$$K = b_o + b_1 \exp\left(-\frac{b_2}{|I_1|}\right) \quad (4.9)$$

$$G = g_o \left[\frac{1 - g_1 \exp(-g_2 J_2^{1/2})}{1 - g_1} \right]. \quad (4.10)$$

In these equations, the b_k and g_k parameters are material constants determined via nonlinear regression fitting to the unloading portions of hydrostatic compression and triaxial compression experiments, as described in Appendix A.* Further descriptions of the physical meanings of the parameters in these equations are given Appendix B. The GeoModel's functional forms for the nonlinear elastic tangent moduli are phenomenological to permit tight empirical fits to experimental data for a wide variety of materials. Suitability of these functions for fitting material data is demonstrated in Chapters 8 and 9, starting on page 96.

Incidentally, it can be shown that an elasticity model of the form in Eq. (4.4) is hyperelastic (i.e., derivable from an isotropic elastic potential) if and only if the shear modulus is constant and the bulk modulus depends at most only on I_1 . Because Eq. (4.34) permits the shear modulus to vary, the GeoModel is *hypoelastic* if $g_1 \neq 0$.

Assigning values to the elastic constants. The bulk modulus K is determined from the local tangent of the elastic part of a pressure vs. volumetric strain plot obtained from hydrostatic testing. Rather than determining the shear modulus directly from a shear loading experiment (where GeoMaterials tend to be weak), the shear modulus is typically found indirectly from triaxial loading data. For triaxial loading, the stress rates are related to the strain rates by†

$$\dot{\epsilon}_A = \frac{\dot{\sigma}_A - 2\nu\dot{\sigma}_L}{E} \quad \text{and} \quad \dot{\epsilon}_L = \frac{-\nu\dot{\sigma}_A + (1-\nu)\dot{\sigma}_L}{E}, \quad (4.11)$$

where E and ν are, respectively, Young's modulus and Poisson's ratio. If E and ν are known, then the bulk modulus K , the Lamé modulus λ , and the shear modulus G may be determined from the well-known elasticity equations [18],

$$K = \frac{E}{3(1-2\nu)} \quad \lambda = \frac{E\nu}{(1+\nu)(1-2\nu)} \quad G = \frac{E}{2(1+\nu)}. \quad (4.12)$$

Because the GeoModel casts its elasticity model in terms of the bulk modulus K and the shear modulus G , the following formulas are convenient for converting various combinations of elastic constants into expressions involving only K and G (see, for example, Ref. [18], page 139):

* The generalized nonlinear elasticity formulas on page 37 may be used when elastic properties appear to be affected by inelastic deformation.

† Here, we are writing Hooke's Law in rate form to allow for the possibility that the elastic moduli might be nonlinear. Thus, the elastic properties used here are the *tangent* moduli (i.e. based on the local slope of an elastic stress vs. strain curve).

$$\lambda = K - \frac{2}{3}G \qquad \nu = \frac{3K-2G}{2(3K+G)} \qquad E = \frac{9KG}{3K+G} \qquad (4.13)$$

$$\frac{E}{\nu} = \frac{18KG}{3K-2G} \qquad \frac{\lambda}{\nu} = \frac{2}{3}(3K+G) \qquad \frac{\nu}{1-\nu} = \frac{3K-2G}{3K+4G} \qquad (4.14)$$

$$\frac{E}{1-\nu} = \frac{18KG}{3K+4G} \qquad 2G + \lambda = K + \frac{4}{3}G \qquad G = \frac{3KE}{9K-E} \qquad (4.15)$$

$$K + \frac{4}{3}G = \frac{E(1-\nu)}{(1+\nu)(1-2\nu)} \quad (\text{uniaxial strain modulus — see Eq. 3.31}). \qquad (4.16)$$

Eq. (4.11) implies that triaxial experiments conducted under constant lateral stress ($\dot{\bar{\sigma}}_L = 0$) satisfy

$$\dot{\bar{\sigma}}_A = E\dot{\bar{\epsilon}}_A. \qquad (\text{this applies if lateral stress is constant}) \qquad (4.17)$$

A fixed lateral stress implies that $\dot{\bar{\sigma}}_A = \dot{\bar{\sigma}}_A - \dot{\bar{\sigma}}_L$. Thus, when a stress-strain curve is obtained by plotting the stress difference $\bar{\sigma}_A - \bar{\sigma}_L$ against the axial strain $\bar{\epsilon}_A$ for a triaxial loading experiment in which the lateral stress is fixed, the local tangent of the curve equals Young's modulus E . With the bulk modulus K having been obtained separately from hydrostatic test data, Eq. (4.15c) may then be used to determine the tangent shear modulus G .

The elastic limit (yield surface)

Like most plasticity models, the GeoModel begins each solution phase (i.e., each time step) by tentatively presuming that the loading is elastic. This produces a trial elastic stress, which is then checked to see if it is inside or on the yield surface. If so, the tentative assumption of elasticity is validated and the actual updated stress is set equal to the trial elastic stress. If, on the other hand, the trial elastic stress falls outside the yield surface, then the tentative assumption of elastic response was wrong, and the solution phase is then solved anew using the equations governing inelastic deformation. Before discussing these inelastic governing equations, we must first characterize the yield surface itself. We will begin by discussing yield surfaces in some generality and then progressively work towards the precise functional form for the GeoModel yield surface.

Mathematically, the GeoModel is a generalized plasticity model. The term “plasticity” is broadened to include not only the usual flow of material via dislocations (a phenomenon that has actually been observed in brittle materials when they are loaded under extraordinarily high confining pressure), but also any other mechanisms that lead to a marked departure from elasticity. Examples include crack growth, void collapse, or perhaps even phase transition. Rather than explicitly tracking each of these microscale failure mechanisms explicitly, the “yield” surface itself characterizes *them all* in an ensemble phenomenological manner. If the stress state $(\sigma_1, \sigma_2, \sigma_3)$ is “not too severe,” then material response will be elastic and therefore reversible (non-dissipative). Once the stress becomes critically severe, however, the material will undergo irreversible structural

changes that manifest as inelastic strains (nonrecoverable upon removal of the load). The material response is elastic whenever the stress is on the *inside* of the yield surface. If continuing to apply elasticity theory would move the stress into regions outside the yield surface, then plasticity equations are applied.

The GeoModel yield criterion and yield function are

GEOMODEL YIELD CRITERION:

$$\sqrt{J_2^\xi} = \frac{[F_f(I_1) - N]\sqrt{F_c(I_1, \kappa)}}{\Gamma(\bar{\theta}^\xi)}. \quad (4.18)$$

GEOMODEL YIELD FUNCTION:

$$f(\underline{\underline{\sigma}}, \underline{\underline{\alpha}}, \kappa) = J_2^\xi \Gamma^2(\bar{\theta}^\xi) - [F_f(I_1) - N]^2 F_c(I_1, \kappa). \quad (4.19)$$

The remainder of this chapter is devoted to motivating the functional forms of these equations and defining the numerous variables that appear in them. Briefly, the yield *function* f is defined such that elastic states satisfy $f < 0$. The yield *criterion* corresponds to $f = 0$. The “building block” functions F_f and Γ are used to describe the elastic limit caused by the presence of microcracks, whereas the function F_c accounts for strength reduction by porosity. The function F_f represents the ultimate limit on the amount of shear the material can support in the absence of pores (i.e., F_f represents the softening transition *limit* threshold, sketched in Fig. 1.1, resulting exclusively from microcracks). The material parameter N characterizes the maximum allowed translation of the yield surface when kinematic hardening is enabled, in which case J_2^ξ is the second invariant of the *shifted* stress tensor $\underline{\underline{\xi}} = \underline{\underline{S}} - \underline{\underline{\alpha}}$, where $\underline{\underline{\alpha}}$ is the backstress. When kinematic hardening is disabled (i.e., when $\underline{\underline{N}}$ is specified to be zero), the backstress will be zero and therefore J_2^ξ would be simply the invariant of the stress deviator. The function F_f describes the *limit* strength, whereas $F_f - N$ defines the *yield* threshold associated with cracks, which can evolve toward the limit surface via kinematic hardening as explained later in the context of Fig. 4.7. The function $\Gamma(\bar{\theta}^\xi)$, where $\bar{\theta}^\xi$ is the Lode angle of the shifted stress, is used to account for differences in material strength in triaxial extension and triaxial compression. By appearing as a multiple of $[F_f - N]^2$, the function F_c accommodates material weakening caused by porosity. The function F_c depends on an internal state variable κ whose value controls the hydrostatic elastic limit, as explained later in the context of Figs. 4.4, 4.5, and 4.15.

The principal goal of this section is to describe in great detail the physical motivations of the GeoModel yield criterion cited in Eq. (4.18). This criterion describes the geometrical shape of the yield surface in stress space. For rocks and rock-like materials, the yield surface will have a shape similar to the one illustrated in Fig. 1.0 (page 1).^{*} Figure 1.0(b) shows a “side” **meridional profile** of the yield surface in **bold**, along with a family of other profiles from which the yield surface might have evolved over time (via continuously varying values of the κ internal state variable); Fig. 4.7 shows a similar plot when kinematic hardening is allowed. Very little of the yield surface in Fig. 1.0(b) exists in the tensile domain (left side of the meridional plot), implying that materials of this type are very weak in tension.

Figure 1.0(c) shows the yield surface profile from a perspective looking down onto a plane — called an **octahedral plane** — that is perpendicular to the [111] symmetry axis and therefore represents a cross-section of the yield surface at a given pressure. Since the onset of yield must not depend on the ordering of the principal stresses, the yield surface for *any* isotropic yield model possesses 120° rotational symmetry about the hydrostat (i.e., the [111] axis), as well as reflective symmetry about any of the triaxial compression or triaxial extension axes labeled TXC and TXE in Fig. 1.0(c). As seen in Fig. 1.0(c), the octahedral profile is somewhat triangular in shape. This periodic asymmetry corresponds to differences in the failure limit under triaxial compression (TXC) and triaxial extension (TXE). Because the yield surface is farther from the origin on a TXC axis than on a TXE axis, this material has higher strength in TXC than in TXE. The $\Gamma(\bar{\theta})$ function characterizes the *shape* of the octahedral profile because r is proportional to $1/\Gamma(\bar{\theta})$. The *size* of the octahedral profile at various pressures is governed by the functions F_f and F_c .

Elastic stress states are “inside” the yield surface ($f < 0$). Stress states for which $f = 0$ are said to be “on the yield surface.” Like classical plasticity models, the yield surface in the GeoModel characterizes the point of departure from elastic to inelastic behavior. When the stress is on the yield surface, and if applying elasticity theory would result in an updated stress that falls outside the yield surface, then plasticity equations will be applied. Stress states outside the yield surface for which $f > 0$ are unachievable except through a hardening evolution of the internal state variables (κ and/or $\underline{\alpha}$) corresponding to a fundamental change of the underlying microstructure of the material. Stresses outside the *limit* surface are unachievable by *any* quasistatic means.

The internal state variable κ controls the location of the yield cap (wire frame in Fig. 1.0a on page 1). When κ increases in response to pore collapse, octahedral profiles that pass through the cap will expand isotropically (i.e., the octahedral profile changes size, but not shape, and it does so without translating in stress space). The amount of isotropic expansion or contraction varies with pressure in such a manner that the family of yield surfaces corresponding to various values of κ is bounded by the shear limit surface, $\sqrt{J_2} = F_f(I_1)/\Gamma(\bar{\theta})$.

^{*} At the user’s option, the GeoModel parameters can be set to alternatively duplicate classical idealized Von Mises or Mohr-Coulomb theory. Doing this would be inappropriate when modeling real materials, but it can be useful in benchmark testing.

Though not needed in many applications, the GeoModel supports kinematic hardening for which the symmetry axis of the yield surface is permitted to shift in stress space so that the invariants in the yield function are based on the **shifted stress** tensor, defined

$$\xi_{ij} \equiv S_{ij} - \alpha_{ij}. \quad (4.20)$$

As illustrated in Fig. 4.1, the **backstress** α_{ij} is a deviatoric tensor-valued internal state variable that defines the origin about which the yield surface is centered. When the backstress tensor changes, the yield surface translates in stress space, thereby supporting deformation-induced anisotropy (Bauschinger effect) in a limited capacity. The backstress is initially zero,

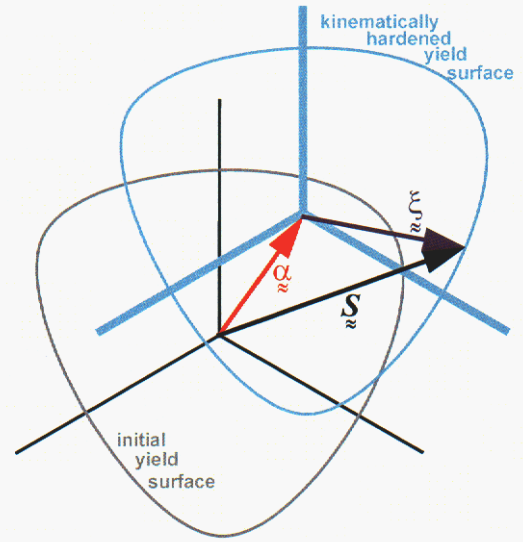


Figure 4.1. Backstress and shifted stress.

but then evolves according to an evolution equation described in detail on page 59. The GeoModel is otherwise fully isotropic, both elastically and plastically. Consequently, the yield function is isotropic with respect to the *shifted stress* deviator ξ_{ij} , implying that it depends on the invariants of the shifted stress deviator, as well as I_1 and an internal state variable κ that characterizes *isotropic* hardening caused by void collapse or softening caused by porosity increases. Specifically, the GeoModel yield function is of the form

$$f = f(I_1, J_2^\xi, J_3^\xi; \kappa), \quad (4.21)$$

where

$$J_2^\xi = \frac{1}{2} \text{tr} \xi^2 \quad \text{and} \quad J_3^\xi = \frac{1}{3} \text{tr} \xi^3. \quad (4.22)$$

In this section, we seek to describe the size and shape of the yield surface at an instant frozen in time. Thus, we will focus on how the yield function depends mathematically on the stress invariants (I_1, J_2^ξ, J_3^ξ), with the internal state variables (κ and α) regarded as constants. The means by which the yield surface evolves in response to time variation of κ and/or α is discussed separately.

Before discussing the physical foundations of the GeoModel yield function in Eq. (4.19), we will first discuss qualitative features of any yield function of the more general form in Eq. (4.21). Given that an isotropic yield function possesses alternating 30° symmetry about the [111] direction in stress space, the yield function in Eq. (4.21) is most naturally cast in terms of the cylindrical Lode coordinates as

$$f = f(r, \bar{\theta}, \bar{z}; \kappa), \quad (4.23)$$

where these Lode coordinates are defined with respect to the kinematically *shifted* origin in stress space. For any given values of $\bar{\theta}$, \bar{z} , and κ , there must exist only one radius r that is a solution to $f(r, \bar{\theta}, \bar{z}; \kappa) = 0$ (otherwise, the yield surface would not be convex). Thus, without loss in generality, elastic stress states for *any* isotropic yield function always can be characterized in the general functional form

$$r < g(\bar{\theta}, \bar{z}; \kappa), \quad (4.24)$$

where $g(\bar{\theta}, \bar{z}; \kappa)$ is regarded as a material function determined from experimental data and is introduced here only to discuss the structure of isotropic yield functions in generality (i.e., the GeoModel has an *implied* “ g ” function, but does not construct one explicitly). The yield function corresponding to Eq. (4.24) may be written

$$f = r^2 - [g(\bar{\theta}, \bar{z}; \kappa)]^2 \quad (\text{Any isotropic yield function can be written in this form.}) \quad (4.25)$$

At present, the GeoModel assumes that the *shape* of the octahedral yield profile is the same at all pressures — only its *size* varies with pressure.* Moreover, the GeoModel presumes that the shape of the octahedral yield profile is constant in time (i.e., it does not evolve to any different *shape* in response to plastic deformation even though it can permissibly vary in size and translate in stress space). Consequently, the GeoModel’s yield function is structured such that $g(\bar{\theta}, \bar{z}; \kappa)$ is *separable* into the product of two distinct functions, one depending only on $\bar{\theta}$ and the other depending only on \bar{z} and κ , permitting Eq. (4.24) to be structured in the general form:

$$r < h_1(\bar{\theta})h_2(\bar{z}; \kappa) \quad (\text{This form results from a separability assumption.}) \quad (4.26)$$

As was the case with the g function, h_1 and h_2 have been introduced here only to illustrate the basic structure of the GeoModel’s yield function. The GeoModel’s specific formulations will be discussed soon. A degree of ambiguity exists in the definitions of h_1 and h_2 because they may be replaced respectively by ηh_1 and h_2/η for any scalar η without loss in generality. To remove this ambiguity, the function h_1 is scaled such that it merely describes the *shape* of the octahedral profile (i.e., the view of the yield surface looking down the [111] direction). The function h_2 defines the meridional profile of the yield function, and therefore this function also defines the *size* of the octahedral profile.

The GeoModel aims to model rocks and rock-like brittle materials. The mechanical behavior of such materials is typically driven by two underlying mechanisms: porosity and microcracks. To date, microphysical research has focused on the effects of only one of these mechanisms at a time. Figure 4.2(a) shows the qualitative shape of the meridional profile typically that is predicted when only porosity is considered. In this case, the meridional yield profile is a “cap” function that is essentially flat like a Von Mises profile for a large range of pressures (\bar{z} is proportional to pressure), and then the profile drops to zero when pressure becomes large enough to collapse voids. Figure 4.2(b) shows the general

* Some evidence suggests that the octahedral yield profile should in fact vary in shape from strongly triangular at low pressures to nearly circular at extraordinarily high pressures [23]. Consequently, the GeoModel’s current assumption of a constant octahedral profile shape might change in future releases.

shape of a meridian profile that is typically predicted for theories that consider only the influence of microcracks *without* considering porosity. Microcracks lead to low strength in tension, but strength increases as pressure is increased because pressure generates additional friction at crack faces, thereby reducing the shear load suffered by the matrix material. The GeoModel, unifies these separate microscale theories to obtain a combined porosity and microcrack model as sketched qualitatively in Fig. 4.2(c). Loosely speaking, the GeoModel obtains the combined meridional yield function by multiplying the individual porosity and microcrack profiles (and scaling the ordinate appropriately to match data).

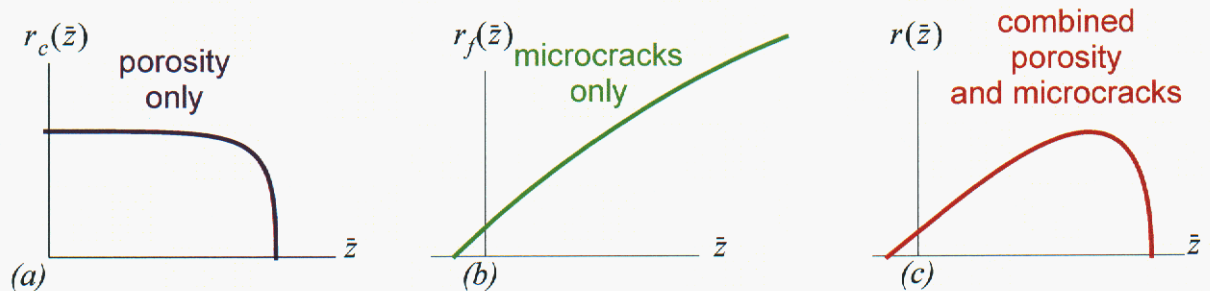


Figure 4.2. Qualitatively meridional profile shapes resulting from (a) porosity alone, (b) microcracks alone, and (c) porosity and microcracks in combination.

To date, the *combined* effect of voids and microcracks remains a poorly developed branch of materials constitutive modeling. Some early models simply asserted that a material is elastic (safe from yield) only if it is safe from both crack growth and void collapse, with each criterion tested *separately*. However, as illustrated in Fig. 4.3(a), this approach results in a discontinuous slope in the meridional yield profile and fails to account for interactions between voids and cracks. The GeoModel [Fig. 4.3(b)], phenomenologically permits cracks and voids to interact in a way that results in a continuously differentiable meridional profile, making the GeoModel better-suited for reproducing observed data.

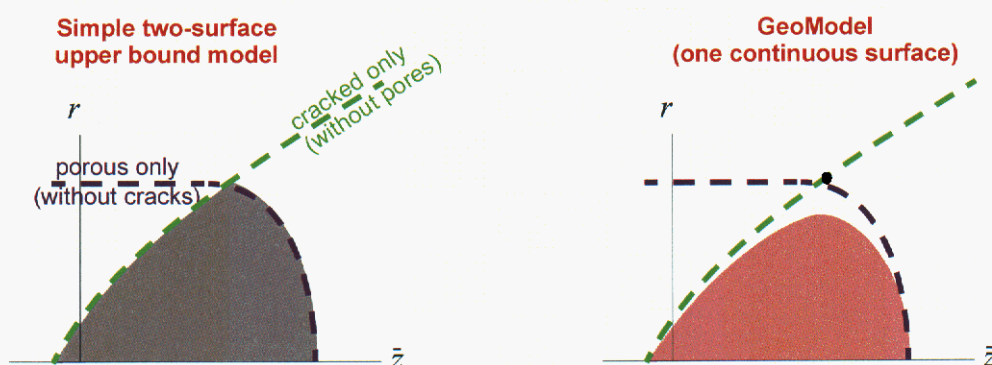


Figure 4.3. Distinction between two-surface upper-bound models and the GeoModel.

The GeoModel achieves a *combined* porous+cracked yield surface by multiplying the fracture function $r_f(\bar{z})$ in Fig. 4.2(b) times the cap function $r_c(\bar{z})$ in Fig. 4.2(a) so that

$$r(\bar{z}) \text{ is proportional to } r_f(\bar{z})r_c(\bar{z}). \quad (4.27)$$

The proportionality factor depends on the Lode angle $\bar{\theta}$ so that the equivalent shear stress at yield (which, recall, is simply a constant multiple of r) can be made lower in TXE than in TXC. Cap functions depend on the porosity level (which controls where the cap curve intersects the z -axis). The curvature of a cap function controls the degree to which porosity affects the shear response. Although the GeoModel does not explicitly track porosity, it does include an internal state variable κ that equivalently accounts for the *presence* of porosity. As explained later (page 50), the value of κ and one additional material constant, R , determine both the cap curvature and the location where the cap intersects the hydrostat (the \bar{z} axis). Thus, the cap function $r_c(\bar{z})$ implicitly depends on κ and R .

Recalling that the Lode cylindrical radius r equals $\sqrt{2J_2^\xi}$ and the Lode axial coordinate z is proportional to I_1 , the GeoModel implements the notion of multiplying fracture and cap functions by using Eq. (3.40) to express Eq. (4.27) in terms of stress invariants instead of Lode coordinates, so the GeoModel yield function is of the form

$$\sqrt{J_2^\xi} = \frac{f_f(\bar{I}_1)f_c(\bar{I}_1)}{\Gamma(\bar{\theta})}. \quad (4.28)$$

Comparing with Eq. (4.18), the f and F functions are related by

$$f_f = F_f - N \quad \text{and} \quad f_c = \sqrt{F_c}. \quad (4.29)$$

The invariant J_2^ξ is computed using the *shifted* stress tensor $\xi \equiv \underline{\underline{S}} - \underline{\underline{\alpha}}$, where $\underline{\underline{\alpha}}$ is the deviatoric tensor-valued backstress that is nonzero only when kinematic hardening is enabled. Thus, in addition to depending explicitly on the stress tensor, the yield criterion depends implicitly on material constants and on two internal state variables, κ (mentioned earlier) and $\underline{\underline{\alpha}}$.

The fracture function f_f characterizes the cracking-related portion of the meridional yield profile. The GeoModel cap function f_c is normalized to have a peak value of 1. The function $\Gamma(\bar{\theta})$ characterizes the Lode angle dependence of the meridional profile and is normalized to equal 1 in triaxial compression ($\bar{\theta} = 30^\circ$). At different Lode angles, Γ usually has values *greater* than 1, which (because it is a *divisor* in Eq. 4.28) reduces equivalent shear strength. Rather than regarding Γ as a strength reducer, it can be alternatively interpreted as a *stress intensifier*. Qualitatively, these functions are typically shaped as shown in Fig. 4.4.

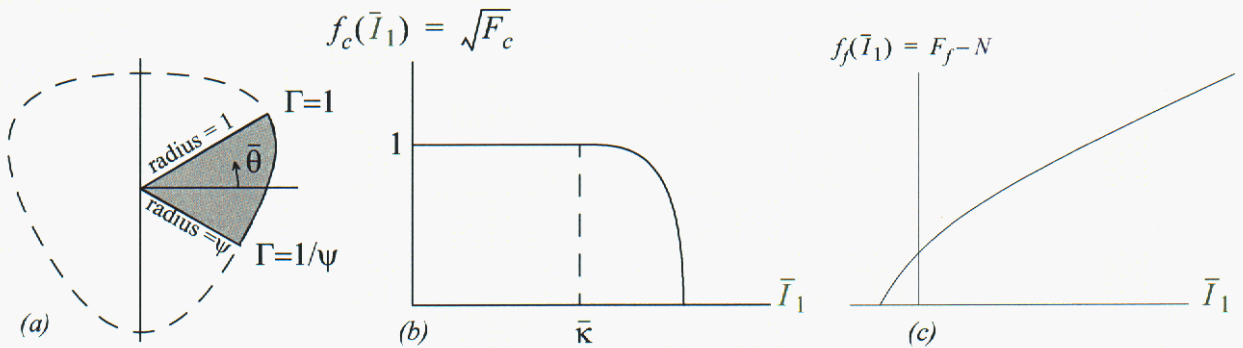


Figure 4.4. Basic shapes of the three key functions that characterize the composite shape of the yield surface. (a) Lode angle dependence, (b) porosity cap curve, (c) limit failure curve. The Lode angle function $\Gamma(\bar{\theta})$ is the reciprocal of the radius in the octahedral plane, making it best regarded as a stress intensifier; $\Gamma(\bar{\theta})$ is normalized to equal 1 in triaxial compression, which implies that it must equal $1/\psi$ in triaxial extension (where ψ is the TXE/TXC strength ratio). Shear influence on void collapse begins at the point where the cap function branches into an ellipse. Since the cap function is multiplied by the fracture curve, this transition point also marks where the composite GeoModel failure surface branches away from f_f , beyond which macroscale response is influenced simultaneously by both cracks and voids. For pure (shear-free) hydrostatic compression, void collapse begins at the point where the ellipse intersects the horizontal. Only the function f_f has dimensions of stress (the others are dimensionless).

As explained on page 43, the precise expression for the Γ function is determined by user-specification of two parameters: the TXE/TXC strength ratio ψ and an integer-valued option (**J3TYPE**), which controls the manner in which the octahedral profile radius varies from the value $1/\psi$ at TXE to 1 at TXC. As explained below, the porosity (cap) function f_c is defined by two parameters: the initial intersection p_0 on the horizontal axis and the eccentricity or “shape factor” R for the ellipse (i.e., the width to height ratio of the ellipse). As explained on page 56, the GeoModel internally computes evolution of the cap function resulting from void collapse. As explained on page 41, the very important f_f function, which reflects influence of microcracks, is determined by fitting triaxial compression data to an exponential spline [up to five parameters (a_1, a_2, a_3, a_4, N)]. Standard experiments (needed to assign values to these parameters) are discussed in Appendix A. The remainder of this chapter is dedicated to providing further details about the three key functions f_c, f_f , and Γ used in the GeoModel.

The cap function, f_c . Under compression, the pores in a material can irreversibly collapse, thereby resulting in permanent (plastic) volume changes when the load is removed. Plastic volume changes can occur for porous media even if the matrix material is plastically incompressible. Permanent volume changes can also occur if a material undergoes an irreversible phase transformation. The GeoModel supports plastic volume changes, but it does so without explicitly modeling the underlying microphysical mechanisms. Nonetheless, the GeoModel does reflect the influence of micromechanical theory by phenomenologically incorporating plastic volume changes observed in hydrostatic loading. To motivate the GeoModel's cap theory, we will explain the equations and their qualitative features in the context of porosity, but keep in mind that any other microphysical compactive mechanisms are equally well accommodated by the phenomenological cap model.

The cap function f_c accounts for the presence of pores in a material by controlling where the yield function will intersect the \bar{I}_1 axis in compression. This intersection point corresponds to $J_2 = 0$ and, because we are considering compressive states, we will denote the value of \bar{I}_1 at the intersection point by $\bar{I}_1 = \bar{X}$, where $\bar{X}/3$ is the pressure (positive in compression) at which inelastic deformation commences in *purely hydrostatic* loading for a given level of porosity. As voids compress out, the value of \bar{X} will change, as explained later when we discuss the evolution equations for the GeoModel's internal state variable κ . Porosity also degrades material *shear* strength because, recalling Eq. (4.28), the cap function effectively reduces the nonporous yield strength, defined previously by the fracture function f_f .

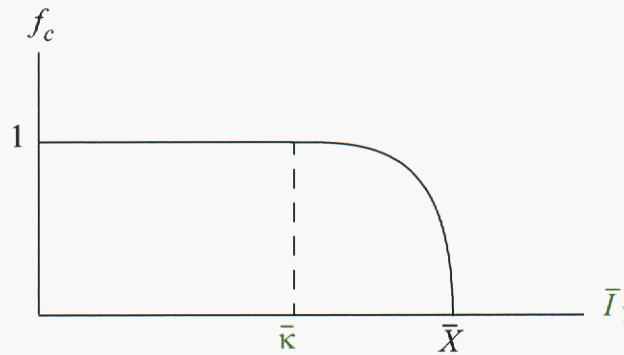


Figure 4.5. GeoModel cap function

The GeoModel employs a cap function* defined

$$f_c^2(\bar{I}_1, \kappa) = \begin{cases} 1 & \text{if } \bar{I}_1 < \bar{\kappa} \\ 1 - \left(\frac{\bar{I}_1 - \bar{\kappa}}{\bar{X} - \bar{\kappa}} \right)^2 & \text{otherwise.} \end{cases} \quad (4.30)$$

* evaluated in the code by a Pelessone [34] function, $f_c^2(\bar{I}_1, \bar{\kappa}) = 1 - \frac{(\bar{I}_1 - \bar{\kappa})(|\bar{I}_1 - \bar{\kappa}| + (\bar{I}_1 - \bar{\kappa}))}{2(\bar{X} - \bar{\kappa})^2}$.

Neither $\bar{\kappa}$ nor \bar{X} are user-supplied material parameters. Instead, these variables are computed internally within the GeoModel code by enforcing consistency with more intuitive user-supplied parameters obtained from hydrostatic testing (see page 55).

The equation of the elliptical portion of the cap curve is

$$f_c^2 + \left(\frac{\bar{I}_1 - \bar{\kappa}}{\bar{X} - \bar{\kappa}} \right)^2 = 1. \quad (4.31)$$

The intersection point \bar{X} will be later related to the value of $\bar{\kappa}$ so that knowledge of the internal state variable $\bar{\kappa}$ will be sufficient to compute a value for \bar{X} . For now, while describing the geometry of the yield surface, both $\bar{\kappa}$ and \bar{X} should be regarded as internal state variables whose values are computed internally in the GeoModel using evolution equations discussed later. Rather than using f_c directly, recall that the GeoModel uses the function F_c that is simply the square of f_c given in Eq. (4.30):

$$F_c = f_c^2. \quad (4.32)$$

Elastic-plastic coupling. The cap model is used when the material being studied contains enough porosity (or highly compliant second phase inclusions) so that inelastic volume reduction become possible through irreversible reduction of void space. Intuitively, one might expect the elastic moduli to stiffen as voids collapse, but the material might actually become more elastically compliant as shown in Fig. 8.4 (a phenomenon that might be explained, for example, by rubblization of a ligament network). Regardless of its microphysical origins, the elastic moduli are permitted to vary with plastic strain by generalizing the nonlinear elastic moduli expressions in Eqs. (4.9) and (4.10) to

$$K = f_K \left\{ \left[b_o + b_1 \exp\left(-\frac{b_2}{|I_1|}\right) \right] - b_3 \text{Exp}\left(-\frac{b_4}{|\bar{\epsilon}_v^p|}\right) \right\} \quad (4.33)$$

$$G = f_G \left\{ g_o \left[\frac{1 - g_1 \exp(-g_2 J_2^{1/2})}{1 - g_1} \right] - g_3 \text{Exp}\left(-\frac{g_4}{\gamma_{\text{equiv}}^p}\right) \right\}. \quad (4.34)$$

In the absence of joints, the scale factors f_G and f_K equal 1.0; otherwise, they are computed internally within the GeoModel as described in a separate sequel report. In the above equations, γ_{equiv}^p is the equivalent plastic shear strain (which, for proportional loading, is conjugate to the equivalent shear stress, $\sqrt{J_2}$), and $\bar{\epsilon}_v^p$ is the plastic compaction volume change. Mathematically,

$$\gamma_{\text{equiv}}^p = \int \sqrt{2} \left\| \dot{\gamma}^p \right\| dt \quad (4.35)$$

$$\bar{\epsilon}_v^p = \int \text{tr} \dot{\epsilon}^p dt. \quad (4.36)$$

Though defined mathematically as stated, the GeoModel computes the plastic volume change, $\bar{\epsilon}_v^p$ indirectly, as explained later in the context of Eq. (4.67).

Meridional shear limiter function, F_f . In a loose sense, the previous sub-section described the GeoModel’s cap function f_c by considering a material that contained pores, but no cracks. In this sub-section, we describe the GeoModel’s fracture function f_f by considering a material that contains microcracks *but no porosity*. Numerous microphysical analyses (as well as a preponderance of data) suggest that, for microcracked media, the onset of “yield” depends on all three stress invariants, which implies that the yield function for microcracked media must depend on all three cylindrical Lode coordinates. The GeoModel supports this singularly common prediction of microscale damage theory. Though they differ in specific details, microphysical damage theories and laboratory observations for brittle materials also tend to share the following qualitative features:

- At a given mean stress, yield in triaxial extension (TXE) occurs at a lower stress than in triaxial compression (TXC), which implies that octahedral yield profiles are generally triangular (or distorted hexagon) in shape, with the triangle apex being located on TXC axes, as sketched in Fig. 1.0(c) on page 1.
- Brittle materials are very weak in tension. This implies that the meridional yield profile will include few if any tensile stress states. Brittle materials are also vulnerable to shear cracking at low pressures, but they become able to support increasingly large shear stresses as pressure is increased because friction at crack faces helps reduce the shear load that must be suffered by the matrix material itself. Thus, in the absence of porosity, the meridional profile is expected to monotonically increase with pressure.
- When microscale theories regard brittle crack fracture to be the *only* failure mechanism, they predict that the material strength (i.e., the Lode radius at failure) will increase monotonically with increasing pressure, so that the meridional profile expands in an ever-expanding cone-like shape like the limit surface in Fig. 1.1. Microphysical idealizations such as Mohr-Coulomb theory predict the meridional profile is a straight line whose slope is directly related to the friction coefficient. When microscale theories allow for both crack growth and ductility of the matrix material, they predict that the increase in strength from friction will continue only until ductile yield (at extraordinarily high pressures) becomes more likely; such theories correspond to a meridional yield profile that is cone-like at low to moderate pressures but asymptotes to a zero slope (like a Von Mises cylinder) at high pressures.

Given the wide variety of microscale predictions for the meridional profile, the GeoModel is equipped with a four-parameter exponential spline that is capable of replicating any of these microphysical idealized theories, as well as actual observed material yield and rupture response at low and moderate pressures (i.e., at pressures well below the cap elastic limit) so that observed data primarily reflect microcrack damage rather than combined cracking with pore collapse (covered elsewhere in this report).

In the meridional plane (i.e., at a given value of the Lode angle), the **yield surface** characterizes the transition boundary for inelastic flow. Stress states that were, at one time, outside the yield surface might become realizable through hardening evolution of the yield surface. However, the allowable amount of hardening is not unbounded. At some point, the material will fail catastrophically (i.e., rupture). Often, the stress at rupture is *smaller* than the peak stress. Stress-strain curves might or might not exhibit post-peak softening, depending on whether or not the experiment is stress-controlled or strain-controlled.

The *peak* stress (not the stress at rupture) defines the stress-carrying limit of the material. As first mentioned on page 5, the **limit surface** is the boundary of all stress states that the material is *capable* of supporting. Many of these achievable stress states can be reached only through inelastic processes. Appendix A (step 4 on page A-5) describes in detail how to determine the limit surface from experimental data. Mathematically, the limit surface is characterized by a limit function that is similar in form to the yield function. Specifically, the limit surface is defined by $F(\underline{\sigma}) = 0$, where

$$F(\underline{\sigma}) = J_2(\underline{\sigma}) - \frac{F_f^2[I_1(\underline{\sigma})]}{\Gamma[\bar{\theta}(\underline{\sigma})]}. \quad (4.37)$$

The limit function $F(\underline{\sigma})$ depends *only* on $\underline{\sigma}$, not on any internal state variables. A yield function $f(\underline{\sigma}, \underline{\alpha}, \kappa)$, on the other hand, depends on the backstress tensor $\underline{\alpha}$ and on the scalar internal state variable κ . Unlike a yield surface, which can evolve over time because it depends on time-varying internal state variables, the limit surface is *fixed* in stress space. The yield function is presumed to share some qualitative features with the shear limit surface, but depends additionally on internal state variables as follows:

$$f(\underline{\sigma}, \underline{\alpha}, \kappa) = J_2(\underline{\xi}) - \frac{\{F_f[I_1(\underline{\sigma})] - N\}^2 F_c(I_1(\underline{\sigma}), \kappa)}{\Gamma[\bar{\theta}(\underline{\xi})]}, \quad \text{where } \underline{\xi} \equiv \underline{\sigma} - \underline{\alpha}. \quad (4.38)$$

When examining experimental data, it is generally easier to determine the maximum limit point than the point at which plasticity first begins. Consequently, the GeoModel provides an empirical fitting function F_f for the limit surface in the meridional plane, and the initial meridional yield surface is simply $F_f - N$, reduced perhaps by a cap function F_c if the material initially contains voids. Comparing Eq. (4.38) with (4.37) reveals that the yield surface inherits its octahedral profile *shape* (i.e., its Lode angle dependence) from the limit surface. The *size* of the yield octahedral profile is generally smaller than the limit surface profile because of the multiplier (cap) function F_c , which represents the effect of porosity. The yield surface origin is also offset from the limit surface origin by an amount governed by the kinematic hardening backstress tensor $\underline{\alpha}$. The limit surface always has a [111] symmetry axis *passing through the actual (not kinematically shifted) origin* in stress space. When kinematic hardening is enabled, the yield surface has a symmetry axis parallel to [111] that is off-set so that it does *not* pass through the origin.

When advancing the solution, the initial meridional profile can harden kinematically and/or isotropically. The equations governing yield surface evolution are designed to permit only a limited amount of hardening. As sketched in Fig. 4.6, the initial yield surface is permitted to translate upward in the meridional plane by no more than a user-specified limit N .

When the yield surface has reached the limit surface *and when the stress itself lies on the limit surface*, the material will begin to soften. At that point, a *constitutive-level* description of material response no longer remains possible; the host code must intervene by inserting void or by invoking special elements capable of supporting displacement discontinuities. The limit surface marks the point at which a continuum material model is inadequate to characterize macroscale material response because softening localization becomes possible. Before reaching the limit surface, material response is handled entirely by the GeoModel.

The shifted shear limiter function $F_f(I_1) - N$ defines how the shear stress at yield varies with pressure for a *non-porous*, but microcracked, material in its initial (virgin) state. When this microcrack yield function is combined with the cap function $F_c(I_1, \kappa)$ the actual shear stress at yield is further reduced because porosity makes inelasticity possible even for purely hydrostatic compression (i.e., loading along the \bar{I}_1 axis). The GeoModel evolves this combined porous yield function in such a way that the yield surface grows up to the limit surface. The GeoModel does not handle material response *after*

reaching the limit surface. Properly, upon receiving a “limit-arrival” signal, the host code must, at this time, initiate scale-dependent softening localization through the use of void

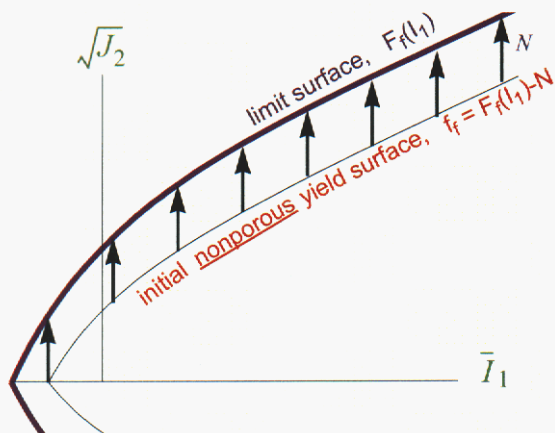


Figure 4.6. *Kinematic hardening.* The user defines parameters (a_1, a_2, a_3, a_4) for the ultimate shear limit surface. The initial yield surface is identical except shifted down by a user specified amount N . Kinematic hardening allows the initial yield surface to translate until reaching the ultimate failure surface (at which point, the host code must initiate “element death” or perhaps some other strategy for supporting macroscale softening).

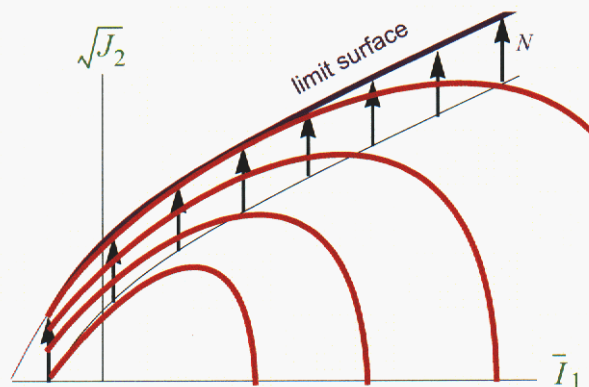


Figure 4.7. *Yield surface evolution with both microcracking and porosity.* For real materials, that contain both cracks and voids, it is difficult to identify a single envelope for the combined porous/cracked fracture yield function f_f . However, ultimate failure data can be more readily mapped out.

insertion or special elements that support displacement discontinuities. If the host code *fails* to initiate a softening algorithm, the GeoModel will treat the limit surface as if it were a nonhardening yield surface (making its post-peak predictions robust, but undoubtedly inaccurate).

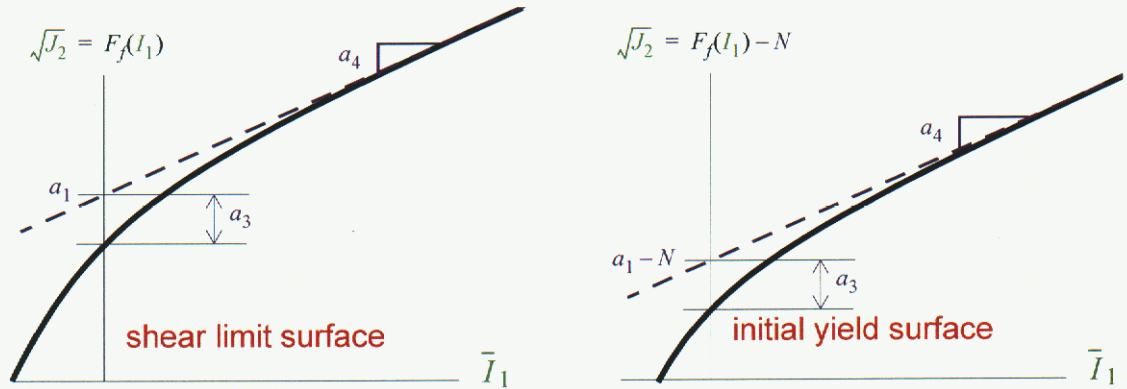


Figure 4.8. Shear limiter function (unshifted and shifted). The shifted function should be regarded as a nominal shape of the yield surface in the meridional plane, although porosity further lowers and distorts the meridional yield profile by multiplying the shifted shear limit function by F_c .

The GeoModel supports modeling microcracked material by providing flexible fitting functions that can reproduce octahedral and meridional yield profiles observed for real materials. In particular, the shear limit function used in the GeoModel is of the form

$$F_f(I_1) = a_1 - a_3 e^{-a_2 \bar{I}_1} + a_4 \bar{I}_1, \text{ where } \bar{I}_1 = -I_1 \quad \text{shear limit surface in TXC. (4.39)}$$

where the a_k are user-specified material parameters determined from experimental data as explained in Appendix A. The initial (nonporous) meridional yield profile is

$$f_f(I_1) = F_f(I_1) - N \quad \text{initial yield surface (non-porous). (4.40)}$$

where N is the user-specified shift factor. Therefore, $a_1 - N$ is the zero pressure intercept of the nonporous meridional yield surface on the $\sqrt{J_2}$ axis. Frequently, N is taken to be zero. The shear limiter function, Eq. (4.39), asymptotes to a linear envelope, as indicated in Fig. 4.8. To force the material to obey a Von-Mises type yield response at extremely high pressures, the slope coefficient a_4 is merely set to zero.

Let us now explain why the shear limiter function has the general shape depicted in Fig. 4.8. Then we will list constraints on the model parameters necessary to achieve this shape. Brittle materials fail at very low shear stresses when the pressure is low, but they are able to sustain higher levels of shear stress without failing if loaded under higher confining pressures. Consequently, the shear limiter function is expected to increase monotonically with pressure. Or, since \bar{I}_1 is proportional to the pressure, F_f is expected to increase monotonically with \bar{I}_1 . Furthermore, a fundamental tenant from plasticity theory is that the yield function must be semi-convex, which implies that the second partial derivative of $F_f(I_1)$ must be negative or zero. When we speak of the “shear” stress at failure,

we are effectively speaking of the value of the Lode radius at failure corresponding to the Lode angle for the stress state. For any cylindrical coordinate system — including the Lode system — the radius must always be non-negative and therefore F_f is defined only over the domain for which it yields positive values. Finally, in its virgin state, any material should be unfailed at zero stress, which means that the origin must fall below the meridional yield profile. All of these physical considerations lead to the following constraints on allowable values for the parameters:

$$a_1 - a_3 - N \geq 0 \quad \text{unloaded virgin material must be below yield} \quad (4.41)$$

$$a_2 a_3 + a_4 \geq 0 \quad \text{non-negative slope at low pressures} \quad (4.42)$$

$$a_2 > 0 \quad \text{positive Lode radius} \quad (4.43)$$

$$a_3 \geq 0 \quad \text{convexity condition} \quad (4.44)$$

$$a_4 \geq 0. \quad \text{non-negative slope at high pressures} \quad (4.45)$$

Specific values for these model parameters are determined from triaxial test data, as explained in Fig. 3.3 on page 16 (and in Figs A.4 and A.5 of Appendix A). Sample fits of the GeoModel's shear limit function to data can be found in Fig. 8.1 on page 96 and Fig. 8.5 on page 99.

The complete GeoModel yield function.

Equation (4.28) is the yield *criterion*. The yield *function* f must be negative for all elastic states (inside the yield surface), zero for all stress states satisfying the yield criterion (on the yield surface), and positive for all stress states (outside the yield surface) that cannot be reached except through an inelastic process — if at all. For computational reasons, the GeoModel's yield function is based on the square of Eq. (4.28):

$$f = \Gamma^2(\bar{\theta}^\xi) J_2^\xi - f_f^2(I_1) f_c^2(I_1, \kappa). \quad (4.46)$$

When kinematic hardening is used, the stress invariants, $\bar{\theta}^\xi$ and J_2^ξ , are those for the kinematically shifted stress tensor, $\xi \equiv \underline{\underline{S}} - \underline{\underline{\alpha}}$. Otherwise, when kinematic hardening is disabled, these are simply the stress invariants. Of course, I_1 is the first invariant I_1^σ of the stress tensor $\underline{\underline{\sigma}}$. (Since backstress $\underline{\underline{\alpha}}$ is deviatoric, $I_1^\xi = 0$).

The building block functions f_f and f_c are implemented in the GeoModel in a slightly altered form by being expressed in terms of the shear limit function F_f and an alternative (computationally more efficient) cap function F_c :

$$f_f(I_1) = F_f(I_1) - N \quad (4.47)$$

$$f_c(I_1, \kappa) = \sqrt{F_c(I_1, \kappa)}. \quad (4.48)$$

The first of these equations allows the user to specify a maximum amount, N , that the yield function is permitted to translate under kinematic hardening. Thus, the function F_f can be regarded as a “limit” or “softening” envelope, beyond which stresses can *never* be reached quasistatically (not even via hardening). The second equation recasts the f_c function as the square root of a different function F_c for computational reasons. The second

equation also shows explicitly the presence of the internal state variable κ related to the isotropic hardening part of the GeoModel associated with void collapse. The internal state variable κ marks the branch point where combined porous/cracked yield surface deviates from the nonporous yield surface. As explained on page 56, this branch point is determined internally within the GeoModel in a manner that ensures consistency with measured hydrostatic data.

In terms of the new building block functions, the critical Lode radius in triaxial compression (TXC), where $\Gamma(\bar{\theta}) = 1$, may be expressed as a function of the Lode axial coordinate z as

$$r^{\text{TXC}} = \frac{(F_f(\sqrt{3} z) - N)\sqrt{F_c(\sqrt{3} z, \kappa)}}{\sqrt{2}}. \quad (4.49)$$

Plotting r^{TXC} vs. z (at a given value of κ) will produce a *geometrically accurate* visualization of the meridional yield profile. Often we instead plot $\sqrt{J_2}$ vs. \bar{I}_1 to label the axes with more broadly recognized stress measures, but in doing so we are actually showing a geometrically distorted view of the yield profile, as explained on page 23.

Substituting Eqs. (4.47) and (4.48) into (4.46) gives the yield criterion cited at the beginning of this section [Eq. 4.18].

The “J3TYPE” Lode-angle function, Γ . This section describes available functional forms for the Lode angle dependence function $\Gamma(\bar{\theta})$. This function controls the shape of the octahedral yield profile. Since this function controls only the *shape*, not size, of the octahedral profile, its magnitude is inconsequential. The Γ function is normalized to equal unity in TXC ($\bar{\theta} = +30^\circ$).^{*} At other Lode angles, $\Gamma(\bar{\theta}) > 1$. Thus, since $\Gamma(\bar{\theta})$ appears in the yield function as a *multiplier* of J_2^ξ , it acts as a pseudo stress *raiser*, causing yield to occur at smaller values of J_2^ξ at Lode angles differing from the fiducial (TXC) angle where $\Gamma(\bar{\theta}) = 1$. To ensure convexity of the octahedral yield profile, the Lode angle function must satisfy

$$\Gamma''(\bar{\theta}) + \Gamma(\bar{\theta}) \geq 0. \quad (4.50)$$

A hallmark trait of rocks and rock-like materials (concrete, ceramics, etc.) is a higher strength in triaxial compression than in triaxial tension at any given mean pressure. Loosely speaking, this characteristic results from friction at crack faces being able to carry a larger portion of the load under compression, therefore sparing the surrounding matrix material from having to carry the entire resolved shear stress at crack tips. Classical Mohr-Coulomb theory, which is supported by the GeoModel primarily for comparisons with ide-

^{*} With this normalization, the f_f meridional function then quantifies the pressure-varying *size* of octahedral profiles

alized analytical solutions, has an octahedral profile in the shape of a distorted hexagon, causing considerable computational difficulties when dealing with the vertices. The computational attractiveness of removing yield surface corners has motivated numerous proposals of smoothed three-invariant models for frictional materials [29,28,3,47,7], and Lade [30] was among the first efforts to additionally include curvature in the meridional plane. According to Borja, et. al. [6], there is evidence that smoothed yield surfaces capture mechanical response more accurately than vertex models, but these authors point to no data to back up this claim. The GeoModel presently supports three yield-type options (specified by a value of 1, 2, or 3 for the user parameter, `J3TYPE`):

1. Gudehus (an efficient smoothed profile, with restrictions on convexity)
2. Willam-Warnke (a relatively inefficient smooth profile with no convexity constraints)
3. Mohr-Coulomb (distorted hexagon polygon)

The Gudehus and Willam-Warnke options both correspond to fully differentiable yield functions (no vertices). The Mohr-Coulomb option (which is available principally for comparisons with analytical solutions) is differentiable everywhere except at triaxial states where yield surface vertices require special numerical handling.*

Recognizing logistical constraints of most laboratories, the GeoModel presumes that experimental data are available *at most* only for a limited number of canonical loading paths: perhaps triaxial extension ($\bar{\theta} = -\pi/6$), perhaps simple shear ($\bar{\theta} = 0$), and almost certainly triaxial compression ($\bar{\theta} = \pi/6$). Regardless of which yield-type (Gudehus, Willam-Warnke, or Mohr-Coulomb) is selected, the shape of the octahedral yield profile is described, in part, by user specification of a parameter ψ , equal to the **triaxial extension/compression (TXE/TXC) strength ratio** at a given pressure. The GeoModel presumes that only the *size* of the octahedral yield profile — not its shape — varies with pressure. Consequently, the strength ratio ψ equals its user-specified value at *all* pressures and throughout the entirety of the simulation (i.e., ψ is a *constant*, not a time varying internal state variable). Appendix A gives instructions for inferring a value of ψ from experimental data.

* The GeoModel averages directions on either side of the vertex if the strain rate points within the limiting (Koiter) fan of unit normals. If the strain rate points within a sextant of the octahedral plane, then the normal in that sextant is used.

Precise functional forms of available Lode angle functions are given below:

$$1. \text{ Gudehus: } \Gamma(\bar{\theta}) = \frac{1}{2} \left[1 + \sin 3\bar{\theta} + \frac{1}{\psi} (1 - \sin 3\bar{\theta}) \right].$$

To satisfy the convexity requirement of Eq. (4.50), the strength ratio must satisfy $\frac{7}{9} < \psi < \frac{9}{7}$.

$$2. \text{ Willam-Warnke: } \Gamma(\bar{\theta}) = \frac{4(1-\psi^2)\cos^2\alpha^* + (2\psi-1)^2}{2(1-\psi^2)\cos\alpha^* + (2\psi-1)\sqrt{4(1-\psi^2)\cos^2\alpha^* + 5\psi^2 - 4\psi}},$$

where $\alpha^* = \frac{\pi}{6} + \bar{\theta}$. The Willam-Warnke option is convex for $\frac{1}{2} \leq \psi \leq 2$.

$$3. \text{ Mohr-Coulomb: } \Gamma(\bar{\theta}) = \frac{2\sqrt{3}}{3 - \sin\phi} \left(\cos\bar{\theta} - \frac{\sin\phi \sin\bar{\theta}}{\sqrt{3}} \right). \text{ Here, the internal friction}$$

angle ϕ is the angle of the failure envelope in the Mohr-diagram ($\tan\phi = \mu$, where μ is the coefficient of friction). Within the GeoModel, ϕ is determined from the user-supplied strength ratio by $\sin\phi = 3\frac{(1-\psi)}{1+\psi}$. The Mohr-Coulomb option is convex for $\frac{1}{2} \leq \psi \leq 2$.

These three options are distinguished by how the octahedral yield profile varies in stress space in the transition from TXE to simple shear to TXC at a fixed pressure. Graphs of the octahedral yield profile corresponding to any of the above options may be constructed by parametrically plotting

$$x = r \cos \bar{\Theta} \quad y = r \sin \bar{\Theta} \quad (4.51)$$

$$\text{Here, } r = \frac{\sqrt{2}}{\Gamma(\bar{\theta})}, \quad \text{where } \bar{\theta} = \frac{1}{3} \text{ArcSin}(\sin 3\bar{\Theta}). \quad (4.52)$$

The angle $\bar{\Theta}$ varies from 0 to 360° , and therefore $\bar{\theta}$ varies between -30° and $+30^\circ$.

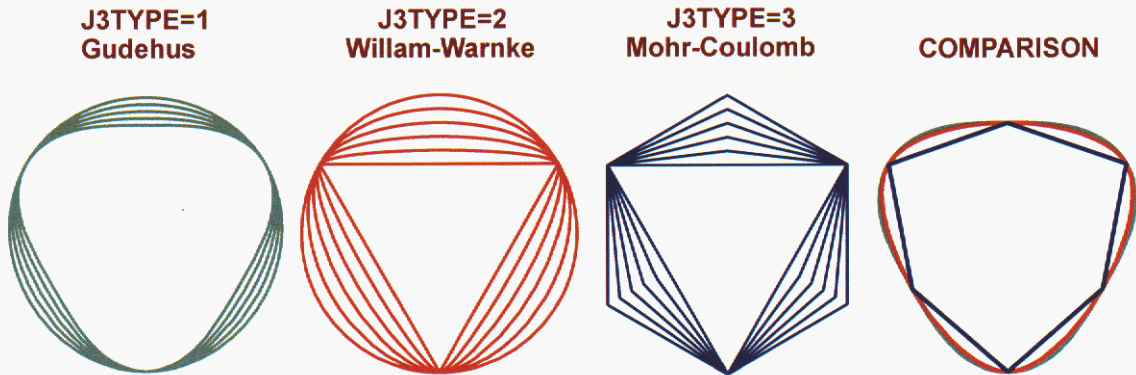


Figure 4.9. Octahedral yield profiles, plotted at allowable values of the strength ratio. The comparison plot corresponds to a strength ratio of $\psi=0.8$. The $\Gamma(\bar{\theta})$ function is defined so that all models return a value of 1 in triaxial compression.

As illustrated in Fig. 4.9, the Mohr-Coulomb model ($J3TYPE=3$) interpolates linearly in octahedral stress space, resulting in a distorted hexagon if $1/2 < \psi < 1$, a perfect hexagon (Tresca) if $\psi=1$, and a triangle if $\psi = 1/2$. For a detailed explanation of the Mohr-Coulomb formulation, see Appendix B (page B-22). The Mohr-Coulomb model has yield surface vertices at $\bar{\theta} = \pm\pi/6$, which results in extra computational effort to determine plastic strain rates in triaxial states. The Gudehus and Willam-Warnke options, on the other hand, involve no yield surface vertices, which speeds up computations. The Gudehus option is the default because of its computational simplicity, but it supports only a limited range of TXE/TXC strength ratios, the Willam-Warnke option should be used if a rounded but strongly triangular octahedral yield profile is desired. Appendix A (STEP 6) provides guidance for selecting the Lode angle option most appropriate for matching experimental data.

The GeoModel subsumes many simpler (classical) models as special cases. For example, if failure is hypothesized to occur when the largest principal stress (or strain) reaches a critical value, then the octahedral yield profile will be a triangle. If, on the other hand, failure is presumed when the equivalent shear stress reaches a critical value, independent of the Lode angle (like a Von Mises or Drucker-Prager criterion), then the octahedral yield profile is a circle, which can be modeled with the Gudehus option. As a rule, any classical failure criterion that is expressed directly in terms of the principal stresses will imply an appropriate J3TYPE option (and an appropriate value for the TXE/TXC ratio), but such criteria will *also* imply functional constraints on the meridional failure function f_f as well, which requires appropriate GeoModel inputs to mimic. Simplified GeoModel input sets, corresponding to these classical special-case idealized theories may be found at the end of Appendix B.

Octahedral profile plots like the ones shown in Fig. 4.9 are most illuminating from a qualitative perspective. However, for parameterizing the GeoModel to quantitative laboratory data, simple plots of Γ vs. $\bar{\theta}$ are more useful. Fig. 4.10 shows the $\Gamma(\bar{\theta})$ functions for each of the J3TYPE options. In all cases, the lower bound on Γ is 1.0 at TXC.

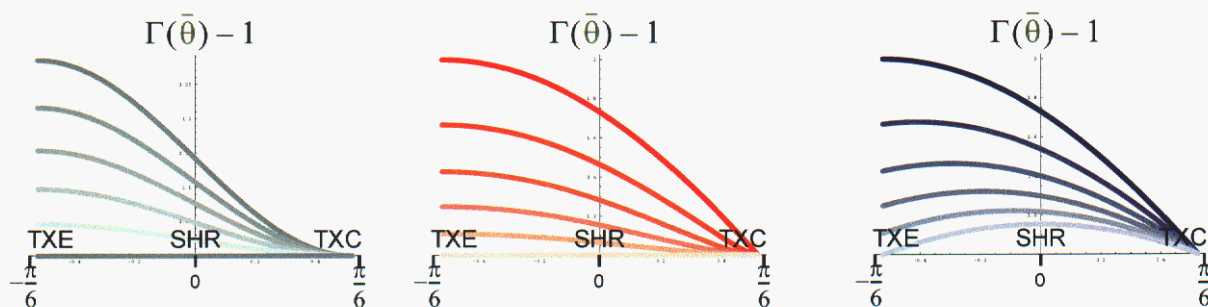


Figure 4.10. Lode angle function (for various ψ strength ratios) plotted vs. the Lode angle varying from -30 degrees (TXE) to $+30$ degrees (TXC). The larger the value of Γ , the smaller the radial distance to the octahedral yield profile and therefore the smaller the shear failure strength. The Gudehus and Willam-Warnke options both predict lowest strength (largest value of Γ) at TXE, whereas Mohr-Coulomb theory predicts lowest strength at an intermediate Lode angle somewhere between TXE and TXC. For example, when $\psi = 1$, Mohr-Coulomb theory reduces to Tresca theory and the lowest strength (highest Γ) occurs at the zero Lode angle (pure shear).

Advancing the solution (groundwork discussion)

So far, we have discussed how some microphysically based, but generally oversimplified theories can be used to predict *theoretical* shapes of yield or failure surfaces. The GeoModel implicitly captures microscale phenomena by using *macroscale* measurable variables in phenomenological manner. Direct use of idealized theories would require initializing and evolving microscale quantities (such as porosity) that are impractical to measure in the laboratory. Therefore, the algebraic *structure* of functions used in the GeoModel is guided by idealized microscale theories, but recast in terms of directly measurable macroscopic variables. Simplified failure criteria help guide choices for interpolation functions to be fitted to real *observed* data that likely reflect the specific phenomena considered in microscale idealizations and possibly some other “unknown” sources of inelastic flow.

Microphysical theories are also used to guide how the GeoModel treats the partitioning of inelastic flow, once it begins. For example, most theories of inelastic flow (including the GeoModel) presume that the total strain rate $\dot{\underline{\underline{\varepsilon}}}$ can be partitioned additively as

$$\dot{\underline{\underline{\varepsilon}}} = \dot{\underline{\underline{\varepsilon}}}^e + \dot{\underline{\underline{\varepsilon}}}^p, \quad (4.53)$$

where $\dot{\underline{\underline{\varepsilon}}}^e$ represents the elastic (or recoverable) part of the strain rate and $\dot{\underline{\underline{\varepsilon}}}^p$ denotes the “plastic” part of the strain rate. More correctly, $\dot{\underline{\underline{\varepsilon}}}^p$ represents the *inelastic* strain rate, which reflects contributions from any and all sources of inelastic material response. Many classical theories presume that the *direction* of the plastic strain rate is parallel to the normal to the yield surface. In this case, since the normal to the yield surface can be obtained by the gradient of the yield function $f(\underline{\underline{\sigma}}, \underline{\underline{\alpha}}, \kappa)$, the plastic part of the strain rate is presumed to be of the form

$$\dot{\underline{\underline{\varepsilon}}}_{ij}^p = \dot{\lambda} \left(\frac{\partial f}{\partial \sigma_{ij}} \right)_{\underline{\underline{\alpha}}, \kappa}, \quad (4.54)$$

where $\dot{\lambda}$ is a multiplier (called the **consistency parameter**) determined by demanding that the stress must remain on the yield surface during inelastic loading. The subscripts on the partial derivative merely indicate that the internal state variables are held constant. When the plastic strain rate direction is determined from the stress gradient of the yield function, as shown here, the model is said to be “associative” (to indicate that the plastic strain rate is associated with the yield function*).

* For materials that exhibit elastic-plastic coupling, the terms “associativity” and “normality” can have distinct meanings, depending on whether the portion of the total strain rate attributable to rates of elastic moduli is absorbed into the elastic strain rate or the inelastic strain rate. When the coupling terms (from *rates* of elastic moduli) are incorporated into the inelastic strain rate, normality and associativity are *not* interchangeable terms. If the coupling terms are incorporated into the elastic strain rate, then associativity and normality are interchangeable, but at the cost that the elastic strain rate ceases to be an exact differential with respect to deformation.

While the GeoModel does support associativity at user request, many researchers report that normality tends to over-predict the amount of volumetric plastic strain [43]. Therefore, *non*-normality is supported in the GeoModel as well. For non-normality the user specifies a **flow function** $\phi(\underline{\sigma}, \underline{\alpha}, \kappa)$ such that*

$$\dot{\varepsilon}_{ij}^p = \dot{\lambda} \left(\frac{\partial \phi}{\partial \sigma_{ij}} \right)_{\underline{\alpha}, \kappa}. \quad (4.55)$$

The plastic strain rate $\dot{\varepsilon}_{ij}^p$ includes both deviatoric and isotropic parts. If the flow potential depends on the first invariant I_1 , then applying Eq. (3.21), the *volumetric* plastic strain rate is

$$\dot{\varepsilon}_v^p = \text{tr} \dot{\varepsilon}^p = 3 \dot{\lambda} \frac{\partial \phi}{\partial I_1}. \quad (4.56)$$

The plastic strain rate points normal to the isosurface $\phi = 0$.[†] If the flow function is associative, then the plastic potential function is identical to the yield function and the plastic strain rate will therefore point normal to the yield surface. Flow surface vertices reside at points where the flow potential is nondifferentiable, in which case the plastic strain rate points within a “cone of limiting normals” (Koiter fan) at the vertex and is determined through additionally considering the trial elastic stress rate associated with the total strain rate.

In the GeoModel, the functional form of ϕ is the same as that of f , but with different values for material constants. Specifically, the flow potential ϕ can be made to differ from the yield function by assigning values to a_2^{PF} , a_4^{PF} , R^{PF} , and ψ^{PF} that differ from their counterpart parameters (a_2 , a_4 , R , ψ) used to define the yield surface. For associativity, the potential function parameters should be given values identical to their counterparts in the yield function.

If continuing to apply elasticity theory would result in a predicted stress lying outside the yield surface, the governing equations are no longer elastic. At this point, the strain rate is decomposed into two parts, elastic plus plastic, as mentioned in Eq. (4.53). The stress rate is determined by applying elasticity. That is,

$$\dot{\sigma}_{ij} = C_{ijkl} \dot{\varepsilon}_{ij}^e = C_{ijkl} (\dot{\varepsilon}_{ij} - \dot{\varepsilon}_{ij}^p), \quad (4.57)$$

* While considerable data does exist to *suggest* that the inelastic strain rate is *not* directed normal to the yield surface for some materials, such behavior is not well understood. The mathematical validity of assuming existence of a non-associated flow potential function has been called into question by Sandler and Pucik [40,37], who have demonstrated that such a model is inherently unstable, inadmissibly generating unbounded energy from quiescent states.

† Because the current stress might not reside on the isosurface $\phi = 0$, the GeoModel projects the stress to the nearest point on this isosurface. The need for such revisions is rarely recognized in plasticity programs (and casts doubt on the very notion flow potentials).

where C_{ijkl} denotes the isotropic tangent elastic stiffness tensor. In Eq. (4.57), our goal is to compute the stress *rate*. The current state is known, and therefore the instantaneous stress state and elastic moduli are known. In numerical implementations of constitutive models, the strain rate is known (it is provided by the host code after solution of the momentum equation). Thus, the only unknown in this equation is the plastic strain rate. Equation (4.55) allows us to compute the *direction* of the plastic strain rate from the known instantaneous stress state. Thus, after substitution of Eq. (4.55) into (4.57), the stress rate can be written

$$\dot{\sigma}_{ij} = C_{ijkl} \dot{\epsilon}_{ij}^e = C_{ijkl} \left[\dot{\epsilon}_{ij} - \dot{\lambda} \left(\frac{\partial \phi}{\partial \sigma_{ij}} \right)_{\underline{\alpha}, \kappa} \right]. \quad (4.58)$$

Everything on the right-hand-side of this equation is known except the value of the consistency parameter, $\dot{\lambda}$.

The consistency parameter is obtained by demanding that, not only must the stress be on the yield surface during plastic loading ($f = 0$), it must also *remain on the yield surface throughout a plastic loading interval*. Thus, $\dot{f} = 0$ during plastic loading. The yield function f depends on the stress, but it also depends on the isotropic hardening internal state variable, κ and (if applicable) on the kinematic hardening backstress state variable tensor α_{ij} . Thus, the assertion that $\dot{f} = 0$ can be written via the chain rule as

$$\dot{f} = \frac{\partial f}{\partial \sigma_{ij}} \dot{\sigma}_{ij} + \frac{\partial f}{\partial \kappa} \dot{\kappa} + \frac{\partial f}{\partial \alpha_{ij}} \dot{\alpha}_{ij} = 0. \quad (4.59)$$

The first term may be simplified through application of Eq. (3.20). The last two terms reflect the fact that the yield surface can evolve in shape and translate in stress space during inelastic loading. In what follows, we will present “evolution equations” that govern how the state variables change in response to plastic flow. It will be argued that the evolution of each internal state variable should be proportional to the plastic strain rate. Equivalently, these rates must be proportional to our unknown plastic consistency parameter $\dot{\lambda}$. By substituting Eq. (4.58) and these soon-to-be-derived evolution equations for the internal state variables into Eq. (4.59) we will be able to solve Eq. (4.59) for the consistency parameter $\dot{\lambda}$. Once the consistency parameter is known, it can be substituted into Eq. (4.58) to obtain the stress rate, which may then be integrated numerically to update the stress. With the consistency parameter $\dot{\lambda}$ known, then *rates* of internal state variables (ISVs) become known through their evolution equations, allowing the ISVs themselves to be updated to the end of the timestep. Thus, the key to advancing the solution is to now derive in detail the internal state variable evolution equations.

Evolution equations

Equation (4.59) may be used to determine the plastic consistency parameter $\dot{\lambda}$ if hardening evolution laws can be found for which the rate of each internal state variable (κ and α_{ij}) is proportional to $\dot{\lambda}$. Once the plastic consistency parameter is known, the evolution laws may be integrated through time to model the time varying hardening evolution of the yield surface.

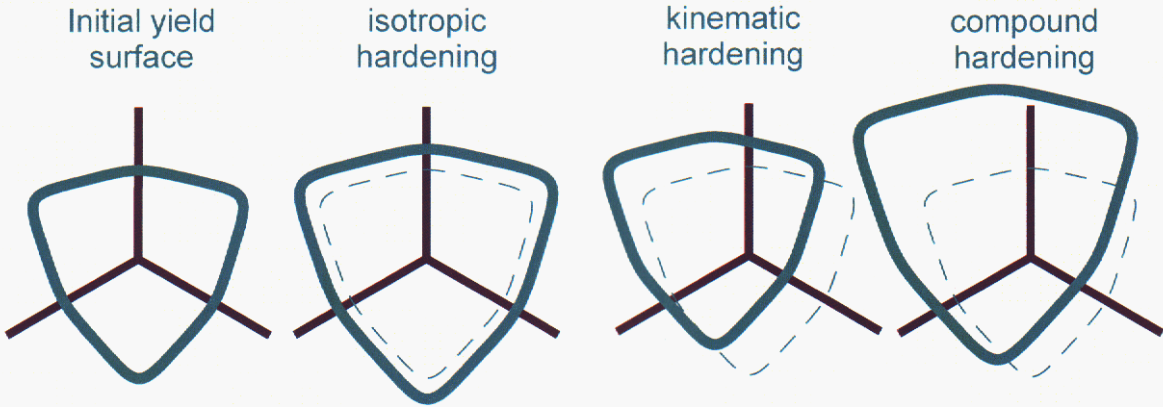


Figure 4.11. *Hardening mechanisms.* At a given pressure, isotropic hardening entails an increase in size, kinematic hardening translates the yield surface, and compound hardening includes both mechanisms. Softening corresponds to a yield surface *contraction*.

As indicated in Fig. 4.11, isotropic hardening (governed by κ and related to void collapse) causes a change in *size* of octahedral yield profiles, while kinematic hardening (governed by the backstress tensor α_{ij}) produces a *translation* of all octahedral yield profiles. In general, both types of hardening can occur simultaneously.

In this section, we will derive explicit expressions for an isotropic hardening modulus h_κ and a kinematic hardening tensor, \mathbf{H}_α , such that the evolution of the internal state variables may be written in the forms

$$\dot{\kappa} = h_\kappa \dot{\lambda} \quad (4.60)$$

and

$$\dot{\alpha}_{ij} = \mathbf{H}_\alpha \dot{\lambda}. \quad (4.61)$$

Later, substituting these expressions into Eq. (4.59) will lead to an expression for the plastic consistency parameter $\dot{\lambda}$. Once the consistency parameter is known, the above equations can be themselves integrated through time to update κ and α_{ij} .

Evolution equation for the porosity-related internal state variable, κ .

We begin this section with some background discussion about the meaning of the internal state variable κ , connecting it to some classical microphysical theories for purely porous (non-cracked) materials. The GeoModel's re-interpretation of κ for both porous and cracked materials will lead ultimately to an evolution law of the desired form, $\dot{\kappa} = h_\kappa \dot{\lambda}$ where h_κ is called the **isotropic hardening modulus**.

In the GeoModel, void collapse commences at different pressures depending on the amount of shear stress present. The effect of shear stress on void collapse is characterized by the cap function illustrate in Fig. 4.5. Even though void collapse depends on shear stress, *characterizing* this effect requires only specification of two numbers $\bar{\kappa}$ and \bar{X} on the hydrostat [see Fig. 4.5]. In the GeoModel, $\bar{\kappa}$ and \bar{X} are presumed to be interrelated so that knowledge of \bar{X} is sufficient to compute the value of $\bar{\kappa}$. We will discuss this relationship later. For now, we will focus on how the hydrostat intercept \bar{X} should vary as porosity is reduced.

If a material is capable of permanent volume change (i.e., if hydrostatic testing exhibits nonzero residual plastic volumetric strain $\bar{\varepsilon}_v^p$ upon releasing the pressure), then the material likely contains voids. The hydrostat intercept \bar{X} is proportional to the critical “elastic limit” pressure required to initiate irreversible void collapse. Therefore, the larger the porosity, the smaller \bar{X} will be. As porosity is crushed out, the hydrostat intercept will move to the right so that increasing pressure will be required to continue crushing out the pores. Recognizing that $\bar{\varepsilon}_v^p$ is an indirect measure of porosity changes, our first goal is to describe how the relationship between $\bar{\varepsilon}_v^p$ and \bar{X} can be inferred from hydrostatic test data. Then we will discuss the relationship between $\bar{\kappa}$ and \bar{X} . With these two relationships in hand, we will ultimately assert that

$$\dot{\kappa} = \left(\frac{d\bar{\kappa}}{d\bar{X}} \right) \left(\frac{d\bar{X}}{d\bar{\varepsilon}_v^p} \right) \dot{\bar{\varepsilon}}_v^p, \quad (4.62)$$

from which substitution of Eq. (4.56), during hydrostatic compression or compaction dominated processes, will give the evolution equation in the desired form,

$$\dot{\kappa} = h_{\kappa} \dot{\lambda}, \quad \text{where} \quad h_{\kappa} = 3 \left(\frac{d\bar{\kappa}}{d\bar{X}} \right) \left(\frac{d\bar{X}}{d\bar{\varepsilon}_v^p} \right) \frac{\partial \phi}{\partial \bar{I}_1}. \quad (4.63)$$

During dilatation-dominated processes, a different form is used for h_{κ} (see Eq. 4.73).

Relationship between \bar{X} and $\bar{\varepsilon}_v^p$ (the hydrostatic crush curve)

If the *matrix* material for a porous medium is plastically incompressible, then it can be shown [33] that the unloaded porosity Π (i.e., the innate porosity at the rest state, not the slightly different porosity that reflects reversible *elastic* porosity reduction under loading) evolves under plastic loading according to

$$\dot{\Pi} = (1 - \Pi)\dot{\varepsilon}_v^p, \quad (4.64)$$

where Π is the void volume in a sample divided by the total volume of the sample (both volumes are those in the unloaded state), and $\dot{\varepsilon}_v^p$ is the trace of the logarithmic plastic strain rate. To second order accuracy, Eq. (4.64) implies that the *change* in porosity is approximately equal to the plastic volumetric strain:

$$\Pi - \Pi_o \approx \varepsilon_v^p. \quad (4.65)$$

Considering *only* hydrostatic loading, early research on pore collapse focused on deriving and/or experimentally measuring so-called “crush curves” in which porosity in a material is plotted as a function of the applied pressure, as in Fig. 4.12. The GeoModel uses a similar curve, but inferred directly from hydrostatic stress-strain data so that porosity measurements are *not* necessary. By using the cap function, the GeoModel incorporates the results from this specialized *hydrostatic* experiment into the general theory in such a manner that pore collapse will commence at lower pressures in the presence of *shear*. Recall that the cap function, loosely speaking, represents material response in the absence of microcracks. Porous-only theories typically predict meridional cap profiles similar to the GeoModel cap function. For example, Gurson [20] reported the following upper-bound yield criterion (expressed in terms of Lode cylindrical coordinates):

$$r = k \sqrt{f_v^2 + 1 - 2f_v \cosh\left(\frac{z}{\sqrt{2}k}\right)}, \quad (4.66)$$

where k is a constant (the yield stress of the matrix material) and f_v is the porosity. Being independent of the Lode angle, the Gurson yield function is a circle in the octahedral plane; Gurson’s *meridional* profile is compared with the GeoModel’s cap function in Fig. 4.13 for various porosities. As porosity goes to zero, the meridional profile approaches the pressure insensitive Von-Mises profile for the matrix material (in other words, in the absence of microcracks, the yield surface becomes a cylinder in stress space as the porosity goes to zero). This property holds only in the absence of microcracks. When microcracks are later included, the common envelope of yield surfaces will be the shear *fracture* curve F_f .

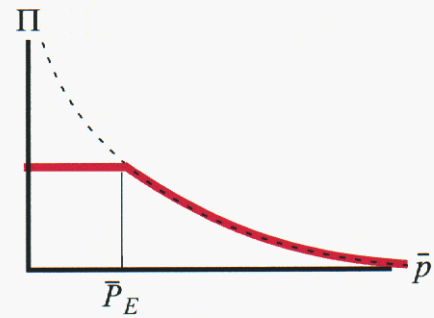


Figure 4.12. A conventional porosity crush curve (dashed) and state path (solid). Porosity is constant until a critical elastic limit pressure \bar{P}_E is reached. Thereafter, porosity is reduced as pressure is increased.

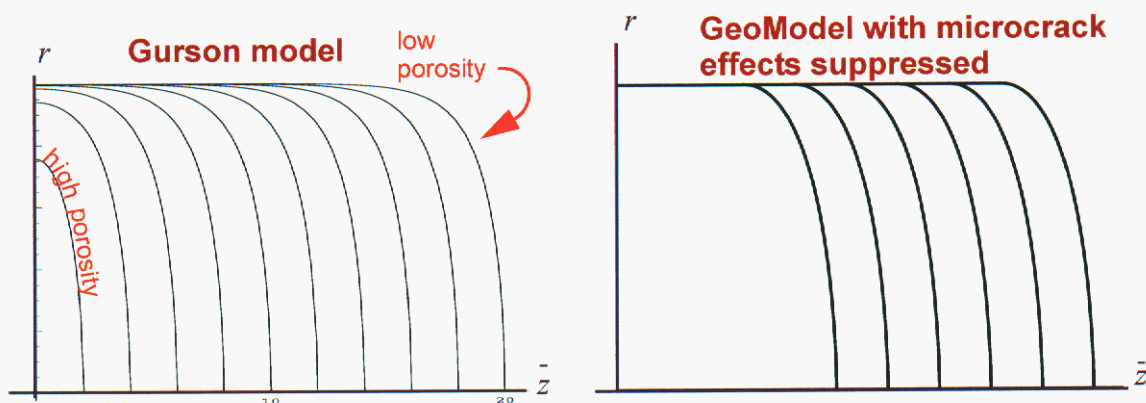


Figure 4.13. The Gurson theory for porous yield surfaces compared with the GeoModel cap function at various values of the internal state variable κ . Qualitatively, the theories are similar. When microcrack effects are included, the GeoModel profiles at various porosities form a pressure-dependent envelope, as in Fig. 1.0(b) on page 1, instead of the horizontal Von-Mises-like envelope shown here.

Under Gurson theory, the key material properties are *microphysical* (the yield stress k for the matrix material and the porosity f_v), which are difficult to measure directly. To obtain analytical results, these theories must resort to over simplistic assumptions about the matrix material and pore morphology (e.g., Gurson theory presumes perfectly spherical voids arranged in a perfectly periodic array). Finally, microphysical theories are typically *upper bounds*, which are of limited use in applications since the tightness of the bound is unknown.

Rather than *directly* using models like Gurson theory, the GeoModel is *guided* by the general trends they predict. Except at extremely high porosity, the Gurson model predicts that the cap surface will be essentially *flat* for a large range of pressures (z -coordinates). The loss in shear strength caused by pores is pronounced over only a small range of pressures near the hydrostatic limit pressure. This region (beyond which the yield surface noticeably branches down to zero) is called the **cap** region. As seen in Figure 4.13, Gurson theory predicts the yield surface will evolve with porosity in such a manner that the cap essentially translates along the pressure (z) axis — the curvature of the cap region does not change significantly. The GeoModel supports these general trends by using a computationally simpler Rubin-Sandler cap function which is simply constant until a critical branch pressure is reached, after which the cap function drops to zero along an ellipse. The cap curve evolves by simple translation along the hydrostat without changes in cap curvature.

In the Gurson model, the current location of the translated cap is a function of the matrix yield stress and the porosity. Rather than using essentially unknowable matrix properties like these as internal state variables, the GeoModel recognizes that the appropriate location for the cap can be determined directly from hydrostatic compression test

data and the branch point at which shear begins to affect pore collapse is presumed in the GeoModel to translate with the hydrostatic limit point. Thus, characterizing how the entire cap function evolves in response to plastic loading boils down to characterizing how the hydrostat intercept point (i.e., where the cap intersects the z -axis) evolves.

The GeoModel presumes that it is experimentally tractable to obtain pressure vs. volumetric strain data. If possible, the experiment should be run to the point of total pore collapse (as in Fig. 3.1 on page 13). The elastic response of the material must be first determined by fitting the unloading curve to the nonlinear elasticity fitting function in Eq. (4.9). “Copies” of the elastic unloading function may be superimposed anywhere on the hydrostatic pressure vs. total strain data. As indicated in Fig. 4.14, the elastic unloading curves can be used to determine a shift distance that must be applied at any given pressure to remove the elastic part of the strain. After applying these shifts, the pressure vs. *total* strain plot is converted to a pressure vs. *plastic* strain plot, called an X-function. The X-function in Fig. 4.14 asymptotes to infinity when the plastic volume strain (i.e., the change in porosity) has reached its maximum value corresponding to all of the pores having been crushed out. Rotating the X-curve and shifting the origin produces a classical crush curve in which porosity is plotted as a function of pressure. The GeoModel never *explicitly* refers to porosity. Instead, the plastic volumetric strain is employed as an indirect measure of porosity changes.

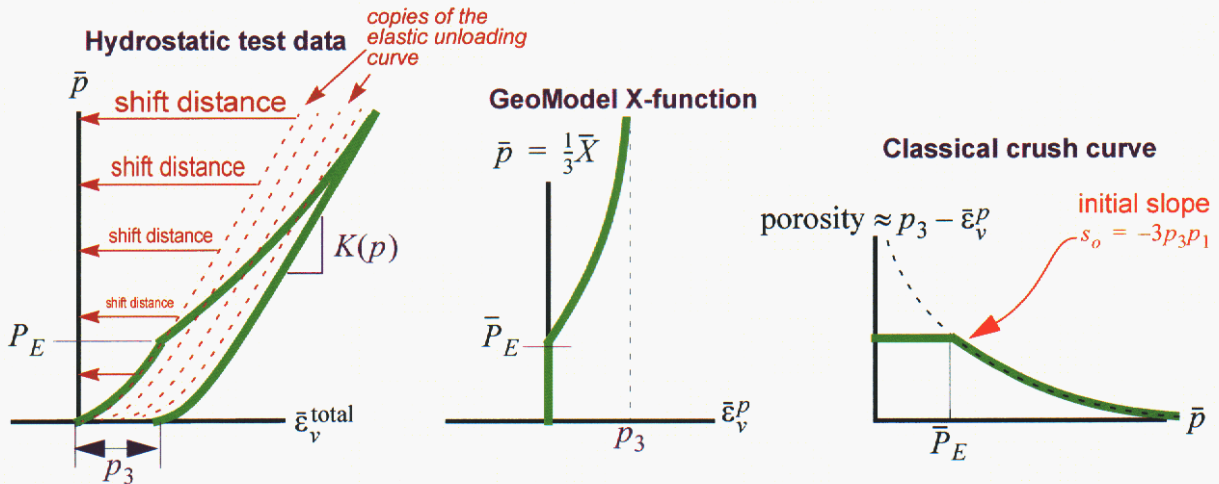


Figure 4.14. Relationship between (a) hydrostatic pressure vs. volumetric strain data, (b) the GeoModel X-function, and (c) a traditional porosity vs. pressure crush curve. Test data are pressure vs. total volumetric strain. Once the elastic unloading curves have been parameterized to the GeoModel fitting functions, the elastic strain at each pressure value may be subtracted from the total strain to generate the X-function. This function asymptotes to a limit value for the plastic strain when all voids have crushed out (and plastic volume changes therefore become negligible). The limit strain is approximately the initial porosity in the material. Rotating the X-plot 90° and moving the origin as shown will produce a traditional porosity vs. pressure crush curve.

Parameterizing the GeoModel so that it will adequately model the changes in the yield surface resulting from pore collapse requires converting hydrostatic pressure vs. volumetric strain data as illustrated in Fig. 4.14 to obtain a classical porosity vs. pressure crush curve in which the porosity is plotted as a function of the pressure \bar{p} . Specialized parame-

terization software is available from the model developers to perform this conversion task and to fit the resulting crush curve to an exponential spline (see Appendix A). The plastic volume strain of a virgin (pre-deformation) material is zero. Therefore the user-specified parameter p_3 is approximately equal to the initial porosity in the material. As pressure is increased from zero, the crush curve [Fig. 4.14(c)] shows that the porosity remains unchanged for a while until an elastic limit pressure \bar{P}_E is reached. Continuing to apply increasing pressure beyond this elastic limit results in irreversible pore collapse and therefore reduction in porosity. The GeoModel allows fitting the post yielding part of the crush curve according to the **crush curve spline** formula,

$$p_3 - \bar{\varepsilon}_v^p = p_3 e^{-(p_1 + p_2 \bar{\xi}) \bar{\xi}}, \quad \text{where} \quad \bar{\xi} = \bar{X} - \bar{p}_0 = 3(p - P_E). \quad (4.67)$$

Here, p_0 , p_1 , p_2 , and p_3 are fitting constants. Referring to the porosity vs. pressure crush curve, these parameters are interpreted physically as follows:

- p_0 equals $-3\bar{P}_E$, where \bar{P}_E is the elastic limit pressure at the initial onset of pore collapse.
- p_1 equals $|s_o|/(3p_3)$, where s_o is the initial slope of the porosity vs. pressure crush curve (see Fig. 4.14).
- p_2 is an optional fitting parameter that may be used if a measured crush curve has an inflection point (i.e., initially concave down, transitioning to concave up at high pressures).
- p_3 is the maximum achievable plastic volume strain, which corresponds approximately to the initial porosity in the material. Complete crushing out of all pores in the material is recognized in the hydrostatic pressure vs. total strain curve if the elastic release curve is tangent to the loading curve.

Equation (4.67) coincides with hydrostatic test data only during pore collapse. During the initial elastic loading, Eq. 4.67 describes the dashed line in Fig. 4.14, which is *not* required to coincide with the data. At pressures above the elastic limit ($\bar{\xi} > 0$), Eq. 4.67 may be used to compute the plastic volumetric strain according to

$$\bar{\varepsilon}_v^p = p_3 [1 - e^{-(p_1 + p_2 \bar{\xi}) \bar{\xi}}], \quad \text{where} \quad \bar{\xi} = \bar{X} - \bar{p}_0 = 3(\bar{p} - \bar{P}_E) \quad (4.68)$$

This relationship may be differentiated to obtain the derivative $d\bar{X}/d\bar{\varepsilon}_v^p$ needed in Eq. (4.63). Now all we need to compute the isotropic hardening modulus h_κ is the relationship between κ and X so that we can substitute the derivative $d\kappa/dX$ into Eq. (4.63).

Relationship between $\bar{\kappa}$ and \bar{X} (cap curvature model)

For a *purely porous* material, Fig. 4.13 suggests that $\bar{\kappa}$ is simply smaller than \bar{X} by a fixed amount. Therefore, knowing \bar{X} is sufficient to determine $\bar{\kappa}$. For a material that contains both pores and microcracks, the relationship between the branch point $\bar{\kappa}$ and \bar{X} is similar, but influenced by the pressure sensitivity of the fracture function. Recall that the continuously differentiable meridional yield function f is constructed by multiplying a function f_f times a cap porosity function f_c . Qualitatively, the fracture function f_f marks the onset of shear crack growth, with significant pressure strengthening being the result of friction at crack faces. This yield envelope function f_f might be lower than the ultimate shear limit envelope F_f if kinematic hardening is allowed. The cap porosity function f_c intersects the hydrostat (\bar{I}_1 -axis) at \bar{X} , marking the point at which pressure *under hydrostatic loading* would be sufficient to induce pore collapse. Variation of the cap function with shear stress (along the ellipse) merely reflects an expectation that pore collapse will commence at a lower pressure than the hydrostatic limit when shear assisted.

Isotropic hardening in the GeoModel is cast in terms of the branch point located at $I_1 = \kappa$ (or, equivalently, $\bar{I}_1 = \bar{\kappa}$) where the yield function f begins to deviate from the envelope function f_f . The height of the branch point b in Fig. 4.15 is considerably lower than the peak height B .

Between the branch and the peak, material response begins to be influenced by porosity, but is still shear crack (dilatation) dominated, and therefore plastic volume *increases* because of crack bulking. Between the peak and the hydrostatic limit point \bar{X} , porosity dominates the material response,

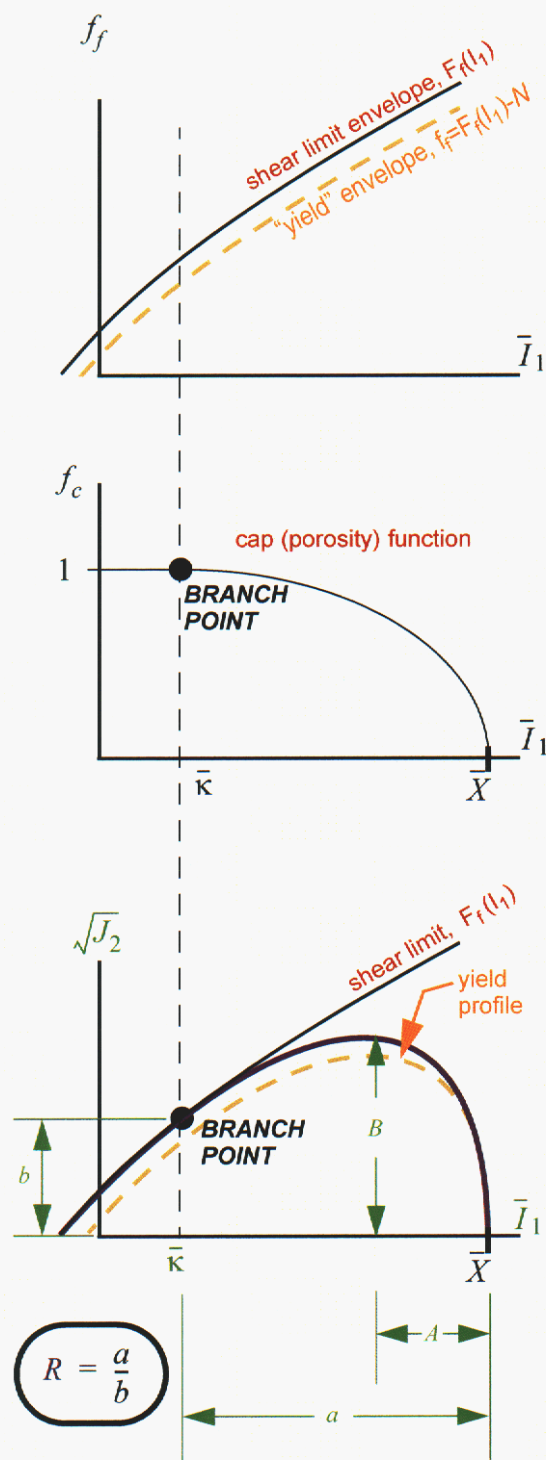


Figure 4.15. Continuously differentiable GeoModel yield function and some characteristic dimensions. The ratio a/b is usually larger than 1, whereas A/B is usually smaller than 1. The bold blue curve is $F_f f_c$. The dashed yield curve is $f_f f_c$.

resulting in plastic volume *compaction* (from pore collapse). At the critical zero-slope point on the yield surface, material response is influenced equally by both cracks and pores so that so that no net volume change is apparent at the macroscale.

Two-surface models [e.g., Ref. 41] typically construct and evolve the yield function by making direct reference to the ratio A/B , which (referring to Fig. 4.15) is typically smaller than unity. The geomodel, however, constructs and evolves its yield function based on the ratio $R \equiv a/b$, which is typically *larger* than unity. This distinction between the two ratios is important to emphasize in publications and presentations to avoid confusion between the GeoModel and conventional two-surface models.

Guided both by trends in observed data and by microphysical theories (e.g., Fig. 4.13), the GeoModel presumes that hardening proceeds such that the ratio between the distances a and b labeled in Fig. 4.15 remains always equal to a user-specified constant R . The axis labels in Fig. 4.15 indicate that $a = \bar{X} - \bar{\kappa}$ and $b = F_f(\kappa)$. Therefore the **cap eccentricity** (also called the cap **shape parameter**) $R = a/b$ is given by $R = (\bar{X} - \bar{\kappa})/F_f(\kappa)$ or, solving for \bar{X} ,

$$\bar{X} = \bar{\kappa} + RF_f(\kappa). \quad (4.69)$$

When written without the overbar denoting the negative, this equation becomes

$$X = \kappa - RF_f(\kappa). \quad (4.70)$$

This expression is evaluated internally within the GeoModel coding to determine X as a function of the internal state variable κ . Differentiating both sides of this equation with respect to κ gives

$$\frac{dX}{d\kappa} = 1 - RF_f'(\kappa). \quad (4.71)$$

The κ evolution law

Substituting Eq. (4.71) into (4.63) gives

$$\dot{\kappa} = h_{\kappa} \dot{\lambda}, \quad (4.72)$$

where the “**isotropic hardening parameter**” h_{κ} is

$$h_{\kappa} = \min \left[\overset{\text{compaction-dominated hardening modulus}}{3 \frac{\partial \Phi}{\partial I_1} \left(\frac{dX/d\varepsilon_v^p}{1 - RF_f'(\kappa)} \right)}, \overset{\text{dilatation-dominated hardening modulus}}{\left(\frac{I_1 - \kappa}{R} \right) \left(\frac{dX/d\varepsilon_v^p}{1 - RF_f'(\kappa)} \right)} \right] \quad (4.73)$$

subject to the constraint, $0 > h_k > -\infty$.^{*} For numerical convenience, this constraint is replaced by $0 > h_k > -0.01b_0^2$, where b_0 is the initial bulk modulus. The derivative $dX/d\varepsilon_v^p$ is found from crush-curve data fitted to Eq. (4.68).

The first term in the minimum function of Eq. (4.73) dominates when the stress state falls on the “compaction dominated” part of the yield surface, labeled in Fig. 4.16, while the second term dominates in the dilatation regime. The second term in the minimum function is guided by trends in observed data.

Even under monotonic loading, the relative position of the stress state on the yield surface can move from compaction to dilatation regimes. Figure 8.6(a) (page 100) shows a triaxial compression load path (angled red arrow) that falls initially on the porosity (compaction) dominated portion of the yield surface, which therefore results in plastic volume reduction and an isotropic expansion of the yield surface. Compaction from void collapse and dilatation from crack bulking are relatively balanced in the vicinity of the critical point. After the stress passes through the critical point, the hardening modulus h_k in Eq. (4.73) transitions from its compaction-dominated value to the dilatation-dominated value.

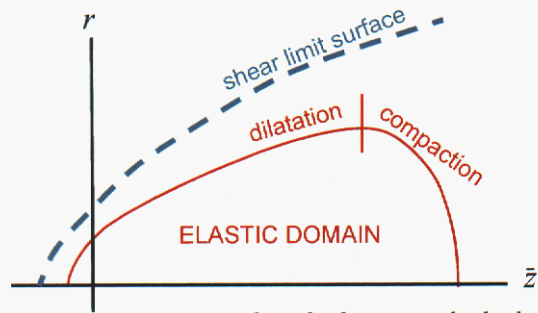


Figure 4.16. Meridional plane in which the magnitude of the stress deviator “ r ” is plotted against $-z$ (which is proportional to the pressure “ p ”). The yield surface (solid) demarks the onset of inelastic flow. Under continued inelastic loading, the yield surface hardens (expands and/or translates) toward the shear limit surface (dashed).

Evolution equation for the kinematic hardening backstress tensor. The GeoModel supports kinematic hardening, but is otherwise isotropic. Kinematic hardening entails using a shifted stress tensor $\xi_{\approx} = \mathfrak{S}_{\approx} - \alpha_{\approx}$ in the yield function instead of the actual stress. The deviatoric tensor internal state variable α_{\approx} is called the **backstress**, and it is computed using evolution equations described here.

Recall that the yield criterion with kinematic hardening is given by

$$J_{\approx}^{\xi} = [F_f(I_1) - N]^2 F_c(I_1), \quad (4.74)$$

where J_{\approx}^{ξ} is the second invariant of the shifted stress,

$$\xi_{\approx} = \mathfrak{S}_{\approx} - \alpha_{\approx}. \quad (4.75)$$

The backstress tensor α_{\approx} is initialized to zero. Upon onset of yielding, the backstress evolves in proportion to the deviatoric part of the plastic strain rate:

^{*} When using the overbar to denote the negative, Eq. (4.72) may be written $\bar{\kappa} = \bar{h}_k \dot{\gamma}$ subject to $0 < \bar{h}_k < \infty$. Thus, since $\dot{\gamma}$ is never negative, this constraint ensures that $\bar{\kappa}$ will never decrease. Physically, this is equivalent to demanding that porosity must always decrease. Increases in porosity (i.e., softening) cannot be accommodated at the material constitutive level — to avoid mesh dependencies of the solution, softening must be handled at the field scale by the host code.

$$\dot{\underline{\alpha}} = HG^\alpha(\underline{\alpha})\dot{\underline{\gamma}}^p, \quad (4.76)$$

$$\text{where } \dot{\underline{\gamma}}^p = \text{dev} \dot{\underline{\varepsilon}}^p = \text{dev} \left(\dot{\lambda} \frac{\partial \Phi}{\partial \underline{\xi}} \right). \quad (4.77)$$

Hence, comparing with Eq. (4.61), the kinematic hardening modulus tensor is given by

$$\underline{H}_\alpha = HG^\alpha(\underline{\alpha}) \text{dev} \left(\frac{\partial \Phi}{\partial \underline{\xi}} \right), \quad (4.78)$$

where H is a material constant and $G^\alpha(\underline{\alpha})$ is a scalar-valued decay function designed to limit the kinematic hardening such that $G^\alpha \rightarrow 0$ as $\underline{\alpha}$ approaches the shear limit surface, $F_f(I_1)$. Since the yield function itself is defined in terms of $F_f(I_1) - N$, the maximum kinematic translation that can occur before reaching the limit surface equals the model offset parameter N . The GeoModel uses the G^α function to “slow down” the rate of hardening as the limit surface is approached so that \underline{H}_α will equal zero upon reaching the limit surface. Specifically, the GeoModel uses the following decay function:

$$G^\alpha(\underline{\alpha}) = 1 - \frac{\sqrt{J_2^\alpha}}{N}, \quad \text{where} \quad J_2^\alpha = \frac{1}{2} \text{tr} \underline{\alpha}^2. \quad (4.79)$$

Kinematic hardening causes the octahedral profile to translate so that it no longer remains centered at the origin (See Fig. 4.11). Consequently, the yield surface will appear to have translated upward in the meridional plane that contains the backstress (see Fig. 4.17). The translation distance equals $\sqrt{J_2^\alpha}$ and Eq. (4.79) prevents this distance from ever exceeding the user-specified offset limit N . Of course, on the meridional plane *perpendicular* to the backstress, the meridional profile will *not* appear to have translated.

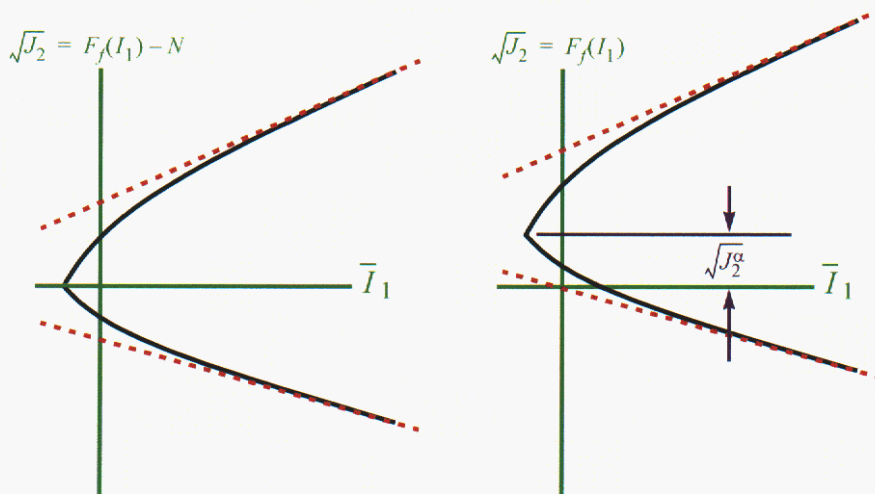


Figure 4.17. The effect of kinematic hardening on the meridional plane that contains the backstress. According to the hardening rule, this meridional profile is permitted to translate in deviatoric stress space by as much as a shift factor N . The meridional plane *perpendicular* to the back stress shows no translation at all.

Advancing the solution (final step, consistency parameter)

Recall from Eq. (4.59) that the consistency parameter $\dot{\lambda}$ is determined from the consistency condition, $\dot{f} = 0$, applied during plastic loading intervals. Specifically,

$$\dot{f} = \frac{\partial f}{\partial \sigma_{ij}} \dot{\sigma}_{ij} + \frac{\partial f}{\partial \alpha_{ij}} \dot{\alpha}_{ij} + \frac{\partial f}{\partial \kappa} \dot{\kappa} = 0. \quad (4.80)$$

Recall the key equations governing the rates of the field and internal state variables:

$$\dot{\sigma}_{ij} = C_{ijkl} \dot{\epsilon}_{ij}^e = C_{ijkl} \dot{\epsilon}_{kl} - C_{ijkl} \dot{\epsilon}_{kl}^p \quad (4.81a)$$

$$\dot{\alpha}_{ij} = H_{ij}^\alpha \dot{\lambda} \quad (4.81b)$$

$$\dot{\kappa} = h_\kappa \dot{\lambda} \quad (4.81c)$$

$$\dot{\epsilon}_{ij}^p = \dot{\lambda} \frac{\partial \phi}{\partial \sigma_{ij}}. \quad (4.81d)$$

With these, the consistency condition in Eq. (4.80) becomes

$$\frac{\partial f}{\partial \sigma_{ij}} C_{ijkl} \left(\dot{\epsilon}_{ij} - \dot{\lambda} \frac{\partial \phi}{\partial \sigma_{ij}} \right) + \frac{\partial f}{\partial \alpha_{ij}} H_{ij}^\alpha \dot{\lambda} + \frac{\partial f}{\partial \kappa} h_\kappa \dot{\lambda} = 0. \quad (4.82)$$

From which it follows that

$$\dot{\lambda} = \frac{1}{\chi} \frac{\partial f}{\partial \sigma_{ij}} C_{ijkl} \dot{\epsilon}_{kl}, \quad (4.83)$$

where

$$\chi = \frac{\partial f}{\partial \sigma_{ij}} C_{ijkl} \frac{\partial \phi}{\partial \sigma_{ij}} - \frac{\partial f}{\partial \alpha_{ij}} H_{ij}^\alpha - \frac{\partial f}{\partial \kappa} h_\kappa. \quad (4.84)$$

Formal equivalence with oblique return algorithms. With the plastic parameter determined from Eq. (4.83), the stress rate may be written

$$\dot{\sigma}_{ij} = \dot{\sigma}_{ij}^E - \frac{A_{ij} B_{kl} \dot{\sigma}_{kl}^E}{\chi}, \quad (4.85)$$

where

$$\dot{\sigma}_{ij}^E = C_{ijkl} \dot{\epsilon}_{kl} \quad (\text{trial elastic stress rate}) \quad (4.86)$$

$$A_{ij} = C_{ijrs} \frac{\partial \phi}{\partial \sigma_{rs}} \quad \text{and} \quad B_{kl} = \frac{\partial f}{\partial \sigma_{mn}}. \quad (4.87)$$

In the GeoModel, the stress state is updated through *direct* integration of the GeoModel plasticity equations. However, for our upcoming discussion of rate dependence, it is important to understand that the update formula in Eq. (4.85) implies that the stress may be alternatively integrated through time by first computing a trial elastic stress σ_{ij}^E at the end of the timestep which may be projected back to the yield surface (which itself has been updated to the end of the step) to determine the final stress. If the trial elastic stress

falls outside the yield surface, plastic flow must have occurred during at least part of the solution interval. Therefore, after evolving the internal state variables appropriately to update the yield surface to the end of the step, it can be shown that Eq. (4.85) implies that the stress at the end of the step may be found by obliquely projecting the trial elastic stress back onto the updated yield surface. Because $\underline{\underline{A}}$ is not generally proportional to $\underline{\underline{B}}$, the projection is oblique to the yield surface even if plastic normality is used. As explained in Chapter 5, the trial stress is projected only *partly* back to the yield surface whenever rate sensitivity is applied.

Quasistatic inelastic tangent stiffness tensor. For any constitutive model, the inelastic tangent stiffness T_{ijkl} is a fourth-order tensor formally equal to the derivative of the stress rate with respect to the total strain rate. That is,

$$\dot{\sigma}_{ij} = T_{ijkl} \dot{\epsilon}_{kl}. \quad (4.88)$$

Therefore, comparing this equation with Eqs. (4.85) and (4.87), the GeoModel's tangent stiffness is given by

$$\boxed{T_{ijkl} = C_{ijkl} - \frac{1}{\chi} P_{ij} Q_{ij}} \quad \text{quasistatic tangent modulus} \quad (4.89)$$

where $P_{ij} = C_{ijrs} \frac{\partial \phi}{\partial \sigma_{rs}}$, $Q_{mn} = \frac{\partial f}{\partial \sigma_{mn}} C_{mnlk}$, and $\chi = \frac{\partial f}{\partial \sigma_{ij}} C_{ijkl} \frac{\partial \phi}{\partial \sigma_{ij}} - \frac{\partial f}{\partial \alpha_{ij}} H G^\alpha \frac{\partial \phi}{\partial \sigma_{ij}} - \frac{\partial f}{\partial \kappa} h_\kappa$.

The tangent stiffness is major symmetric ($T_{ijkl} = T_{klij}$) only for associative models ($f = \phi$).*

Stability issues. The last term in Eq. (4.89) is *subtracted* from the positive-definite elastic stiffness C_{ijkl} , so inelastic flow can potentially make the inelastic tangent stiffness tensor T_{ijkl} non-invertible. In other words, the tangent stiffness tensor might eventually have a zero eigenvalue, marking the onset of softening (yield surface contraction). Whether or not the occurrence of a zero tangent stiffness results in stress-strain softening (i.e., a change from a positive to negative slope in a stress-strain plot) depends on the loading direction. For example, if the strain rate is orthogonal to the null space of a non-invertible tangent stiffness tensor, then no stress-strain softening will be observed and no change in type of the momentum equation will occur even if the yield surface is contracting.

A standing wave (i.e., a non-moving discontinuity in displacement or velocity) is another form of material instability that has been extensively studied in the literature. The acoustic wave speeds (i.e., the speed at which inelastic perturbations can propagate through a material in the direction of a given unit vector \underline{n}) are given by $c = \sqrt{x/\rho}$, where x denotes the eigenvalues of the second-order acoustic tensor,

$$a_{jk} = n_i T_{ijkl} n_l \quad (4.90)$$

* Actually, equivalence of associativity and normality holds only in the absence of elastic-plastic coupling. When elastic moduli can change in response to plastic loading, an associative ($f = \phi$) model will *not* exhibit normality and will *not* have a major-symmetric tangent stiffness [9].

Thus, for the GeoModel, substituting Eq. (4.89) into (4.90),

$$a_{jk} = a_{jk}^e - \frac{1}{\chi} p_j q_k, \quad (4.91)$$

where

$$a_{jk}^e = n_i C_{ijkl} n_l = \text{the elastic acoustic tensor} \quad (4.92)$$

and

$$p_j = n_i C_{ijrs} \frac{\partial \phi}{\partial \sigma_{rs}} \quad \text{and} \quad q_k = \frac{\partial f}{\partial \sigma_{mn}} C_{mnkl} n_l. \quad (4.93)$$

If the plastic tangent stiffness T_{ijkl} is not major symmetric, then the acoustic tensor will not be symmetric. In this case, not only are standing waves ($x = 0$) possible, but so are imaginary wave speeds (flutter instability). A complete spectral analysis of acoustic tensors of the form in Eq. (4.91) is provided in Ref. [9] where every possible ordering of the inelastic wave speeds relative to elastic wave speeds is derived and where every possible acoustic eigenvector is presented. Physically, the eigenvector characterizes the velocity jump direction. If the eigenvector is parallel to the wave propagation direction \mathbf{n} , then the wave is a compression wave. If the eigenvector is perpendicular to \mathbf{n} , the wave is a shear wave. For elastic materials, these are the only two possible kinds of waves, but for inelastic tangent tensors of the form (4.89), other modes are possible.

For rate dependent materials, the question of material stability must be examined anew because, as explained in the next section, the *dynamic* tangent stiffness tensor is generally *stiffer* than the quasistatic tangent stiffness.

5. Rate Dependence

The governing equations discussed so far are rate independent, so they only apply for quasistatic loading. Under high strain rates, the elastic response of a material occurs almost instantaneously, but the physical mechanisms that give rise to observable inelasticity can *not* proceed instantaneously. Materials have inherent “viscosity” or “internal resistance” that retards the rate at which damage can accumulate. For example, cracks grow at a finite speed — they cannot change instantaneously from one size to another. If a stress level is high enough to induce crack growth, then the quasistatic solution for material damage will not be realized unless sufficient time elapses to permit the cracks to change length. Likewise, void collapse takes finite time. Simple inertia also contributes to rate dependence. During the time that cracks are growing towards the quasistatic solution, the stress will drop down toward the quasistatic solution. Until sufficient time has elapsed for the material to equilibrate, the stress state will lie *outside* the yield surface. If the applied strain is released any time during this damage accumulation period, then the total damage will be ultimately lower than it would have been under quasistatic loading through the same strain path.

Viscoplasticity model overview

The evolution of the yield function, and the very character of the inelastic deformation itself, can be dramatically altered by the rate at which loads are applied. In the limit of extraordinarily high load rates (as near the source of an explosion), material response is essentially elastic because insufficient time exists for plasticity to fully develop. At high strain rates, the equation of state (i.e., the pressure-volume part of the elasticity) plays the predominant role in material response. To allow for rate dependence, an overstress model is used. The user specifies a “relaxation” parameter governing the characteristic speed at which the material can respond inelastically. If the loads are applied over a time interval that is significantly smaller than the characteristic response time, then essentially no inelasticity will occur during that interval. If, on the other hand, the loads are applied slowly (as in quasistatic testing), then inelasticity will be evident.

The GeoModel uses a generalized Duvaut-Lions [13] rate-sensitive formulation, illustrated qualitatively in Fig. 5.1. Consider a loading increment Δt during which the strain increment is prescribed to be $\Delta \underline{\underline{\xi}}$. Two limiting solutions for the updated stress can be readily computed: (1) the low-rate (quasistatic) solution $\underline{\underline{\sigma}}^L$ which is found by solving the rate-independent GeoModel equations described previously, and (2) the high-rate solution $\underline{\underline{\sigma}}^H$ corresponding to insufficient time for any plastic damage to develop so that it is simply the trial elastic stress. As explained below and illustrated in Fig. 5.1, the Duvaut-Lions rate formulation is based on a viscoplastic differential equation, the solution of which

shows that the updated stress will be (approximately) a linear interpolation between the low-rate quasistatic plasticity solution $\underline{\underline{\sigma}}^L$ and the high-rate purely elastic solution $\underline{\underline{\sigma}}^H$. In other words, there exists a scalar η between 0 and 1 that depends on the strain rate such that

$$\underline{\underline{\sigma}} \approx \underline{\underline{\sigma}}^L + \eta(\underline{\underline{\sigma}}^H - \underline{\underline{\sigma}}^L). \tag{5.1}$$

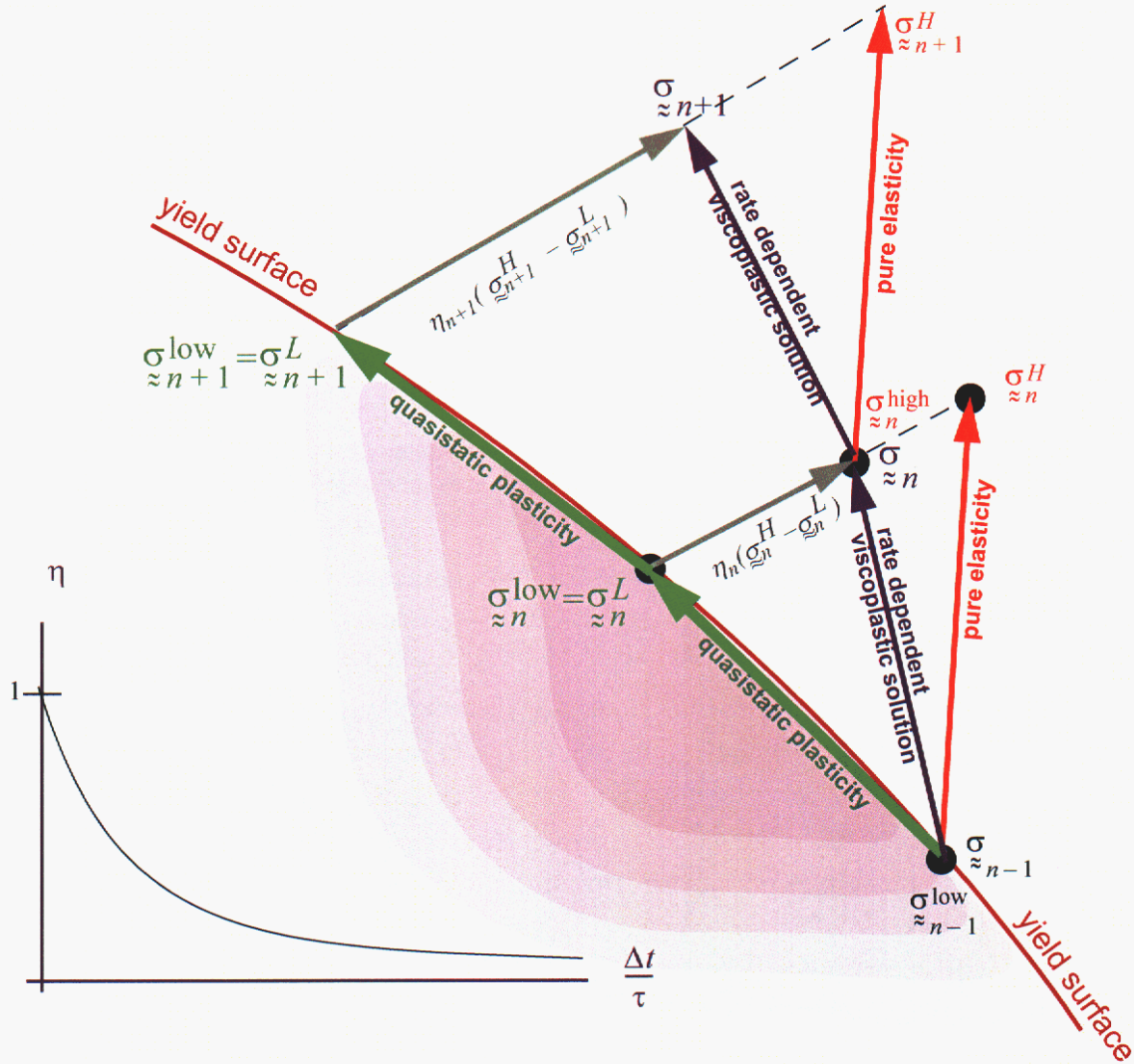


Figure 5.1. Rate dependence. For a given strain increment, two limiting solutions can be readily found. The “low rate” solution $\underline{\underline{\sigma}}^L$, which lies on the yield surface, is the solution to the rate independent GeoModel governing equations. The high rate solution $\underline{\underline{\sigma}}^H$ is simply the trial elastic stress. The actual updated rate-dependent viscoplastic stress $\underline{\underline{\sigma}}$ falls between these two limiting case solutions so that $\underline{\underline{\sigma}} = \underline{\underline{\sigma}}^L + \eta(\underline{\underline{\sigma}}^H - \underline{\underline{\sigma}}^L)$. The inset graph shows how the scale factor η varies with the loading interval. If the loading interval is long relative to the material’s characteristic response time τ , then sufficient time exists to fully develop plastic response and the updated solution therefore coincides with the quasistatic solution $\underline{\underline{\sigma}}^L$. If the loading interval is considerably shorter than the material’s characteristic response time, then the solution will be the high-rate elastic solution.

The update for internal state variables is structured similarly, but uses a somewhat different weighting factor, as explained below. For both the stress and internal state variable updates, the interpolation factor η varies from 1 at high strain rates (when Δt is small) to 0 at low strain rates (when Δt is large), as illustrated in the graph inset of Fig. 5.1, where the abscissa is normalized by a factor τ called the material’s “characteristic” response time. At the end of this chapter, we will describe how the GeoModel assigns a value for the characteristic material response time τ . Incidentally, for simplicity, Fig. 5.1 shows a stationary yield surface. In general, the yield surface will evolve in size or translate according to the hardening rules described earlier.

A time interval Δt is deemed to be “long” if $\Delta t \gg \tau$. A time interval is “short” if $\Delta t \ll \tau$. Soon we solve the viscoplastic equations to prove that, if the initial stress is on the yield surface, then high-rate scale factor internal state variables (ISVs) is

$$\eta = \frac{1 - e^{-\Delta t/\tau}}{\Delta t/\tau}. \quad (5.2)$$

This is also the rate factor for the stress *at the onset of yielding* when $\underline{\underline{\sigma}}$ and $\underline{\underline{\sigma}}^{\text{low}}$ coincide. At the end of a viscoplastic step, the final stress state will *not* lie on the yield surface. We will prove that, in this case, the scale factor is smaller than the value cited in Eq. (5.2). Consequently, the “attraction” that the dynamic stress has for the quasistatic solution increases somewhat as the stress moves farther from the yield surface.

Referring to Fig. 5.2, the η weighting factor is large when the time step is significantly smaller than the characteristic time required for the material’s plasticity solution to develop. Effects of plasticity are apparent in the GeoModel only when the time interval is long or when the characteristic material response time is short so that η will be small. In this case, according to Eq. (5.1), the solution will be near the quasistatic (low-rate) solution $\underline{\underline{\sigma}}^L$.

Figure 5.1 illustrates that the viscoplastic solution will follow a trajectory that is similar to the quasistatic solution except displaced from the yield surface. Consequently, experimental data for high-rate loading scenarios have the *appearance* of inducing a higher yield stress in the material. Unlike some plasticity models, the GeoModel does *not* alter the material yield stress as a function of strain rate. Instead, the overstress model accomplishes the same effect in a much more physically justifiable manner.

Viscoplasticity model derivation

In the context of viscoplasticity, an inviscid (rate-independent) solution $\underline{\underline{\sigma}}^L$ for the stress is presumed to exist. Likewise inviscid (rate-independent) solutions q_L are presumed available for the internal state variables, here denoted collectively by “ q ”. These limiting case solutions are merely the solutions of the rate-independent GeoModel equations described in earlier chapters. Viscous effects are incorporated by presuming that the strain rate is decomposed as the sum of an elastic part $\dot{\underline{\underline{\varepsilon}}}^e$ plus a *viscoplastic* part $\dot{\underline{\underline{\varepsilon}}}^{vp}$:

$$\dot{\underline{\underline{\varepsilon}}} = \dot{\underline{\underline{\varepsilon}}}^e + \dot{\underline{\underline{\varepsilon}}}^{vp}. \quad (5.3)$$

The viscoplastic part of the strain rate includes both the usual plastic strain rate from the quasistatic (low-rate) solution as well as additional (retarding) contributions resulting from viscosity. The viscoplastic strain rate is governed by

$$\dot{\underline{\underline{\varepsilon}}}^{vp} = \frac{1}{\tau} C_{ijkl}^{-1} [\sigma_{kl} - \sigma_{kl}^{\text{low}}]. \quad (5.4)$$

The fourth-order tensor C_{ijkl}^{-1} is the elastic compliance (inverse of the stiffness), τ is a material parameter called the relaxation time, and $\underline{\underline{\sigma}}^{\text{low}}$ is the rate-independent stress solution whose value at the beginning of a time increment Δt is tracked as an extra state variable (called **QSSIGXX**, **QSSIGYY**, etc. in Appendix B).^{*} At the end of the time interval, $\underline{\underline{\sigma}}^{\text{low}}$ ultimately has the value $\underline{\underline{\sigma}}^L$, which is found by integrating the rate-independent GeoModel equations from the earlier chapters. During viscoplastic loading, each internal state variable q is presumed to vary according to

$$\dot{q} = \frac{-1}{\tau} [q - q^{\text{low}}]. \quad (5.5)$$

Here q^{low} is the value of the internal state variable (κ or $\underline{\underline{\alpha}}$) throughout the time interval, initially being equal to q_0 at the beginning of the step, and (through application of the rate-independent GeoModel) ultimately equalling the low rate solution q_L at the end of the step. Like the inviscid quasistatic stress, the inviscid quasistatic ISVs (**QSEL**, **QSB-SXX**, etc.) must be tracked as distinct extra state variables.

The stress rate is, as usual, given by the elastic stiffness acting on the elastic part of the strain rate: $\dot{\sigma}_{ij} = C_{ijkl} \dot{\varepsilon}_{kl}^e$. Thus, using Eq. (5.3), the stress rate may be written

$$\dot{\sigma}_{ij} = \dot{\sigma}_{ij}^{\text{high}} - \frac{1}{\tau} (\sigma_{ij} - \sigma_{ij}^{\text{low}}), \quad \text{where} \quad \dot{\sigma}_{ij}^{\text{high}} \equiv C_{ijkl} \dot{\varepsilon}_{kl}. \quad (5.6)$$

Here, $\dot{\sigma}_{ij}^{\text{high}}$ is the elastic trial stress rate, and therefore $\sigma_{ij}^{\text{high}}$ is the time varying elastic trial stress that ultimately equals the high-rate solution σ_{ij}^H at the end of the step.

^{*} The “low” or “inviscid” stresses must be tracked independently. They cannot be inferred by projecting the actual stress onto the yield surface. Attempting to do so causes undesirable results in rate-dependent load-unload cycles.

Eq. (5.6) is a set of linear first-order differential equations which may be integrated exactly over a time step with the use of integrating factors [19] *provided that* σ_{ij}^{low} *is known as a function of time throughout the time step*. In principal, we would need to solve the rate independent equations *analytically* over the entire time step to integrate Eq. (5.6) exactly, but this is not tractable in practice. In what follows, we will describe how the time history of σ_{ij}^{low} can instead be well approximated over the step. First, let's introduce a change of variables by defining

$$u_{ij} \equiv \sigma_{ij} - \sigma_{ij}^{\text{high}}, \quad (5.7)$$

so that the governing equation for the stress rate may be written

$$\dot{u}_{ij} = -\frac{1}{\tau}(u_{ij} + \sigma_{ij}^{\text{high}} - \sigma_{ij}^{\text{low}}). \quad (5.8)$$

This equation can be solved exactly if the time variation of $\underline{\underline{\sigma}}^{\text{high}} - \underline{\underline{\sigma}}^{\text{low}}$ is known throughout the time step. Time variation of $\underline{\underline{\sigma}}^{\text{low}}$ is governed by known quasistatic rate equations. Consequently, the dynamic accuracy can be maximized by presuming that the *rate* of $\underline{\underline{\sigma}}^{\text{low}}$ is constant over the step so that $\underline{\underline{\sigma}}^{\text{low}}$ itself is approximated to vary linearly over the step.

Recall that the final solution $\underline{\underline{\sigma}}^H - \underline{\underline{\sigma}}^L$ can be presumed known at the end of the step because $\underline{\underline{\sigma}}^H$ is found by integrating the elasticity equations and $\underline{\underline{\sigma}}^L$ is found separately by integrating the inviscid quasistatic plasticity equations. Similarly, the difference $\underline{\underline{\sigma}}_0^{\text{high}} - \underline{\underline{\sigma}}_0^{\text{low}}$ is known at the beginning of the step because $\underline{\underline{\sigma}}_0^{\text{high}}$ is $\underline{\underline{\sigma}}$ at the beginning of the step and $\underline{\underline{\sigma}}_0^{\text{low}}$ is retrieved from the saved quasistatic stress extra state variable array. The high-rate stress $\underline{\underline{\sigma}}^{\text{high}}$ is simply the elastic trial stress. Thus, it varies linearly through time from its initial to final value (with small higher-order nonlinearities if the strain rate and/or elastic moduli are not constant). The quasistatic stress rate $\dot{\underline{\underline{\sigma}}}^{\text{low}}$ is an oblique projection of the trial stress rate onto the yield surface, so $\underline{\underline{\sigma}}^{\text{low}}$ also varies approximately linearly through time (with nonlinear effects from flow potential surface curvature being higher order). Thus, we may call on the mean value theorem to assert that

$$(\underline{\underline{\sigma}}^{\text{high}} - \underline{\underline{\sigma}}^{\text{low}}) \approx (\underline{\underline{\sigma}}^H - \underline{\underline{\sigma}}^L) \left(\frac{t - t_0}{\Delta t} \right) + (\underline{\underline{\sigma}}_0^{\text{high}} - \underline{\underline{\sigma}}_0^{\text{low}}) \left(1 - \frac{t - t_0}{\Delta t} \right). \quad (5.9)$$

With this approximation, the ODE in Eq. (5.8) may be solved exactly. Since $\underline{\underline{\sigma}}_0^{\text{high}}$ equals $\underline{\underline{\sigma}}_0$ at the beginning of the step, the initial condition is that $u_{ij} = 0$ when $t = t_0$. Integrating the ODE, evaluating the result at the end of the step, and applying the definition of u_{ij} to obtain the updated solution for σ_{ij} eventually gives

$$\underline{\underline{\sigma}}^{\text{FINAL}} = \underline{\underline{\sigma}}^L + R_H(\underline{\underline{\sigma}}^H - \underline{\underline{\sigma}}^L) + r_h(\underline{\underline{\sigma}}_0^{\text{high}} - \underline{\underline{\sigma}}_0^{\text{low}}), \quad (5.10)$$

where

$$R_H = \frac{1 - e^{-\Delta t/\tau}}{\Delta t/\tau} \quad \text{and} \quad r_h = e^{-\Delta t/\tau} - R_H. \quad (5.11)$$

With the presence of the last term, the solution in Eq. (5.10) is not *precisely* of the form shown in Eq. (5.1) unless $\bar{\sigma}_0^{\text{high}} = \bar{\sigma}_0^{\text{low}}$. As seen in timestep “n-1” in Fig. 5.1, the initial values for the “high” and “low” rate paths coincide only at the *onset* of plasticity. Eq. (5.10) can be put into the form of Eq. (5.1) if we approximate that $\bar{\sigma}_0^{\text{high}} - \bar{\sigma}_0^{\text{low}}$ is *parallel* to $\bar{\sigma}^H - \bar{\sigma}^L$. With this assumption, Eq. (5.1) becomes

$$\bar{\sigma}^{\text{FINAL}} = \bar{\sigma}^L + \eta(\bar{\sigma}^H - \bar{\sigma}^L), \quad (5.12)$$

where

$$\eta = R_H + r_h \Upsilon \quad (5.13)$$

and

$$\Upsilon \equiv \frac{\left\| \frac{\sigma^{\text{high}} - \sigma^{\text{low}}}{z_0} \right\|}{\left\| \frac{\sigma^H - \sigma^L}{z} \right\|}. \quad (5.14)$$

Fig. 5.2 shows how the weighting factor η varies with the stress difference ratio Υ appearing in the last term of Eq. (5.13). For plastic loading, Υ equals 0 only when the initial state is on the yield surface. Otherwise, beyond this onset of yielding moment, Υ increases, eventually asymptoting to 1 under steady strain rates. The lowering of the rate factor η caused by nonzero Υ makes the dynamic stress more strongly attracted to the quasistatic solution as the distance between them increases.

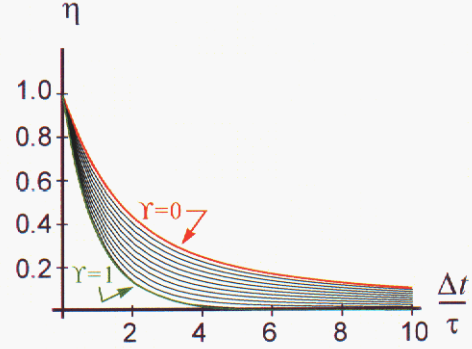


Figure 5.2. High-rate weighting factor at various initial states. The largest weight factor (upper red curve) applies when the initial stress is on the yield surface. The factor is lower if the initial state is already off the yield surface at the beginning of the step.

For the rate dependent update of internal state variables, Eq. (5.5) can be integrated analytically if the time variation of q over the step is approximated by $q^{\text{low}} = q_H + (q_L - q_H)(t - t_o)/\Delta t$. The resulting solution for q is

$$q^{\text{FINAL}} = q_L + R_H(q_H - q_L), \quad (5.15)$$

where the high-rate weight factor R_H is the same as in Eq. (5.11). The weight factor R_H for the internal state variables differs from the weight factor η for the stress because the two problems have different initial conditions. Recall that the material responds elastically at extremely high rates. Hence, because the internal state variables can evolve only when plasticity occurs, the high rate solution q_H for any internal state variables is simply its value at the beginning of the time increment.

Limiting case. If a strain rate is held constant for a long enough period then the difference between the dynamic stress σ_{ij} and the inviscid stress σ_{ij}^L will sometimes reach a steady-state value in the laboratory. In this case, the equations outlined in this chapter imply that this steady state stress difference is given by

$$\sigma_{ij} - \sigma_{ij}^L = \frac{\tau}{\chi} P_{ij} Q_{mn} \dot{\epsilon}_{mn} \quad (5.16)$$

where χ , P_{ij} , and Q_{ij} are defined in Eq. (4.89).

In the very simplified context of non-hardening Von-Mises plasticity, this equation becomes

$$\sigma_{ij} - \sigma_{ij}^L = (2G\tau)\hat{S}_{ij}\hat{S}_{mn}\dot{\epsilon}_{mn} \quad (5.17)$$

where G is the shear modulus and \hat{S}_{ij} is a unit tensor in the direction of the stress deviator. For example,

$$[\hat{S}] = \frac{1}{\sqrt{2}} \begin{bmatrix} 0 & 1 & 0 \\ 1 & 0 & 0 \\ 0 & 0 & 0 \end{bmatrix} \text{ for simple shear} \quad (5.18)$$

$$[\hat{S}] = \frac{1}{\sqrt{6}} \begin{bmatrix} 2 & 0 & 0 \\ 0 & -1 & 0 \\ 0 & 0 & -1 \end{bmatrix} \text{ for uniaxial (axisymmetric) loading} \quad (5.19)$$

Therefore, in the case of simple shear for non-hardening Von Mises plasticity, Eq. (5.17) implies that

$$\sigma_{12} - \sigma_{12}^L = 2G\tau\dot{\epsilon}_{12} \quad \text{for simple shear} \quad (5.20)$$

$$\sigma_{11} - \sigma_{11}^L = \frac{4G}{3}\tau\dot{\epsilon}_{11} \quad \text{for uniaxial (axisymmetric) loading} \quad (5.21)$$

These simple analytical results can be used to trend-test the numerical implementation of rate sensitivity, as described in Fig. 5.3.

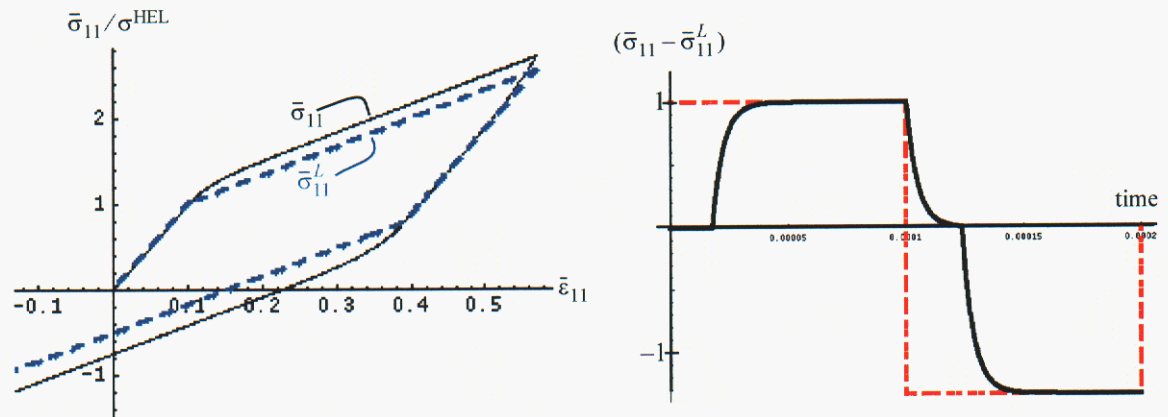


Figure 5.3. Rate dependence in uniaxial strain loading of a nonhardening pressure-insensitive material. In the stress-strain plot, the normalizer σ^{HEL} is the quasistatic uniaxial yield stress. The dynamic (black) stress-strain plot exhibits an apparent increase in strength relative to the quasistatic (dashed blue) solution. This rate-induced stress difference is plotted in the second figure (normalized by the peak value), where the dashed red line shows the analytical asymptote envelope from Eq. (5.21). This calculation included a lower strength in tension (interestingly, the difference between dynamic and quasistatic strengths is higher in tension).

Assigning a value to the characteristic material time

The GeoModel permits the user to control the value of the characteristic time through the use of up to seven *positive-valued* parameters, T_1 through T_7 which are employed in the code to assign a value of the characteristic time according to the following formulas:

$$\tau = \begin{cases} f(\dot{\epsilon}^{\text{equiv}}) & \text{if } \bar{\epsilon}_v^p \leq 0 \\ T_6 f(\dot{\epsilon}^{\text{equiv}}) (1 + (\langle T_7 (\bar{I}_1 + T_5) \rangle)^2) & \text{if } \bar{\epsilon}_v^p > 0 \text{ and } \bar{I}_1 \geq -T_5 \end{cases}, \quad (5.22)$$

where

$$f(\dot{\epsilon}^{\text{equiv}}) = T_1 \left(\frac{1}{\dot{\epsilon}^{\text{equiv}}} \right)^{T_2}, \quad \text{and} \quad \dot{\epsilon}^{\text{equiv}} = \left\| \frac{\dot{\epsilon}}{\bar{\epsilon}} \right\|, \quad (5.23)$$

$$\text{and } \langle x \rangle = \begin{cases} 0 & \text{if } x \leq 0 \\ x & \text{if } x > 0 \end{cases} \quad (\text{McCauley brackets}). \quad (5.24)$$

If a *constant* characteristic time τ is desired, then set $T_1 = \tau$, and all other T 's to zero. Fig. 5.3 used a constant τ , as did the simple-shear rate-dependent simulation shown in Fig. 7.8(b) on page 92.

Suitability of the GeoModel's overstress rate-dependence theory for predicting laboratory data is illustrated in Fig. 8.9 on page 103.

Thermodynamics considerations

At present, the GeoModel's equation of state is incorporated within the purely mechanical model — it contains no thermal terms (i.e., terms involving material properties such as the specific heat and Grüneisen parameter). Nonetheless, the GeoModel's nonlinear elasticity model has been successfully fitted to Hugoniot shock data. How can this be? In thermodynamics, pressure is typically expressed as a function of two variables: the density ρ and a thermal variable (usually temperature or entropy). For example,

$$p = f(\rho, T). \quad (5.25)$$

In thermodynamics, you can always use a purely mechanical equation of state if you restrict the class of allowable problems so that one or two of the thermal variables are inter-related in some known way. If, for example, you restrict attention to isothermal loading, then the pressure will be expressible in the form $p = F(\rho)$, where the “material constants” in the equation (such as the bulk modulus) must be set to their isothermal values. Likewise, if you can consider only adiabatic loading, then the pressure is again expressible as a mechanical function if the parameters such as the bulk modulus are set to their adiabatic values.

The GeoModel is parameterized at low pressure and low strain rates under isothermal conditions (room temperature), but at high pressures and high strain rates under adiabatic conditions. Thus, the non-linear fit for the bulk modulus may be regarded to transition from isothermal to adiabatic properties as pressure is increased. This implies a vague “domain of applicability” for the mechanical GeoModel. Specifically, the model may be used for problems where low pressure regions are also isothermal (and near room temperature) and high pressure regions are adiabatic (high rate). Without information on the thermal properties of the material, the validity of the mechanical GeoModel in other domains cannot be ascertained. In particular, using the model in high-rate/low-pressure applications (acoustics) or low-rate/high pressure problems (e.g., creep of underground salt bodies) will possibly require re-parameterization.

A good method for gauging the degree to which the mechanical GeoModel can be applied in broad thermodynamic domains would be to compare *isothermally* measured elastic moduli (inferred by the slope of a stress strain curve) with acoustically measured moduli, which are the *low-pressure isentropic* elastic constants. The difference between the isothermal and isentropic bulk modulus (at a given pressure) is proportional to the square of the thermal expansion coefficient divided by the specific heat. Thus, if no differences are observed between the isothermal and isentropic moduli at a given pressure, the domain of applicability of the purely mechanical model is likely broad.

6. GeoModel Numerical Solution scheme

Aside from kinematic hardening, the GeoModel is isotropic and therefore the yield function depends only on principal stresses. An eigenvalue analysis is avoided by casting the yield function in terms of stress invariants. The principal stress directions (eigenvectors) are not needed to evaluate the yield function. For any isotropic elasticity model, however, evolution of plastic response must allow for rotation of principal stress directions caused by the elastic portion of the loading. Thus, the governing equations must be cast in incremental tensorial form, requiring all six independent components of symmetric tensors to be passed to the model. Careful numerical integration schemes [6] are required to ensure accuracy and convergence.

This chapter begins with a description of how the GeoModel is to be used within a host (finite-element) code, followed by a discussion of the influence of material softening on *field-scale* stability (i.e., stability of the spatial finite-element solution, not stability of the GeoModel's internal time integration algorithm). Next, GeoModel installation instructions are provided that describe the public* subroutines and memory requirements. Following a summary of plotable GeoModel output, the GeoModel's time integration algorithm is briefly summarized.

Role of the GeoModel within a finite-element program

The GeoModel is designed for use in host codes (typically finite-element programs) that solve the momentum balance PDE,

$$\frac{\partial \sigma_{ik}}{\partial x_k} + f_i = \rho a_i, \quad (6.1)$$

where σ_{ik} is the *spatial* Cauchy stress tensor (denoted $\underline{\underline{\sigma}}^{\text{spatial}}$ in Eq. 3.39), x_k is the spatial position vector, f_i is the body force per unit volume, ρ is the mass density, and a_i is the material acceleration that is related to the spatial velocity field v_i by material time derivative

$$a_i = \frac{\partial v_i}{\partial t} + \frac{\partial v_i}{\partial x_k} v_k = \frac{Dv_i}{Dt} = \left(\frac{\partial v_i}{\partial t} \right)_X \quad (6.2)$$

* i.e., called directly from the host code.

Here, $\underline{\mathbf{X}}$ is the time-zero reference position vector, which serves to identify Lagrangean material points. The spatial position vector $\underline{\mathbf{x}}$ is related to the reference position $\underline{\mathbf{X}}$ through the deformation mapping function, such that the deformation gradient tensor is

$$F_{ij} = \left(\frac{\partial x_i}{\partial X_j} \right)_t \quad (6.3)$$

The stress and velocity fields (as well as displacement or velocity boundary conditions) are known at the beginning of each time step, so that application of Eq. (6.1) permits evaluation of the acceleration field. In most host codes, the updated position of a material particle is computed to second-order accuracy with respect to the time step Δt through application of

$$\underline{\mathbf{x}}^{n+1} = \underline{\mathbf{x}}^n + \left(\frac{\partial \underline{\mathbf{x}}}{\partial t} \right)_{\underline{\mathbf{x}}}^n \Delta t + \frac{1}{2} \left(\frac{\partial^2 \underline{\mathbf{x}}}{\partial t^2} \right)_{\underline{\mathbf{x}}}^n (\Delta t)^2 \quad (6.4)$$

or

$$\underline{\mathbf{x}}^{n+1} = \underline{\mathbf{x}}^n + \underline{\mathbf{v}}^n \Delta t + \frac{1}{2} \underline{\mathbf{a}}^n (\Delta t)^2. \quad (6.5)$$

Equivalently,

$$\underline{\mathbf{x}}^{n+1} = \underline{\mathbf{x}}^n + \underline{\mathbf{v}}^{n+1/2} \Delta t, \quad (6.6)$$

$$\text{where } \underline{\mathbf{v}}^{n+1/2} \equiv \underline{\mathbf{v}}^n + \frac{1}{2} \underline{\mathbf{a}}^n \Delta t. \quad (6.7)$$

To date, all installations of the GeoModel have approximated the *unrotated* strain rate by the *unrotated* symmetric part of the velocity gradient defined in Eq. (4.3), evaluated at the half-step by using the velocity field in Eq. (6.7). The GeoModel integrates the unrotated strain rate to predict the *unrotated* stress at the end of the step, which must then be rotated into the spatial configuration by the host code. As mentioned on page 20 (and clarified later in this chapter), optimizing the accuracy of the *spatial* solution for problems involving massive material rotation requires the host code to apply its un/rotation operations using polar rotation tensors that are consistent with the part of the time step (beginning, half, or end) at which un/rotation operations are required.

Of course, once the GeoModel and any other constitutive models in the problem have been applied to determine stresses at the end of a time step, Eq. (6.1) may be integrated again to update the acceleration field, thus launching a new timestep cycle.

Spatial stability (mesh dependence/loss of strong ellipticity)

As rock deforms inelastically, the initial yield surface (lower curve in Fig. 4.16) evolves toward — and is not permitted to evolve *beyond* — the limit surface (upper curve in Fig. 4.16). If the stress reaches the limit surface, the rock has, in a loose sense, failed catastrophically. More correctly, the GeoModel has reached the limit of its applicability because large scale cracking and subsequent loss in strength *cannot be modeled locally at the constitutive level*. Material softening generally produces a change in type of the momentum equation, requiring intervention from the host code to change its solution scheme appropriately (for further details, see page 61). In the GeoModel, the state variable “**CRACK**” is a flag equaling 1.00 whenever a principal stress (or I_1) cut-off has been applied or 2.00 when the stress has reached the limit surface and can harden no further; otherwise “**CRACK**” equals 0.0. In either case, a positive value of “**CRACK**” marks the onset of softening.

Because the GeoModel comes equipped with its own flags for failure, this model should *not* be used with other fracture models such as a maximum principal stress criterion. Instead, the “**CRACK**” flag should be queried by the host code to determine when it is appropriate to add void (when pressure is tensile) or to apply discontinuous shear displacement element shape functions (when pressure is compressive) or to apply any other appropriate response* to material softening that will ensure localization response that converges as the spatial mesh size is reduced.

If the host code fails to activate any special response when the “**CRACK**” flag becomes nonzero, the GeoModel will continue to run, but its predictions are suspect. Without a meaningful host-code response to failure, the geomodel will handle the inelastic response at the limit state in a manner similar to non-hardening plasticity (i.e., rather than properly softening down away from the limit state, the GeoModel will force the stress to dwell at the limit state). To summarize, the GeoModel is intended to model *only* the portion of material response that is appropriate to compute at the local constitutive level. The GeoModel sends flags back to the host code at the *onset* of softening (a non-local phenomenon). The *host code* is responsible for responding appropriately to these flags by initiating material softening.

* We are investigating a field-scale softening strategy that introduces a length scale based on Weibull perturbations of the material strength field, which is especially appealing because (unlike “element death” and cohesive zone models) it can be easily justified physically. Specifically, softening results from sub-grid-scale flaw clustering, which can be shown to have a Weibull (or nearly Weibull) distribution and can be parameterized via standard laboratory-scale experiments. Preliminary investigations [4] have shown that Weibull-like softening strategies lead to *very* realistic fragmentation patterns and are mesh-independent.

GeoModel files, subroutines, memory requirements, and model installation requirements.

This section is a software requirements specification that must be followed by anyone who installs the GeoModel into a host code.* The GeoModel is designed to be implemented into multiple host codes without *any* revision of the source code. As described below, the model has *three* public† subroutines (**GEOCHK**, **GEORXV**, and **ISOTROPIC_GEOMATERIAL_CALC**). To support portability, the GeoModel conforms to Sandia’s Model Interface Guidelines (MIG) [10]. Therefore, the model presumes that calculations entail three distinct phases, the first two of which are performed at start-up while the last one is applied for every element at every timestep:

1. **User input.** The GeoModel requires the host code to acquire user input values and save them into a single array using the keywords and ordering listed in Appendix B. This property array must be passed to the subroutine **GEOCHK** for “domain certification” (i.e., verifying that input values fall within allowable ranges, as explained on page 81). Additionally, the routine **GEOCHK** sets defaults for unspecified user inputs.
2. **Storage.** To be portable, the GeoModel does not actually *allocate* storage for internal state variables (ISVs) — this is the responsibility of the host because data lay-out varies from code to code. The GeoModel provides a *list* of storage requirements by requiring the host code to call subroutine **GEORXV**. This routine returns physical dimensions, initial values, plot keywords, and advection requirements for each internal state variable. To use this routine, the host code loops over the *lists* returned by **GEORXV** to then allocate the storage, define plot options, and initialize the ISV fields.
3. **Execution.** Every cycle, **ISOTROPIC_GEOMATERIAL_CALC** must be called to update the stress to the end of the step. Detailed descriptions of the input-output arguments are provided below.

The GeoModel must, upon occasion, relay messages to the user or terminate the calculation. Log message protocols and bombing procedures vary among host codes. For portability, the GeoModel follows MIG guidelines by calling subroutines **LOGMES**, **FATERR**, or **BOMBED** whenever it needs to relay messages to the user, log fatal errors, or terminate calculations, respectively. These routines are *not* part of the GeoModel source code. Because these actions require host-code responses that vary from code to code, these routines must be written and maintained by the host-code architects. Likewise, a routine called **TOKENS** (used only in the extra variable request routine) is expected to pre-exist in the host code. Any host code that *already* supports MIG models will already have these MIG-utilities in their repository. Host code architects of non-MIG-compliant codes may request sample MIG-utilities that they may customize to suit their own code’s protocols for information passing and code termination.

* Any deviation from these model installation instructions (as well as any modification of the GeoModel source code itself) may result in loss of technical support. Model installers who believe that a deviation from these instructions is warranted are encouraged to contact the GeoModel developers.

† i.e., routines that are called directly from the host code. All other routines in the GeoModel are “private” and should not be called by the host. To serve codes that re-mesh, one additional public routine, **isotropic_geomaterial_state**, is available that will repair advection errors.

The GeoModel source code is available in both FORTRAN 77 and 90. To date, large-scale production codes have used the F77 version to best ensure portability, so those routines will be described here. The F90 routines, which are not significantly different, are generated from the F77 master files to ensure consistency.

Arguments passed to and from the GeoModel driver routine

The following list describes variables passed between the host code and the GeoModel's driver routine (`isotropic_geomaterial_calc`):

INPUT:

- **NBLK**: The number of cells or finite elements to be processed. Parallel codes send only one cell at a time (**NBLK=1**).
- **NINSV**: The number of internal state variables for the GeoModel.
- **DT**: The time step
- **PROP**: the user-input array, filled with real numbers, as summarized at the top of the nomenclature table in Appendix B and also summarized within the source code prolog itself.
- **SIG**: The unrotated Cauchy stress tensor at time n . The six independent components of the stress must be passed in the ordering $\{\sigma_{11}, \sigma_{22}, \sigma_{33}, \sigma_{12}, \sigma_{23}, \sigma_{31}\}$. Within the FORTRAN, this array is dimensioned "**SIG(6, NBLK)**" so that the stress components for any given finite element are in six contiguous memory locations.
- **D**: The unrotated strain rate tensor, preferably evaluated at time $n+1/2$ because the GeoModel treats the strain rate tensor as constant over the entire interval. Most codes approximate the strain rate tensor as the unrotated symmetric part of the velocity gradient (see Eq. 4.3). Component ordering and contiguous storage are the same as for stress.
- **SV**: the internal state variable array containing reals, as described in the nomenclature table in Appendix B.

OUTPUT:

- **SIG**: The unrotated stress tensor at time $n+1$. The component ordering is the same as described above.
- **SV**: The internal state variable array (updated to time $n+1$)
- **USM**: Uniaxial strain (constrained) elastic modulus equal to $H = K + \frac{4}{3}G$. The host code may use the USM output to compute an upper bound on the wave speed ($\sqrt{H/\rho}$, where ρ is mass density) when setting the timestep.

These arguments require unrotation of spatial stress at time n , unrotation of the strain rate at time $n+1/2$, and rotation of the updated stress back to the spatial frame at time $n+1$. For problems involving significant material rotation, this requires using *three* different polar rotation tensors [14]. For moderate rotation problems, it might be acceptable to use the rotation tensor evaluated at time $n+1/2$ for all three operations, but the accuracy consequences of this simplified approach have not been carefully examined in the computational mechanics literature.

PLOTTABLE OUTPUT

In addition to the stress, any variable in the **SV** state variable array is available for plotting. The plot keywords (and ordering of variables in the **SV** array) are listed in Nomenclature Appendix B.

As mentioned earlier, the “**CRACK**” flag may be plotted to visualize softening regions. The “**INDEX**” flag may be plotted to locate regions that are now *or have ever* deformed inelastically (even if elastic at the given instant). To visualize regions that are *currently* deforming inelastically, the “**SHEAR**” variable should be plotted.

The “**SHEAR**” variable is an informational output, equal to zero during elastic cycles and equaling a measure of normality of the trial elastic stress rate during plastic intervals. Specifically, as illustrated in Fig. 6.1, “**SHEAR**” ranges from zero when the trial stress rate is tangent to the yield surface to unity when it is normal to the yield surface; an intermediate value of “**SHEAR**” indicates oblique plastic loading relative to the yield surface. While “**SHEAR**” quantifies the plastic loading direction relative to the yield surface, the internal state variable “**DCSP**”, which is the plastic consistency parameter $\dot{\lambda}$, may be plotted as a measure of the *magnitude* or intensity of plastic loading.

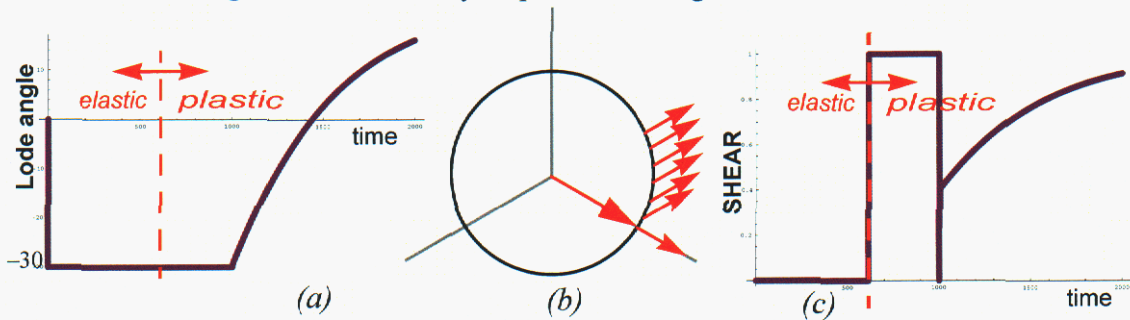


Figure 6.1. Meaning of the “**SHEAR**” output variable. This calculation uses a Von Mises yield surface. The strain rate remains in triaxial extension for half of the calculation, which is why the Lode angle (a) is initially constant at -30° . During this interval, the stress reaches the yield surface and continues to push directly against it, which is why **SHEAR** (c) jumps to and holds at 1.0. Halfway through the problem, the strain rate direction is changed in stress space [as indicated by arrows in (b)] to move the stress toward triaxial compression. At the beginning of this transition, **SHEAR** first jumps to 0.5 where the normal and tangential components are equal, and moves back toward 1.0 as the tangential component decays.

The “**EQDOT**” variable may be plotted to gain an overall sense of intensity of the current strain rate. Small values of “**EQDOT**” correspond to relatively quiescent regions. Plotting “**EQPS**” will show equivalent plastic shear strain, while “**EQPV**” gives plastic volume strain (and is roughly equal to the porosity change from inelastic void collapse).

The stress invariant “**I1**” is three times the negative of pressure. “**ROOTJ2**” may be regarded as a scalar measure of effective shear stress and is proportional to the radial coordinate of the stress in the octahedral plane. The Lode angle, “**LODE**”, quantifies the angular location of the stress in the octahedral plane, and it varies from 30 for triaxial compression to -30 for triaxial extension (0 for simple or pure shear). If kinematic hardening is enabled, “**BACKRN**” quantifies the distance that the origin of the octahedral profile has shifted in stress space.

The complete list of other (less useful) plotable output is in Appendix B.

GeoModel algorithm

The GeoModel presumes that the strain rate is constant throughout the entire step, and the stress is integrated as follows:

Rate independent (inviscid) part of the viscoplasticity equations.

- STEP 1. To guard against unpredictable host-code advection errors (or similar corruption of the updated state from the last time step), apply a return algorithm to ensure the initial stress is on or inside the yield surface.
- STEP 2. Compute the nonlinear elastic tangent moduli appropriate to the stress at time n .
- STEP 3. Apply Hooke's law in rate form to obtain the elastic stress rate at time n .
- STEP 4. Integrate the elastic stress rate using first-order differencing to obtain an estimate for the trial elastic stress at the end of the step.
- STEP 5. Evaluate the yield function at the trial elastic stress. If the yield function evaluates to a negative number, the trial elastic stress is accepted as the final updated stress, and the inviscid algorithm returns (i.e., go to STEP 16). Otherwise, continue.
- STEP 6. To reach this step, the trial elastic stress state was found to lie outside the yield surface. At this point, the time step is divided into an internally determined number of subcycles. All subsequent steps described below this point apply to the smaller time steps associated with subcycles.
- STEP 7. Evaluate the gradients of the yield function for eventual use in Eq. (4.83).
- STEP 8. Evaluate the flow potential gradients for eventual use in Eqs. (4.87) and (4.85)
- STEP 9. Evaluate the isotropic hardening coefficient h_{κ} in Eq. (4.72).
- STEP 10. Evaluate the G^{α} function in Eq. (4.76).
- STEP 11. Apply Eq. (4.83) to obtain the consistency parameter.
- STEP 12. Use forward differencing (within the subcycle) to integrate Eqs. (4.72) and (4.76), thereby updating the internal state variables, κ and α_{ij} . Similarly integrate Eq. (4.85) to advance the stress to the end of the subcycle.
- STEP 13. The above steps will have directly integrated the governing equations through the end of the subcycle, so the updated stress will be *in principle* already on the yield surface. However, guard against slight round-off and integration errors by applying an iterative return correction to place the stress *exactly* on the yield surface.
- STEP 14. Increment the subcycle counter, and save the partially updated inviscid internal state variables.
- STEP 15. If subcycles remain to be evaluated, go to STEP 7. Otherwise, continue to STEP 16.

Viscous part of the viscoplasticity equations.

- STEP 16. The previous set of steps govern computation of the equilibrium state. Now apply Eq. (5.22) to compute the characteristic material response time.
- STEP 17. Using the trial elastic stress corresponding to an update to the end of the time step, apply Eq. (5.10) to compute the dynamic stress. Apply Eq. (5.15) to similarly compute the dynamic values of internal state variables to account for rate sensitivity.
- STEP 18. Save the values of the internal state variables into the state variable array.
- STEP 19. STOP.

7. Software “confidence building” activities

This chapter describes progress towards Software Quality Assurance (SQA), which encompasses a broad range of activities including code maintenance, documentation, and (most importantly) code verification. “Code verification” is defined by the IEEE [22] as “formal proof of program correctness” in the sense that the governing equations are numerically solved correctly within a tolerable degree of accuracy. Model *validation** will not be discussed until Chapter 9.

We make no claims at this point that the GeoModel software has been exhaustively verified. In other words, we cannot state with *absolute* certainty that the governing equations presented in this report are in fact solved correctly. One might challenge the Verification and Validation (V&V) community to prove that “formal proof of program correctness” is even possible. Realistically, the confidence one can place in the veracity of any model prediction can be based only on the extent to which documented evidence *suggests* that the equations are solved correctly. It seems acceptable, therefore, to speak of varying *degrees of progress* towards verification†, or, more generally, varying degrees of SQA. In this sense, the GeoModel has undergone a higher level of SQA than is normally applied to modern material constitutive models of comparable complexity.‡ Even though we claim that the GeoModel’s verification and SQA status is above average, we do *not* assert that such activities have progressed to the point where we consider the job “finished.” Here in this chapter, we aim only to build confidence in the GeoModel by summarizing some of the SQA activities that have been applied to the GeoModel to date (a comprehensive *detailed* discourse would fall well outside the scope of this report).

Once a constitutive model is installed within a host code, it becomes only a single component of a much *larger* and *different* model (the finite-element code). Constitutive SQA should include ensuring that the model can be installed and run in a variety of host codes, but verification of the installation is primarily a *host code* (not constitutive) responsibility. Constitutive SQA in the context of larger-scale model integration is limited to pro-

* Whereas “Verification” seeks to confirm that the equations are solved correctly without questioning their appropriateness, “validation” compares model predictions against experimental data to determine whether or not the equations themselves are indeed suitable for the application.

† Suppose, for example, that one constitutive model has been verified for both uniaxial strain and simple shear, whereas another one has been tested only in uniaxial strain. If these are the only tests, *neither* model is “well verified,” but the first one is certainly *better* verified.

‡ From a practical (rather than philosophical) standpoint, the complexity of a model must be considered when speaking about how well a model has been validated. With a given level of financial and computational resources, solids models cannot be tested to the same level of certainty as fluids models. Conclusively demonstrating only *first-order* accuracy of an anisotropic solid constitutive model would require more than *twenty* times the effort needed to verify first-order accuracy of a simple fluids model (this follows because a general anisotropic stiffness tensor has 21 independent components, and therefore 21 independent strain paths would be required to conclusively verify accuracy; moreover comprehensive testing for solids models requires coordinate invariance tests that are not needed for scalar fluids models).

viding adequate model installation instructions (including operational constraints), delivering correct solutions to the constitutive governing equations, and ensuring that the model will, wherever feasible, “trap” invalid calling arguments (much as a compiler “traps” IEEE errors such as division by zero).

Numerical schemes for solving field PDEs (such as Navier-Stokes equation or Maxwell’s electromagnetism equations) have received considerable attention in the V&V literature, while verification of *constitutive models* has been relatively ignored. Constitutive models are *sub-components* within field-scale calculations. As such, a *partitioning* of responsibility for SQA is needed. (As an analogy, note that the quality assurance responsibilities for a turn-signal manufacturer must be different from those of an automobile manufacturer.) *Constitutive* verification aims to build confidence that the model will return correct solutions to the governing equations, *presuming* that the host code sends inputs falling within the admissible domain for the model. SQA may additionally include some checking of the inputs themselves, as long as doing so does not compromise efficiency. When a host code sends inadmissible inputs (such as corrupted strain rates caused by mesh entanglement, advection, or artificial viscosity errors), then correcting such errors is *not* the responsibility of a constitutive modeler unless it can be proved *by the host code developers* that such errors originated from constitutive model output errors.

Similarly, because the GeoModel is a *local* constitutive model (i.e., because it does not solve space-time PDEs), demonstrating convergence with respect to the *spatial* mesh is not a GeoModel verification responsibility. It is well known that mesh dependence can occur when local constitutive models permit material softening. Therefore, we regard *suppression* of softening as an implicit software requirement specification because our customers (finite-element code teams) do not have the code infrastructure that is needed to properly handle the change in type of their governing PDEs that occurs upon softening. Until such enhancements are made *at the host code (not constitutive) level*, the GeoModel predicts only the *onset* of catastrophic failure, not its subsequent evolution into macroscale fragments and fractures.

In the lexicon of Ref. [25], “static” SQA testing is a prerequisite to the verification process that encompasses tests that are performed without running the code. To date, the GeoModel has undergone the following static SQA:

- **Independent* line-by-line review of the source code.** The source code was aggressively inspected to locate and remove possibilities for IEEE errors (e.g. trying to take the ArcSin of a number larger than unity†, dividing by zero, etc.). Another goal was to confirm that the equations being solved in the code were indeed the equations documented in this report.
- **Model domain certification (preventing “Garbage In \Rightarrow Garbage Out”).** No function or set of equations is well posed without a domain of applicability. The domain for the GeoModel includes constraints on run-time subroutine arguments (e.g., the backstress must be deviatoric) as well as constraints on the input parameters (e.g., the bulk modulus must be positive). Except where computational efficiency would be degraded, SQA includes appraising quality of both user input and run-time arguments sent from the host code. A new routine (`geochk`) was recently added to the GeoModel that terminates calculations if the user-input falls outside allowable ranges. Run-time testing of this routine is discussed in the next section. Direct run-time testing of *time varying* subroutine arguments is computationally inefficient, so the GeoModel’s domain certification for variable calling arguments relies primarily on our model installation instructions (page 75), which serve as software requirement specifications that must be obeyed by the host code developers.
- **Portability and version control.** The GeoModel has been designed such that it can be implemented in multiple host codes *without altering the source code*, thus allowing the GeoModel developers to maintain a single master version. A host code owner who faithfully obeys the model installation instructions on page 75 may update the GeoModel by simply replacing three FORTRAN files (posted on WebFileShare under keyword “GeoModel”) with the latest GeoModel release and then recompiling. Each GeoModel release is identified by a six digit code‡ that prints to the screen at run time. The GeoModel has been compiled on multiple platforms (Sun, Dell, and HP workstations or clusters running Linux and/or Windows) in multiple host codes (Alegra, Presto, Pronto, JAS3D, and two independent drivers) using multiple commercial compilers (gnu, pgf77, pgf90, and Compaq visual FORTRAN). The source code compiles without warnings when using stringent SQA options (such as `-Wall -O3` in the gnu compiler).
- **Model documentation.** *This report* is the first publication that describes the numerical algorithm, provides input definitions, and gives model installation instructions that describe how SQA responsibilities are partitioned between the model and the host code.
- **Technical support.** Two stand-alone single-cell codes that exercise the GeoModel under prescribed strain and stress paths are available to assist host (finite-element) code owners verify their GeoModel installations. The GeoModel includes a “problem-resolution” feature that generates a debugging file (`geo.barf`) and terminates calculations whenever unacceptable solution quality is detected. The debugging file may be emailed

* Here, “independent” (which is not synonymous with “unbiased”) means that the source code has been inspected by an individual who has not written the code. GeoModel code inspection was first performed by Brannon (the second author of this report) upon joining this modeling effort at the beginning of fiscal year 2003-04. Subsequent new code revisions and enhancements have been reviewed by the member of the Fossum-Brannon team who did *not* write the new code.

† This can happen because of slight round-off errors, as in `ASIN(1.0000001)`.

‡ The code is simply the release date in the form “yymmdd”.

For example, “GeoModel version 040526” was released in 2004 on May 26.

to the GeoModel team, who can import it into their driver to resolve the problem quickly.

So-called “dynamic” SQA refers to tests performed by actually running GeoModel. Some of the dynamic SQA activities to date are summarized here. A detailed documentation of all GeoModel SQA would require a second report itself, so the following list should be regarded as simply an overview. A small number specific examples will be given later.

- **Model domain certification:** The “geochk” feature for checking quality of user inputs was tested by confirming that the GeoModel would abort when *intentionally* sent invalid inputs. As explained below, the “geobarf” problem-resolution feature can often *indirectly* trap invalid forcing functions (caused, for example, by mesh entanglement). However, the *responsibility* for sending valid forcing functions to the GeoModel remains the onus of the host code, not the GeoModel.
- **Run-time monitoring of the solution quality:** The problem-resolution (geo.barf) feature has been verified to (1) detect “Garbage Out” predictions such as negative plastic work, (2) terminate calculations, and (3) write a debugging file that can be emailed to model developers to determine whether the problem was caused by bad user input, bad arguments passed from the host code, or a bug in the internal coding.
- **Driver regression testing:** Two stand-alone drivers are available for exercising the GeoModel in a homogenous deformation field.* Considerable dynamic testing was performed using our research (non-production) model driver that allows visualizing (and algebraically processing) the output within Mathematica [48]. The other driver [36], which runs either from a command line or from an Excel front-end (see Fig.7.1), is now also deployed in the WISDM materials information database [21], allowing the predictions of the GeoModel to be compared directly against experimental calibration data. These drivers have been used to assemble a suite of regression tests (hydrostatic loading, two types of shear loading, uniaxial strain, uniaxial stress, biaxial plane stress, and numerous mixed load-unload problems using a variety of input parameters), several of which are simple enough to admit analytical solutions for verification purposes. The driver regression problems (15 problems to date) are all re-run and inspected for undesirable changes whenever *any* change is made to the GeoModel.
- **Trend testing:** Engineering judgement was used to ensure that solutions vary as expected when parameters change. For example, Fig. 6.1 depicted a simple trend test in which analytical (exact) arguments could be used to prove that the “SHEAR” should equal 1.0 at the onset of yielding and should dwell at 1.0 until the loading direction changes, after which it should drop instantaneously to 0.5 and then asymptote to 1.0. Similarly, Figs. 5.3 and Figure 7.8b confirmed that increasing the GeoModel’s characteristic response time (see Eq. 5.22) would indeed produce the analytically predicted increase in the apparent strength of the material. These tests were quite valuable because they allowed correction of a serious bug in an earlier version of the GeoModel where the response trend upon *load reversal* was clearly flawed. Trend and robustness testing also demands that the GeoModel must predict *qualitatively* reasonable trends when subjected to deformations that exceed what is expected in applications (e.g., massively large elongations or pressures). For example, one problem in our driver regression suite verifies that load/unload curves do indeed asymptote toward each other under hydrostatic compression as sketched in Fig. 3.1 and verified in Fig. 7.1. Many other trend tests such as these have been conducted, but (for lack of space) will not be described in detail in this report.

* Stand-alone testing obviates many constraints and sources of *non-constitutive* errors in production finite-element simulations (artificial viscosity, hour-glassing, time-step control, boundary-condition errors, code compilation and run-time overhead, etc.).

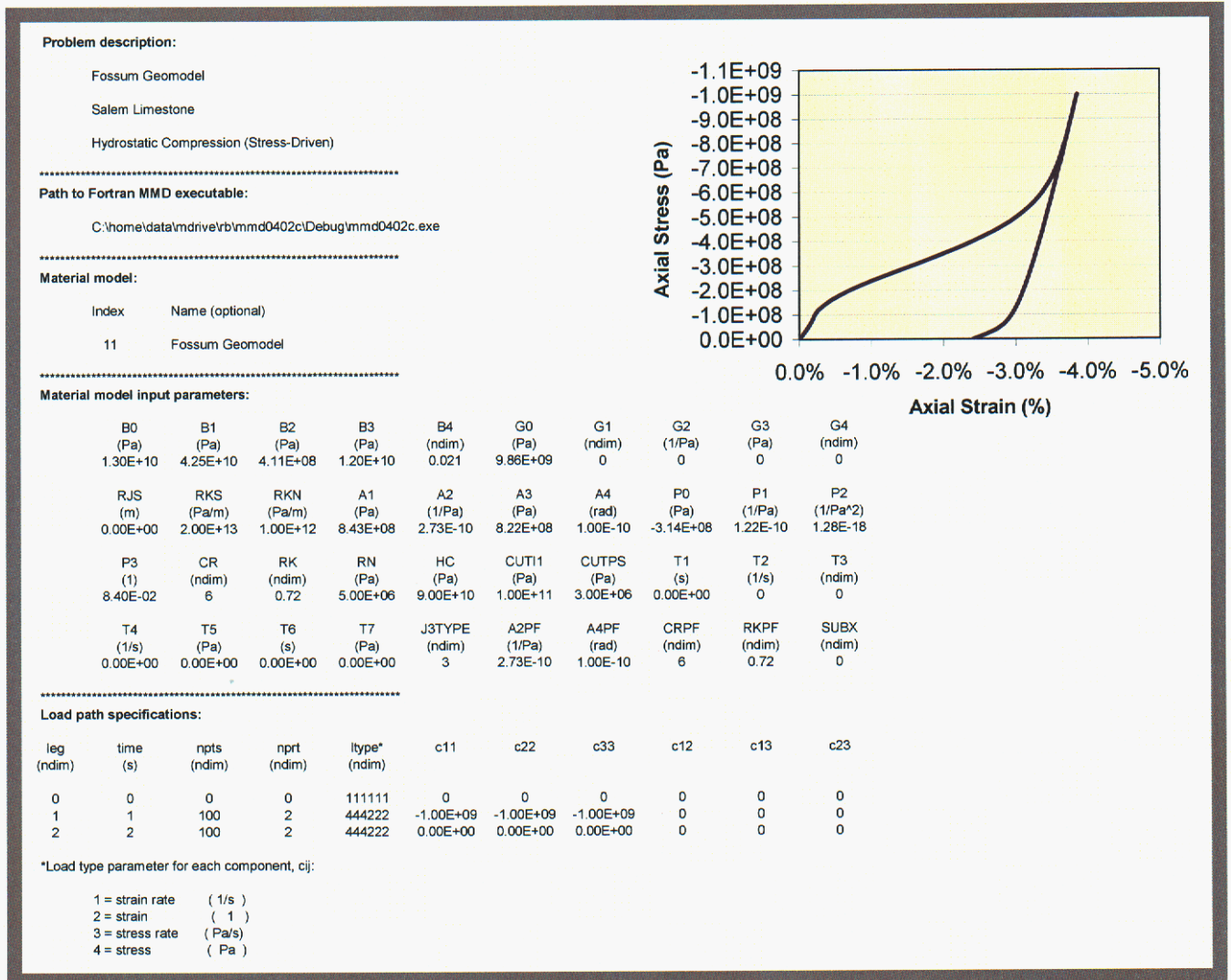


Figure 7.1. Screen shot of the MS Excel interface for the GeoModel material-model driver (MMD). This tool serves as a reliable platform for exercising the GeoModel under homogeneous deformations in a simplified host code architecture that is free from solution corruption caused by *unneeded* finite-element code features such as artificial viscosity, wave motion, contact algorithms, etc.

- **Symmetry testing:** Consistent predictions were verified for identical loading applied in different directions (e.g. uniaxial strain in the 1-direction compared with the 2-direction). Consistency has also been tested for stress paths that intersect the yield surface at symmetrically equivalent points and for trial stress rates normal to the yield surface (to verify that the stress rate had no tangential component).
- **Extensive comparison testing:*** To date, the GeoModel has been implemented in five finite-element codes: (ALEGRA [8,49], PRESTO [26], JAS3D [5], EPIC [24], legacy PRONTO3D [45]). A disturbing number of discrepancies (e.g., wave arrival times differing by as much as 10% or peak stresses differing by almost an order of magnitude) have been identified by comparing predictions for the *same problem* simulated by different finite-element codes. In all but a few cases, these discrepancies have been traced to *host-code-level (not constitutive-level)* errors (e.g., hour-glassing, handling of boundary conditions, artificial viscosity, time-step control, etc.). Resolving such discrepancies is the model verification responsibility of the host code owners, not the GeoModel developers.† The ability of the GeoModel to reduce to simpler models (e.g., nonhardening elastoplasticity) has often proved invaluable in determining if a simulation problem originates from the GeoModel or elsewhere in the host code. When, for example, an undesired feature in a calculation persists even when the GeoModel is run using simplified parameters, a comparison test can be performed using the existing (presumably better verified) independent version of that model within the finite-element code. We have, for example, often compared a host code's standard elasticity model with the GeoModel run in an elastic mode. In one instance where a discrepancy was traced to the GeoModel, it was attributed to failure of the code owner to follow the GeoModel installation instructions (page 75). In a few cases, comparison testing did indeed reveal GeoModel bugs that have since been corrected.
- **Comparison with exact analytical solutions:** Analytical solutions are not available to verify all of the GeoModel's features acting *simultaneously*. However, each GeoModel feature has been individually verified to ensure that the promised *quantitative* material response is delivered (e.g., accurate tracking of a specified porosity crush curve, exact apparent strengthening in high rate loading, etc.). Depending on how the model parameters are set, the GeoModel can be idealized to a form for which some problems admit exact solutions. One example is that of a linear Mohr-Coulomb material with an associative or a non-associative flow rule in homogeneous loading. This class of problems was recently studied in a verification and benchmarking activity sponsored by the Defense Threat Reduction Agency (DTRA) through its Advanced Concepts Technology Demonstration (ACTD) Project. These exercises were part of a larger Verification and Validation (V&V) effort to increase confidence in prediction of low-yield nuclear damage of underground (tunnel) facilities in jointed (in situ) rock mass. The problems are designed to increase in complexity, by invoking additional physics in the material models, until a level is reached that is deemed sufficient to model precision field tests. This work will be described in further detail later in this chapter.

* Testing a numerical model in multiple host codes has been vital to our SQA process. If two codes agree, then no conclusion may be drawn. If, however, two codes predict different answers, then at least one of them is not solving the equations properly (or is not solving the same equations). Resolving such discrepancies has *time and again* expedited bug identification and resolution.

† Incidentally, the disquieting frequency of bugs originating within the host code (not the constitutive model) reiterates the importance of specialized constitutive model drivers in constitutive model verification. Constitutive models should *not* use finite-element codes as their primary verification platform.

- **Consideration of the method of manufactured solutions (MMS):** The MMS method of SQA entails *first* solving an inverse problem in which simple (e.g., quadratically varying) analytical time histories for the *response* functions are substituted into the governing differential operators to obtain (probably with the assistance of a symbolic mathematics program such as *Mathematica*) an expression for the *input* functions that would produce the pre-specified response function. The numerical model is then sent this *analytically determined* input function to verify that the original (pre-selected) response function is recovered. For the GeoModel, using MMS would require pre-selecting an analytically simple stress history to determine a strain history to use as input in the numerical simulation. To date, this technique has not been used in the GeoModel verification process. Solving the inverse problem is quite difficult because the GeoModel’s differential operators are “branched” (one set is used during elastic deformation, while another is used during plastic loading, and the internal state variable evolution equations themselves are coupled to the location of the stress on the current yield surface). However, by using simplified model input parameters, solving the inverse problem might be tractable, so MMS might indeed prove useful in the ongoing (still incomplete) GeoModel verification process.
- **order-of-convergence:*** Time steps for complicated plasticity models often must be much smaller than the time step used by the host (finite-element) code. The GeoModel’s governing equations change upon reaching yield, and this transition typically occurs somewhere in the middle of the host code’s time step, which implies that the constitutive model must break the step into elastic and plastic parts. Moreover, further subcycling within the constitutive model is required to avoid “drift” of internal state variables into non-physical or inconsistent domains.† Subcycling complicates the meaning of a convergence study performed at the host code level. Preliminary tests (see page 86) indicate that *each subcycle* within the GeoModel is first-order convergent, but (recall the last footnote on page 79) we have not yet performed sufficient tests to consider this claim fully verified for a broad variety of load paths. Subcycling in the GeoModel has been massively improved over earlier versions. Problems that formerly took 2000 code steps to converge to an acceptable accuracy‡ can now be run to the same pointwise accuracy in only 10 apparent *host-code* steps (internally, the GeoModel still runs ~2000 subcycle steps, but this improvement in allowable *host-code* step size is essential in field-scale finite-element simulations). An independent research effort [16] is nearing completion in which an implicit integration scheme has been developed for a *simplified* version of the GeoModel, but verification of its order-of-convergence is not yet completed.

* The term “order-of-convergence” is preferred over “order-of-accuracy” because a converged solution is never necessarily a *correct* solution. For example, if the return direction is incorrect in a classical predictor-corrector plasticity scheme, then the algorithm will converge, *but to the wrong result*. The GeoModel, by the way, does not use a return method — it explicitly integrates the equations, using subcycling to assist with the change of governing equations upon yielding.

† Of course, higher-order integration is also an option, but the total computational overhead sometimes exceed that of a well-written subcycling algorithm. Moreover, higher-order integration algorithms are notoriously difficult to maintain when the governing equations themselves are being revised during parallel development of the physical theory.

‡ At this stage in our ongoing verification process, we are using so-called “viewgraph” assessment of accuracy in which solutions are compared visually by plotting them together. This easy assessment method simply *bounds* the discrepancy between two seemingly overlaying plots to be less than differences perceptible to the human eye relative to the size of the graph.

Preliminary convergence testing. Let $F(x)$ denote a fine-resolution solution curve (e.g. stress as a function of strain) corresponding to N evenly spaced time steps. Let $f(x)$ denote a coarser solution corresponding to $n < N$ time steps. In both cases, the continuous curves $F(x)$ and $f(x)$ are here regarded as piecewise linear interpolations between discrete function values at the timesteps. Both curves are normalized by the peak value of $F(x)$.

The “integrated discrepancy” is defined

$$\left(\sum_{K=1}^N [F(x_K) - f(x_K)]^2 \right)^{1/2} \quad (7.1)$$

The “pointwise discrepancy” is defined

$$\left(\sum_{k=1}^n [F(x_k) - f(x_k)]^2 \right)^{1/2} \quad (7.2)$$

Figure 7.3 shows that the basic algorithm *without subcycling* is first-order accurate. Figure 7.2 shows that subcycling makes the solution nearly pointwise converged (discrepancy $\approx 2^{-6}$) even for inordinately coarse calculations of 1 to 3 time steps. This highly desirable behavior can be of paramount importance when the model is run in finite-element codes that take large steps.

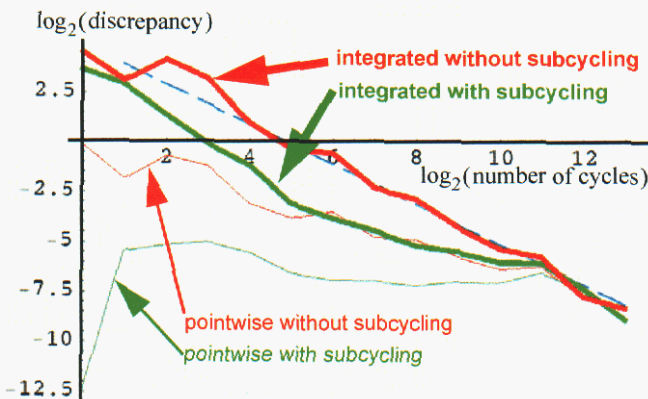


Figure 7.3. Rate of convergence. The dashed blue line (shown for reference) has a slope exactly equal to -1 .

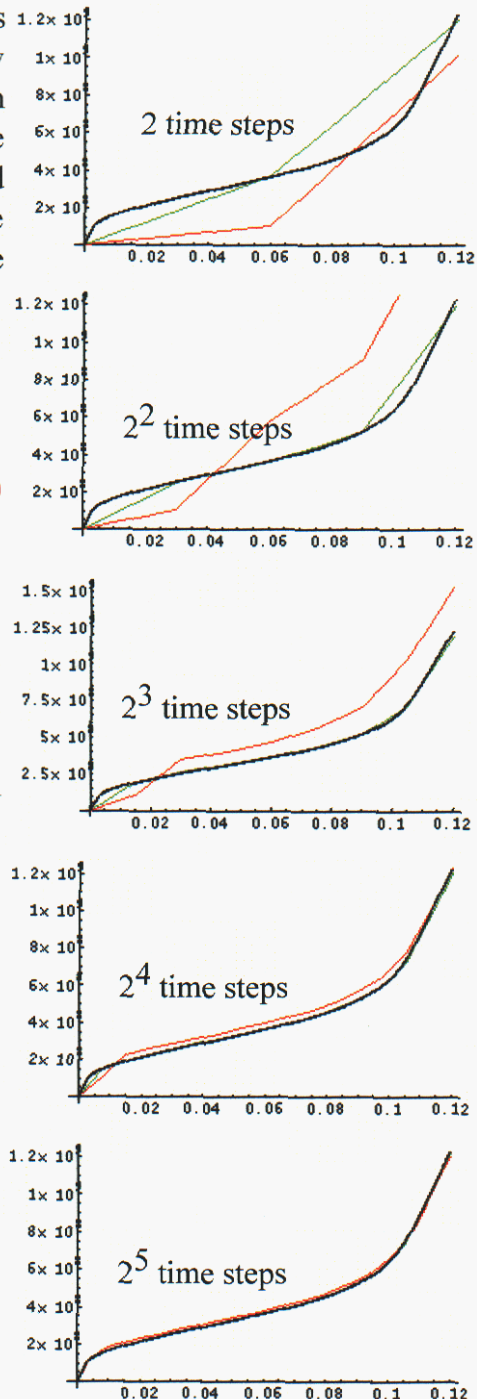


Figure 7.2. Subcycling test for hydrostatic loading. The ordinate is the first stress invariant I_1 and the abscissa is volumetric strain $\bar{\epsilon}_v$. Red is without subcycling. Green is with subcycling. Black, $F(x)$, corresponds to 2^{15} time steps.

Verification: single-element problems (regression suite)

A single-element problem is one for which the stress and strain fields do not vary in space. As summarized below, this section presents four different single-element load paths, each separately solved using two different GeoModel parameter sets (associative and non-associative linear Mohr-Coulomb — see Appendix B, page B-22). To determine corresponding sets of material parameters for the GeoModel, the linear Mohr-Coulomb parameters were used to create simulated data pairs for the limit state and plastic potential functions. Following the instructions in Appendix A, GeoModel was then fitted to these data pairs to determine the limit-state parameters ψ, a_1, a_2, a_3, a_4 and non-associative material parameters $\{\psi^{PF}, a_2^{PF}, a_1^{PF}\}$. The compaction parameters $\{R, R^{PF}, p_0, p_1, p_2, p_3\}$ were selected such that no compaction occurred over the stress range specified for the load paths. Likewise, hardening and rate dependence were disabled. Results are summarized in Figs. 7.4 through 7.7.

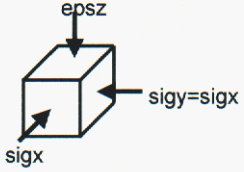
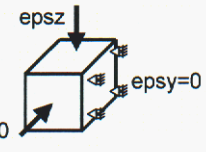
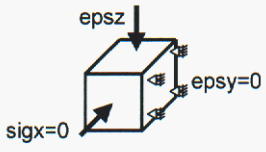
	TXC0			<ul style="list-style-type: none"> • Simple load paths clearly demonstrate basic model response • Run for both full and partial associativity • Triaxial Compression <ul style="list-style-type: none"> — Activates compression meridian — Same load path as a real lab test • Reduced Triaxial Extension <ul style="list-style-type: none"> — Activates extension meridian — Same load path as a real lab test • Plane Strain <ul style="list-style-type: none"> — Activates meridians at Lode angle(s) (triaxiality) between compression and extension 	
	Point	sigx=sigy	epsz		
1	0	0.000000			
2	0	0.005000			
3	0	0.003274			
	TXC20				
	Point	sigx=sigy	epsz		
	1	0	0.000000		
	2	20	0.000310		
	3	20	0.005000		
4	20	0.002060			
	RTX100				
	Point	sigx=sigy	epsz		
	1	0	0.000000		
	2	100	0.001548		
	3	100	-0.005000		
4	100	-0.002295			
	PSTRN				
	Point	epsz			
	1	0.000000			
	2	0.010000			
	3	0.008391			

Table 7.1: Mohr-Coulomb Parameters for single-element verification testing

Parameter (Material Properties)	Symbol	Associative	Non-associative
Young’s Modulus	E	31.0 GPa	31.0 GPa
Poisson’s Ratio	ν	0.26	0.26
Friction angle	ϕ	29°	26°
Dilation angle	ω	29°	14°
Cohesion	S_o	15.7 MPa	15.7 MPa
Dry bulk density	ρ	2.34 MPa/m ³	2.34 MPa/m ³

SINGLE ELEMENT VERIFICATION RESULTS UNCONFINED COMPRESSION

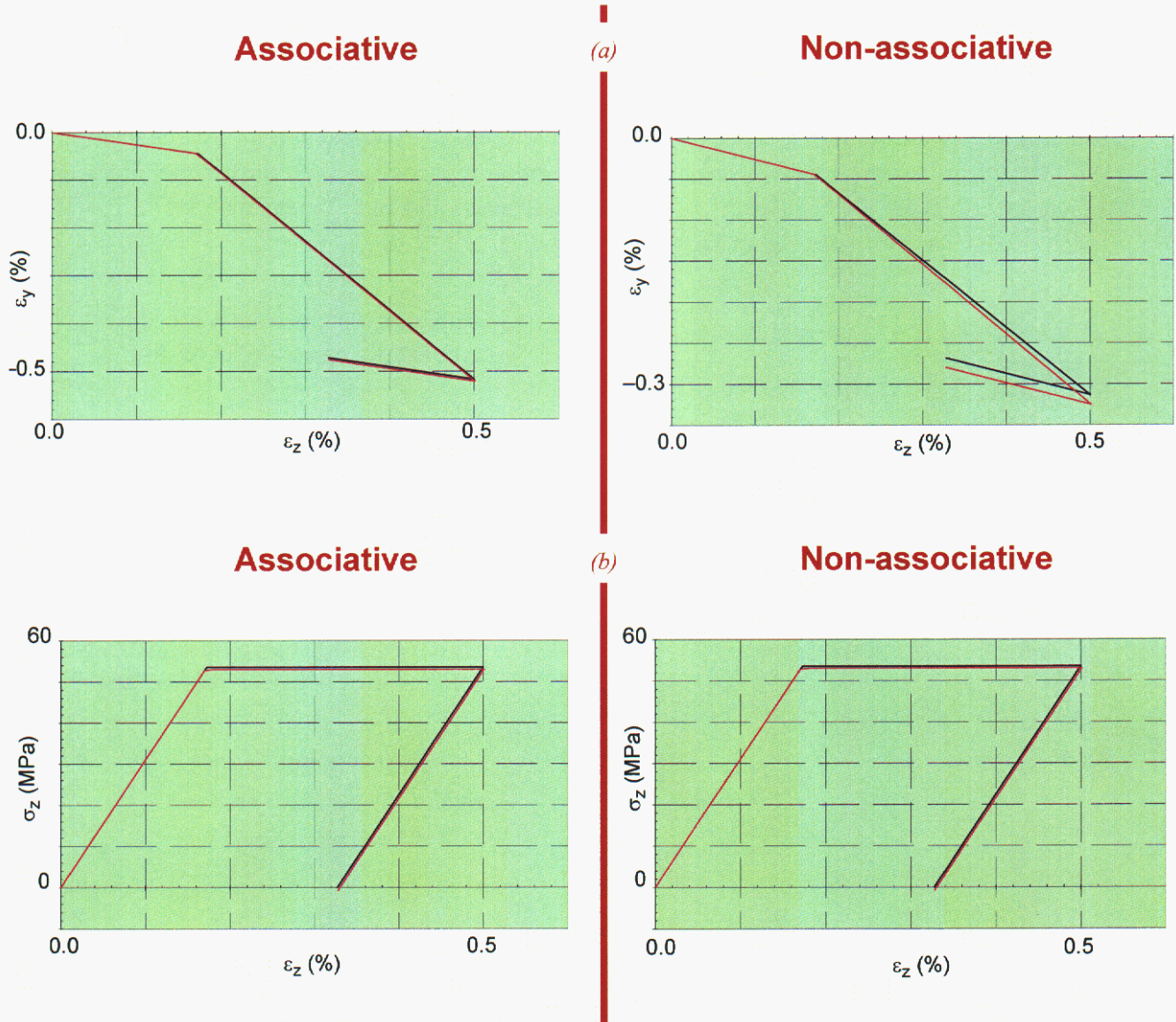


Figure 7.4. Unconfined compression. Exact (black) solutions compared with ALEGRA GeoModel simulation (pink). (a) lateral strain vs. axial strain (b) Stress vs. strain.

SINGLE ELEMENT VERIFICATION RESULTS 20 MPa TRIAXIAL COMPRESSION

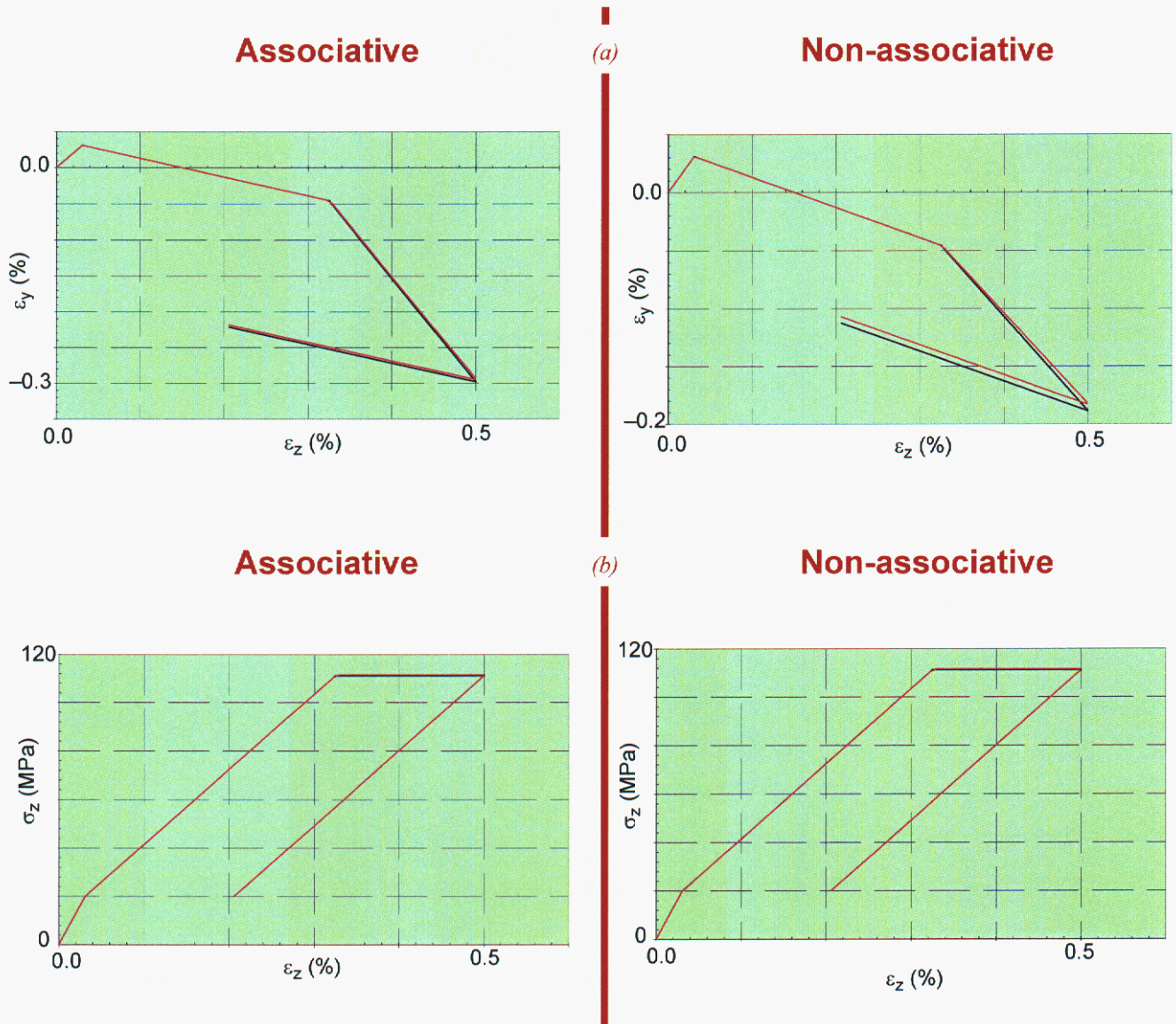


Figure 7.5. 20 MPa triaxial compression. Exact (black) solutions compared with ALEGRA GeoModel simulation (pink). (a) lateral strain vs. axial strain (b) Stress vs. strain.

SINGLE ELEMENT VERIFICATION RESULTS REDUCED TRIAXIAL EXTENSION

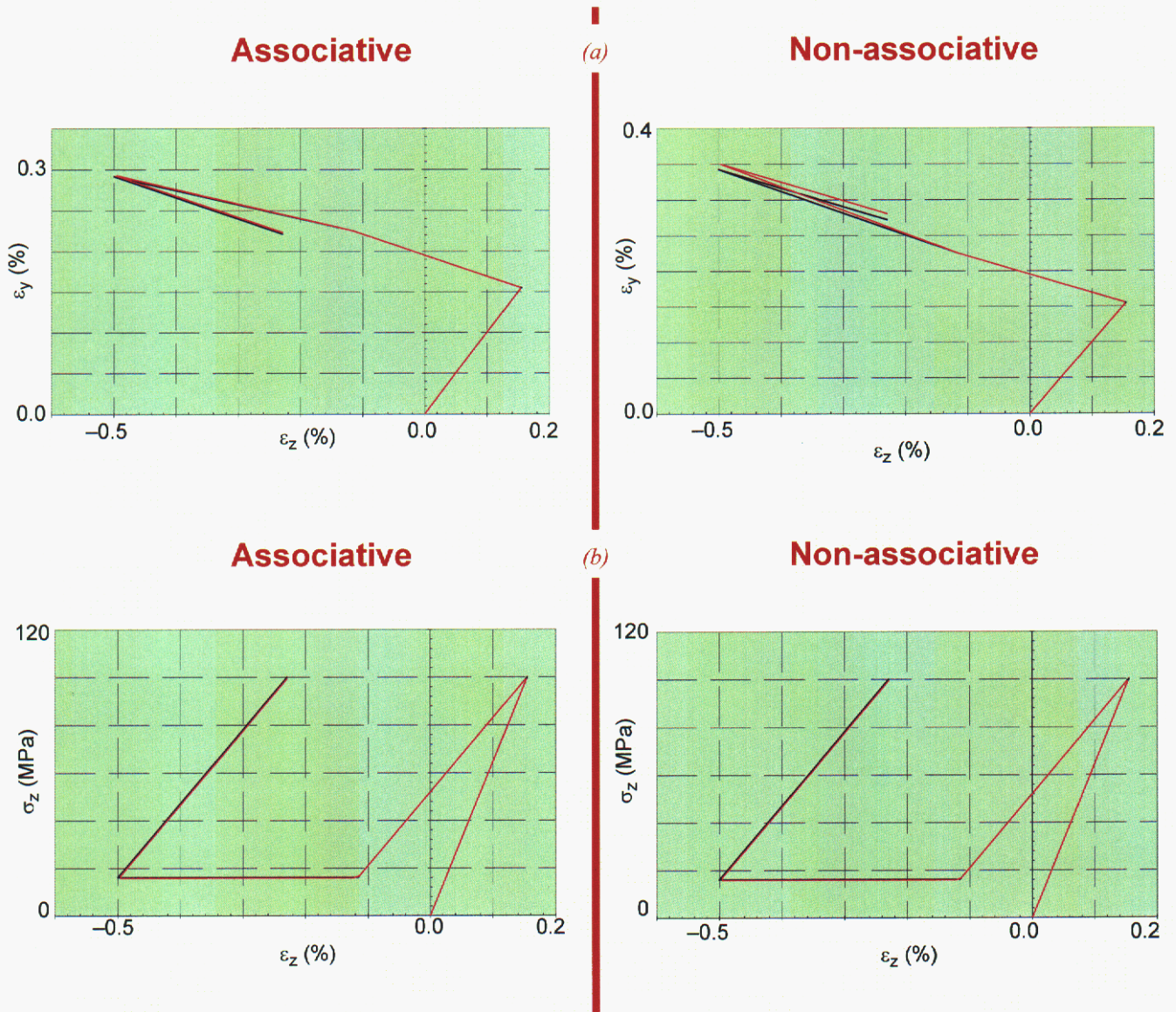


Figure 7.6. *Reduced triaxial extension.* Exact (black) solutions compared with ALEGRA GeoModel simulation (pink). (a) lateral strain vs. axial strain (b) Stress vs. strain.

SINGLE ELEMENT VERIFICATION RESULTS PLANE STRAIN

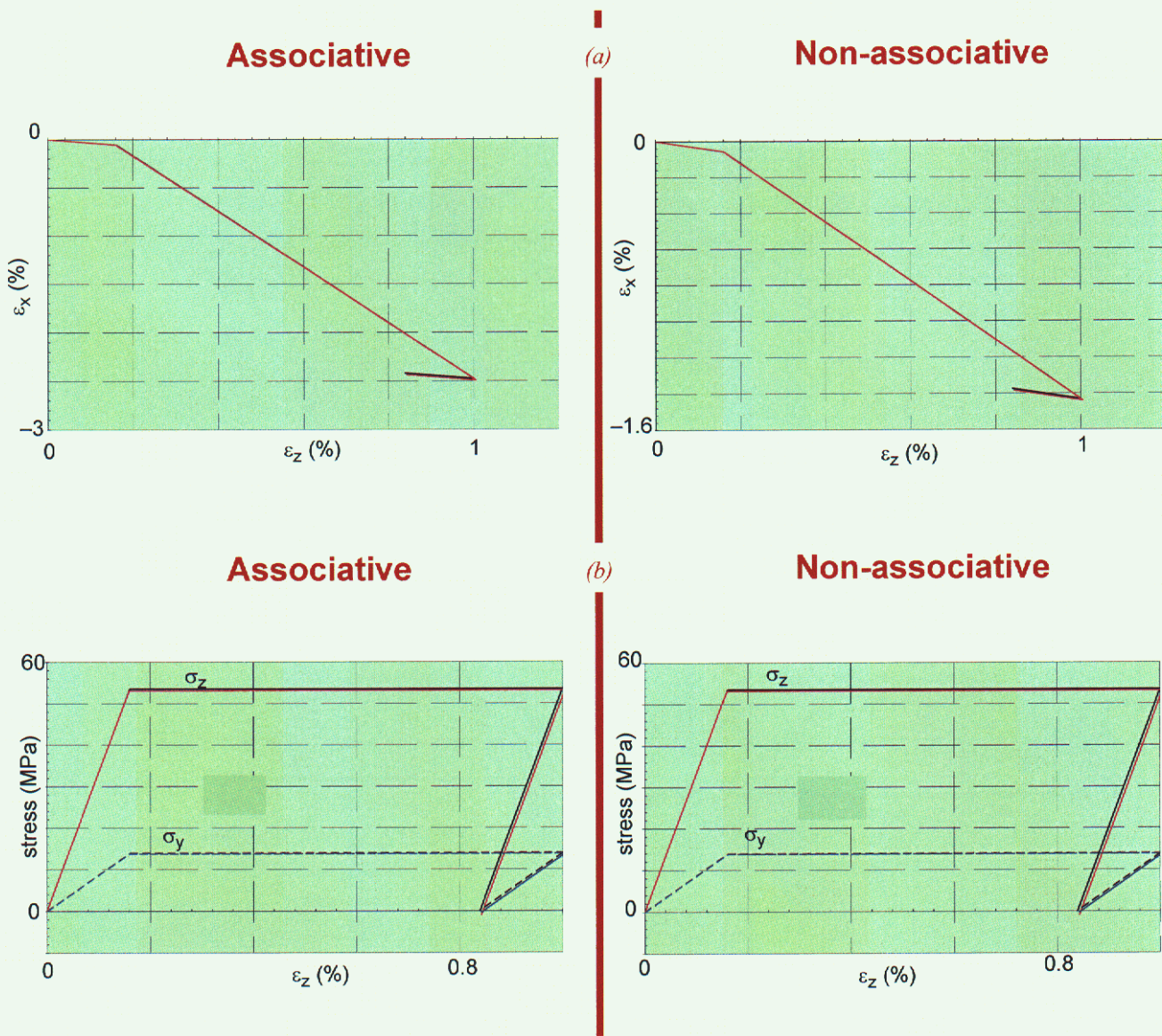


Figure 7.7. Plane Strain. Exact (black) solutions compared with ALEGRA GeoModel simulation (pink).
(a) lateral strain vs. axial strain (b) Stress vs. strain.

Discussion.

In Fig. 7.7, predictions of the GeoModel overlay the analytical results.* Though not yet proved conclusively, we contend that the slight discrepancy apparent in Figs 7.4 and 7.5 arises *not from constitutive model errors*, but instead from host code errors in the handling of stress boundary conditions. The fully strain-controlled problem (Fig. 7.7) exhibits no significant solution discrepancy. However, moderate error is apparent in Figs 7.4 and 7.5, which involve *two* stress boundary conditions (the lateral stresses). Like most constitutive models, the GeoModel takes strain rate as input and returns updated stress as output. If the host finite-element code handles stress boundary conditions improperly, then it will have slight errors in the strain rate that it sends to the GeoModel, thereby causing predictions to deviate slightly from analytical solutions. Such errors are not uncommon when dynamic finite-element codes are used to attempt to simulate homogeneous deformations.† To reiterate, we believe boundary condition errors in the host code (not the GeoModel) are responsible for the solution errors, and we anticipate re-running these simulations in a true constitutive model driver to verify this claim.

Other single-element tests. Whenever the source code is changed, we perform approximately 20 single-feature single-element verification checks for each of our regression tests performed under loading that is simple enough to admit analytical solutions.

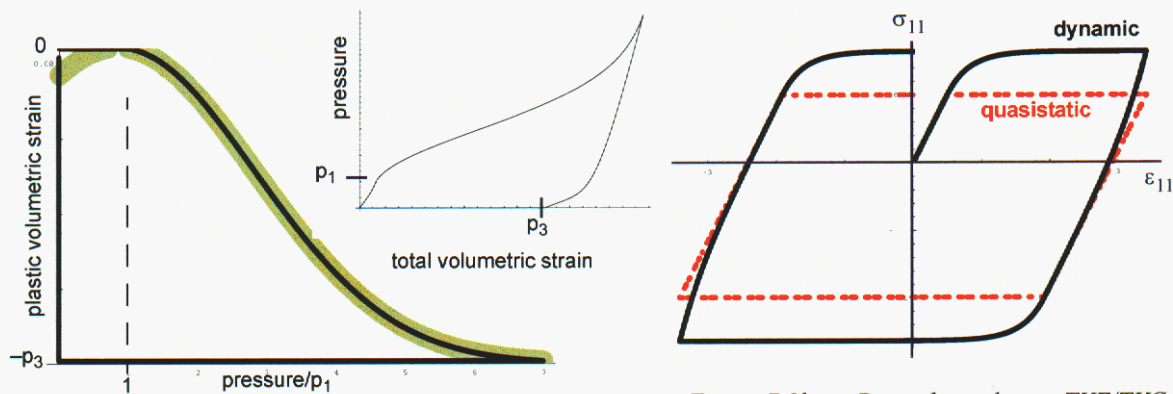


Figure 7.8a. Crush curve and hydrostatic loading verification.

Figure 7.8b. Rate dependence TXE/TXC ratio verification for triaxial load/unload.

Fig. 7.8a depicts results from a hydrostatic loading simulation in which plastic volumetric strain (\mathbf{EQPV}) is plotted against pressure ($-\mathbf{I1}/3$). The thick yellow curve in Fig. 7.8a is the crush curve (Eq. 4.67) determined independently by user specified values of the GeoModel parameters p_1, p_2, p_3 . The *predicted* volumetric strain ϵ_v^p (black line in Fig 7.8a) is verified to remain zero until the pressure reaches the crush curve, after which

* Precisely *quantifying* verification error lags far behind other more important constitutive SQA priorities, so we will be satisfied here and throughout this chapter with assessing agreement between computed and analytical results via a so-called “viewgraph metric,” where the error is nebulously bounded by what can be perceived visually, given the plot size.

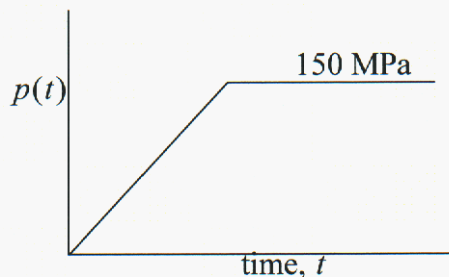
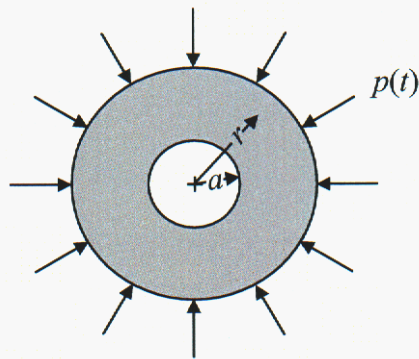
† The only way to ensure a precisely homogeneous deformation in a dynamics finite-element code is to bypass solution of the momentum equation. More correctly, homogeneous loading requires a body force \mathbf{b} identically equal to particle acceleration \mathbf{a} , making the momentum equation trivial.

it drops along the crush curve as it should. The stress-strain curve (inset in 7.8a) unloads correctly to the user-specified peak strain parameter p_3 . For *non-hydrostatic* loading, we have verified (trend-test) that shear-enhanced pore collapse causes inelasticity to commence *prior* to the pressure reaching the crush curve.

Fig. 7.8b simultaneously verifies the GeoModel's ability to predict an apparent increase in strength under dynamic loading and its ability to predict different strengths in triaxial extension vs. compression. In that problem, pressure dependence of yield was suppressed and the TXE/TXC strength ratio was set to 1/2, resulting in a tensile strength half as large as the compressive strength.*

Verification: Hendren & Ayier pressurized cylinder

The problem depicted below, solved for subcases of associative and non-associative flow, involves a circular tunnel in a Mohr-Coulomb material loaded in a plane strain configuration. A DTRA contractor provided the analytical solutions. The material parameters are the same as those used in the previous verification problems.



Geometry

Tunnel radius	a	1 m	1 m
Far field radius	b	10 m	10 m

Loading

Internal pressure	p_a	0	0
Far field pressure	p_b	0-150 MPa	0-150 MPa

The results in Fig. 7.9 show that the GeoModel solutions agree with analytical results. Though not confirmed conclusively, the very slight discrepancies are hypothesized to result from different strain definitions used in the GeoModel and analytical solution (or possibly host code traction boundary condition issues similar to those discussed earlier).

* The TXE/TXC strength ratio applies to TXE and TXC states at the same pressure. When pressure dependence of yield is allowed, the TXE peak in a verification test like this will not *and should not* be 1/2 the magnitude of the TXC peak.

HENDRON & AYIER VERIFICATION RESULTS

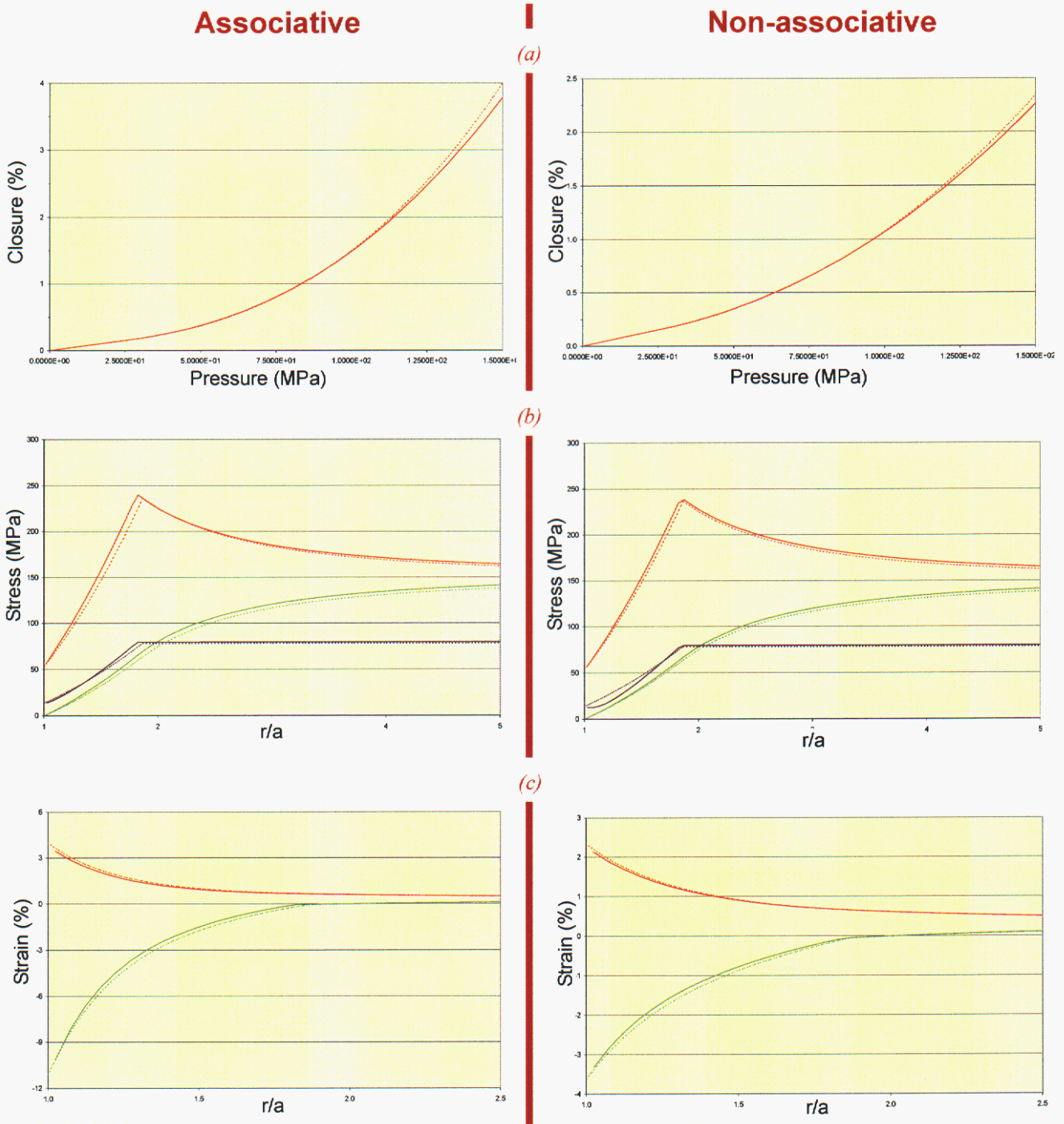


Figure 7.9. Hendron & Ayier verification problem. Exact (dash) solutions compared with ALEGRA GeoModel simulation (solid). (a) Tunnel closure vs. far-field pressure (b) Stress components vs. normalized range, (c) strain components vs. normalized range.

Elastic free-field wave form (finite-element verification)

This section describes a field-scale test for verifying installation of the GeoModel in host finite-element codes. As emphasized earlier, verifying a constitutive model is distinct from verifying its implementation within a finite-element code. After a constitutive model becomes one of *many* components within a much larger finite-element model, the potential sources of solution error expand to now include boundary conditions, artificial viscosity, and other aspects of the host code’s method of solving the partial differential equation that governs momentum balance.

As indicated in Fig. 7.10, a time varying velocity (identical to the one later discussed on page 107) was applied at the boundary of a spherical cavity (radius 204m). The GeoModel’s yield features were disabled to allow predictions for the velocity at the outer radius (470m) to be compared with an analytical *elasticity* solution.* Implementations of the GeoModel in two finite-element codes were tested. One code was unable to reproduce the correct response because of bugs in roller boundary conditions. Fig. 7.11 demonstrates that the second code (JAS3D)

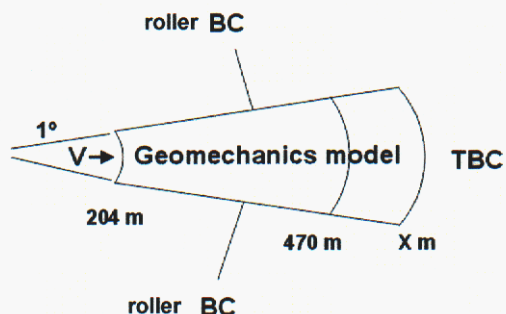


Figure 7.10. Spherical cavity geometry.

was capable of reproducing the analytical solution well enough to suggest that *the GeoModel* is performing correctly. While the moderate solution error might be attributable to the analytical solution’s presumption of small strains, further study (by the code owners, not the GeoModel developers) is warranted to determine if the solution errors result from under-integration, or some other aspect of the finite-element model such as artificial viscosity (both codes’ solutions were strongly affected by artificial viscosity — default settings for artificial viscosity were insufficient to reproduce the analytical results). This elasticity verification problem is revisited and generalized in the *plasticity* validation test on page 107, where code predictions are compared with data.

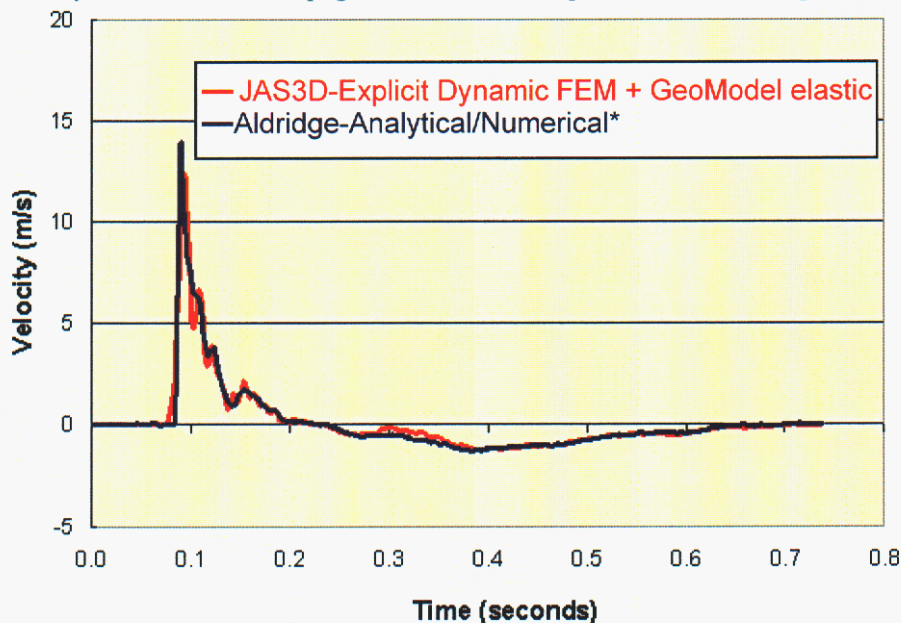


Figure 7.11. Finite-element vs. analytical/numerical elastic wave velocity at 470 meters from a velocity spherical cavity source at 204 meters.

* Aldridge’s analytical solution [1] is expressed in terms of integrals that are evaluated numerically in the frequency domain using independent software provided by Aldridge.

8. Parameterization (calibration)

Appendix A describes how to characterize a material for the GeoModel. Using these procedures, several materials have already been fit, as summarized in Fig. 8.1 (compare these with Figs. 1.1 and 3.3). GeoModel parameters for these materials are in Appendix B.

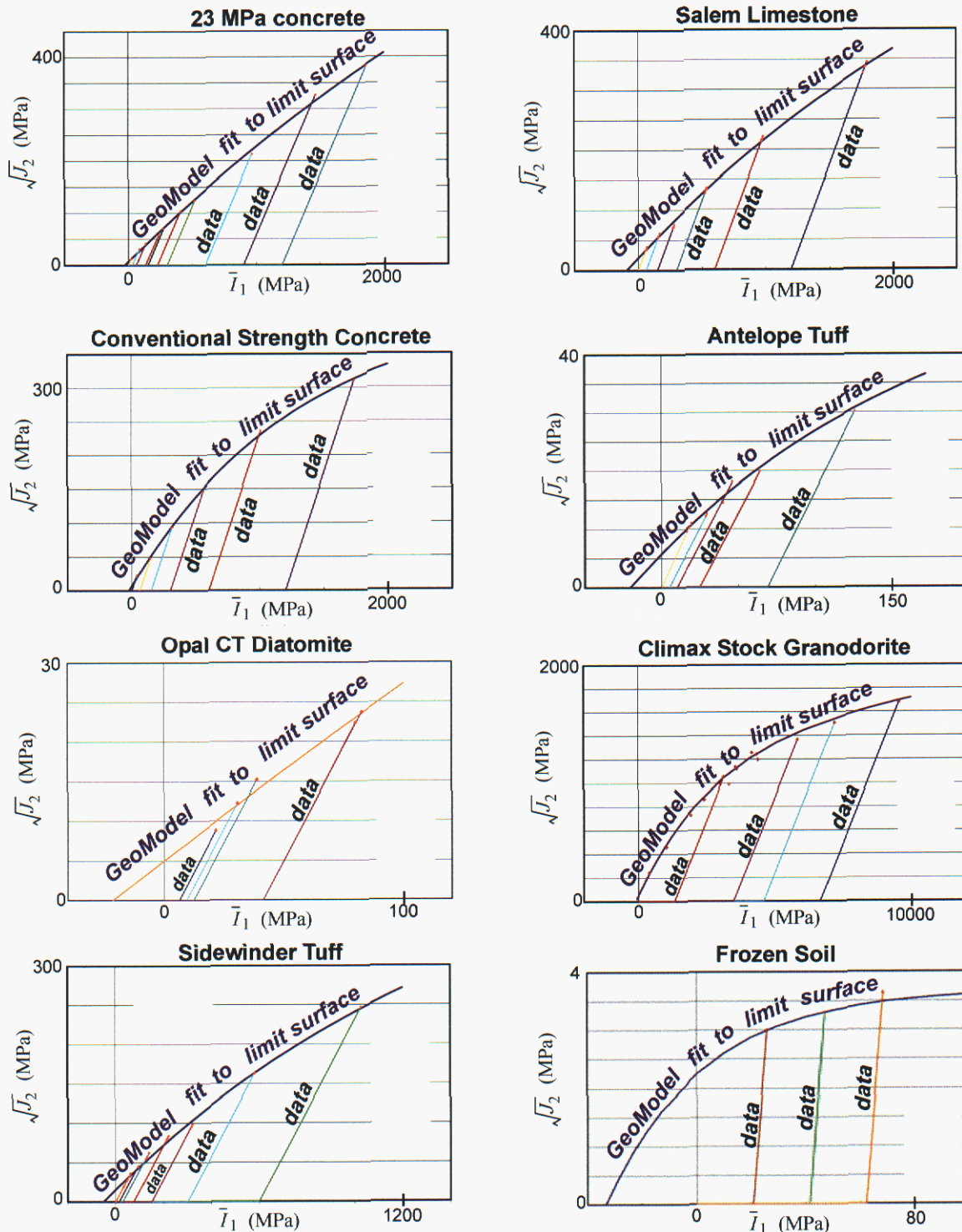


Figure 8.1. Meridional limit curves for some materials already parameterized to the GeoModel.

Nonlinear elasticity

Figures 8.2 and 8.3 demonstrate the ability of the GeoModel's nonlinear elasticity fitting functions (Eqs. 4.10 and 4.9) to reproduce nonlinear elasticity data. Parameters were assigned using the least-squares model calibration tools described in Appendix A.

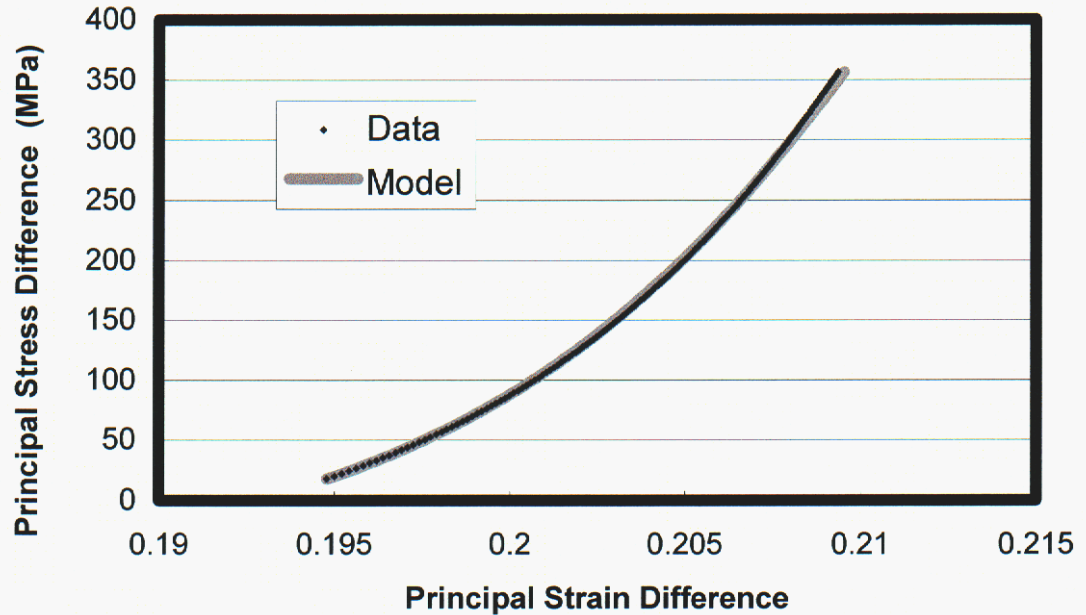


Figure 8.2. *Nonlinear elasticity in shear.* This figure shows the GeoModel fit to concrete data [46] from the unload portion of a triaxial compression test conducted at a confining pressure of 200 MPa. Here, the principal stress difference is plotted against the principal strain difference, thereby making the slope equal to twice the shear modulus.

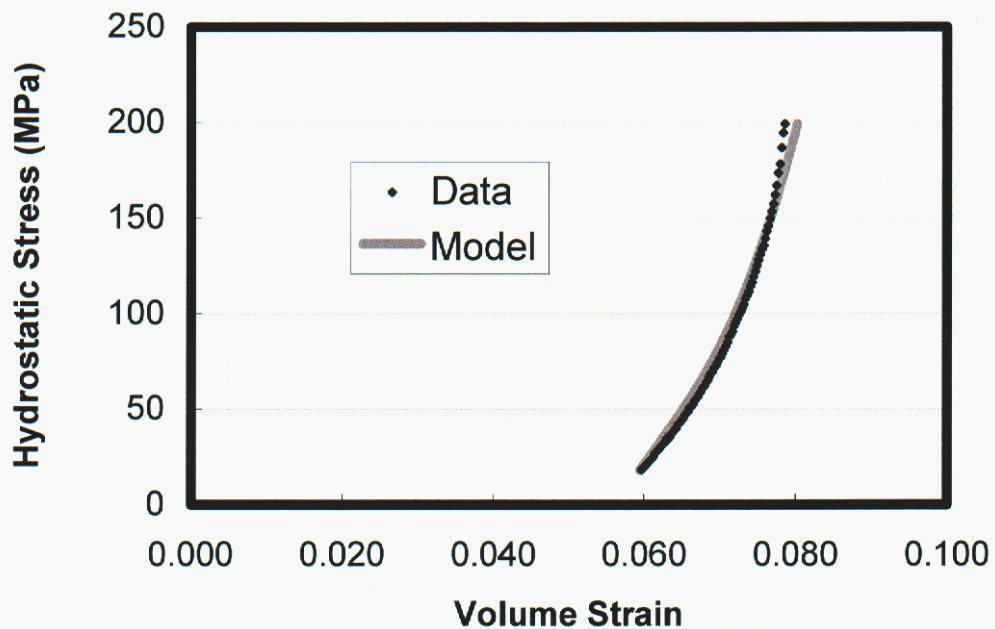


Figure 8.3. *Nonlinear elasticity in hydrostatic loading.* This figure shows the GeoModel fit to concrete data [46] from the unload portion of a hydrostatic compression test from 200 MPa. Here, the slope equals the bulk modulus.

Elastic-plastic coupling

For many materials, elastic moduli are unaffected by inelastic deformation. However, Fig. 8.4 shows data for a material whose elastic properties *are* affected by inelasticity. Modeling this effect requires using the enhanced moduli fitting functions, Eqs. (4.33) and (4.34), which permit the shear and bulk moduli to vary with equivalent plastic strain (determined from data by the residual strain upon unloading to a zero stress, as explained in Appendix A). For the GeoModel to be considered a good fit to data, the simulated unloading curves merely need to be parallel to experimental unloading curves (not necessarily overlapping unless the data and simulation unload from the same strain).

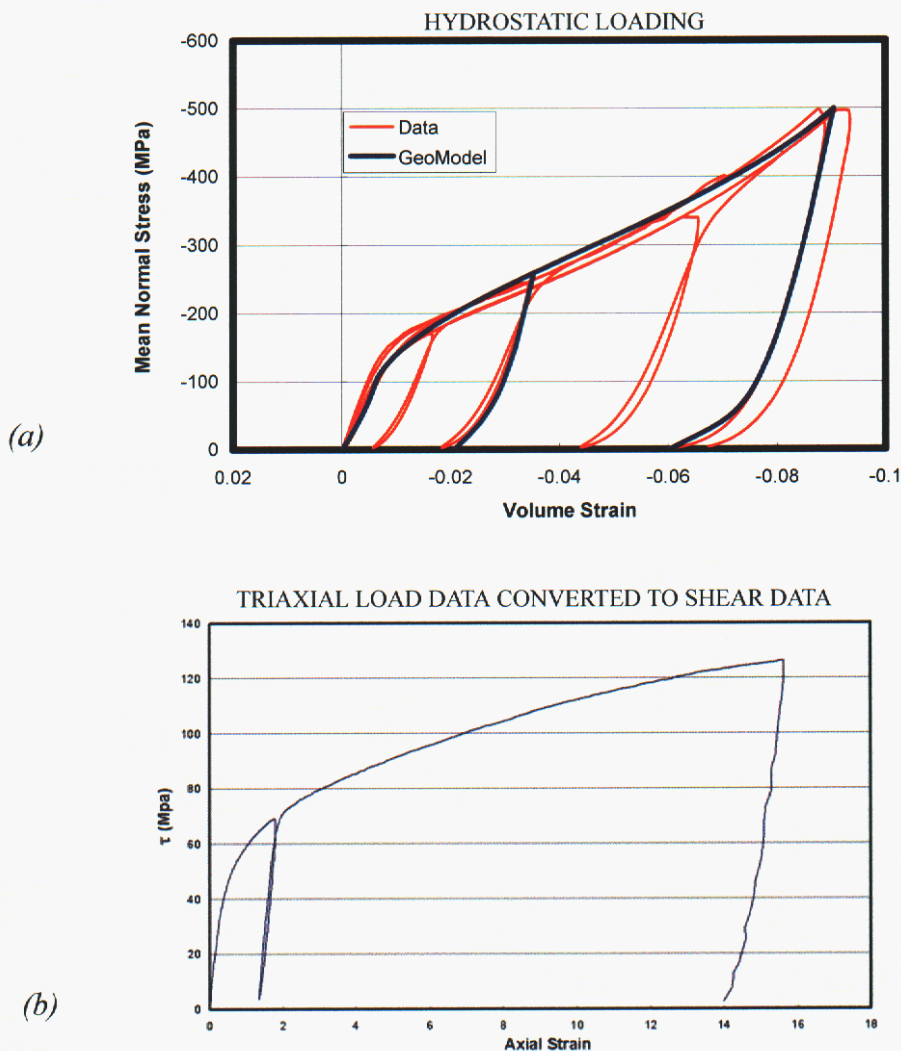


Figure 8.4. Elastic-plastic coupling: deformation-induced changes in elastic moduli (Salem Limestone). (a) the tangent bulk modulus can change in response to changes in porosity (i.e., volumetric plastic strain). (b) Likewise, the tangent shear modulus, especially at low shear stresses, can change in response to plastic deformation.

Triaxial Compression

Triaxial compression (TXC) and triaxial extension (TXE) testing is integral to parameterization of the GeoModel. By performing a series of tests, as described in Fig. 3.3, the limit state (onset of softening) can be mapped out. For example, Fig. A.5(a) on page A-6 shows raw data from a suite of TXC tests, indicating how the peak values in each test provide one data point on the GeoModel limit surface Fig. A.5(b). Data from a similar set of experiments for concrete, along with the GeoModel least-squares fit of Eq. (4.8) are shown in Fig. 8.5. Figure 8.1 shows similar plots for other materials. Appendix A describes the least-squares fitting procedures in more detail.

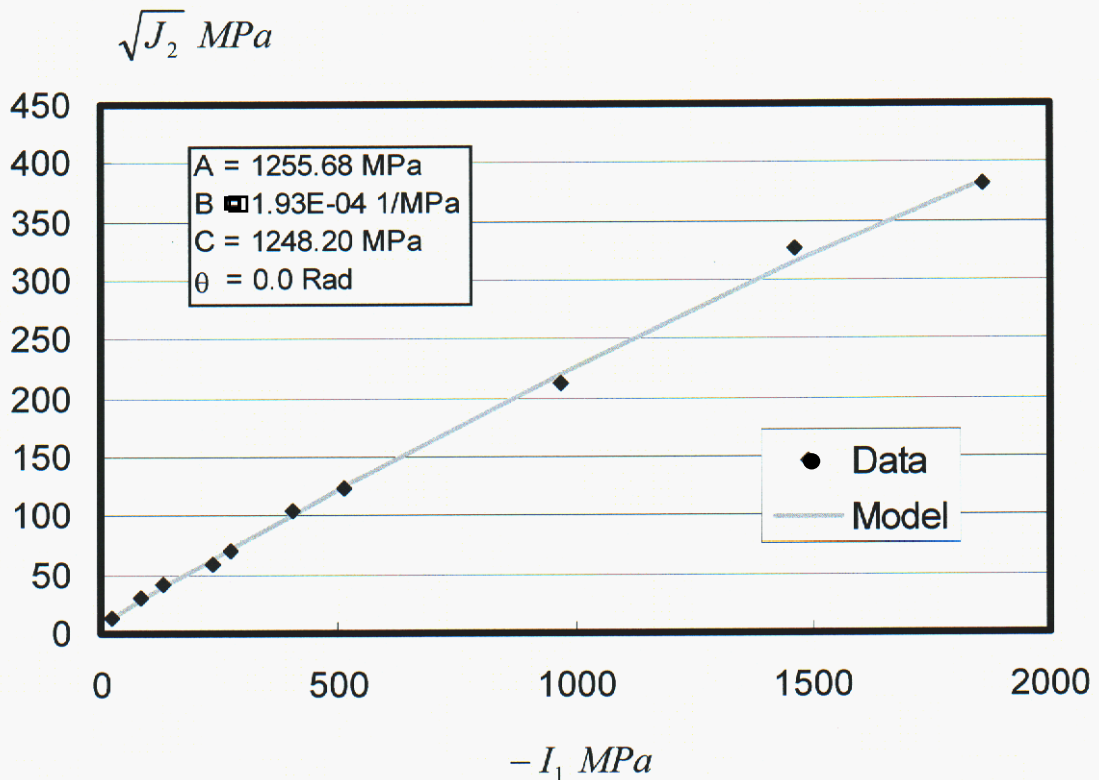


Figure 8.5. Shear failure limit curve compared with concrete data. Ref. [46].

Recall that triaxial testing normally begins with a hydrostatic “load-up” phase, indicated by the horizontal red arrow Fig. 8.6a (where $\sqrt{J_2} = 0$). During the hydrostatic leg, deformation is initially nonlinearly elastic until the virgin yield surface is reached, at which time microscale stress concentrations caused by the presence of pores become too large to resist elastically. Continuing to push the hydrostatic stress to higher levels results in inelastic pore collapse with associated hardening (expansion) of the yield surface. In Fig. 8.6, the target hydrostatic stress state for a given experiment (which marks the transition from the hydrostatic leg to the triaxial leg) was $P = 400$ MPa, giving an I_1 value of -1200 MPa. Pressure-volume data taken during the hydrostatic leg may be used to deter-

mine the GeoModel parameters $\{p_0, p_1, p_2, p_3\}$ by following instructions in Appendix A. Because multiple triaxial experiments must be performed to fully characterize a geological material, variations observed during hydrostatic loading from different tests can be used to quantify the material property variability.

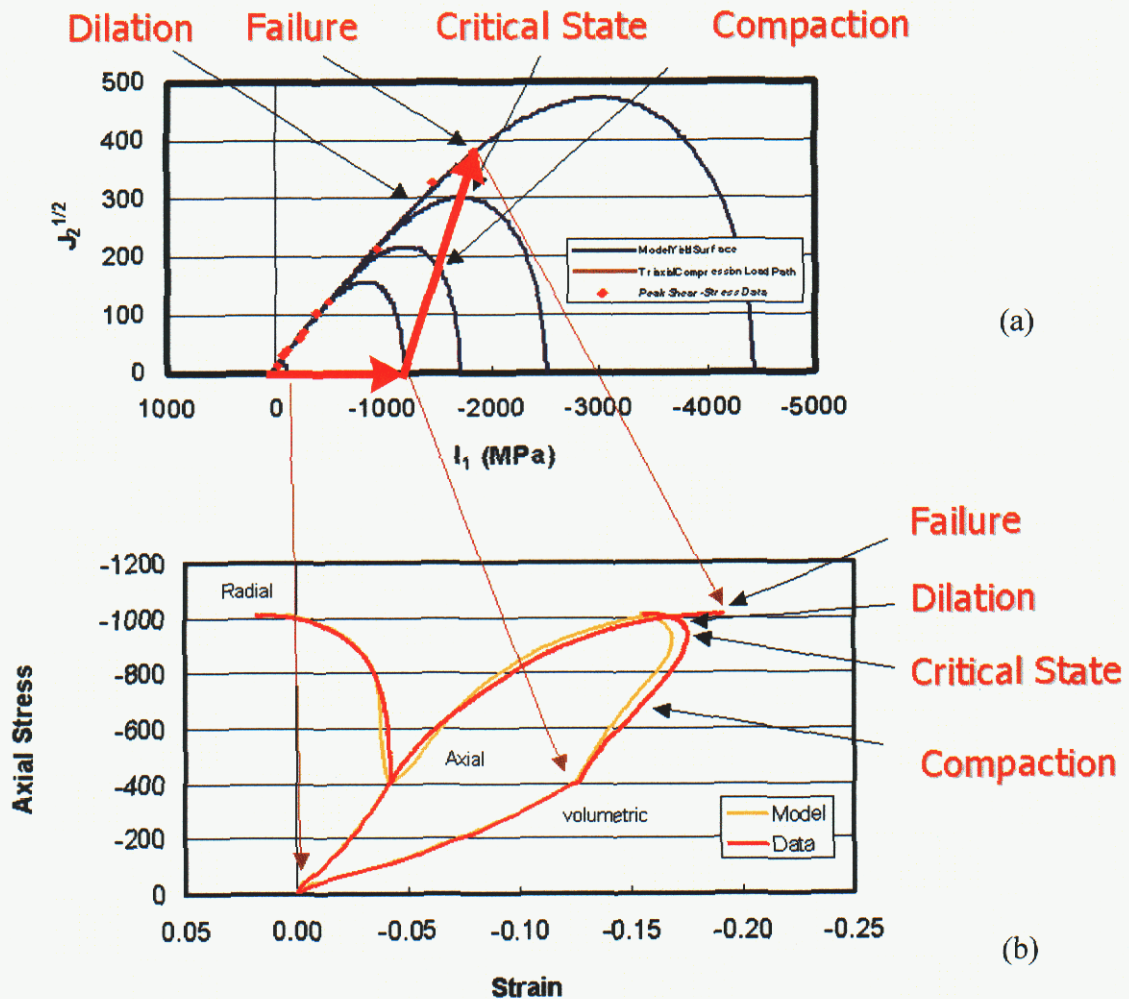


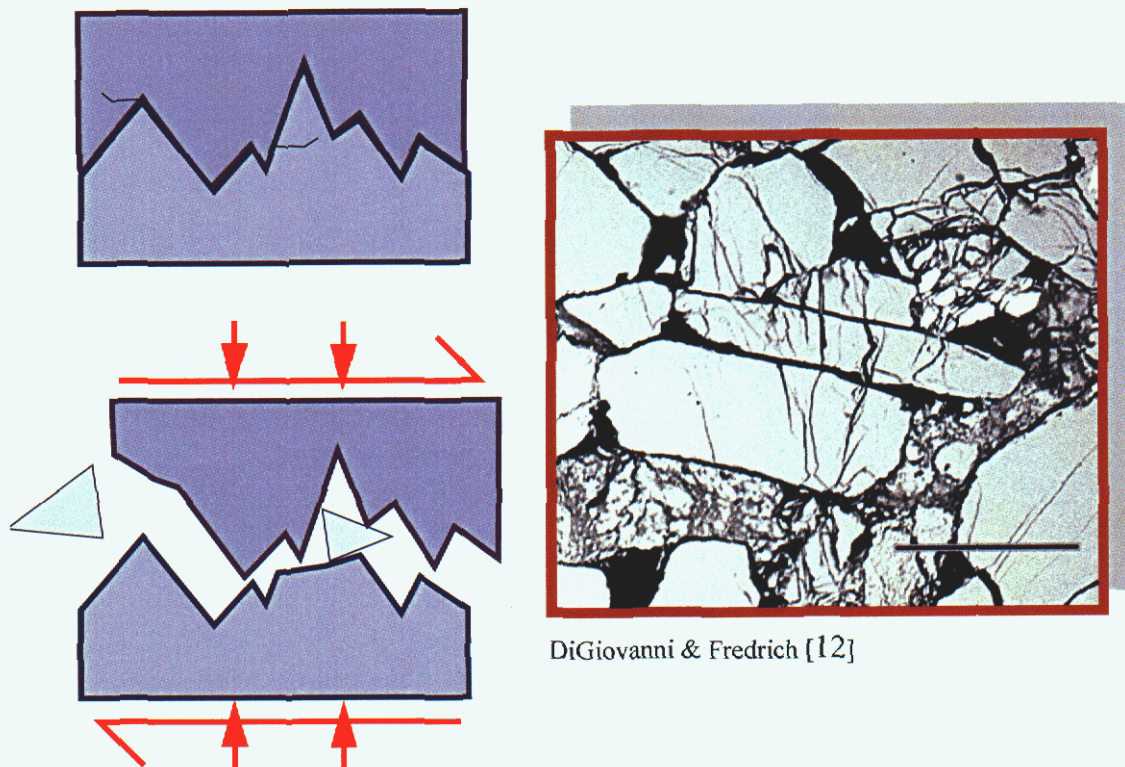
Figure 8.6. Progression of the hardening yield surface (family of blue lines) under a triaxial compression test (red path), illustrated with correspondence of the meridional plane to the stress-strain diagram.

The straight red line segments shown show this two-stage stress trajectory (hydrostatic loading followed by triaxial loading) in the meridional plot of $\sqrt{J_2}$ (which is proportional to the effective shear) versus \bar{I}_1 . Shear-enhanced dilatation corresponds to reaching a zero local yield slope.

After the hydrostatic leg, the triaxial leg (angled red arrow in Fig. 8.6a) commences by increasing the axial load on the specimen while holding the lateral stress constant. As explained on page 16, the stress path follows a straight trajectory in the meridional plane with a slope given by

$$\frac{d(\sqrt{J_2})}{d(\bar{I}_1)} = \frac{1}{\sqrt{3}} \quad (8.1)$$

The transition from hydrostatic to triaxial loading is reflected by a pronounced change in slope in the stress-strain plot of Fig. 8.6. As the axial stress is increased during the triaxial leg, the yield surfaces continues to harden outward even more, now further assisted by the presence of a nonzero stress deviator. In Fig. 8.6 the slope of the yield surface is initially negative at the stress state (i.e., where the straight red load path and curved blue yield surface lines intersect). Consequently, the outward *normal* to the yield surface during this early part of the triaxial phase has both a deviatoric component *and* a *compressive isotropic component*. When the normal to the yield surface is compressive, the inelastic volumetric strain will be compressive as well. However, the isotropic component of the yield surface normal *changes direction* towards the end of the triaxial leg (i.e., the local slope of the yield surface changes sign), which means that the inelastic volumetric strain is *dilatational* (expanding) even though all stress components are compressive. The “critical state” at which the yield surface has a zero local slope on the load path marks the onset of shear-enhanced dilatation. Thus, as illustrated qualitatively in Fig. 8.7 and explained in detail in Appendix A, triaxial loading is used to determine parameters in the GeoModel that govern yield surface evolution and cap curvature.



DiGiovanni & Fredrich [12]

Figure 8.7. Shear-enhanced dilatation under compression. The exaggerated schematic shows that crack faces must overcome surface incompatibilities — they cannot slip over each other without opening even if they are in compression. Moreover, fragments of broken material can become lodged in the crack face and cause crack opening by their rotation. Crack kinking (in the direction of Mode I loading) further contributes to the dilatation associated with crack opening. The dark regions in the micrograph [12] are pores (which collapse under sufficient pressure). The cracks in inclusions produce “micro-rubble” that ultimately generates, through rotation, inelastic volume increase under shear loading even if all principal stresses are compressive.

Physically, an increase in inelastic volume during compression (which is quite commonly observed for brittle materials) is typically attributed to the growth of microcracks under shear. As the surfaces of these cracks move relative to one another, the crack must open up (dilatate) both to overcome geometric incompatibilities in their surface roughness and to permit crack kinking. This interpretation of shear-enhanced dilatation is illustrated schematically and through SEM imaging in Fig. 8.7.

Parameterization: Rate dependence

The GeoModel's relaxation parameters (T_1, \dots, T_7) may be determined through a series of lab-scale laterally-confined Kolsky bar tests [Fig. 8.8] in which a sample is subjected to uniaxial compression at various strain rates.

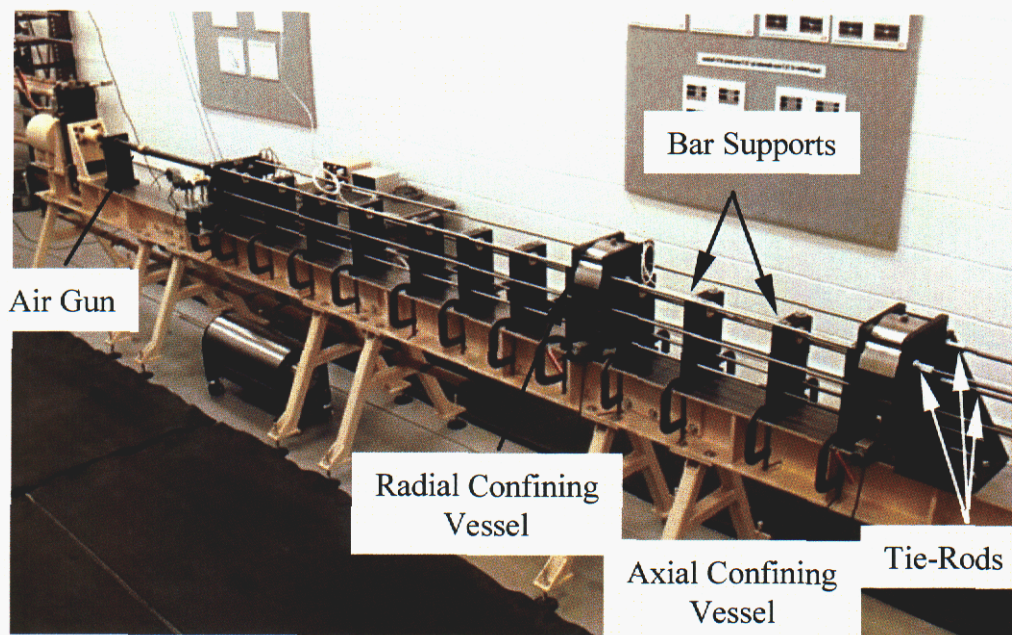


Figure 8.8. Kolsky (split Hopkinson) bar apparatus used to obtain data in Fig. 8.9

Figure 8.9 shows results for a series of Kolsky (split Hopkinson) bar strain rate tests conducted on unconfined compression specimens of Salem Limestone [17]. The peak stress in these experiments is used to assign values of the GeoModel relaxation parameters to properly correlate apparent strength with strain rate. As seen, the unconfined compressive strength increases with strain rate and is well-accommodated by GeoModel theory.

For a discussion of how the data in Fig. 8.9b are used to assign values to $\{T_1, \dots, T_7\}$, see Appendix A.

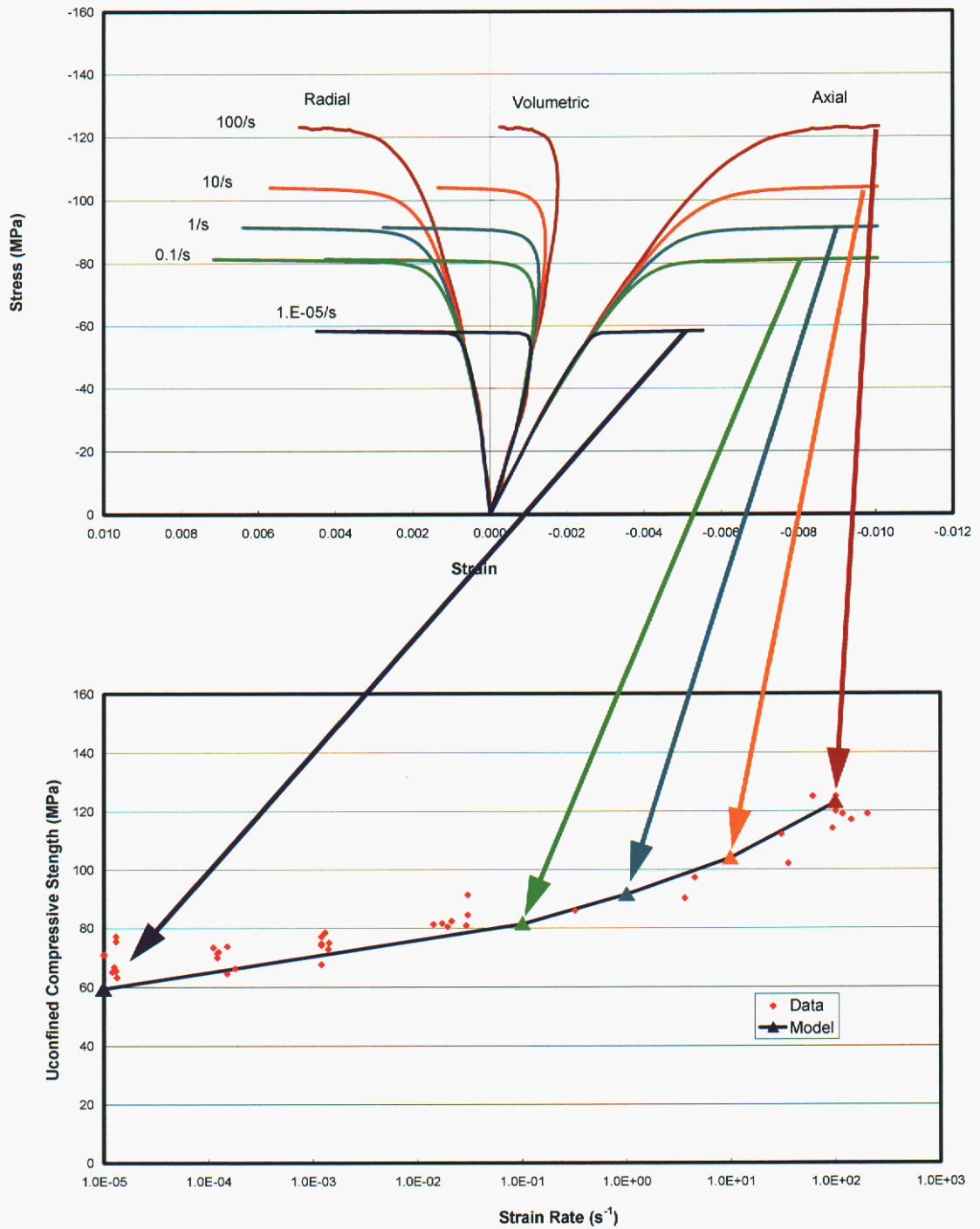


Figure 8.9. Suitability of the GeoModel overstress rate-dependence model to match observed data. (a) Model predictions of stress-strain behavior at various strain rates. (b) Corresponding Kolsky (Hopkinson) bar unconfined compressive strength as a function of strain rate

9. Building confidence in the physical theory

In a weak sense, demonstrating (as we did in the previous chapter) that the GeoModel is capable of being parameterized from controlled laboratory data lends some credibility to the physical foundations of the model. However, truly *validating* a model after its parameters have been determined from standard laboratory data requires showing that the model can, *without any change in pre-calibrated parameters*, predict material response under different (non-calibration) loading scenarios. Ideally, to validate *a constitutive model* (not its implementation into a host finite-element code), one would prefer to compare the model predictions against test data from homogeneous loading experiments that were different from the homogeneous loading tests conducted for calibration.

Thorough testing of any material constitutive model *along with its implementation in a host code* must, of course, include simulation of applications for which model predictions can be compared with structural response measurements. The goal is to assess the degree to which the integrated model (i.e., its installation into a host code) is capable of predicting material system response to non-trivial loading scenarios.

Parameterization entails fitting to a subset of discrete points in parameterization data tables (e.g., as described on page 99, the limit function is parameterized by using only the *peak* stress values, not all values measured in the test). Model validation therefore includes assessing the fitted model's ability to interpolate well between *other* points in these stress-strain response curves (i.e., points that were *not* used in calibration). Similarly, the GeoModel's rate dependence parameters are determined by using only the *peak* stress values in Kolsky bar experiments. Therefore, the model's ability to match the *other* data points in those experiments is a validation test.

In addition to merely ensuring that all data in parameterization tests are well modeled, a better validation test should exercise the model in application domains in which multiple physical mechanisms are acting simultaneously. The goal is to assess whether or not the GeoModel parameterization instructions in Appendix A can lead to a high-quality set of material model properties that are *predictive* in general loading scenarios. This chapter describes some validation problems that have been studied to date. In all cases, these problems were run *using only the single GeoModel parameter set obtained from calibrating to other data for the material — no parameter adjustments were made to improve model agreement for these tests*.

Post-calibration Triaxial loading

The nonlinear elasticity Eqs. (4.9) and (4.10) are parameterized from shear and hydrostatic unloading data. The shear limit function Eq. (4.39) parameterized through *peak states* in triaxial testing. The crush curve Eq. (4.67) parameterized through purely hydrostatic testing. Once parameterized in this way, the GeoModel may be applied to predict the irreversible plastically-hardening stress-strain response at a *variety* of other stress paths. For example, Fig. 9.1 compares GeoModel predictions with simple triaxial data at various confining pressures (these simulations all use *a single set* of GeoModel parameter values).

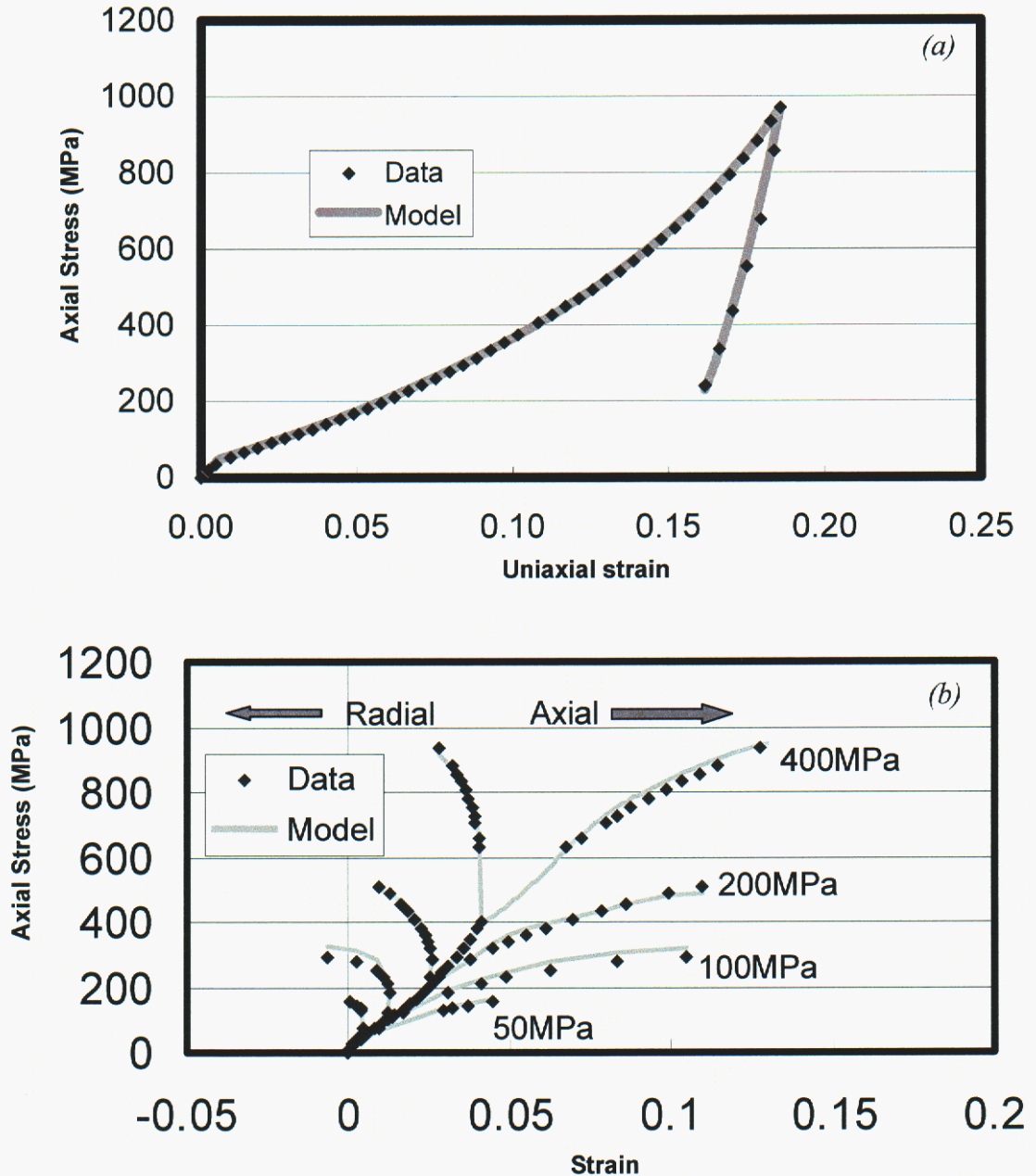


Figure 9.1. (a) GeoModel prediction of uniaxial strain loading. (b) GeoModel predictions of triaxial stress-strain response at various confining pressures. From Ref. [46]. The ability of a single parameter set to agree so remarkably well with this suite of data is a validation.

Field-scale penetration

Figure 9.2 shows results from a *pre-test* prediction of depth of penetration and displacement histories. In tests like these, material constitutive models are often considered “above average” if they are predictive within 20%. As seen, the GeoModel performed exceptionally well by this metric.

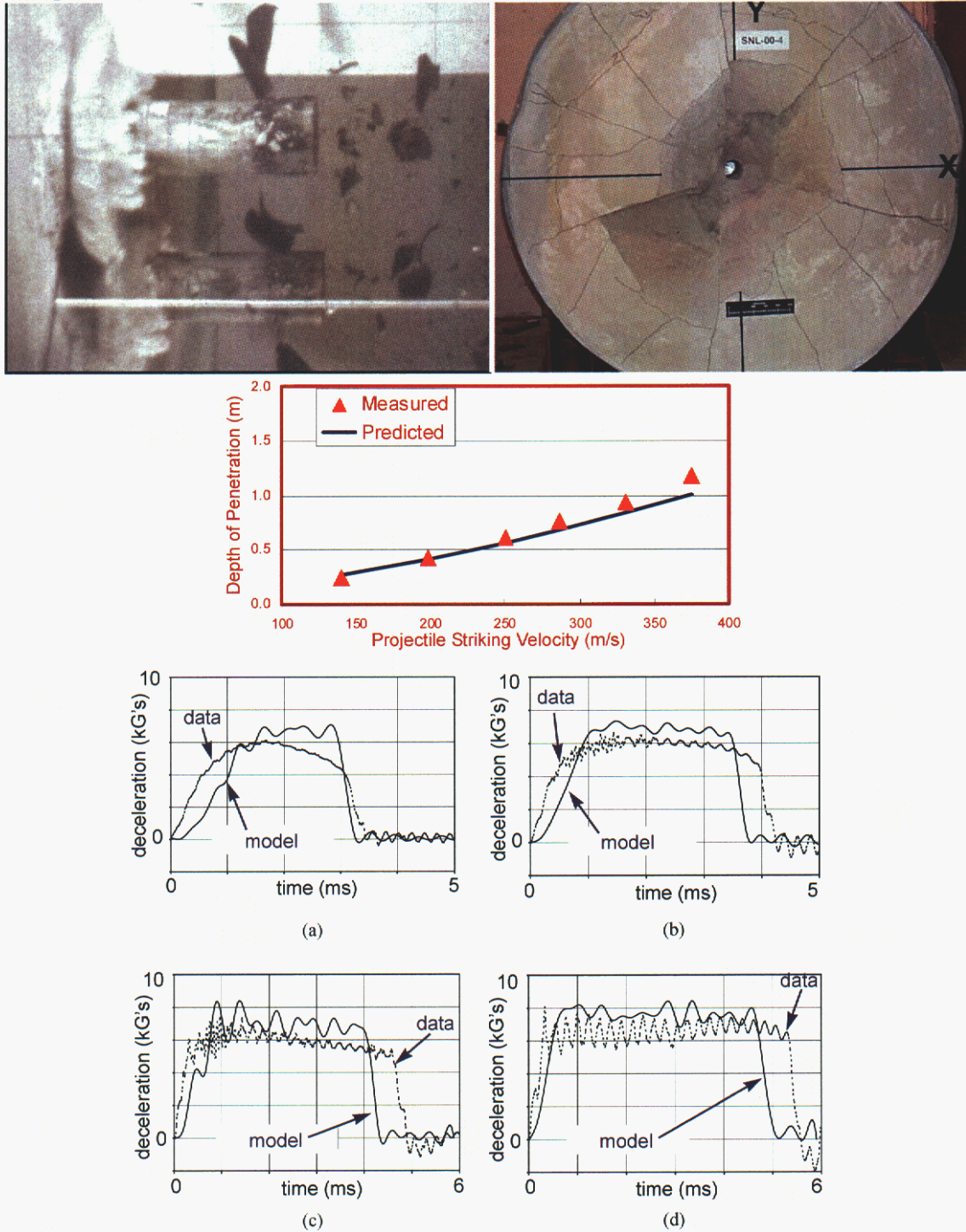


Figure 9.2. After the GeoModel was fitted to laboratory-scale material property tests, it was used to predict projectile penetration depth using spherical cavity expansion analysis.

Free field wave form for spherical shock loading

Figure 9.4 shows displacement and velocity histories for an underground test in which a wave propagates from an explosive point source. A measured velocity history at a point 204 meters from the source was used as the velocity boundary condition of the simulation. The goal was to predict a second measured velocity history at a point 470 meters from the source (see Fig. 9.3). Unlike the similar *elasticity* verification test described on page 95, this validation test used elastic-*plastic* field-scale parameters that were determined by applying the GeoModel's calibration procedures described in Appendix A (*back-fitting alteration of these independently determined calibration parameters was disallowed, as should be the case for any validation test*).

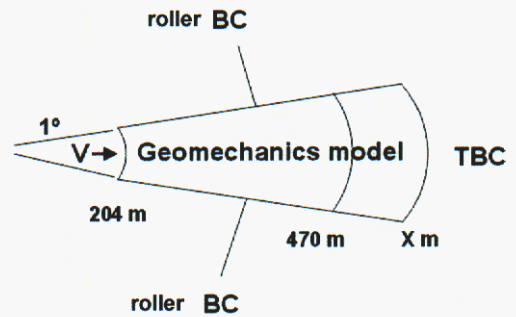


Figure 9.3. Spherical cavity geometry.

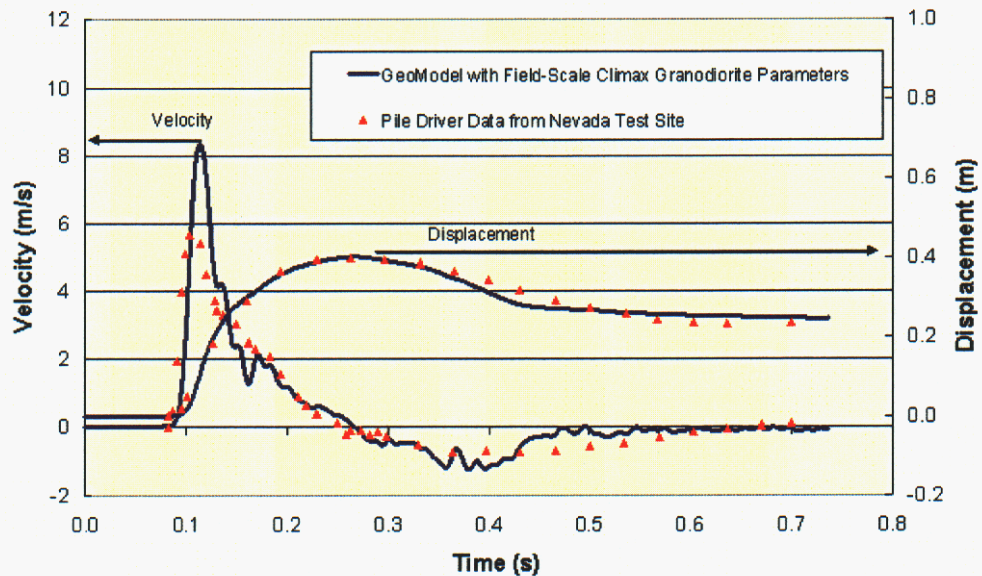


Figure 9.4. GeoModel + JAS3D finite-element prediction (blue) vs. measured (red) velocity and displacement at 470 m. from a spherical cavity velocity source at 204 meters.

The GeoModel (along with its implementation within the host finite-element code, JAS3D) comes far closer to matching data than simpler models such as non-hardening Von Mises plasticity, indicating that the GeoModel's advanced physical features (especially pressure sensitivity) are important. Because the GeoModel falls short of a *compelling* agreement with data, further study is warranted. Unlike the verification study presented on page 95, this validation simulation is over-predicting peak velocity. As was the case in the verification study, code predictions were strongly affected by artificial viscosity, suggesting that disagreement with data *might* be rooted in host code problems as much as shortcomings of the GeoModel. Of course, natural spatial variability of in-situ rock (which is neglected in the simulation) may play a role, as might the response time of gauges used to acquire the data, or myriad other possible error sources.

This concludes our overview of preliminary validation testing. More extensive model validation activities (now underway) require publication of this theory and user's guide to provide a resource document that allows analysts to apply the GeoModel properly.

10. Closing Remarks

The preceding chapters have attempted to elucidate the physical foundations and domain of applicability of Sandia's GeoModel. This model was developed in response to the need for a predictive model that could be used for a wide range of applications while maintaining numerical tractability in the context of Sandia's solid mechanics finite-element software. Three key applications for this work are in projectile penetration research, analysis of hard and deeply buried targets, and reservoir-scale modeling of formation compaction caused by pore pressure drawdown during oil or gas production. With the emergence of the capability to simulate the large-scale mechanical behavior of complex geosystems by virtue of recent advances in software and hardware, Sandia recognized the need to enhance the material modeling capabilities for geomaterials. A large-scale, long-term effort was begun that brings together activities in laboratory testing, basic research, software development, verification, validation, documentation, and quality assurance. The goal is to provide a rock mechanics predictive capability that fully accounts for the complex nature of in situ rock masses. While this is an on-going program, the GeoModel has reached a stage of maturity that warrants documentation of the effort to date. The GeoModel is a genuine unification and generalization of simpler models, and as such it is capable of satisfying the needs of almost any structural application involving geomaterials. While "first-principles" microscale theories have influenced the general model framework, physically motivated phenomenological judgements about relations between stress and strain have been given ultimate priority to more accurately match observed laboratory behavior.

In the laboratory, most rocks exhibit nonlinear elastic deformation upon unloading and re-loading, hysteresis loops, different behavior in extension than in compression, strain-rate sensitivity, pressure dependence, and post-peak softening. Moreover, high porosity rocks under compressive mean stresses and non-zero deviatoric stresses, involve a complex interplay of deformations from competing mechanisms including pore collapse and microcrack-microvoid development, which occur simultaneously allowing macroscopic pre-failure dilatation to occur even as pores continue to collapse. In addition, the strain-rate sensitivity of some porous rocks depends on the predominant deformation mechanism, e.g., the strain-rate sensitivity of shear and extensional failure is different from that of pore collapse, and the strain-rate sensitivity itself may be pressure dependent. This report summarizes the progress toward achieving a realistic rock constitutive theory that can be calibrated via standard laboratory experiments and is numerically *tractable* for massively parallel calculations using tens of millions of three-dimensional finite elements and loading conditions that involve ground shock and other non-quiescent processes. While the GeoModel has achieved many of the stated objectives, there is still much to be accomplished. Current model-enhancement activities (to be documented in future reports) include pressure dependence of the extension/compression strength ratio, softening and failure (fracture), anisotropic jointed rock behavior (as observed in situ), and natural spatial variability resulting in localization.

APPENDIX A.

Parameterizing the GeoModel

The following steps describe how to determine values for parameters used in the GeoModel. In many cases, specialized parameterization software (e.g., **HYDROFIT**, **SHEARFIT**, etc.) was used to perform nonlinear regression to determine optimized parameter values. This supplemental software, which applies nonlinear least squares fitting is available from Arlo Fossum. Alternatively, nonlinear optimization is available via the “Solver” add-in of MS Excel.

STEP 1. Use hydrostatic pressure vs. total volumetric strain data to obtain the nonlinear elastic bulk modulus parameters (b_0 , b_1 , and b_2) as well as the crush curve parameters p_0 , p_3 , p_1 , p_2 . Hydrostatic data are used to obtain the nonlinear bulk modulus parameters in Eq. (4.9),

$$K = b_0 + b_1 \exp\left(-\frac{b_2}{|I_1|}\right) \quad (\text{A.1})$$

as well as the parameters in the crush curve, Eq. (4.68),

$$p_3 - \bar{\varepsilon}_v^p = p_3 e^{-(p_1 + p_2 \bar{\xi}) \bar{\xi}}, \text{ where } \bar{\xi} = \bar{X} - \bar{p}_0 = 3(\bar{p} - \bar{P}_E) \quad (\text{A.2})$$

First express data as a column or space delimited table with the first column being total volume strain $\bar{\varepsilon}_v^{\text{tot}}$ and the next column $\bar{X} = 3\bar{p}$, where \bar{p} is the pressure (positive in compression). Determine the parameters in Eq. (A.1) using Fossum’s **HYDROFIT** program* (which assumes linear elasticity when $\bar{X} < \bar{p}_0$). The **HYDROFIT** program employs standard nonlinear regression fitting procedures [35] and includes parameter sensitivities [i.e., derivatives of Eq. (4.68) with respect to each parameter]. The input file for the **HYDROFIT** program contains one line with five values (initial guesses for the parameters p_3 , p_1 , p_2 , p_0 , b_0 in that order) and a second line that contains five integers, each having a value 1 or 0 to indicate whether that parameter is to be optimized (if not, its value is fixed). The peak inelastic volume strain, p_3 , roughly equals the initial porosity. Refer to Fig. 4.14 for guidance on how to set initial guesses for the other crush parameters. The **HYDROFIT** program outputs optimized values for p_0 , p_3 , p_1 , p_2 , b_0 , b_1 , and b_2 .

* **HYDROFIT** is available upon request. At present, this software presumes linear elasticity when $\bar{X} < \bar{p}_0$. If the data show nonlinear elasticity, as in Fig. A.1, **HYDROFIT** will provide only approximate parameter values. At present, fitting nonlinear parameters is not automated.

APPENDIX A. Parameterizing the GeoModel

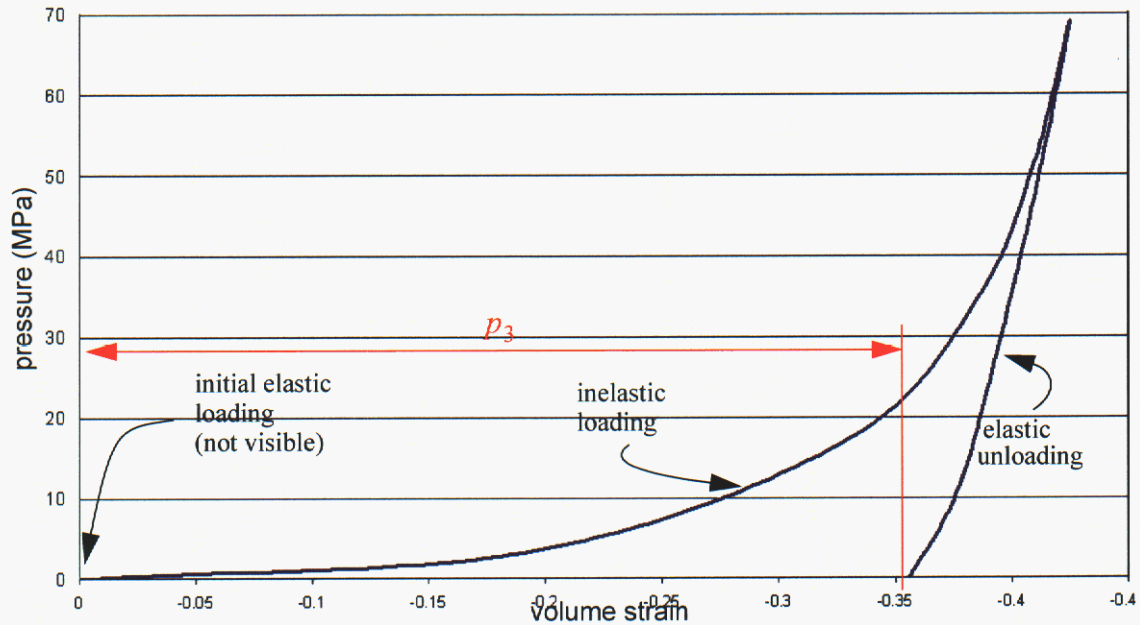


Figure A.1. *Ideal hydrostatic parameterization data.* The unloading portion is used to obtain the elastic bulk modulus parameters b_0 , b_1 , and b_2 . With these parameters, the **HYDROFIT** program converts the loading portion of the data to a crush curve (see Fig. 4.14), and employs nonlinear regression to obtain the crush parameters p_0 , p_1 , p_1 , and p_2 . For this material (a ceramic powder, zircoa), the initial elastic loading curve is so small in comparison to the scale that it is not visible.

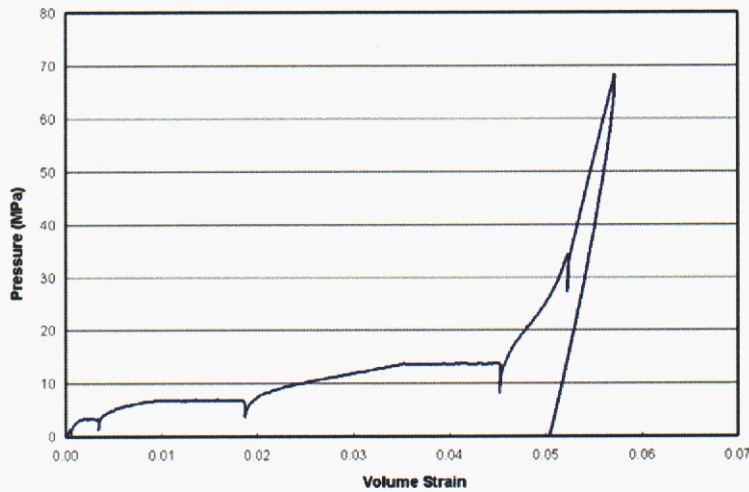


Figure A.2. *Less-preferable hydrostatic parameterization data.* Like the data for the material shown in Fig. A.1, this hydrostatic compression test (for frozen soil) was conducted nearly to full pore collapse, but the loading curve shows signs of material creep, which is not included in the GeoModel.

STEP 2. Use triaxial compression data to obtain the shear modulus

parameters g_0 , g_1 , and g_2 . This step determines the parameters in Eq. (4.10),

$$G = g_0 \left[\frac{1 - g_1 \exp(-g_2 J_2^{1/2})}{1 - g_1} \right] \quad (\text{A.3})$$

Arrange the triaxial data as a two-column table, the first column being the axial strain ε_A and the second column being the stress difference $(\sigma_A - \sigma_L)$. Then use nonlinear least squares regression analysis to obtain the shear modulus parameters g_0 , g_1 , and g_2 .

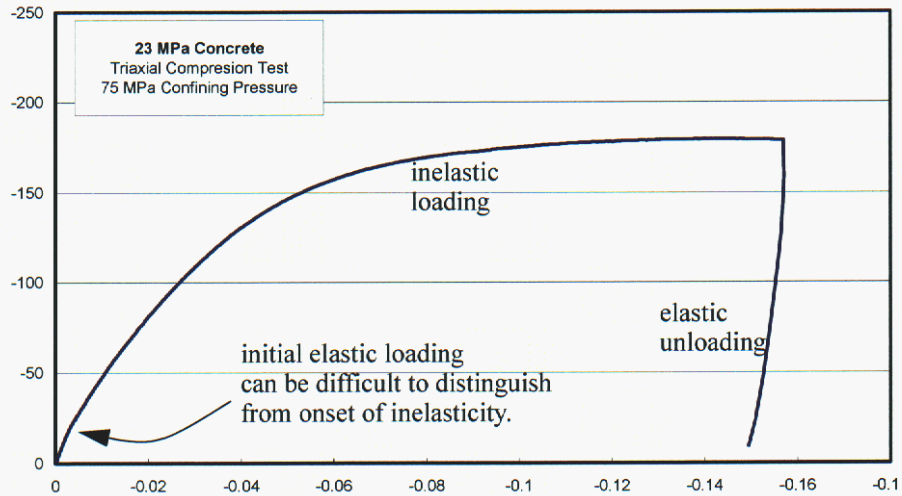


Figure A.3. Data representative of a triaxial compression parameterization test. The slope of the unloading curve is the nonlinear tangent Young's modulus. Through standard moduli conversion formulas from linear elasticity, the previously determined bulk modulus parameters are used to obtain the elastic shear modulus parameters g_0 , g_1 , and g_2 .

As illustrated in Fig. 3.3 in the main text, triaxial testing is typically performed as a two-stage process in which the material is first compressed hydrostatically to a given pressure. Then, during the second (triaxial) leg, the lateral stress is held fixed while the axial stress is varied. Only the elastic *unloading* data should be used for determining the nonlinear elastic shear modulus parameters. As explained on page 28, the plot of stress difference $(\sigma_A - \sigma_L)$ vs. axial strain ε_A will have a slope equal to Young's modulus E . Rather than directly using Young's modulus E as a user-specified material parameter, the GeoModel requires the *shear modulus* G . Recall that the nonlinear elastic bulk modulus K was found previously in step 1. The **SHEARFIT** program computes the shear modulus G from K and E by using the standard linear elasticity formula, $G = \frac{3KE}{9K - E}$, cited in Eq. (4.15). If fitting to rock

data, Poisson's ratio, $\nu = (3K - E)/(6K)$, is typically in the neighborhood of 0.2 (this is a useful “sanity” check).

STEP 3. **(optional) maintain a record of all peak stress states ever measured for every available quasistatic load-to-failure experiment ever performed for the material of interest.** The softening threshold (peak limit) envelope is the boundary of any and *all* stress states quasistatically achievable for the material, including both elastically obtainable stress states and stress states that can be reached only through inelastic deformation. Unlike a yield surface, which is the boundary of *elastically* obtainable stresses (and which therefore will, in general, evolve as the microstructure is altered in response to inelastic deformation), the limit envelope is fixed in time (see Fig. 1.1 on page 5). All achievable yield surfaces (an infinite set) are contained within the *single* limit envelope. Characterizing the limit envelope requires numerous different experiments. Typically, each *individual* experiment has precisely one stress state at which the second stress invariant J_2 achieves a peak value. If the material softens before rupturing, the value of J_2 at failure might be lower than J_2^{peak} . It is the *peak* that is of interest, not the post-softening value at failure.

For every available quasistatic load-to-failure experiment, find the stress state at which J_2 is larger than for any of the other stress states in that experiment. Construct a table of data triplets $(\bar{I}_1^{\text{@peak}}, \sqrt{J_2^{\text{peak}}}, \bar{\theta}^{\text{@peak}})$, where $\bar{I}_1^{\text{@peak}}$ and $\bar{\theta}^{\text{@peak}}$ are the values of \bar{I}_1 and $\bar{\theta}$ at the stress state for which J_2 is at its peak value. The number of entries in your peak stress table will equal the number of experiments run to failure. The goal here is to gather sufficient data to parameterize both the Lode angle function $\Gamma(\bar{\theta})$ and the shear limit envelope in Eq. (4.39),

$$F_f(I_1) = (a_1 - a_3 e^{-a_2 \bar{I}_1}) + a_4 \bar{I}_1, \text{ where } \bar{I}_1 = -I_1 \text{ (shear limit function).} \quad (\text{A.4})$$

STEP 4. Use peak stresses from a family of triaxial compression tests to determine the shear failure envelope parameters a_1 , a_2 , a_3 , and a_4 .

Recall that the F_f function represents a peak shear limit envelope in the meridional plane for which $\sqrt{J_2}$ is plotted against \bar{I}_1 for triaxial compression (TXC) stress states. Thus, the set of all stress states ever observed in TXC (Lode angle $\bar{\theta} = +30^\circ$) must fall below the curve $\sqrt{J_2} = F_f(I_1)$, modulo experimental scatter. Stated differently, this curve defines boundary of all stress states that ever have been (or ever *can* be) observed in quasistatic TXC loading. A sufficient number of TXC experiments must be conducted under various confining pressures so that the bounding surface begins to take form. On other meridional planes (i.e., at other Lode angles), the GeoModel theory presumes the bounding curve is adequately described by $\sqrt{J_2} = F_f(I_1)/\Gamma(\bar{\theta})$, which simply means that the GeoModel presumes that the limit function at *non-TXC* Lode angles is simply a scalar multiple of the TXC function. Once the F_f function has been determined in this parameterization step, the peak stress data at other Lode angles will be used later to determine the Γ proportionality function.

Using only the TXC ($\bar{\theta} = 30^\circ$) data create a scatter plot of all ever-achieved TXC values of $\sqrt{J_2}$ and \bar{I}_1 . A scatter plot of all TXC stress data measured at various confining pressures might look somewhat as sketched below:

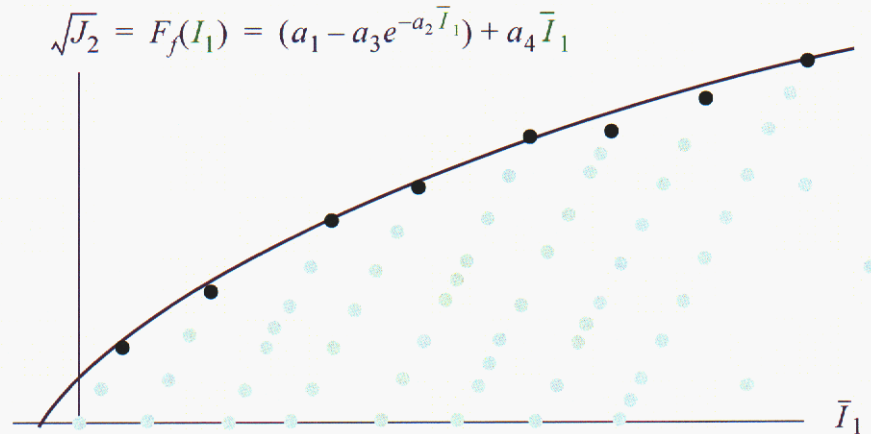


Figure A.4. A family of TXC tests conducted to failure. The boundary of data points defines the F_f function. All other (sub-peak) data points fall below this line. Plots like the are shown for various materials in Fig. 8.1.

In Fig. A.4, the *peak* data pairs (darkened dots) correspond to the $\bar{\theta}^{\text{@peak}} = 30^\circ$ values from your table of peak-stress invariants collected in STEP 3. A suite of actual TXC experiments for porcelanite is shown in Fig. A.5, along with further

illustration of how discrete peak points from these experiments are transferred to a limit surface meridional plot for fitting to Eq. (A.4)

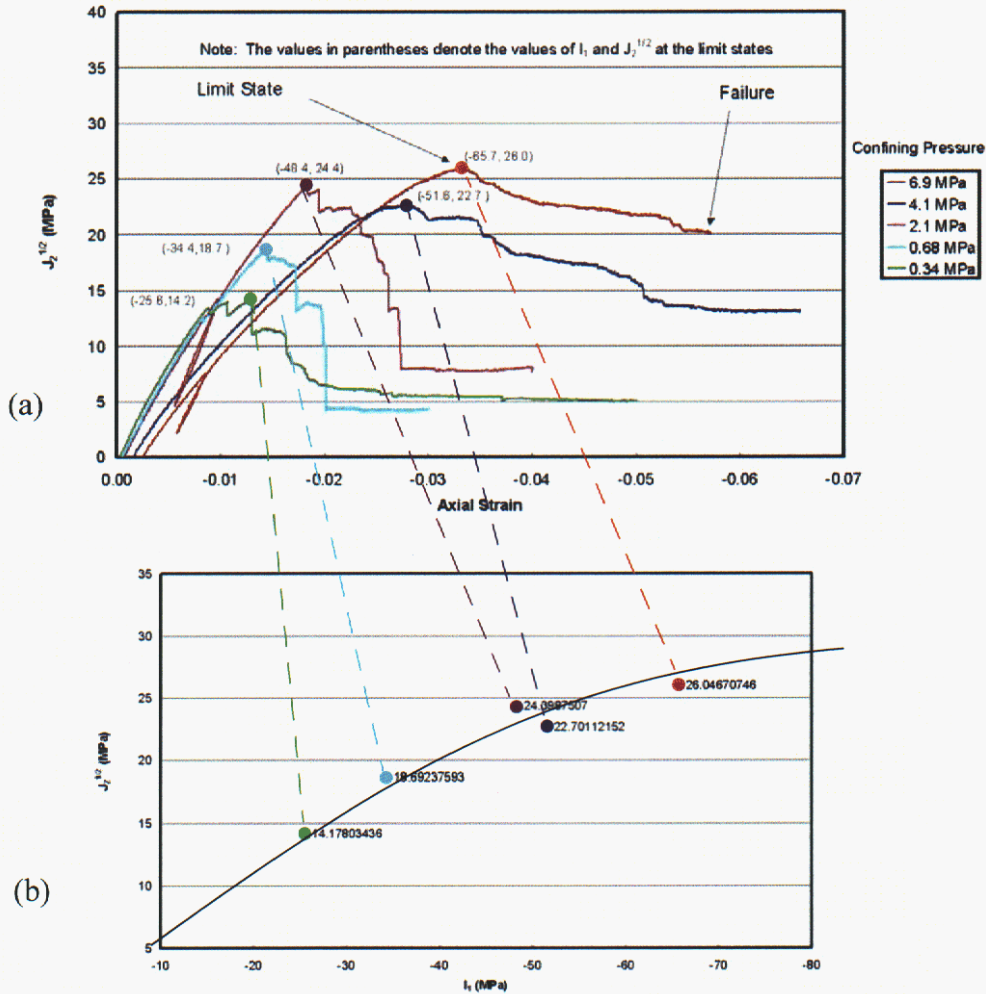


Figure A.5. TXC stress-strain plots and extraction of their peak values to construct the meridional limit curve (data are for porcelanite). (a) Each shear stress $\sqrt{J_2}$ vs. axial strain plot has exactly one peak value, as labeled. The value of I_1 at this peak is found by applying Eq. (3.28), $\bar{I}_1 = \sqrt{3}\bar{\tau} + 3\bar{\sigma}_L$ with $\bar{\tau} = \sqrt{J_2^{\text{peak}}}$ and $\bar{\sigma}_L$ equal to the lateral confining pressure for the test. (b) The peak states are transferred to a plot of $\sqrt{J_2}$ vs. \bar{I}_1 for fitting to the F_f meridional limit function.

Once enough TXC experiments have been conducted for a well-defined shear limit boundary to emerge, the next step is to determine values of a_1 , a_2 , a_3 , and a_4 that best fit the F_f function to this boundary.

Given triaxial stress difference $\bar{\sigma}_A - \bar{\sigma}_L$ vs. axial strain $\bar{\epsilon}_L$ data, Eqs. (3.28) and (3.29) show that value of J_2 at peak is given by $\sqrt{J_2^{\text{peak}}} = |\bar{\sigma}_A - \bar{\sigma}_L|^{\text{peak}} / \sqrt{3}$ and the value of I_1 (i.e., the trace of the stress) at peak equals $I_1^{\text{@peak}} = 3\bar{\sigma}_L + (\bar{\sigma}_A - \bar{\sigma}_L)^{\text{peak}}$, where $\bar{\sigma}_L$ is the (constant) lateral confining pressure. The $(\bar{I}_1^{\text{@peak}}, \sqrt{J_2^{\text{peak}}})$ data pairs from TXC experiments (i.e., those for which $\bar{\theta}^{\text{@peak}} = +30^\circ$) may be fed into a nonlinear regression parameterization program, **SHEARFIT** (available upon request) to

optimize the parameters in Eq. (A.4). To use this program, create an input file containing, in the first line, your initial guesses for a_1, a_2, a_3, a_4 and, in the second line, four logical integers (0 or 1) to indicate whether or not to optimize on the corresponding parameter. Refer to Fig. 4.1(a) to help decide appropriate initial guesses. If the data suggest a linear envelope at high pressures, then your first guess for a_4 should be an approximation of the slope of this envelope. If in doubt, take $a_4 = 0.0$ (i.e., assume the data asymptote to a constant value as pressure goes to infinity). Eyeball the data to set your first guess for a_1 equal to the zero-pressure value of the linear asymptote line (extrapolate visually if necessary), set a_3 to equal a_1 minus your best estimate for the *actual* ordinate intercept of the low-pressure data (again, extrapolate if necessary). Finally, set a_2 to equal an estimate for the initial (low-pressure) slope of the data divided by a_3 . Using these initial guesses, the **SHEARFIT** program applies nonlinear regression and outputs values for the a_1, a_2, a_3 , and a_4 parameters.

BEWARE: In typical TXC experiments, all principal stresses are compressive, making it is possible that **SHEARFIT** will return a meridional fit to the *available* data that corresponds to a shear limit envelope that does *not* corral the origin (implying *nonphysically* that zero stress is “unachievable”). If this occurs, you might want to append your table of observed $(\bar{I}_1^{\text{@peak}}, \sqrt{J_2^{\text{peak}}})$ data with an entry $(-I_1^{\text{limit}}, 0)$, where I_1^{limit} is your best estimate for the theoretical hydrostatic *tensile* strength of the material (therefore $-I_1^{\text{limit}}$ is a *negative* number). Include this entry multiple times if necessary to force it to have greater weight in the nonlinear regression (or, preferably, perform more experiments to obtain a larger number of *real* data points at low values of I_1).

STEP 5. Use peak stresses from a family of triaxial extension tests to determine the extension to compression ratio ψ . As was done above for TXC tests, construct a table of $(\bar{I}_1^{\text{peak}}, \sqrt{J_2^{\text{peak}}})$ data pairs corresponding to peak attained stresses in triaxial *extension* (TXE). These are the data pairs in your peak data table from STEP 3 that correspond to $\bar{\theta}^{\text{@peak}} = -30^\circ$. For each of these TXE data pairs, compute

$$\psi = \frac{\sqrt{J_2^{\text{peak in TXE}}}}{F_f(\bar{I}_1^{\text{@ peak in TXE}})} \quad (\text{A.5})$$

where F_f is the TXC shear limit function parameterized in the previous step. Of course, each TXE experiment is likely to result in slightly different values for ψ . At present, the GeoModel presumes that the TXE/TXC ratio ψ is constant.

APPENDIX A. Parameterizing the GeoModel

Therefore, set the GeoModel parameter ψ equal to the average of each ψ computed using Eq. (A.5) for each available TXE experiment.

It is possible that the data might imply that the strength ratio ψ must vary with pressure, but the GeoModel presently assumes that ψ is the same at *all pressures*. Thus, until the GeoModel is enhanced to support pressure-varying strength ratios, modeling errors must be managed by measuring the parameter ψ at a confining pressures in the neighborhood where the GeoModel is likely to be applied. Similar statements can be made regarding any and all parameters used to define the GeoModel yield function.

Sometimes, it might be *impractical* — or overly expensive — to obtain TXE data. In this case, an engineering approach for *estimating* ψ presumes that it obeys the same coupling to the meridional profile slope as predicted in classical Mohr-Coulomb theory. Using Eq. (A.4) to set the TXC slope in Eq. B.19 in Appendix B, an estimate for the pressure-varying strength ratio is

$$\psi = \frac{1}{1 + \sqrt{3}[a_4 + a_2 a_3 e^{-a_2 \bar{I}_1}]} \quad (\text{A.6})$$

In the future, we hope to thoroughly explore the merits of this formula, which correlates the strength ratio with the TXC meridional slope. At present, the GeoModel presumes the strength ratio is constant. If, however, the above correlation formula can be substantiated, then we will likely incorporate it into future releases, thereby possibly eliminating the need for a user-specified ψ altogether. Until then, you may evaluate the above formula at a value of \bar{I}_1 in the neighborhood where you plan to apply the GeoModel to obtain a reasonable estimate for ψ .

STEP 6. **Determine the appropriate Lode function option** `J3TYPE`. Recall that the GeoModel's function $\Gamma(\bar{\theta})$ defines the *shape* of the octahedral profile shape for Lode angles spanning the range from TXE ($\bar{\theta} = -30^\circ$) to TXC ($\bar{\theta} = +30^\circ$). The GeoModel parameter `J3TYPE` (see page 45) dictates the functional form to be used for the Γ function. Non-triaxial data are difficult to acquire. If no such data are available, you will need to use engineering judgement as to an appropriate choice for `J3TYPE`. This parameterization step aims to guide the choice in the happy circumstance that non-triaxial data *are* available.

As illustrated in Fig. 4.10, the GeoModel's Γ function is defined to equal 1 in TXC and $1/\psi$ in TXE. Large values of Γ correspond to small shear strengths. In this model parameterization step, all available peak-state data obtained in *non-triaxial* loading paths are considered to help decide an appropriate choice for the `J3TYPE` option. Looping over your table (collected in STEP 3) of "all-observed" peak stress invariant triplets $(\bar{I}_1^{\text{peak}}, \sqrt{J_2^{\text{peak}}}, \bar{\theta}^{\text{peak}})$, especially those at non-triaxial states, create a new two-column table of $(\bar{\theta}, \Gamma)$ data pairs, where

$$\Gamma = \frac{F_f(\bar{I}_1^{\text{@peak}})}{\sqrt{J_2^{\text{peak}}}} \quad (\text{A.7})$$

By comparing a scatter plot of these $(\bar{\theta}, \Gamma)$ data to the graphs in Fig. 4.10, an appropriate choice for `J3TYPE` should be more clear. To assist in the decision, it might be easier to instead scale the ordinate as shown in Fig. A.6. By overlaying data with the family of plots in Fig. A.6 an appropriate choice for `J3TYPE` should be apparent, as illustrated in Fig. A.7. If non-triaxial data are unavailable (a common problem), select `J3TYPE=1` if the material is judged to be moderately ductile; otherwise, select `J3TYPE=3`.

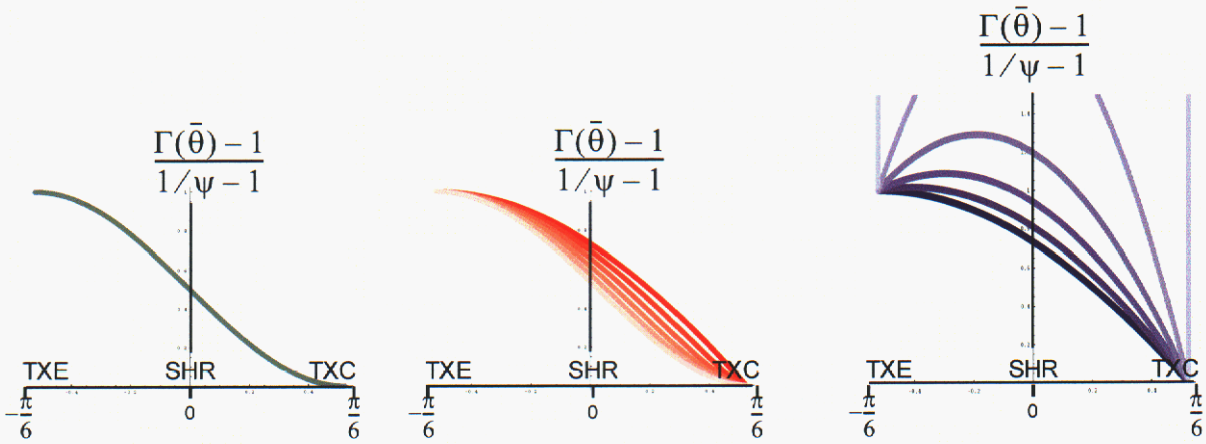


Figure A.6. The Lode function information originally shown in Fig. 4.10 of the main report, now displayed with a transformed ordinate. Knowing that $\Gamma = 1/\psi$ in TXE and $\Gamma = 1$ in TXC, it makes sense to scale the ordinate as shown so that, regardless of the value of ψ , the scaled ordinate equals 1 in TXE and 0 in TXC. With this scaling, all Gudehus Lode functions overlap; the others vary with ψ .

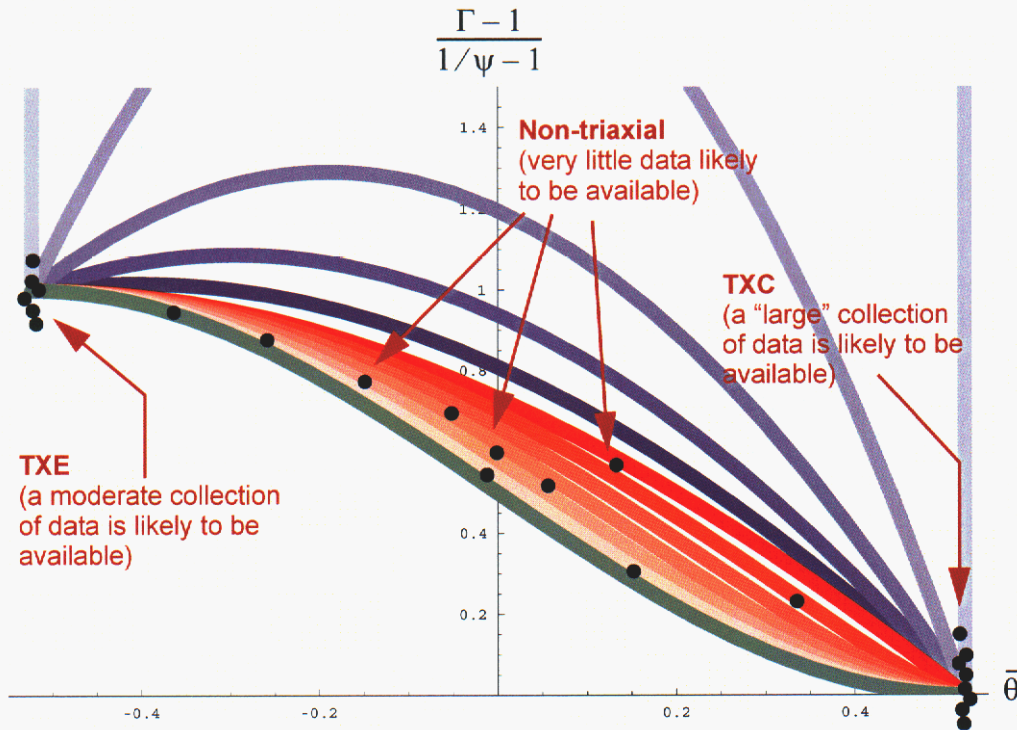


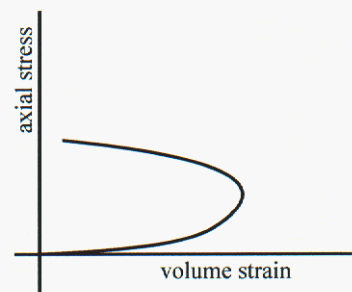
Figure A.7. A sketch of how data might be distributed at non-triaxial states. In this contrived example, most of the data at non-triaxial states falls in the red Willam-Warnke region and therefore `J3TYPE=2` would be appropriate for this material. In practice, data at non-triaxial Lode angles are rarely available. In this case, the user must resort to engineering judgement to decide which `J3TYPE` option to select.

STEP 7. Hardening parameters. In the previous steps, we determined the GeoModel parameters that define the outer limit surface. No stress state outside this fixed (non-evolving) limit surface can be achieved through *any* load path. Consequently, the infinite set of all possible *yield* surfaces must be contained within this limit envelope. Unlike the limit surface, which bounds *all* possible stress states, the yield surface merely bounds the set of *elastically* obtainable stress states. Unlike the limit surface, a yield surface evolves (hardens) through time as a result of microstructural changes induced in the material under inelastic loading. The *initial* yield surface is typically much smaller than the limit surface (see Fig. 1.1 in the main text). Isotropic hardening permits the initial yield surface to expand on octahedral planes (by amounts that vary with pressure) up until the limit surface is reached. Kinematic hardening permits the yield surface to translate in stress space until the limit surface is reached. Both types of hardening may occur simultaneously.

As a rule, the amount of kinematic hardening relative to total stress is high at lower pressures. Therefore, kinematic hardening data are best inferred from unconfined compression tests. In the previous parameterization steps, we determined crush parameter values (p_0, p_1, p_2), elastic parameters ($b_0, b_1, b_2, g_0, g_1, g_2$), the limit surface parameters (a_1, a_2, a_3, a_4, ψ), and `J3TYPE`. Now these values should be used in a finite-element (or single cell driver) implementation of the GeoModel, to obtain a simulated table of axial stress vs. volume strain to compare with available experimental data. The goal is to determine values for the *as-yet-unknown* GeoModel parameters through a systematic simulation sequence. As a first guess, set the “yet-to-be-determined” GeoModel parameters as follows:

- offset `RN=N=0` (i.e. suppress hardening)
- kinematic hardening parameter `HC=1e5`
- shape parameter `CR=R=10`
- plastic potential function parameters for non-associativity `A2PF==A2`, `A4PF==A4`, `RKPF=RK`, `CRPF=CR` (i.e., tentatively assume associativity)
- joint spacing `RJS=s=0.0`
- rate sensitivity parameters `τ1` through `τ7 =0.0` (no rate sensitivity).

Run the finite-element code for unconfined compression and output axial stress vs. volumetric strain (`EVOL`). It is unlikely that this result will replicate observed unconfined compression data on the first try. We ultimately hope to assign values to the above parameters so that the volume strain will “turn around” as Fig. 8.6(b) (even though axial strain increases monotonically, the *volume* strain turns around because of the lateral bulking strains).



APPENDIX A. Parameterizing the GeoModel

The phenomenological fitting functions employed in the GeoModel are designed to extrapolate reasonably well into regions where data are not available, but these functions are also selected in part for computational tractability and they therefore serve only as approximations. Consequently, there will certainly be modeling error. Ideally, one should use regression fitting procedures to select GeoModel hardening parameters that minimize modeling error relative to available data. We have already described the programs “HYDROFIT” for regression optimization of the elastic parameters and SHEARFIT for finding the limit surface parameters, but no similar fitting software has yet been developed to determine the hardening parameters. Consequently, for these parameters, a more traditional exploratory manual search method must be used as described below.

In the following, we will be exploring adjustments of CR, RN, and HC to try to achieve a strain “turn around” at the correct (observed) strain and stress.

If no turn around is apparent in your simulation, try decreasing CR. Continue to decrease CR until turn around occurs. If you get no turn around, bring down the initial yield surface. The intercept on the ordinate on the meridional profile is located at $\sqrt{J_2} = a_1 - a_3$. Try increasing N to a value no larger than $a_1 - a_3$ (our initial guess of $N = 0$ presumed that the initial yield surface coincided with the shear limit surface. By setting N to a nonzero value, we are now permitting kinematic hardening). You will likely see “turn around” start to occur.

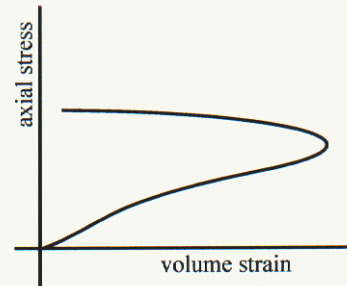
Next try changing HC. Increasing (say, doubling) HC will increase the strain value at which turn-around occurs. Lowering HC lowers the turn-around strain. If you continue to have trouble getting turn around, double check that you have correctly entered the previously determined (*known*) parameter values.

If the turn around stress is too high, try lowering HC.

Once shear-induced dilatation (turn-around) has been adequately modeled for unconfined TXC, go then to high-confinement data. Try changing CR (e.g., from 7 to 10 if computed peak strain is too large).

Go back to unconfined, and work on HC and RN.

Continue to go back and forth until you are satisfied with both confined and unconfined results.



This concludes our guidance for parameterizing new materials to the GeoModel. Further revisions of this manual will likely include additional tips and parameterization experiment suggestions.

APPENDIX B. Nomenclature and Data Sets

This appendix contains three tables defining (1) model parameters, (2) plotable variables, and (3) other symbols or acronyms used internally within this manual. In each table, the first column shows the typeset symbol for the variable. The next column contains the ASCII string used for the variable in code input files and/or within the source code. In the SI units column, a “1” indicates that the variable is dimensionless. A “–” indicates that dimensions vary, while N/A means dimensions are not applicable. The defining equation (or page number) in the last column of the tables cites the location in this report where the quantity is defined or discussed.

Reminder: in mechanics, stress and strain are typically taken positive in tension. However, in applications, they are taken positive in compression. To manage this potentially confusing conflict of conventions, recall

$$\bar{x} \equiv -x$$

DEFINITION OF THE “OVER-BAR”

(B.1)

For example, I_1 denotes the trace of stress (positive in compression). Therefore, $\bar{I}_1 \equiv -I_1$ is positive in compression.

Model Parameters (User Input)

Symbol or Acronym	ASCII Name	Name and meaning	SI units	defining equation
b_0	PROP (1) (B0)	Initial elastic bulk modulus (for intact material if modeling joints). The tangent bulk modulus is given by $K = b_0 + b_1 \exp\left(-\frac{b_2}{ I_1 }\right)$	Pa	Eq. 4.9 Eq. A.1
b_1	PROP (2) (B1)	High pressure coefficient in nonlinear elastic (intact) bulk modulus function (see above formula). For linear elasticity, set $b_1=0$. For nonlinear elasticity, set b_1 so that the Bulk modulus K will asymptote to a value $b_0 + b_1$ at high pressures.	Pa	Eq. 4.9 Eq. A.1
b_2	PROP (3) (B2)	Curvature parameter in nonlinear elastic (intact) bulk modulus function (see above formula). For linear elasticity, set $b_2 = 0$. For nonlinear elasticity, set b_2 to a small value to transition rapidly from the low pressure bulk modulus to the high pressure modulus. Larger values of b_2 will result in a broader transition range.	Pa	Eq. 4.9 Eq. A.1
b_3	PROP (4) (B3)	Coefficient in nonlinear elastic bulk modulus to allow for plasticity-induced changes in the elastic properties. To neglect this effect, set $b_3 = 0$. When this parameter is nonzero, the elastic tangent bulk modulus is computed by $K = f_K \left\{ \left[b_0 + b_1 \exp\left(-\frac{b_2}{ I_1 }\right) \right] - b_3 \text{Exp}\left(-\frac{b_4}{ \varepsilon_V^p }\right) \right\}$	Pa	Eq. 4.33
b_4	PROP (5) (B4)	Power in nonlinear elastic bulk modulus to allow for plasticity-induced changes in the elastic properties. To neglect this effect, set $b_4 = 0$. Otherwise, see above formula.	1	Eq. 4.33
g_0	PROP (6) (G0)	Initial elastic shear modulus (for intact material if modeling joints). The tangent shear modulus is computed by $G = g_0 \left[\frac{1 - g_1 \exp(-g_2 J_2^{1/2})}{1 - g_1} \right]$	Pa	Eq. 4.10 Eq. A.3
g_1	PROP (7) (G1)	Parameter used to define the elastic (intact) shear modulus at large shears (see above formula). Specifically, the shear modulus will asymptote to a value $g_0/(1-g_1)$ as shear stress increases. Must be less than 1.0 . For linear elasticity, set $g_1 = 0$. For the shear modulus to decrease with shearing, set $0 < g_1 < 1$. For the shear modulus to <i>increase</i> with shearing, set $g_1 < 0$.	1	Eq. 4.10 Eq. A.3

Symbol or Acronym	ASCII Name	Name and meaning	SI units	defining equation
g_2	PROP (8) (G2)	Curvature parameter in nonlinear elastic (intact) shear modulus function (see above formula). For linear elasticity, set $g_2 = 0$. For nonlinear elasticity small values of g_2 cause the shear modulus to transition <i>rapidly</i> from its initial value g_0 to its high shear value $g_0/(1-g_1)$. Larger values of g_2 make this transition more gradual.	1/Pa	Eq. 4.10 Eq. A.3
g_3	PROP (9) (G3)	Coefficient in nonlinear elastic shear modulus to allow for plasticity-induced changes in the elastic properties. To neglect this effect, set $g_3 = 0$. When nonzero, the tangent shear modulus is computed by $G = f_G \left\{ g_0 \left[\frac{1 - g_1 \exp(-g_2 J_2^{1/2})}{1 - g_1} \right] - g_3 \text{Exp} \left(-\frac{g_4}{\gamma_{\text{equiv}}^p} \right) \right\}$	Pa	Eq. 4.34
g_4	PROP (10) (G4)	Power in nonlinear elastic shear modulus to allow for plasticity-induced changes in the elastic properties. To neglect this effect, set $g_4 = 0$. Otherwise, see above formula.	1	Eq. 4.34
	PROP (11) (RJS)	Joint spacing. Set this parameter to zero if the material has no geological (or rock-like) faults.	meter	
	PROP (12) (RKS)	Joint shear stiffness. Set this parameter to zero if the material has no geological (or rock-like) faults.	Pa	
	PROP (13) (RKN)	Joint normal stiffness. Set this parameter to zero if the material has no geological (or rock-like) faults.	Pa	
a_1	PROP (14) (A1)	Constant term in the fitting function for the meridional profile, $F_f(I_1) = a_1 - a_3 e^{-a_2 \bar{T}_1} + a_4 \bar{T}_1$, for the ultimate shear limit surface. Here, $\bar{T}_1 = -\text{tr} \mathbf{g}$ and therefore \bar{T}_1 is three times the pressure. At zero pressure, $F_f(I_1) = a_1 - a_3$ while at high pressure (large \bar{T}_1), $F_f(I_1) \sim a_1 + a_4 \bar{T}_1$. Thus, a_1 is the vertical intercept of the linear <i>asymptote</i> , whereas $a_1 - a_3$ is the vertical intercept of the limit function <i>itself</i> . These are parameters define the ultimate limit curve, at which the maximum possible hardening has occurred and softening is imminent. The initial onset of yield is described by $f_f(I_1) = F_f(I_1) - N$. Thus if fitting to data for yield onset, recognize that the constant term will be lower than a_1 by an amount N.	Pa	Eq. 4.39 Fig. A.4

APPENDIX B. Nomenclature and Data Sets

Symbol or Acronym	ASCII Name	Name and meaning	SI units	defining equation
a_2	PROP (15) (A2)	Curvature decay parameter in the fitting function for the meridional profile, $F_f(I_1) = (a_1 - a_3 e^{-a_2 \bar{I}_1}) + a_4 \bar{I}_1$. Keep in mind that $\bar{I}_1 = -3\bar{p}$, where \bar{p} is pressure. Set $a_2 = 0$ for a linear meridional profile as in Mohr-Coulomb theory. Assign a_2 a large value to quickly asymptote to the high-pressure profile slope.	1/Pa	Eq. 4.39 Fig. A.4
a_3	PROP (16) (A3)	Parameter in the shear limit meridional fit function, $F_f(I_1) = (a_1 - a_3 e^{-a_2 \bar{I}_1}) + a_4 \bar{I}_1$.	Pa ²	Eq. 4.39 Fig. A.4
a_4	PROP (17) (A4)	High-pressure meridional slope parameter in the fit function, $F_f(I_1) = (a_1 - a_3 e^{-a_2 \bar{I}_1}) + a_4 \bar{I}_1$.	1	Eq. 4.39 Fig. A.4
p_0	PROP (18) (P0)	Value of I_1 at the onset of pore collapse for hydrostatic compression of virgin material. This parameter will be negative because I_1 is negative in compression. In the lexicon of traditional p - α crush models, this variable would equal $-3P_E$, where P_E is the elastic limit pressure in hydrostatic compression. In many other publications about the GeoModel, this parameter is denoted X_o.	Pa	Eq. 4.67 Fig. 4.1 4 Eq. A.2
p_1	PROP (19) (P1)	One third of the slope of a porosity vs. pressure crush curve at the elastic limit. In many other publications about the GeoModel, this parameter is denoted D_1.	1/Pa	Eq. 4.67 Fig. 4.14 Eq. A.2
p_2	PROP (20) (P2)	Extra fitting parameter for hydrostatic crush curve data, used when the crush curve has an inflection point. In many other publications about the GeoModel, this parameter is denoted D_2.	1/Pa ²	Eq. 4.67 Fig. 4.14 Eq. A.2
p_3	PROP (21) (P3)	Asymptote (limit) value of the absolute value of the plastic volume strain. This parameter is approximately equal to the initial porosity in the material and may be inferred from hydrostatic crush data. In many other publications about the GeoModel, this parameter is denoted W.	1	Eq. 4.67 Fig. 4.14 Eq. A.2

Symbol or Acronym	ASCII Name	Name and meaning	SI units	defining equation
R	PROP (22) (CR)	Shape parameter that allows porosity to affect shear strength. R equals the eccentricity (width divided by height) of the elliptical cap function, so it is the ratio a/b (not A/B) in Fig. 4.15. This parameter affects the stress level at which dilatation will occur in triaxial compression. If dilatation is occurring too soon, increase the value of R . Decreasing R will decrease the influence of porosity on shear strength and therefore enhance the effect of void space creation associated with crack growth. To replicate older classical pore collapse models (which initiate pore collapse only at a critical pressure, regardless of the level of shear stress), set R to a very small number.	1	Fig. 4.15 Eq. 4.69 pg. A-11
ψ	PROP (23) (RK)	TXE/TXC (triaxial extension to compression) strength ratio. Convexity of the yield surface requires that $1/2 \leq \psi \leq 2$ (or $7/9 \leq \psi \leq 9/7$ if using $\text{J3TYP}=\text{E}=1$). Real materials generally satisfy $1/2 \leq \psi \leq 1$. Future releases of the GeoModel will likely allow ψ to be pressure-dependent.	1	page 45 Fig. 4.4 Eq. A.5
N	PROP (24) (RN)	Off-set parameter. Must be non-negative. Set $N = 0$ to suppress kinematic hardening. For problems with kinematic hardening, the backstress invariant $\sqrt{J_2^g}$ will not be permitted to grow any larger than N . The initial yield surface is defined by $F_f^{\text{initial}}(I_1, N) = F_f(I_1) - N$, where F_f describes the shear limit surface (softening threshold). Roughly speaking, the shear strength can increase by an amount N before softening will commence.	1	Fig. 4.6 Eq. 4.40 page 59 pg. A-11
H	PROP (25) (HC)	Kinematic hardening parameter. Set $H = 0$ and $N = 0$ to suppress kinematic hardening. Otherwise, this parameter affects how “quickly” the yield surface evolves toward the ultimate shear failure surface.	Pa	Eq. 4.76 pg. A-11
I_1^{cut}	PROP (26) (CTI1)	Tensile cut-off in allowable value of the first stress invariant I_1 . Value must be positive. If the first invariant (which is proportional to the negative of pressure) reaches this cut-off value, the isotropic part of the stress is replaced with this value. This parameter is available only temporarily to permit reasonable strength predictions in tension. Current enhancements of this model are focused on more physically rigorous tensile failure modeling. In principle, the yield function should limit achievable values of I_1 . This option is available if the yield function is not cutting off strength at a tensile pressure low enough for the application at hand.	Pa	

APPENDIX B. Nomenclature and Data Sets

Symbol or Acronym	ASCII Name	Name and meaning	SI units	defining equation
—	PROP (27) (CTPS)	Principal stress tensile cut-off. If a predicted principal stress is found to exceed this value, then it is replaced with this value. See discussion regarding the state variable “CRACK” in the next table.	Pa	
T_1	PROP (28) (T1)	Primary rate dependence parameter. To specify a <i>constant</i> intrinsic material response time, set this user input equal to the characteristic response time. Use the other “T” parameters to enable dependence on strain rate and pressure.	sec	Eq. 5.22
T_2	PROP (29) (T2)	Rate dependence parameter. See main text.	1/s	Eq. 5.22
T_3	PROP (30) (T3)	No longer used. Set to zero.	1	Eq. 5.22
T_4	PROP (31) (T4)	No longer used. Set to zero.	1/s	Eq. 5.22
T_5	PROP (32) (T5)	Rate dependence parameter. See main text.	Pa	Eq. 5.22
T_6	PROP (33) (T6)	Rate dependence parameter. See main text.	sec	Eq. 5.22
T_7	PROP (34) (T7)	Rate dependence parameter. See main text.	1/Pa	Eq. 5.22
—	PROP (35) (J3TYPE)	Integer-valued control parameter for specifying the desired type of 3 rd -invariant yield surface: 1 - Gudehaus 2 - Willam-Warnke 3 - Mohr-Coulomb	1	page 45 Fig. A.7
a_2^{PF}	PROP (36) (A2PF)	Potential function parameter (=A2 for associative). Assign this parameter in the same way you would assign a value to a_2 , except that this parameter is used to generate the flow potential surface (i.e., the plastic strain rate will be normal to the flow potential surface). Be sure to set a_2^{PF} equal to a_2 if plastic normality is desired.	1/Pa	page 48
a_4^{PF}	PROP (37) (A4PF)	Potential function parameter (=A4 for associative). Assign this parameter in a manner similar to a_4 except that this parameter will be used to generate the flow potential. Be sure to set a_4^{PF} equal to a_4 if plastic normality is desired.	1	page 48
R^{PF}	PROP (38) (CRPF)	Potential function parameter (=CR for associative). Flow potential analog of the yield surface parameter R . Be sure to set R^{PF} equal to R if plastic normality is desired.	1	page 48

Symbol or Acronym	ASCII Name	Name and meaning	SI units	defining equation
ψ^{PF}	PROP (39) (RKPF)	Potential function parameter (=RK for associative). Flow potential analog of the yield surface parameter ψ . Be sure to set ψ^{PF} equal to ψ if plastic normality is desired.	1	page 48
—	PROP (40) (SUBX)	Subcycle control parameter. If zero, the GeoModel will select an appropriate subcycle step size. If SUBX is non-zero, then the GeoModel's default subcycle increment will be multiplied by 10^{**SUBX} (ten raised to the power). If, for example, you want the code to decrease its subcycle size by a factor of 10, then set SUBX=-1. If you want the subcycle size altered by a factor "x", then set SUBX to the base ten log of "x" [$\log_{10}x = (\ln x)/(\ln 10)$].	1	—

Internal State Variables (Plotable Output)

Symbol or Acronym	ASCII Name	Name and meaning	SI units	defining equation (or page)
κ	SV (1) [KAPPA] ELN EL	The value of I_1 at which the meridional yield profile first branches away from the crack failure surface and begins to morph into the cap function associated with porosity. Recalling that $\kappa = -\bar{\kappa}$, the internal state variable κ typically will be negative. As a rule of thumb: increasing the user-input parameter R will increase κ (and therefore decrease $\bar{\kappa}$). Recalling Fig. 4.15, κ is <i>not</i> the point at which the meridional profile has a zero slope — it is the <i>branching</i> location. The zero slope point is reached at a higher pressure. Isotropic hardening is controlled by the evolution of κ . In the GeoModel physics source code, κ is denoted by <code>ELN</code> or by <code>EL</code> in the subcycling.	Pa	Fig. 4.5 Eq. 4.30 Fig. 4.15 Eq. 4.70
—	SV (2) [INDEX]	Indicator for isotropic plastic hardening. This flag will equal zero up until the first time isotropic hardening (i.e., evolution of the κ state variable) occurs. Thereafter, this flag will equal 1.0 <i>even if the stress later becomes elastic</i> .	1	page 77
$\dot{\varepsilon}^{\text{equiv}}$	SV (3) [EQDOT]	L_2 (Frobenius) norm of input strain rate tensor. $\dot{\varepsilon}^{\text{equiv}} = \sqrt{\dot{\varepsilon}_{ij}\dot{\varepsilon}_{ij}}$	1/s	page 77
I_1	SV (4) [I1]	First stress invariant (positive in tension).	Pa	Eq. 3.9 page 77
$\sqrt{J_2}$	SV (5) [ROOTJ2]	Square root of the second stress invariant $\sqrt{J_2}$ (always positive). This the equivalent shear stress in the material.	Pa	Eq. 3.10 Eq. 3.13 page 77
α_{11}	SV (6) [ALXX]	11 component of the backstress	Pa	page 58
α_{22}	SV (7) [ALYY]	22 component of the backstress	Pa	page 58
α_{33}	SV (8) [ALZZ]	33 component of the backstress	Pa	page 58
α_{12}	SV (9) [ALXY]	12 component of the backstress (= 21 component)	Pa	page 58
α_{23}	SV (10) [ALYZ]	23 component of the backstress (= 32 component)	Pa	page 58
α_{31}	SV (11) [ALXZ]	31 component of the backstress (= 13 component)	Pa	page 58

Symbol or Acronym	ASCH Name	Name and meaning	SI units	defining equation (or page)
G^α	SV(12) [GFUN]	Kinematic hardening decay function, equal to 1.0 initially and then decays down to 0.0 as the max allowable kinematic hardening (determined by the shift parameter N) is approached.	1	Eq. 4.79 page 58
γ_{equiv}^p	SV(13) EQP [EQPFS]	Equivalent uniaxial plastic shear strain (conjugate to $\sqrt{J_2}$). Specifically, $\gamma_{\text{equiv}}^p = \int \sqrt{2} \left\ \dot{\underline{\gamma}}^p \right\ dt$, where $\dot{\underline{\gamma}}^p$ is the deviatoric part of the plastic strain rate $\dot{\underline{\epsilon}}^p$.	1	Eq. 4.35
ϵ_v^p	SV(14) [EQPV]	Equivalent plastic volume strain: $\epsilon_v^p = \int \text{tr} \dot{\underline{\epsilon}}^p dt$.	1	page 77
κ_0	SV(15) [EL0]	Calculated initial value for κ (the cap branch value of I_1). This is not really an internal state variable. Its value will remain constant throughout the calculation. Keep in mind: $\bar{\kappa}$ is typically positive and therefore $\kappa \equiv -\bar{\kappa}$ is typically negative.	Pa	Fig. 4.15
h_κ	SV(16) [HK]	(Isotropic hardening parameter) Proportionality factor appearing in the relationship $\dot{\kappa} = \dot{\lambda} h_\kappa$.	Pa ²	Eq. 4.73
ϵ_v^{tot}	SV(17) [EVOL]	Total volume strain, $\int \text{tr} \dot{\underline{\epsilon}} dt$.	1	page 77
$\sqrt{J_2^\alpha}$	SV(18) [BACKRN]	Square root of the second backstress invariant. This is like the equivalent shear stress, except applied to the backstress. The value of BACKRN is not permitted to exceed the user specified limit value of N	Pa	Eq. 4.79
—	SV(19) [CRACK]	Flag that equals 1.0 at the onset of softening whenever the maximum tensile cut-off has been applied (or when the limit surface is reached). The geomodel simply replaces the stress with the cut-off stress (user input CUTPS). Physically, complete loss in load-carrying ability in the appropriate direction is actually desired. However, simply replacing the principal stress with zero <i>at the constitutive level</i> would result in mesh-dependencies in host codes that lack macroscale fracture services. More advanced codes should examine the internal state variable flag “CRACK” to determine when this cut-off is being applied (and it is therefore appropriate to initiate void insertion, element death or, preferably, more advanced fracture response).	1	page 77

APPENDIX B. Nomenclature and Data Sets

Symbol or Acronym	ASCII Name	Name and meaning	SI units	defining equation (or page)
—	SV (20) [SHEAR]	Flag equal to 0.0 if the material response is elastic. Otherwise, if positive, the response is plastic. The value ranges from 0.0 if the trial stress rate is tangent to the yield surface to 1.0 if the trial stress rate is normal to the yield surface (i.e., pushing directly against it).	1	Fig. 6.1 page 77
f	SV (21) [YIELD] F	Value of the yield function	Pa ²	Eq. 4.46
$\bar{\theta}$	SV (22) [LODE]	Lode angle in degrees ranging from -30 in triaxial extension to +30 in triaxial compression. The Lode angle is frequently denoted β in other publications about the GeoModel.	deg	Eq. 3.40 page 77
σ_{11}^l	SV (23) [QSSIGXX]	Internal GeoModel variable (quasistatic “low” stress)	Pa	Eq. 5.10
σ_{22}^l	SV (24) [QSSIGYY]	Internal GeoModel variable (quasistatic “low” stress)	Pa	Eq. 5.10
σ_{33}^l	SV (25) [QSSIGZZ]	Internal GeoModel variable (quasistatic “low” stress)	Pa	Eq. 5.10
σ_{12}^l	SV (26) [QSSIGXY]	Internal GeoModel variable (quasistatic “low” stress)	Pa	Eq. 5.10
σ_{23}^l	SV (27) [QSSIGYZ]	Internal GeoModel variable (quasistatic “low” stress)	Pa	Eq. 5.10
σ_{31}^l	SV (28) [QSSIGZX]	Internal GeoModel variable (quasistatic “low” stress)	Pa	Eq. 5.10
$\dot{\lambda}$	SV (29) [DCSP]	Plastic consistency parameter.	$\frac{1}{\text{Pa} \cdot \text{s}}$	Eq. 4.55 Eq. 4.83
κ_L	SV (30) [QSEL]	Internal GeoModel variable (quasistatic “low” value of κ). In Eq. 5.15, q_L stands for any internal state variable. This is the particular instance for which $q_L = \kappa_L$, which is the quasistatic value of the isotropic hardening ISV.	Pa	Eq. 5.15
α_{11}^l	SV (31) [QSBSXX]	Quasistatic backstress. In Eq. 5.15, q_L stands for α_{ij}^l .	Pa	Eq. 5.15
α_{22}^l	SV (32) [QSBSYY]	Quasistatic backstress. In Eq. 5.15, q_L stands for α_{ij}^l .	Pa	Eq. 5.15
α_{33}^l	SV (33) [QSBSZZ]	Quasistatic backstress. In Eq. 5.15, q_L stands for α_{ij}^l .	Pa	Eq. 5.15
α_{12}^l	SV (34) [QSBSXY]	Quasistatic backstress. In Eq. 5.15, q_L stands for α_{ij}^l .	Pa	Eq. 5.15
α_{23}^l	SV (35) [QSBSYZ]	Quasistatic backstress. In Eq. 5.15, q_L stands for α_{ij}^l .	Pa	Eq. 5.15
α_{31}^l	SV (36) [QSBSZX]	Quasistatic backstress. In Eq. 5.15, q_L stands for α_{ij}^l .	Pa	Eq. 5.15

Other symbols (used only in this report)

Symbol or Acronym	ASCII Name	Name and meaning	SI units	defining equation (or page)
C_{ijkl}		Fourth-order elastic stiffness tensor	Pa	Eq. 4.4
δ_{ij}	DELTA	Kronecker delta	1	Eq. 2.4
$\Delta\gamma_{ij}^p$	DEIJPL	Deviatoric plastic strain increment = $\left(\dot{\epsilon}_{ij}^p - \frac{1}{3}\dot{\epsilon}_{kk}^p\delta_{ij}\right)\Delta t$	1	—
$\Delta\epsilon_v^p$	VOLPLAS	Plastic volume strain increment = $\dot{\epsilon}_{kk}^p\Delta t$	1	—
	DFDSIG	Derivative of the plastic potential with respect to stress	—	—
t		time	s	—
Δt	DT	time increment	s	—
E		Young's modulus	Pa	Eq. 4.12
f_f		The part of the meridional yield profile function associated with microcracks; $f_f = F_f - N$	Pa	Fig. 4.6 Eq. 4.29
F_f	FF	Meridional shear limiter function	Pa	Eq. 4.39
f_c		The part of the meridional yield profile function associated with porosity; $f_c = \sqrt{F_c}$	1	Fig. 4.5 Eq. 4.29
F_c	FC	Meridional nominal yield function (Pelessone function)	1	Eq. 4.32 Eq. 4.30
ϕ	PHI	Friction angle (for Mohr-Coulomb theory)	1	Eq. B.3
ϕ	G	Flow potential function	Pa ²	Eq. 4.55
Γ	GAMMAP	Octahedral yield shape function (depends on J3TYPE)	1	page 45
$H_{ij}^\alpha, \underline{H}$		Kinematic hardening modulus tensor	Pa	Eq. 4.78
HYD		Acronym: Hydrostatic loading. The stress is diagonal (no shears).		page 13
I_1	RI1	First stress invariant, $I_1 = \text{tr}\underline{\underline{\sigma}}$. This is positive in tension.	Pa	Eq. 3.9
\bar{I}_1		Negative of I_1 . This is positive in compression	Pa	Eq. 3.9

APPENDIX B. Nomenclature and Data Sets

Symbol or Acronym	ASCII Name	Name and meaning	SI units	defining equation (or page)
J_2	RJ2	Second stress invariant, $J_2 = \frac{1}{2}\text{tr}\underline{\underline{S}}^2$ (never negative). Geometrically, $\sqrt{2J_2}$ equals the magnitude of the stress deviator, and it therefore equals the “length” of the projection of the pseudo stress vector in 3D Haigh-Westergaard (stress) space onto the octahedral-plane (i.e., $\sqrt{2J_2}$ is the Lode radius).	Pa ²	Eq. 3.10
J_2^ξ	RELJ2ZP	Second invariant of the shifted stress	Pa ²	page 8 Eq. 4.22
J_3	RJ3	Third stress invariant, $J_3 = \frac{1}{3}\text{tr}\underline{\underline{S}}^3$. This is positive when the stress deviator is closer to TXE than to TXC.	Pa ³	Eq. 3.11
\bar{J}_3		Negative of J_3 . This is positive when the stress deviator is closer to TXC than to TXE.	Pa ³	Eq. 3.11
J_3^ξ	RELJ3ZP	Third invariant of the shifted stress	Pa ³	page 8 Eq. 4.22
ν		Poisson’s ratio	1	Eq. 4.12
p		Mean stress, $p = \frac{1}{3}\text{tr}\underline{\underline{\sigma}} = \frac{I_1}{3}$. The mean stress is positive in compression. The <i>pressure</i> \bar{p} , which is positive in compression is the negative of the mean stress: $\bar{p} = -p$.	Pa	page 11
\bar{p}		Pressure = negative of mean stress, $\bar{p} = -\frac{1}{3}\text{tr}\underline{\underline{\sigma}} = -\frac{I_1}{3}$	Pa	page 11 Eq. 3.12
Π		Porosity (unloaded).	1	Eq. 4.65
	PONE	Code parameter equal to 1.0	1	—
	PTWO	Code parameter equal to 2.0	1	—
	PFOUR	Code parameter equal to 4.0	1	—
$\underline{\underline{R}}_{\approx}$		Polar rotation tensor	1	Eq. 3.39 Eq. 4.3
ρ		mass density	kg/m ³	
$\underline{\underline{S}}_{\approx}$		Stress deviator, $\underline{\underline{S}}_{\approx} = \underline{\underline{\sigma}} - \frac{1}{3}(\text{tr}\underline{\underline{\sigma}})\underline{\underline{I}}$	Pa	Eq. 3.5
$\underline{\underline{\sigma}}_{\approx}$		The stress tensor.	Pa	Eq. 3.1

Symbol or Acronym	ASCII Name	Name and meaning	SI units	defining equation (or page)
SHR		Acronym: Shear loading (one principal value of the stress deviator is zero and the others are therefore negatives of each other). SHR applies even when all principal stresses are compressive — all that matters is the nature of the stress deviator.	N/A	page 18
TXE		Acronym: Triaxial extension: Two “lateral” principal stresses are equal and the distinct eigenvalue is more tensile than the lateral stresses. A stress state can be in TXE even when all principal stresses are compressive — the axial stress merely needs to be <i>less</i> compressive than the lateral stresses.	N/A	page 15
TXC		Acronym: Triaxial compression (two “lateral” principal stresses are equal and the distinct eigenvalue is more compressive than the lateral stresses)	N/A	page 15
\underline{T}		The Hill tensor, defined to be the deviatoric part of \underline{S}^2 and therefore given by $\underline{T} = \underline{S}^2 - \frac{2}{3}J_2\underline{I}$	Pa	
T_{ijkl}		Plastic tangent stiffness tensor	Pa	Eq. 4.89
τ		Signed equivalent shear stress, $\tau = \text{sign}[\sqrt{J_2}, J_3]$. This equals $\pm\sqrt{J_2}$. It is positive when $J_3 \geq 0$, and negative when $J_3 < 0$.	Pa	Eq. 3.13
$\bar{\tau}$		Negative of τ . This is positive when the stress is closer to TXC, and negative when closer to TXE	Pa	Eq. 3.4
τ	TAU	Characteristic material response time	second	Eq. 5.4
$\bar{\theta}^\xi$	RLODE	Lode angle associated with the shifted stress tensor $\underline{\xi} = \underline{\sigma} - \underline{\alpha}$ ($\bar{\theta}^\xi = 30^\circ$ when $\underline{\xi}$ is TXC and $\bar{\theta}^\xi = +30^\circ$ when $\underline{\xi}$ is TXE).	radian (or deg in plot output)	Eq. 3.40
$\sin 3\bar{\theta}^\xi$	SIN3BTAP	Sine of three times the Lode angle $\bar{\theta}^\xi$	1	Eq. 3.40
$\underline{\zeta}$	ZETA	Shifted stress tensor, $\underline{\xi} = \underline{\sigma} - \underline{\alpha}$. When kinematic hardening is activated, the yield surface origin will be at $\underline{\xi} = \underline{0}$ instead of at the zero stress origin. The backstress tensor $\underline{\alpha}$ represents the amount by which the origin has translated.	Pa	page 58

Datasets

This section cites parameters for some materials that have already been fit to the GeoModel. Datasets undergo continual refinement as additional material data become available, so consult the model developers to obtain the latest values. This section concludes with simplified datasets for mimicking simpler classical theories (Von Mises plasticity, Mohr-Coulomb theory, etc.)

NOTE TO ALEGRA USERS: The GeoModel must be run using the “Generic EOS”. Appropriate EOS parameters are quoted at the bottom of each dataset.

Dataset for Salem Limestone

```

$
$ GeoModel parameters for Salem Limestone
$
B0 = 13.0e9      $Pa
B1 = 42.47e9    $Pa
B2 = 0.4107e9   $Pa
B3 = 12.0e9     $Pa
B4 = 0.021      $Dimensionless
G0 = 9.86e9     $Pa
G1 = 0.0        $Dimensionless
G2 = 0.0        $1/Pa
G3 = 0.0        $Pa
G4 = 0.0        $Dimensionless
RJS = 0.0       $Meters
RKS = 0.0       $Pa/Meter
RKN = 0.0       $Pa/Meter
A1 = 843.02e6   $Pa
A2 = 2.731e-10 $1/Pa
A3 = 821.92e6   $Pa
A4 = 1.e-10     $Radians
P0 = -314.4e6   $Pa
P1 = 1.22e-10  $1/Pa
P2 = 1.28e-18  $1/Pa^2
P3 = 0.084      $strain
CR = 6.0        $Dimensionless
RK = .72        $Dimensionless
RN = 12.e6      $Pa
HC = 100000.e6  $Pa
CTI1 = 3.e6     $Pa
CTPS = 1.e6     $Pa
T1 = 4.e-4      $sec
T2 = 0.835      $1/sec
T3 = 0.0        $Dimensionless
T4 = 0.0        $1/sec
T5 = 0.0        $Pa
T6 = 3.0        $sec
T7 = 0.0        $1/Pa
J3TYPE = 3      $Dimensionless
A2PF = 0.0      $$$$$ = zero means A2PF defaults to A2 for normality
A4PF = 0.0      $$$$$ = zero means A4PF defaults to A4 for normality
CRPF = 0.0      $$$$$ = zero means CRPF defaults to CR for normality
RKPF = 0.0      $$$$$ = zero means RKPF defaults to RK for normality
SUBX = 0.        $Dimensionless

$model 2 generic eos
$ rho ref = 2300.      $ kg/m^3
$ tref = 298.         $ K
$ ref sound speed = 5400.0 $ m/s
$end

```

Dataset for Sidewinder Tuff

```

$ GeoModel parameters for Sidewinder Tuff
$ Units are SI
B0 = 4.0e9          $Pa
B1 = 6.5e9          $Pa
B2 = 0.1e9          $Pa
B3 = 0.0            $Pa
B4 = 0.0            $Dimensionless
G0 = 3.69e9        $Pa
G1 = 0.0            $Dimensionless
G2 = 0.0            $1/Pa
G3 = 0.0            $Pa
G4 = 0.0            $Dimensionless
RJS = 0.0           $Meters
RKS = 0.0           $Pa/Meter
RKN = 0.0           $Pa/Meter
A1 = 496.83e6       $Pa
A2 = 6.293e-10      $1/Pa
A3 = 481.08e6       $Pa
A4 = 1.e-10         $Radians
P0 = -70.e6         $Pa
P1 = 1.8e-11        $1/Pa
P2 = 2.15e-19       $1/Pa^2
P3 = 0.08           $strain
CR = 15.0           $Dimensionless
RK = 0.7            $Dimensionless
RN = 0.0            $Pa
HC = 0.0            $Pa
CTI1 = 3.e6         $Pa
CTPS = 1.e6         $Pa
T1 = 0.0            $sec
T2 = 0.0            $1/sec
T3 = 0.0            $Dimensionless
T4 = 0.0            $1/sec
T5 = 0.0            $Pa
T6 = 0.0            $sec
T7 = 0.0            $1/Pa
J3TYPE = 3          $Dimensionless
A2PF = 0.0          $$$$ default = A2 for normality
A4PF = 0.0          $$$$ default = A4 for normality
CRPF = 0.0          $$$$ default = CR for normality
RKPF = 0.0          $$$$ default = RK for normality

$model 2 generic eos
$ rho ref = 1870.    $ kg/m^3
$ tref = 298.        $ K
$ ref sound speed = 2800.0 $m/s
$end

```

Dataset for lab scale intact Climax Granite

```

$
$ GeoModel parameters for Lab-scale Intact Climax Granite
$
B0 = 43.00e9    $Pa
B1 = 750.0e9    $Pa
B2 = 100.0e9    $Pa
B3 = 0.0        $Pa
B4 = 0.0        $Dimensionless
G0 = 34.73e9    $Pa
G1 = 0.0        $Dimensionless
G2 = 0.0        $Pa
G3 = 0.0        $Pa
G4 = 0.0        $Dimensionless
RJS = 0.0       $Meters (Joint spacing)
RKS = 0.0       $Pa/Meter (Joint shear stiffness)
RKN = 0.0       $Pa/Meter
A1 = 1355.e6    $Pa
A2 = 3.43e-10   $1/Pa
A3 = 1328.e6    $Pa
A4 = 3.82e-2    $Dimensionless
P0 = -556.e6    $Pa
P1 = 9.e-14     $1/Pa
P2 = 0.         $1/Pa^2
P3 = 0.05       $strain
CR = 227.5      $Dimensionless
RK = 0.72       $Dimensionless
RN = 17.0e6     $Pa
HC = 150000.e6  $Pa
CTI1 = 30.e6    $Pa
CTPS = 10.e6    $Pa
T1 = 0.0        $sec
T2 = 0.0        $1/sec
T3 = 0.0        $Dimensionless
T4 = 0.0        $1/sec
T5 = 0.0        $Pa
T6 = 0.0        $sec
T7 = 0.0        $1/Pa
J3TYPE = 3      $dimensionless
$ Flow potential parameters (for associativity, equate with yield parameters)
A2PF = 0.0      $zero means will default to equal A2 (associative)
A4PF = 0.0      $zero means will default to equal A4 (associative)
CRPF = 0.0      $zero means will default to equal CR (associative)
RKPF = 0.0      $zero means will default to equal RK (associative)

$model 2 generic eos
$ rho ref = 2635          $kg/m^3
$ tref = 298             $ K
$ ref sound speed = 17847 $m/s
$ end

```

Dataset for field scale jointed Climax Granite

```

$
$ GeoModel parameters for field-scale JOINTED Climax Granite
$
B0 = 43.00e9    $Pa
B1 = 750.0e9    $Pa
B2 = 100.0e9    $Pa
B3 = 0.0        $Pa
B4 = 0.0        $Dimensionless
G0 = 34.73e9    $Pa
G1 = 0.0        $Dimensionless
G2 = 0.0        $Pa
G3 = 0.0        $Pa
G4 = 0.0        $Dimensionless
RJS = 0.06      $Meters (Joint spacing)
RKS = 8.0e10    $Pa/Meter (Joint shear stiffness)
RKN = 1.6e11    $Pa/Meter
A1 = 1379.e6    $Pa
A2 = 6.51e-11   $1/Pa
A3 = 1328.e6    $Pa
A4 = 0.0        $Dimensionless
P0 = -556.e6    $Pa
P1 = 9.e-14     $1/Pa
P2 = 0.         $1/Pa^2
P3 = 0.05       $strain
CR = 227.5      $Dimensionless
RK = 0.80       $Dimensionless
RN = 17.0e6     $Pa
HC = 150000.e6 $Pa
CTI1 = 30.e6    $Pa
CTPS = 10.e6    $Pa
T1 = 0.0        $sec
T2 = 0.0        $1/sec
T3 = 0.0        $Dimensionless
T4 = 0.0        $1/sec
T5 = 0.0        $Pa
T6 = 0.0        $sec
T7 = 0.0        $1/Pa
J3TYPE = 3      $dimensionless
$ Flow potential parameters (for associativity, equate with yield parameters)
A2PF = 0.0      $zero means will default to equal A2 (associative)
A4PF = 0.0      $zero means will default to equal A4 (associative)
CRPF = 0.0      $zero means will default to equal CR (associative)
RKPF = 0.0      $zero means will default to equal RK (associative)

$model 2 generic eos
$ rho ref = 2635          $kg/m^3
$ tref = 298             $ K
$ ref sound speed = 17847 $m/s
$ end

```

Dataset for 23MPa Concrete

```

B0 = 5.5e9           $Pa
B1 = 28.78e9        $Pa
B2 = 0.623e9        $Pa
B3 = 0.0             $Pa
B4 = 0.0             $Dimensionless
G0 = 1.9026e9        $Pa
G1 = 0.890513        $Dimensionless
G2 = 3.55e-9         $1/Pa
G3 = 0.0             $Pa
G4 = 0.0             $Dimensionless
RJS = 0.0            $Meters
RKS = 0.0            $Pa/m
RKN = 0.0            $Pa/m
A1 = 1255.7e6        $Pa
A2 = 1.93e-10        $1/Pa
A3 = 1248.2e6        $Pa
A4 = 0.0             $Radians
P0 = -1.067e8        $Pa
P1 = 7.66e-10        $1/Pa
P2 = 3.88e-20        $1/Pa^2
P3 = 0.1538          $Dimensionless (strain)
CR = 10.0            $Dimensionless
RK = 1.              $Dimensionless
RN = 3.0e6           $Pa
HC = 1.0e11          $Pa
CTI1 = 3e6           $Pa
CTPS = 1.e6          $Pa
T1 = 0.0             $Sec
T2 = 0.0             $1/Sec
T3 = 0.0             $Dimensionless
T4 = 0.0             $1/Sec
T5 = 0.0             $Pa
T6 = 0.0             $Sec
T7 = 0.0             $1/Pa
J3TYPE=3
A2PF = 0.0 $zero defaults to A2 (associative)
A4PF = 0.0 $zero defaults to A4 (associative)
CRPF = 0.0 $zero defaults to CR (associative)
RKPF = 0.0 $zero defaults to RK (associative)
SUBX = 0.0

$model 2 generic eos
$ rho ref = 2030.          $ kg/m^3
$ tref = 298.              $ K
$ ref sound speed = 4500.0 $ m/s
$end

```

Dataset for Conventional Strength Portland Concrete

```

B0 = 1.0954e10      $Pa
B1 = 0.0            $Pa
B2 = 0.0            $Pa
B3 = 0.0            $Pa
B4 = 0.0            $Dimensionless
G0 = 7.5434e9      $Pa
G1 = 0.0            $Dimensionless
G2 = 0.0            $1/Pa
G3 = 0.0            $Pa
G4 = 0.0            $Dimensionless
RJS = 0.0           $Meters
RKS = 0.0           $Pa/m
RKN = 0.0           $Pa/m
A1 = 4.26455e8     $Pa
A2 = 7.51e-10      $1/Pa
A3 = 4.19116e8     $Pa
A4 = 1.0e-10       $Radians
P0 = -1.95520e8    $Pa
P1 = 1.2354e-9     $1/Pa
P2 = 0.0            $1/Pa^2
P3 = 0.065714     $Dimensionless (strain)
CR = 12.0           $Dimensionless
RK = 1.             $Dimensionless
RN = 0.0            $Pa
HC = 0.0            $Pa
CTI1 = 3.0e6       $Pa
CTPS = 1.0e6       $Pa
T1 = 0.0            $Sec
T2 = 0.0            $1/Sec
T3 = 0.0            $Dimensionless
T4 = 0.0            $1/Sec
T5 = 0.0            $Pa
T6 = 0.0            $Sec
T7 = 0.0            $1/Pa
J3TYPE=3
A2PF = 0.0 $zero defaults to A2 (associative)
A4PF = 0.0 $zero defaults to A4 (associative)
CRPF = 0.0 $zero defaults to CR (associative)
RKPF = 0.0 $zero defaults to RK (associative)
SUBX = 0.0

$model 2 generic eos
$ rho ref = 2250. $(kg/cubic meter)
$ tref = 298.
$ ref sound speed = 3056.0
$end

```

Datasets for mimicking classical (simplified) models

The GeoModel is truly a unification of many simpler theories. By appropriately setting parameters, the GeoModel can be made to exactly replicate results from simpler idealized theories, as illustrated below.

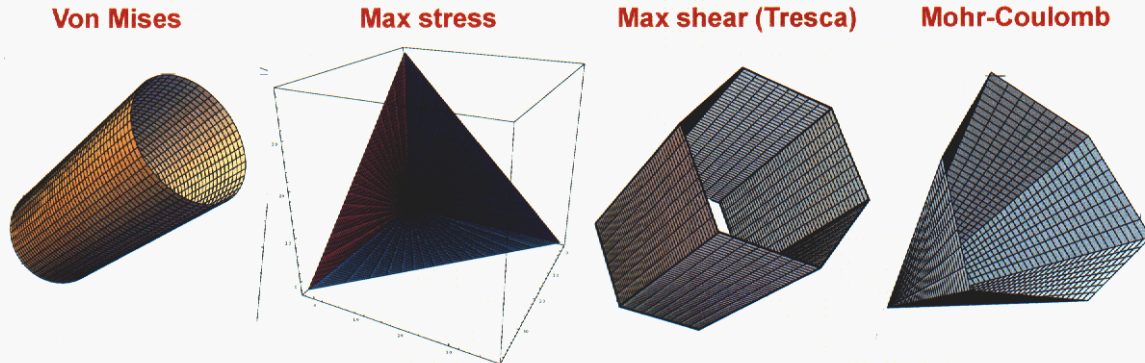


Figure B.1. Other yield surface shapes supported by the GeoModel. The grid lines shown on these sketches correspond to lines of constant z and constant θ .

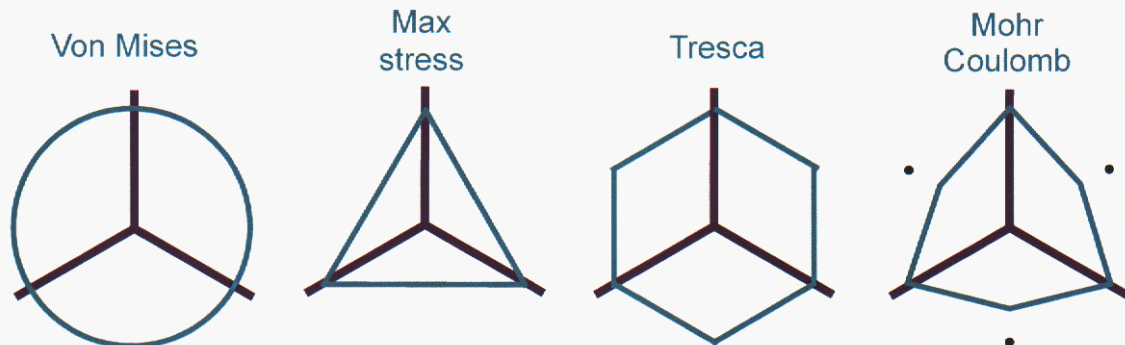


Figure B.2. Classical simplified yield surfaces in the octahedral plane. None of these models adequately describes rock failure surfaces, but the failure surfaces for real rocks sometimes share some qualitative features with these models, depending on the level of confining pressure. In these figures, the axes represent projections of the compressive principal stress axes onto the octahedral plane, taking stress to be positive in *tension*. For the max stress and Mohr-Coulomb models, the size of the octahedral profile increases with pressure. For all of these models, the meridional profile is a straight line.

In most finite-element codes, you can modify an existing data set (e.g., one for a real material) by simply redefining a material parameter *in a separate input line*, leaving the original value unchanged. By deviating from a correct input set to a “toy” input set in this way (rather than over-writing preferred values), you can retain a record of what the material parameters *should be*, thereby mitigating unintentional dissemination of physically bad input sets.

The following specialized input sets use an “aprepro” syntax to show where you need to provide values. Specifically, all required or computed values appear in braces `{}`. Specify numerical values wherever “**VALUE**” appears, and then ensure all other values in braces are computed as shown (they can be computed by hand or piped into aprepro).

Von-Mises material. Von Mises theory can be duplicated by using the following simplified set of GeoModel input values:

```

$
$ GeoModel parameters for replicating non-hardening Von-Mises plasticity
$ All parameters not listed are defaulted to zero.
$ Items in braces must be replaced with numbers
$
A1      = {yield_stress_in_shear = VALUE}
B0      = {linear_elastic_bulk_modulus = VALUE}
G0      = {linear_elastic_shear_modulus = VALUE}

J3TYPE = 1    $Use Gudehaus, which is capable of a circular octohedral profile
RK      = 1    $Set TXE/TXC ratio = 1.0 to make a circlular octahedral profile
P0      = -1.e99 $make yield in hydrostatic compression impossible
CTI1    = 1.e99 $ set pressure cut-off to "infinity"
CTPS    = 1.e99 $ set shear cut-off to "infinity"
CR = 0.001 $ minimize the size of the curved part of the cap
A2 = 0.0
A4 = 0.0
P3 = 0.0
HC=0.0
    T1 = 0.          $sec
    T2 = 0.          $1/sec
    T3 = 0.          $Dimensionless
    T4 = 0.          $1/sec
    T5 = 0.          $Pa
    T6 = 0.          $sec
    T7 = 0.          $1/Pa
RN=0.
P0=-1.e11
A2PF = 0.0
A4PF = 0.0
CRPF = 0.0
RKPF = 0.0

```

This list presumes that your implementation of the GeoModel sets defaults for unlisted parameters.

Maximum Principal Stress failure. The very simplistic fracture criterion that initiates failure when the largest principal stress reaches a critical value can be modeled in the GeoModel by using the following parameter set:

```

$ GeoModel parameters for duplicating a maximum principal stress criterion
$
${max_allowed_principal_stress = VALUE}
B0 = {VALUE}    $bulk modulus
G0 = {VALUE}    $shear_modulus
P0 = -1.e99    $ turn off the cap function
J3TYPE=3
A1={SQRT(3)*max_allowed_principal_stress}
A4={1/SQRT(3.0)}
RK = 0.5
A4PF = {1/SQRT(3.0)}
RKPF = 0.5

```

This list presumes that your implementation of the GeoModel sets defaults for unlisted parameters.

Tresca. The simplistic criterion that a material fails when its largest shear stress reaches a critical value can be modeled by using the following GeoModel parameters:

```
$ User must specify values in braces
B0 = {bulk_modulus}
G0 = {shear_modulus}
P0 = -1.e99      $ turn off the cap function
J3TYPE=3
A1={2.0**yield_stress_in_shear/sqrt(3.0)}
RK = 1.0
RKPF = 1.0
```

This list presumes that your implementation of the GeoModel sets defaults for unlisted parameters.

Mohr-Coulomb.

Classical Mohr-Coulomb theory for brittle failure can be derived from an idealization that the material contains a large population of equal sized cracks. Being all the same size, any given crack loaded in pure shear will fail (grow) if the resolved shear stress τ on the crack face exceeds a critical threshold value S_0 . If a crack face is additionally subjected to a normal compressive stress $\bar{\sigma}_N$, then the applied shear τ needed to induce crack growth must be larger than S_0 by an amount $\tau^{\text{fric}} = \mu \bar{\sigma}_N$, where μ is the coefficient of friction. Stated differently, a given crack is safe from failure if

$$\tau - \tau^{\text{fric}} < S_0, \tag{B.2}$$

or, recalling that $\tau^{\text{fric}} = \mu \bar{\sigma}_N$,

$$\tau - \tan\phi \bar{\sigma}_N < S_0, \quad \text{where} \quad \tan\phi \equiv \mu \tag{B.3}$$

This criterion must be satisfied by *all cracks* in the material. Since Mohr-Coulomb theory arises from an idealization that the material contains a large population of cracks (uniformly random in orientation), a material is safe from failure under general stress states only if all points on the Mohr’s diagram for the stress fall below the “failure line” defined by $\tau = S_0 + \tan\phi \bar{\sigma}_N$. Failure is therefore deemed to occur when the outer Mohr’s circle first “kisses” the failure line. Working out the geometry of Fig. B.3, a circle of radius R , centered at $\bar{\sigma}_N = C$, will be tangent to the failure line if and only if

$$R = S_0 \cos\phi + C \sin\phi \tag{B.4}$$

For the outer Mohr’s circle,

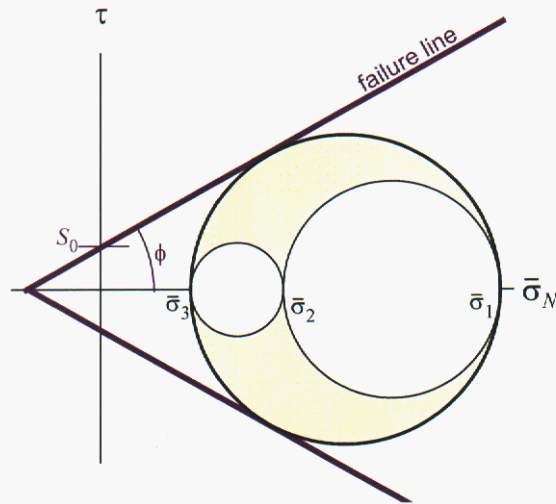


Figure B.3. A stress at the limit state under Mohr-Coulomb theory.

$$R = \frac{\bar{\sigma}_1 - \bar{\sigma}_3}{2} \quad \text{and} \quad C = \frac{\bar{\sigma}_1 + \bar{\sigma}_3}{2} \quad (\text{B.5})$$

or, removing the overbars (defined such that $\bar{\sigma}_k = -\sigma_k$),

$$R = \frac{\sigma_3 - \sigma_1}{2} \quad \text{and} \quad C = \frac{-(\sigma_3 + \sigma_1)}{2} \quad (\text{B.6})$$

Substituting these into Eq. (B.4) gives

$$\boxed{\frac{\sigma_3 - \sigma_1}{2} = S_0 \cos \phi - \frac{\sigma_3 + \sigma_1}{2} \sin \phi} \quad (\text{B.7})$$

This is the Mohr-Coulomb failure criterion cast in terms of principal stresses. Eqs. (3.43a) and (3.43c) on page 24 of the main report imply

$$\frac{\sigma_3 - \sigma_1}{2} = \sqrt{J_2} \cos \bar{\theta} \quad (\text{B.8a})$$

$$\frac{\sigma_3 + \sigma_1}{2} = \frac{I_1}{3} - \frac{\sqrt{J_2}}{\sqrt{3}} \sin \bar{\theta}. \quad (\text{B.9b})$$

Therefore, the stress invariant version of Eq. (B.7) is

$$\sqrt{J_2} \cos \bar{\theta} = S_0 \cos \phi - \frac{I_1}{3} \sin \phi + \frac{\sqrt{J_2}}{\sqrt{3}} \sin \bar{\theta} \sin \phi, \quad (\text{B.10})$$

or, solving for $\sqrt{J_2}$,

$$\sqrt{J_2} = \frac{S_0 \cos \phi - \frac{I_1}{3} \sin \phi}{\cos \bar{\theta} - \frac{1}{\sqrt{3}} \sin \bar{\theta} \sin \phi}. \quad (\text{B.11})$$

Recall from Eq. (4.39) that the GeoModel's limit function F_f fits the *triaxial compression* (TXC) meridional profile to the following functional form

$$\sqrt{J_2} = a_1 - a_3 e^{-a_2 \bar{I}_1} + a_4 \bar{I}_1 \quad \text{in TXC } (\bar{\theta} = 30^\circ) \quad (\text{B.12})$$

In triaxial compression (TXC), the Lode angle is $\bar{\theta} = 30^\circ$ so that

$$\cos \bar{\theta} = \cos 30^\circ = \frac{\sqrt{3}}{2} \quad \text{and} \quad \sin \bar{\theta} = \sin 30^\circ = \frac{1}{2} \quad (\text{B.13})$$

Therefore, Eq. (B.11) specializes to TXC loading as

$$\sqrt{J_2} = \frac{2\sqrt{3}}{3 - \sin \phi} \left(S_0 \cos \phi - \frac{I_1}{3} \sin \phi \right) \quad (\text{Mohr-Coulomb in TXC}) \quad (\text{B.14})$$

Being careful to note that $\bar{I}_1 = -I_1$, comparing this result with Eq. (B.12) implies that the GeoModel limit surface parameters for Mohr-Coulomb theory should be set as

$$a_1 = \left(\frac{2\sqrt{3}}{3 - \sin\phi} \right) S_0 \cos\phi \quad (\text{B.15a})$$

$$a_2 = 0 \quad (\text{B.15b})$$

$$a_3 = 0 \quad (\text{B.15c})$$

$$a_4 = \left(\frac{2\sqrt{3}}{3 - \sin\phi} \right) \frac{\sin\phi}{3} \quad (\text{B.15d})$$

Therefore, the general Mohr-Coulomb criterion in Eq. (B.11) may be written in the form required for the GeoModel as

$$\begin{aligned} \sqrt{J_2} \Gamma(\bar{\theta}) &= f_f(\bar{I}_1) f_c(\bar{I}_1), \\ \text{where } f_f(\bar{I}_1) &= a_1 + a_4 \bar{I}_1, \quad f_c(\bar{I}_1) = 1 \\ \text{and } \Gamma(\bar{\theta}) &= \frac{2\sqrt{3}}{3 - \sin\phi} \left(\cos\bar{\theta} - \frac{\sin\phi \sin\bar{\theta}}{\sqrt{3}} \right) \end{aligned} \quad (\text{B.16})$$

Naturally, `J3TYPE=3` is appropriate. Moreover, to make the cap function f_c equal to 1, the cap and crush curve features should be disabled as described on page B-26. Classical Mohr-Coulomb theory is meant to apply to brittle rupture, so kinematic hardening should be disabled as described on page B-26. An appropriate value for the TXE/TXC strength ratio ψ must be determined by evaluating Eq. (B.11) in TXE where $\bar{\theta} = -30^\circ$:

$$\sqrt{J_2} = \frac{2\sqrt{3}}{3 + \sin\phi} \left(S_0 \cos\phi - \frac{I_1}{3} \sin\phi \right) \quad (\text{Mohr-Coulomb in TXE}) \quad (\text{B.17})$$

The TXE/TXC strength ratio is then given by the ratio of the right-hand sides of Eqs. (B.17) and (B.14):

$$\psi = \frac{3 - \sin\phi}{3 + \sin\phi} \quad (\text{B.18})$$

For this classical Mohr-Coulomb theory, the slope of the TXC meridional profile, $d\sqrt{J_2}/d\bar{I}_1$, equals a_4 . Therefore, $\sin\phi$ may be eliminated from Eqs. (B.15d) and (B.18) to reveal that the TXE/TXC strength ratio is coupled to the slope of the TXC meridional profile according to

$$\psi = \frac{1}{1 + \sqrt{3}A}, \quad \text{where } A \equiv \left(\frac{\partial \sqrt{J_2}}{\partial \bar{I}_1} \right)_{\bar{\theta}=30^\circ} \quad (\text{B.19})$$

This relationship will be explored in future releases of the GeoModel for allowing pressure dependence of the octahedral profile *shape* when (unlike Mohr-Coulomb theory) the meridional profile has a non-constant slope.

Below, we show the skeleton required for setting the GeoModel inputs to run classical Mohr-Coulomb theory. This input set also shows how to set parameters if you wish to run with non-associativity (where the flow potential function differs from the yield function only by having a different value for ϕ). Values for (a_1, a_2, a_3, a_4) and for $(a_2^{\text{PF}}, a_4^{\text{PF}})$ are set by using Eq. (B.15). Values for ψ and ψ^{PF} are set by using Eq. (B.18).

```

$ GeoModel parameters for duplicating a classical Mohr-Coulomb material
$ in BOTH the octahedral and meridional profiles.
$
$ Replace every occurrence of "VALUE" in this file with the appropriate
$ Mohr-Coulomb parameter. You may generate GeoModel input values for the
$ by using the command 'aprepro this_file output_file'. Preferably, if
$ your finite element code supports embedded aprepro directives, then
$ drop this file DIRECTLY into your finite element GeoModel input block.
$
$ {friction_angle = VALUE}      $angle "phi" in GeoModel Appendix B
$ {dilation_angle = VALUE}     $for associativity, this equals "phi"
$
$ {cohesion = VALUE}           $parameter "S_sub0" in GeoModel Appendix B
$                               $This equals yield stress in simple shear.

$ Let Aprepro compute some helper quantities
$ {scalef = 2.0*sqrt(3)/(3.0-sin(friction_angle))}
$ {scaleg = 2.0*sqrt(3)/(3.0-sin(dilation_angle))}
$
B0 = {VALUE} $bulk modulus
G0 = {VALUE} $shear modulus
J3TYPE=3
A1 = {scalef*cohesion*cos(friction_angle)}
A2 = 0.0
A3 = 0.0
A4 = {scalef*sin(friction_angle)/3.0}
RK = {(3.0-sin(friction_angle))/(3.0+sin(friction_angle))}
A1PF = {scaleg*cohesion*cos(dilation_angle)}
A4PF = {scaleg*sin(dilation_angle)/3.0}
RKPF = {(3.0-sin(dilation_angle))/(3.0+sin(dilation_angle))}
P0 = -1.e99      $ turn off the cap and crush-curve features
P1 = 0.0        $ no cap
P2 = 0.0        $ no cap
P3 = 0.0        $ zero porosity
CR = 0.001     $ prevent cap influence on shear response
CRPF = 0.001   $ prevent cap influence on shear response
HC = 0.0       $ disable kinematic hardening
RN = 0.0       $ disable kinematic hardening

```

This list presumes that your implementation of the GeoModel sets defaults for unlisted parameters.

To conclude this appendix, sub-input sets are summarized for controlling various features of the GeoModel.

Sub-input set for linear elasticity.

```
B1 = 0.0
B2 = 0.0
B3 = 0.0
B4 = 0.0
G1 = 0.0
G2 = 0.0
G3 = 0.0
G4 = 0.0
```

Set **B0** to the constant bulk modulus and set **G0** to the constant shear modulus. To additionally disable any form of plasticity, set **A1** to a very large number and disable cut-offs as well as the cap and crush curve as described below.

Sub-input set for “turning off” all rate dependence.

```
T1 = 0.0
T2 = 0.0
T3 = 0.0
T4 = 0.0
T5 = 0.0
T6 = 0.0
T7 = 0.0
```

For **LINEAR** rate dependence, set **T1** to the material's characteristic response time and all other **T** parameters to zero.

Sub-input set for disabling kinematic hardening.

```
HC=0.0
RN=0.0
```

Sub-input set for associativity.

```
CRPF=0.0
RKPF=0.0
A2PF=0.0
A4PF=0.0
```

This list presumes that your implementation of the GeoModel sets defaults for unlisted parameters. If not, associativity requires that all parameters that end in “PF” be set equal to their yield parameter counterparts.

Sub-input set for disabling cap and crush curve.

```
P0      = -1.e99   $put the cap at infinity
P1 = 0.0
P2 = 0.0
P3 = 0.0          $set porosity to zero
CR = 0.001       $ minimize the size of the curved part of the cap
```

This list presumes that your implementation of the GeoModel sets defaults for unlisted parameters. The GeoModel user-input processor and initializer will recognize these inputs as “cap disablers” and adjust the model appropriately.

Sub-input set for disabling tensile cut-off limits.

```
CTI1   = 1.e99   $ set pressure (I1) cut-off to “infinity”
CTPS   = 1.e99   $ set principal stress cut-off to “infinity”
```

This list presumes that your implementation of the GeoModel sets defaults for unlisted parameters.

REFERENCES

- ¹ ALDRIDGE, D.F. (2002) Elastic wave radiation from a pressurized spherical cavity, Sandia National Laboratories Report SAND2002-1882, Albuquerque, NM.
- ² ARGUELLO, J.G., A.F. FOSSUM, D.H. ZEUCH and K.G. EWSUK. (2001) Continuum-based FEM modeling of alumina powder compaction. *KONA*, 19: 166-177.
- ³ ARGYRIS, J.H., FAUST, G., SZIMMAT, J., WARNKE, E.P., and WILLAM, K.J. (1974) Recent developments in the finite element analysis of prestressed concrete reactor vessel, *Nuclear Engrg. Des.* 28, p. 42-75.
- ⁴ BECKER, R. (2003) Lawrence Livermore National Laboratories, unpublished presentation materials.
- ⁵ BLANFORD, M.L. (1998) Jas3d: A multi-strategy iterative code for solid mechanics analysis. Unpublished. Sandia National Laboratories.
- ⁶ BORJA, RONALDO I., SAMA, KOSSI M., and SANZ, PABLO F. (2003) On the numerical integration of three invariant elastoplasticity constitutive models, *Comput. Methods Appl. Mech. Engr.* 192, p. 1227-1258.
- ⁷ BOSWELL, L.F. and CHEN, Z. (1987) A general failure criterion for plain concrete, *Int. J. Solids Struct.* 23, p. 621-630
- ⁸ BOUCHERON, E.A., K.H. BROWN, K.G. BUDGE, S.P. BURNS, D.E. CARROLL, S.K. CARROLL, M.A. CHRISTON, R.R. DRAKE, C.G. GARASI, T.A. HALL, J.S. PEERY, S.V. PETNEY, J. ROBBINS, A.C. ROBINSON, R.M. SUMMERS, T.E. VOTH, and M.K. WONG (2002) ALEGRA: User Input and Physics Descriptions Version 4.2, Sandia National Laboratories Report SAND2002-2775, Albuquerque, NM.
- ⁹ BRANNON, R.M. and W.J. DRUGAN (1993) Influence of non-classical elastic-plastic constitutive features on shock wave existence and spectral solutions, *J. Mech. Phys. Solids* 41:2, p. 297-330.
- ¹⁰ BRANNON, R.M. and M. K. WONG (1996) MIG Version 0.0 Model Interface Guidelines: Rules to Accelerate Installation of Numerical Models Into Any Compliant Parent Code," Sandia National Laboratories Report SAND96-2000, Albuquerque, NM.
- ¹¹ BRANNON, R.M. (2004) Rotation and Reflection: a review of useful theorems associated with orthogonal tensors. Sandia National Laboratories Report SAND-2003-XXXX, Albuquerque, NM, *in process*.
- ¹² DIGIOVANNI, A.A. and J.T. FREDRICH (2003) private communication, Sandia National Laboratories, Albuquerque, NM 87185, USA.
- ¹³ DUVAUT, G. and J.L. LIONS (1972) *Les Inequations en Mecanique et en Physique*, Dunod, Paris.
- ¹⁴ FARNSWORTH, G.V. and A.C. ROBINSON (2003) Improved Kinematic Options in ALEGRA, Sandia National Laboratories Report SAND2003-4510, Albuquerque, NM.
- ¹⁵ FOSSUM, A.F. and R.M. BRANNON (2004) Unified compaction/dilation, strain-rate sensitive, constitutive model for rock mechanics structural analysis applications, *ARMA/NARMS 04-546*, in press.
- ¹⁶ FOSTER, C.D., R.A. REGUEIRO, A.F. FOSSUM, and R.I. BORJA (2004) Implicit numerical integration of a three-invariant, isotropic/kinematic hardening cap plasticity model for geomaterials, *submitted to Elsevier Science*.
- ¹⁷ FREW, D.J., M.J. FORRESTAL, and W. CHEN (2001) A split Hopkinson Pressure Bar Technique to determine compressive stress-strain data for rock materials, *Experimental Mechanics*, 41: 40-46.
- ¹⁸ FUNG, Y.C. (1965) **Foundations of Solid Mechanics**, Prentice-Hall, Englewood Cliffs, NJ.
- ¹⁹ GREENBERG, M.D. (1978) **Foundations of Applied Mathematics**, Prentice-Hall, Englewood Cliffs, NJ.
- ²⁰ GURSON, A.L. (1977) *J. Engng Mater. Technol.*, 99, p. 2.
- ²¹ HOFFMAN, E.L., C.A. LAVIN (2004) WISDM: Weapons Information System and Data Management, Version 2.2.0., Apr. 2002. Sandia National Laboratories. Electronic. Sandia Network.
- ²² JAY, F. (1984), Ed., **IEEE Standard Dictionary of Electrical and Electronic Terms**, Institute of Electrical and Electronic Engineers, ANSI/IEEE Std. 100-1984.
- ²³ JIANG, J., PIETRUSZCZAK, S. (1988) Convexity of yield loci for pressure sensitive materials, *Comput. Geotech.* 5, p. 51-63.
- ²⁴ JOHNSON, G.R. et al. (1994) User Instructions for the 1995 Version of the EPIC Code, Alliant Techsystems, Inc., technical report, Hopkins, Minnesota.

- ²⁵ KNUPP, P. and K. SALARI (2000) Code verification by the method of manufactured solutions, Sandia National Laboratories Report SAND2000-1444, Albuquerque, NM.
- ²⁶ KOTERAS, J.R. and A.S. GULLERUD (2002) **Verification of Computer Codes in Computational Science and Engineering**, Chapman & Hall/CRC.
- ²⁷ LUBLINER, J. (1990) **Plasticity Theory**, Macmillan, New York, NY.
- ²⁸ MATSUOKA, H., and NAKAI, T. (1974) Stress-deformation and strength characteristics of soil under three different principal stresses, *Proc. JSCE* **232**, p. 59-70.
- ²⁹ LADE, P.V., and DUNCAN, J.M. (1975) Elastoplastic stress-strain theory for cohesionless soil, *J. Geotech. Engrg. Div., ASCE* **101**, p. 1037-1053.
- ³⁰ LADE, P.V. (1977) Elasto-plastic stress-strain theory for cohesionless soil with curved yield surfaces, *Int. J. Solids Struct.* **13**, p. 1019-1035.
- ³¹ LUBLINER, JACOB (1990) **Plasticity Theory**, MacMillian, New York.
- ³² MALVERN, L.E. (1969) **Introduction to the Mechanics of a Continuous Medium**, Prentice-Hall, Englewood Cliffs, NJ
- ³³ NEEDLEMAN, A. and J.R. RICE (1978) *Mech. Mater.* **7**, p. 163.
- ³⁴ PELESSONE, D. (1989) A modified formulation of the cap model Gulf Atomic Report GA-C19579, prepared for the Defense Nuclear Agency under Contract DNA-001086-C-0277, January.
- ³⁵ PRESS, W.H., FLANNERY, B.P., TEUKOLSKY, S.A., VETTERLING, W.T. (1992) **Numerical Recipes in FORTRAN**, Cambridge University Press, Melbourne, Australia.
- ³⁶ PUCIK, T.A. (2004) Memorandum of Record, Material Model Driver, 11 April 2004, Pucik Consulting Services.
- ³⁷ PUCIK, T.A. (1993) "A case study of instability and nonuniqueness induced by nonassociated plastic flow", Unpublished Manuscript.
- ³⁸ RASHID, M (1993) Incremental kinematics for finite-element applications. *Int. J. Numerical Meth. in Engr.* **36**, no.23, pp. 3937-3956.
- ³⁹ ROACHE, P.J. (1998) **Verification and Validation in Computational Science and Engineering**, Hermosa publishers, Albuquerque, NM.
- ⁴⁰ SANDLER, I.S. and T.A. PUCIK (1994) Non-uniqueness in dynamic rate-independent non-associated plasticity, in G.Z. Voyiadjis, *et al.* (eds.) **Mechanics of Materials and Structures**, Elsevier Science B.V., New York, pp. 221-240.
- ⁴¹ SANDLER, I.S. and D. RUBIN (1979) An algorithm and a modular subroutine for the cap model, *Int. J. Numer. & Anal. Meth. Geomech.* **3**, p. 173.
- ⁴² SCHWER, L.E., Y.D. MURRY (1994) A three-invariant smooth cap model with mixed hardening, *Int. J. for Num. And Anal. Mech. In Geomech.* **18**: 657-688.
- ⁴³ SENSEY, P.E., A.F. FOSSUM, & T.W. PFEIFLE (1983) Non-associative constitutive laws for low porosity rocks, *Int. J. for Num. and Analytical Meth. in Geomech.* **7**, pp. 101-115.
- ⁴⁴ SIMONS, D. (2003) Single-Element Load Paths to Complement ACTD V&V Problems 1&2, Northrop Grumman Information Technology unpublished presentation slides for ACTD V&V Working Group Meeting, Albuquerque, NM 17 April 2003.
- ⁴⁵ TAYLOR, L.M. and D.P. FLANNAGAN (1989) PRONTO 3D a three-dimensional transient solid dynamics program, Sandia National Laboratories Report SAND87-1912, Albuquerque, NM.
- ⁴⁶ WARREN, T.L., A.F. FOSSUM, and D.J. FREW (2004) Penetration into low strength (23 MPa) concrete: target characterization and simulations. *Int J. Impact Engr.* (accepted).
- ⁴⁷ WILLAM, K.J. and WARNKE, E.P. (1975) Constitutive model for the triaxial behavior of concrete, ISMES Seminar on Concrete Structures Subjected to Triaxial Stresses, Bergamo, Italy, p. 1-30.
- ⁴⁸ WOLFRAM, STEPHEN, **The Mathematica Book**, 4th Ed, Cambridge Univ. Press, 1999.
- ⁴⁹ WONG, M.K., J.R. Weatherby, C.D. Turner, A.C. Robinson, T.A. Haill, D.E. Carroll (2001) Physics Applications in the ALEGRA Framework, *First MIT Conference on Computational Fluid and Solid Mechanics*, June, 2001.

Distribution:

- 4 Applied Research Associates
2760 Eisenhower Avenue, Suite 308
Alexandria, VA 22314
Attn : Scott Blouin
Eric Furbee
Kent Goering
Michale Reed
- 1 Rich Becker
Lawrence Livermore National Laboratory
P. O. Box 808
Livermore, CA 94550
- 1 David Benson
Department of AMES, 0411
University of California; San Diego
La Jolla, CA 92093-0411
- 1 William Bruchey
509 Jacob Tome Highway
Port Deposit, MD 21904-1763
- 1 Dan Burgess
ITT Consultant
1530 Pamela Crest
Redlands, CA 92373
- 1 MS 39180 Kent T. Danielson
Senior Computational Engineer
Network Computing Services, Inc.
Army HPC Research Center at
U.S. Army Engineer Research and Development Center
Waterways Experiment Station
3909 Halls Ferry Rd, CEERD-GM-I
Vicksburg, MS 39180
- 2 Defense Threat Reduction Agency
1680 Texas Street SE
Kirtland AFB, NM 87117-5669
Attn: Eric Rinehart
Ed Tremba
- 1 Michael Greenfield
AMSRD-ARL-WM-TD

Aberdeen Proving Ground
Maryland, 21005-5069

4 Lawrence Livermore National Laboratory
7000 East Ave., Livermore, CA 94550-9234
P.O. Box 808, Livermore, CA 94551-0808
Attn: Lew Glen, MS L200 (1)
Francois Hueze, MS L200 (1)
Tarabay Antouin, MS L206 (1)
Greg Kaye, MS L126 (1)

1 Dr. Kirk S. Hansen
Senior Staff Research Physicist
Shell International Exploration and Production Inc.
Untegrated Technology Development
200 North Dairy Ashford
Houston, Texas 77079

1 Brian Leavy
US Army Research Laboratory
AMSRD-ARL-WM-TA
Aberdeen Proving Ground, MD 21005- 5066

1 Dr. Richard D. Lewis
Program Manager
Technology Directorate
Defense Threat Reduction Agency
6801 Telegraph Road
Alexandria, VA 22310-3398

1 Herb Lindberg
ITT Consultant
18388 Chaparral Drive
Penn Valley, CA 95946

5 Los Alamos National Labs
P.O. Box 1663
Los Alamos, NM 87545
Attn: Dave Steedman, MS F607 (1)
Bob Swift, MS F665 (1)
Wendee Brunish, MS F665 (1)
Ted Carney, MS F665 (1)
Greg Valentine, MS D462 (1)

1 Jay Merritt
ITT Consultant

13086 Oak Crest Drive
Yucaipa, CA 92399-9762

1 Kelly Minnick
NAWCWD 478200D
2400 E Pilot Plant Road, STOP 5402
China Lake, CA 93555-6107

1 Hubert Meyer
AMSRD-ARL-WM-TD
Aberdeen Proving Ground
Maryland, 21005-5069

1 Dr. Michael J. Normandia
US Army Research Laboratory
AMSRD-ARL-WM-TA
Aberdeen Proving Ground, MD 21005

1 Tom Pucik
Pucik Consulting Services
13243 Warren Avenue
Los Angeles, CA 90066-1750

1 K.T. Ramesh
Dept. of Mechanical Engineering
Johns Hopkins University
Latrobe Hall, Room #1
Baltimore, MD 21218

1 John Rowe
PM
Combat Systems
ATTN: SFAE-GCS-CS (John Rowe)
65011 East Eleven Mile Road
Warren, MI 48397-5000

1 Professor John Rudnicki
Department of Civil and Environmental Engineering
and Department of Mechanical Engineering
Northwestern University
2145 Sheridan Road
Evanston, IL. 60208-3109

1 RE/SPEC Inc
3824 Jet Drive, P.O. Box 725
Rapid City, SD 57709-0725
Attn: Gary Callahan

1 Scott E. Schoenfeld
Chief, Impact Physics Branch
AMSRD-ARL-WM-TD
Aberdeen Proving Ground
Maryland, 21005-5069

1 Len Schwer
Schwer Engineering & Consulting
6122 Aaron Court
Windsor, CA 95492-8651

1 Paul E. Senseny
FM Global Research
1151 Boston-Providence Turnpike
Norwood, MA 02062-9102

1 Allen D. Shirley
Building 221
Dahlgren Division
Naval Surface Warfare Center
17320 Dahlgren Road
Dahlgren, VA 22448

1 Dr. Gene Sevin
1782 Kenton Cr.
Lyndhurst, OH 44124

1 Don Simons
Northrop Grumman Information Technology
P.O. Box 471
San Pedro, CA 90733-0471

2 Titan Research & Technology
9410 Topanga Canyon Blvd. Suite 104
Chatsworth, CA 91311-5771
Attn: Russ England
Y. Marvin Ito

1 Dr. Yen Tu, P.E.
Computational Mechanics Branch
Munitions Directorate
101 W. Eglin Blvd., Ste 337

Eglin AFB, FL 32542-6810

1 Dr. Azra Nur Tutuncu
Fluid & Cement Technologies
Global Implementation Leader
Shell International Exploration and Production, Inc.
EP Technology – Wells
P.O. Box 481
Houston, Texas 77001-0481

3 US Army Engineer R&D Center
3909 Halls Ferry Road
Vicksburg, MS 39180-6199
Attn: James D. Cargile
Joe Zelasko
Steve Akers

1 Hong Wang
Post-doc research fellow
Structure Ceramics Group
Div of Metals and Ceramics
Oak Ridge National Laboratory
P.O. Box 2008, MS 6068
Oak Ridge, TN 37830

1 Wolfgang Wawersik
410 Live Oak Loop Rd., NE
Albuquerque, NM 87112

1 Weidlinger Associates, Inc.
4410 El Camino Real, Suite 110
Los Altos, CA 94022
Attn: Howard Levine

1 Prof. Kaspar Willam
CivilEng-Civil,Env&Arch Engin
University of Colorado at Boulder
428 UCB
Boulder, CO 80309-0428

1 T.W. Wright
US Army Research Laboratory
AMSRL-WM-T
4600 Deer Creek Loop
Aberdeen Proving Ground

MD 21005-5069

1	MS 316	P. Yarrington, 9230
1	MS 321	W.J. Camp, 9200
1	MS 370	M.E. Kipp, 9232
1		T.G. Trucano, 9211
1	MS 372	J.F. Holland, 9127
1		J. Jung, 9127
1		D.B. Longcope, 9127
1		G.W. Wellman, 9127
1		Henry Duong, 9127
1		Joe Bishop, 9127
1	MS 376	J.G. Arguello, 9126
1		J.S. Rath, 9127
1		C.M. Stone, 9127
5	MS 378	S. Burns, 9231
1		S.A. Silling, 9232
1		R.M. Summers, 9231
1		P.A. Taylor, 9232
1		J. Robbins, 9231
1		A.C. Robinson, 9231
1		T. Voth, 9231
1		M.K. Wong, 9231
1	MS 380	S.W. Key, 9142
1	MS 437	J.M. McGlaun, 2830
1	MS 521	S.T. Montgomery, 2561
1	MS 576	B.K. Cook, 5531
1	MS 701	P.B. Davies, 6100
1		J.A. Merson, 6102
1	MS 706	D.J. Borns, 6113
1	MS 706	D.E. Munson, 6113
1	MS 735	R.E. Finely, 6115
1	MS 748	S.B. Rodriguez, 6863
1	MS 750	G.J. Elbring, 6116
1		J.T. Fredrich, 6116
1		T.E. Hinkebein, 6118
5	MS 751	R.M. Brannon, 6117
1		D. R. Bronowski, 6117
1		L.S. Costin, 6117
5		A.F. Fossum, 6117
1		Katherine Gaither, 6117
1		R.D. Hardy, 6117
1		J.H. Hofer, 6117
1		D.J. Holcomb, 6117
1		R.P. Jensen, 6117
1		A.R. Lappin, 6117

1		M.Y. Lee, 6117
1		W.A. Olsson, 6117
1		T. Pfeifle, 6117
1		S.R. Sobolik, 6117
1		E.O. Strack, 6117
1	MS 771	F.D. Hansen, 6820
1	MS 834	J.E. Johannes, 9114
1	MS 836	E.S. Hertel, 9116
1	MS 847	W.W. Attaway, 9134
1		H.S. Morgan, 9120
1	MS 893	J.V. Cox, 9123
1		C.A. Lavin, 9123
1		C.S. Lo, 9123
1		J. Pott, 9123
1		W.M. Scherzinger, 9123
1	MS 1089	F.B. Nimick, 6101
1	MS 1160	D.J. Frew, 15412
1		T.L. Warren, 15412
1		D.A. Dederman, 15412
1	MS 1181	T.J. Vogler, 1647
1	MS 9042	D. Kletzli, 8774
1		M.L. Chiesa, 8774
1	MS 9161	E.P. Chen, 8763
1	MS 9201	E.L. Hoffman, 9519
1	MS 9405	E.B. Marin, 8763
3		R.A. Regueiro, 8763.
2	MS 731	Bldg. 823 Library
1	MS 9018	Central Technical Files, 8945-1
2	MS 899	Technical Library, 9616

